MICHIEL WAPPEROM

A THERMODYNAMICS-BASED SIMULATION FRAMEWORK

for modelling of geological CO_2 sequestration

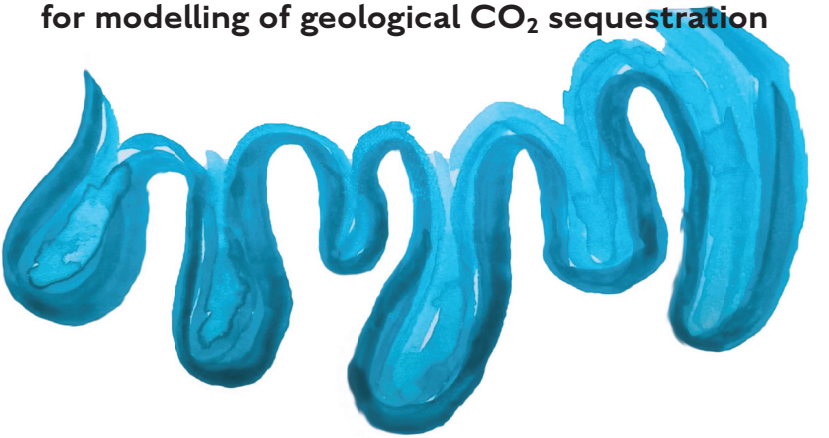

A THERMODYNAMICS-BASED SIMULATION FRAMEWORK
MICHIEL WAPPEROM

A thermodynamics-based simulation framework for modelling of geological CO_2 sequestration

A thermodynamics-based simulation framework for modelling of geological CO_2 sequestration

Dissertation

for the purpose of obtaining the degree of doctor
at Delft University of Technology
by the authority of the Rector Magnificus, prof. dr. ir. H. Bijl,
chair of the Board for Doctorates
to be defended publicly on
Thursday 16 April 2026 at 15:00

by

Michiel Benjamin WAPPEROM

This dissertation has been approved by the promotors.

Composition of the doctoral committee:

Rector Magnificus,	chairperson
Dr. D.V. Voskov,	Delft University of Technology, *promotor*
Dr. D.V. Nichita,	Universite de Pau et des Pays de l'Adour, France, *promotor*
Independent members:	
Dr. R. Farajdazeh,	Delft University of Technology
Prof. dr. ir. T.J.H. Vlugt,	Delft University of Technology
Dr. W. Yan,	Danmarks Tekniske Universitet, Denmark
Prof. dr. ir. C. Secuianu,	University Politehnica of Bucharest, Romania
Dr. H. Gross,	TotalEnergies, USA
Prof. dr. H. Hajibeygi,	Delft University of Technology, reserve member

Keywords: equilibrium thermodynamics, reservoir simulation, CO_2 sequestration

Cover by: Michiel Wapperom and Berk Adsan

An electronic copy of this dissertation is available at
https://repository.tudelft.nl/.

There is no branch of mathematics, however abstract, which may not some day be applied to phenomena of the real world.

Nikolai Lobachevsky

The original source is, of course, Gibbs.

Edward Guggenheim

Contents

Summary

In an attempt to decarbonize industries and support the transition to a sustainable energy supply, subsurface technologies will play a vital role. Security and responsible use of the subsurface for a wide range of decarbonizing technologies require proper understanding and management of all activities. In order to understand the dynamics of all processes involved while having only limited information about underground conditions, numerical simulation presents a pivotal tool for any subsurface operation. Numerical simulation of CO_2 sequestration operations, in particular, aims to model complex multiphase, multiphysics dynamics and demands advanced simulation technology. The conditions for CO_2 injection for storage expose a range of physical phenomena that require careful thermodynamic and physical modelling. The interaction of CO_2 and impurities with brines and residual hydrocarbons, combined with the rather different operational conditions from conventional hydrocarbon production, give rise to complex physical interactions at different scales. To make predictions of subsurface processes whilst having highly limited physical and geological information, reservoir simulation becomes a useful tool only if it addresses the uncertainties and representativeness of the inputs. Despite the availability of more computational efficiency, however, the accuracy of prediction from simulation models is only as good as the physical representation of fluid flow. Accordingly, a greatly improved understanding of subsurface processes can be achieved by means of advanced fluid modelling. This entails an efficient coupling of thermodynamics and fluid flow, an advanced computational framework that enables modelling of complex physics whilst handling nonlinearities appropriately.

This dissertation is set out to develop a robust, flexible and efficient thermodynamics-based simulation framework that is primarily intended for modelling of geological CO_2 sequestration. Using the Operator-Based Linearization (OBL) approach, the thermal-compositional formulation that is available in the existing open-DARTS simulation software is utilized and complex multiphase physics are solved at only discrete points in the parameter space. The main benefit of the OBL technique for such simulations is that the computational burden of thermodynamic calculations is limited and only requires computation of uncomputed supporting points for (multi-)linear interpolation. Furthermore, partial derivatives of all terms are readily obtained by performing interpolation. Hence, the computational load of thermodynamic modelling routines is effectively minimized and the simulation architecture is readily extended to any state specification. The integration of DARTS-flash into the OBL framework for physical modelling extends its applicability to model complex multiphase mixtures containing brine, reservoir fluids, CO_2 and impurities.

Accurate and consistent thermodynamic modelling, coupled with the mass and energy conservation equations, is able to capture effectively the interplay of thermal-compositional phenomena at different scales. Through a thorough review of fundamental thermodynamics, computational techniques and available branches of thermodynamic models, a computational framework is established to solve phase equilibria of reservoir mixtures with brine and CO_2. Starting from a geometrical interpretation of the phase equilibrium problem, efficient initialization procedures are formulated to perform two- and three-phase equilibrium calculations that is readily extended to a higher number of phases. In addition, the approach allows for straightforward use of multiple thermodynamic models together. A hybrid-EoS model that uses a specific fugacity-activity model for the aqueous phase and a Van der Waals-type cubic equation of state for the non-aqueous fluid phases is introduced and validated against experimental data of multiphase mixtures of brine and reservoir fluids. Similarly, the hydrate equation of state is added in the same setup to include different hydrate types into the model. Moreover, the flash procedures are extended to calculate phase equilibria in *PH*- and *PS*-specifications in line with state-of-the-art computational methods for inner and outer loops of the nested algorithms, including fully analytical partial derivatives.

The thermal-compositional framework is applied to a set of simulation scenarios relevant to geological CO_2 sequestration. Two conventional targets for CO_2 injection – saline aquifers and depleted hydrocarbon fields – are investigated in terms of typical conditions and dominating physical phenomena. By means of two recent benchmark studies for CO_2 storage in aquifers, the *FluidFlower* and *SPE11*, the combination of DARTS and DARTS-flash is demonstrated to capture plume migration and capillary trapping, as well as enhanced dissolution and impurity impacts that is in accordance with experimental data and modelling efforts throughout the community. Simulation of CO_2 sequestration in depleted hydrocarbon reservoirs is modelled here in a simplified radial model that mimics the conditions of the highly depleted Porthos field off the coast of Rotterdam, Netherlands. It is, however, a less resolved field of study, as thermal-compositional effects related to expansion cooling and phase changes are much more pronounced. This introduces additional nonlinearities to the simulation from thermodynamic, as well as multiphase flow points of view. While a *PH*-formulation is able to resolve the former, this matter still requires thorough investigation of all coupled processes and nonlinearities to come up with appropriate heuristics. Additionally, the OBL framework is extended to include gas hydrates into the simulation model. By use of a kinetic description of hydrate formation and dissociation, a set of core-scale methane- and CO_2-hydrate formation experiments and field-scale dissociation scenarios for gas production is reproduced from literature.

Samenvatting

In een poging om industriële CO_2-uitstoot te verminderen en een transitie naar een duurzame energievoorziening in te zetten, zullen ondergrondse technologieën een sleutelrol spelen. Veilig en verantwoord gebruik van de ondergrond voor uiteenlopende koolstofarme technologieën vereist een grondig begrip en zorgvuldig beheer van alle ondergrondse activiteiten. Omdat directe waarnemingen van de ondergrond beperkt zijn, vormt numerieke simulatie een onmisbaar hulpmiddel om de dynamiek van ondergrondse processen te doorgronden. Numerieke simulatie van CO_2-opslagoperaties, in het bijzonder, is gericht op het modelleren van buitengewoon complexe meerfasige en multifysische dynamica. De specifieke omstandigheden tijdens CO_2-injectie brengen een breed scala aan fysische processen met zich die een zorgvuldige thermodynamische en fysische modellering vereisen. De interactie van CO_2, onzuiverheden, zout water en resterende koolwaterstoffen uit geologische lagen, in combinatie met de afwijkende operationele omstandigheden ten opzichte van conventionele olie- en gasproductie, leidt tot complexe verschijnselen over verschillende schalen. Aangezien de fysische en geologische informatie over het reservoir doorgaans beperkt is, biedt reservoirsimulatie alleen betrouwbare voorspellingen wanneer de onzekerheden en representativiteit van de input expliciet worden meegenomen. Hoewel de rekencapaciteit sterk is toegenomen, blijft de nauwkeurigheid van simulaties afhankelijk van de fysische weergave van het stromingsmodel. Een beter begrip van ondergrondse processen kan dan ook slechts worden bereikt door middel van geavanceerde vloeistofmodellering, waarin thermodynamica en stromingsleer op efficiënte wijze worden gekoppeld binnen een computationeel raamwerk dat non-lineariteiten adequaat kan behandelen.

Dit proefschrift richt zich op de ontwikkeling van een robuust, flexibel en efficiënt simulatiekader op basis van thermodynamische modellering, dat primair bedoeld is voor de modellering van geologische CO_2-opslag. Er wordt gebruikgemaakt van de thermisch-compositionele formulering van de open-source DARTS simulatiesoftware, die de Operator-Based Linearization (OBL) techniek hanteert. Binnen deze methode hoeven complexe meerfasige fysica slechts te worden opgelost op discrete punten binnen het domein van het probleem. Het belangrijkste voordeel van de OBL-techniek is dat de rekenlast van thermodynamische berekeningen aanzienlijk wordt gereduceerd, aangezien enkel nieuwe steunpunten voor (multi-)lineaire interpolatie hoeven te worden bepaald. Daarnaast kunnen partiële afgeleiden van alle termen direct uit de interpolatie worden verkregen. Hierdoor wordt de rekentijd voor thermodynamische modellering geminimaliseerd en kan de simulatiearchitectuur eenvoudig worden uitgebreid naar verschillende toestandspecificaties. Door de integratie van DARTS-flash in het OBL-raamwerk

wordt de toepasbaarheid voor fysische modellering verder vergroot en kunnen complexe meerfasige mengsels van zout water, reservoirvloeistoffen, CO_2 en onzuiverheden worden gemodelleerd.

Een nauwkeurige en consistente thermodynamische beschrijving, gekoppeld aan de massa- en energiebalansvergelijkingen, maakt het mogelijk om de wisselwerking tussen thermisch-compositionele verschijnselen realistisch weer te geven. Op basis van concepten uit de fundamentele thermodynamica, computationele technieken en thermodynamische modellen is een raamwerk ontwikkeld voor het berekenen van fase-evenwichten in reservoirmengsels met zout water en CO_2. Vanuit een geometrische interpretatie van het fase-evenwichtsprobleem zijn efficiënte procedures opgesteld voor twee- en driefasige evenwichtsberekeningen (*flash*), die eenvoudig zijn uit te breiden naar systemen met meer fasen. De voorgestelde aanpak maakt tevens het simultaan gebruik van meerdere thermodynamische modellen mogelijk. In dit kader is een hybrid-EoS model (van *equation of state*, EoS, toestandsvergelijking) ontwikkeld, op basis van een specifiek *fugacity-activity*-model (vluchtigheid-activiteit) voor de waterige fase en een Van der Waals-type kubieke EoS voor de niet-waterige fasen. Dit model is gevalideerd aan de hand van experimentele data voor mengsels van zout water en reservoirvloeistoffen. Op vergelijkbare wijze is de gashydraat-EoS geïntegreerd om verschillende hydraattypen in de modellen op te nemen. De ontwikkelde flashprocedures zijn uitgebreid om fase-evenwichten te berekenen onder *PH*- en *PS*-specificaties, conform recente computationele methoden voor geneste algoritmen en inclusief volledig analytische partiële afgeleiden.

Het thermisch-compositionele raamwerk is toegepast op een reeks simulatie-scenario's die relevant zijn voor geologische CO_2-opslag. Twee conventionele doelwitten voor CO_2-injectie – aquifers en uitgeputte olie- en gasreservoirs – zijn onderzocht met betrekking tot hun karakteristieke omstandigheden. Aan de hand van recente studies voor CO_2-opslag in aquifers, *FluidFlower* en *SPE11*, is aangetoond dat de combinatie van DARTS en DARTS-flash in staat is om CO_2-migratie en capillaire insluiting, alsook dichtheidsgedreven oplossing en invloed van onzuiverheden adequaat te reproduceren, in overeenstemming met experimentele data en andere onderzoeken. De simulatie van CO_2-injectie in uitgeputte olie- en gasvelden is uitgevoerd met een radiaal model dat de omstandigheden van het gedepleteerde Porthos-veld voor de kust van Rotterdam benadert. Dit onderzoeksgebied is tot op heden beperkt uitgewerkt, mede omdat fysische effecten zoals expansiekoeling en faseovergangen hier sterker tot uiting komen. Deze verschijnselen introduceren bijkomende non-lineariteiten, zowel vanuit thermodynamisch als stromingskundig perspectief. Hoewel een *PH*-formulering in staat is het eerste te beschrijven, is verdere analyse nodig om de gekoppelde complexiteit in detail te karakteriseren en geschikte heuristieken te ontwikkelen. Daarnaast is het OBL-raamwerk uitgebreid met een beschrijving van gashydraten. Door toepassing van een kinetisch model voor hydraatvorming en -dissociatie zijn experimentele waarnemingen voor CH_4- en CO_2-hydraatvorming op laboratoriumschaal, alsmede scenarios voor gasproductie van hydraten op reservoirschaal, succesvol gereproduceerd op basis van literatuurdata.

Preface

Behind us is a long history of climate awareness and over ten years since the Paris agreement, perhaps the most significant global effort to incentivize climate action. Considerable progress has been made since and society seemed to be making an encouraging transition away from fossil fuels. Recent worldwide hostilities have, however, taken over to push these sustainable efforts to the background. It has never been so clear that besides environmental concerns, the world would be better off being less reliant on oil and gas. It is hardly a question whether geopolitics would be so complicated and uncertain if it was not for oil interests. We have come a long way from the Inconvenient Truth regarding human-induced climate change to having cheaper electricity from renewables than from burning fossil fuels today. Yet, we should keep pushing in the right direction because the climate crisis does not resolve by itself.

Behind me, too, is a long journey, filled with a purpose that I somehow had to serve since the Inconvenient Truth was posed. Finding myself on the boundary between energy transition and oil and gas industry, it is not easy to separate the idealism and pragmatism. From a realistic perspective, we are aware that not all industries are ready to operate free of hydrocarbons and we cannot deny that greenhouse gases will continue to be emitted. And even if we no longer actively investigate oil and gas topics, we must appreciate the knowledge from decades of research in our field that current day developments are building on. If it was not for the petroleum industry, the progress in many fields of engineering, thermodynamics and fluid dynamics in particular, would not have been made nearly as far. A topic that is seemingly directly connected to serve the interests of fossil giants, however, the idea to sequester CO_2 in deep geological layers is faced with much skepticism from the public. Of course, this research is directly or indirectly applicable to involve oil production, but we can put it to good use if we want to. It is a dilemma that comes up in any discussion, be it with friends and strangers or in public debate and in politics. I believe, however, that we can make the most effective energy transition if we make use of the existing expertise and infrastructure from oil and gas operations. It is one of the best shots we have to mitigate a climate disaster.

In front of you is my thesis in which I have tried to outline as complete as possible the developments of the thermal-compositional simulation framework for geological CO_2 sequestration. It is two-fold, with the development of a consistent and robust multiphase flash routine as a prerequisite to incorporate any complex physics into the dynamic simulation. Despite minor, yet crucial modifications to the simulation framework, the majority of the convergence problems of our simulations was directly related to errors on the thermodynamics side. Application of the flash to

simulations exposes all edge cases, all tricky mixtures and trace compositions that are obvious to the human eye but extremely tedious for numerical implementation. Now, I think that it is safe to say that the most pressing of basic bugs and mistakes for this part of the modelling framework have been resolved. The simulation technology that we have built over the years is ready to be extended to investigate realistic fluid flow relevant to field-scale operations of real energy transition applications. These are famous last words, but at the beginning of my time at TU Delft I would have signed up for the chance to create such an end product and to contribute to making the energy transition progress.

Michiel Wapperom
Delft, April, 2026

1

Introduction

Earth's natural resources have historically provided a sheer inexhaustible driving force for global human and technological development. Sustained economical growth has significantly improved living standards, brought extraordinary technological progress and supported an expansion of global population from 1 billion in 1800 to 8.2 billion in 2025. This economic growth, however, has traditionally relied on the intensive consumption of resources and energy. We have come to increasing concerns about reaching physical limits of Earth's reserves and harmful interference with ecosystems and global climate. Meanwhile, developing economies in predominantly Asia and Africa are catching up, leading to inevitable additional demand for energy and raw materials. To maintain a balance between prosperous societies and a thriving natural environment, it will be of utmost importance to adopt a responsible attitude towards making use of Earth's riches and protecting the vulnerable ecosystems.

Subsurface development has always been integral to the most basic demands: resource extraction, energy production and storage, water supply. There is the advent of sustainable energy sources such as solar, wind and tidal energy. There is the future promise of nuclear fusion and we are making technological advancements moving towards circular economies. Despite all that, global demand for energy and resources cannot be expected to diminish in the foreseeable future. Moreover, even if we were to reach fully sustainable economies today, we would have to get rid of excess atmospheric CO_2 from preceding industrial activity regardless. It has become increasingly evident that the accumulation of greenhouse gases in the atmosphere has come to pass beyond rather irreversible tipping points in the global ecosystem [1].

Proper management of subsurface activities should be a primary concern. Not only from a safety perspective, but also from the point of view to undertake all operations in a productive and energy-efficient manner. Security and responsible use of the subsurface will become even more crucial with the advent of a range of new decarbonizing technologies. To understand the dynamics of all processes involved while having only limited information about underground conditions, numerical simulation presents a pivotal tool for any subsurface operation.

Reservoir simulation for CO_2 sequestration

Numerical tools for reservoir simulation emerged in the 1970s, in a desire to predict and improve production from hydrocarbon and geothermal reservoirs [2, 3]. Most early reservoir simulators dealt with relatively simple fluid models. Soon, advanced simulation codes with coupled multiphysics dynamics of multiphase fluid flow were being developed for complex systems involving natural gas and oil [4, 5], water- and steamflooding [6, 7], and gas injection processes [8, 9]. Utilization of different formulations to resolve representative physics [10] and advances in efficient linear and nonlinear solvers for ever-growing grid sizes and physical complexity proved crucial for practical use of numerical simulation in field applications [11–14]. Later, purely fluid-flow focused simulation models were extended to include additional physics such as thermal-compositional effects [15, 16], geomechanics [17, 18] and (geo-)chemistry [19–21], expanding the range of applications to predict increasingly complex reservoir dynamics.

For numerical simulation of CO_2 sequestration operations, in particular, modelling of complex multiphase, multiphysics dynamics is involved. While (thermal-)compositional simulation and models for multiphase flow were around for hydrocarbon production, the conditions for CO_2 injection for storage expose a range of physical phenomena that require careful thermodynamic and physical modelling. The interaction of CO_2 and impurities with brines and residual hydrocarbons give rise to complex physical interactions at different scales. In addition, operational conditions are often rather different from conventional hydrocarbon production. Under cold and depleted conditions, injected CO_2 could form a separate liquid phase and introduce highly nonlinear thermodynamic behaviour. Severe expansion cooling and phase changes in the wellbore and near-wellbore region can amplify these conditions, inducing the risk of damage to formation and facilities from freezing and hydrate formation [22, 23]. In addition, the presence of highly saline brine could drive complex interactions between the nearly dry CO_2 injection stream, residual water, precipitating salt and capillary backflow [24, 25].

Reservoir simulation entails only a sub-stage of a larger workflow that involves geophysical exploration and data gathering, geological modelling, well logging and monitoring. To make predictions of subsurface processes whilst having highly limited physical and geological information, reservoir simulation becomes a useful tool only if it addresses the uncertainties and representativeness of the inputs. In practice, this means that large ensembles of relatively finely discretized geological realizations are simulated, demanding huge computational resources. Fortunately, advances in hardware and software design have resulted in extraordinary gains in computer power, as well as efficient parallelization of computations on GPU architectures and AI-based developments for proxy models and preconditioners. This has opened up possibilities to run ever larger and more complex models.

Despite the availability of more computational efficiency, however, the accuracy of prediction from simulation models is only as good as the physical representation of fluid flow. Accordingly, a greatly improved understanding of subsurface processes can be achieved by means of advanced fluid modelling. Contrary to the discretized representation of the reservoir, the accuracy of the multiphysics representation of

fluid flow at Darcy scale has been mathematically established and provides, to a certain extent, a physical ground truth. An improved physical and thermodynamic description thus objectively enhances the quality of a simulation.

Thermodynamic calculations are at the core of compositional simulation. Using the overall composition formulation for solving the conservation equations, the thermodynamic relations can be effectively decoupled from the mass and energy balance [10, 26]. This opens up possibilities to model complex phase behaviour without compromising the linear and nonlinear solvers for flow. However, a thermodynamic equilibrium is then required in each grid cell and at every nonlinear iteration of every timestep, quickly growing to amount to a limiting factor in computational speed. Moreover, a single failure of the thermodynamic modelling routine may hinder convergence of the global conservation equations or propagate an error into following timesteps. Efficient use of parallel computation may improve performance on the level of linear system assembly, but there is not much to gain by parallelizing the small and dense systems for thermodynamic calculations themselves. In addition, the severe nonlinearities introduced by phase transitions, narrow-boiling mixtures and critical points may result in convergence problems when one uses temperature as a variable. While isothermal flashes are inherently less complex than other formulations, the convergence problems can be resolved by using an enthalpy-based specification. This requires a more complex and perhaps less easily parallelizable isenthalpic flash routine.

Recently, alternative approaches have been proposed to relieve the burden of complex physics calculation from simulation and essentially decouple thermodynamics from the flow equations. Voskov and Tchelepi [27] introduced the concept of Compositional Space Parametrization (CSP), in which the compositional space was discretized analogous to how geological models are discretized into a mesh. Phase equilibrium for linear system assembly was then obtained by interpolation of the thermodynamic state with precomputed values at the discrete points [9, 16]. Along similar lines, the CSP concept was later extended to describe full state-dependent terms as they appear in the governing equations and interpolate the terms and obtain partial derivatives for Jacobian assembly using the Operator-Based Linearization (OBL) approach [28, 29]. This technique has been applied to a variety of subsurface energy transition applications [30–32] and was released as open-source software recently [33].

Still, any continuous or discrete modelling approach for capturing complex thermodynamic systems relies on robust, efficient and accurate thermodynamic modelling routines. Furthermore, the benefits of parametrization techniques may start to diminish with certain complexity and dimensionality of the problem, as well as with specific physical problems such as those involving ions and chemistry. Hence, the development of smart and efficient solutions for thermodynamic modelling remains a necessary pillar of any simulation software.

Thermodynamic modelling

The fundamental concepts of classical thermodynamics were developed in the early industrial age in an attempt to improve the efficiency of steam engines. From observed principles, the concepts of internal energy and entropy were introduced and the first and second laws were formulated, making statements about the total energy of a system and the direction for processes to occur spontaneously. Despite these efforts, the development of heat engines didn't benefit a lot from the theory of equilibrium thermodynamics. Nevertheless, the formalization of the fundamental equation and other thermodynamic state functions by Gibbs in the 19th century has become fundamental to our understanding of physical phenomena in many corners of the sciences. In fact, it still forms the basis of most thermodynamic modelling today.

Before the advent of thermodynamic models for widespread engineering use, fluid modelling was informed by approximate thermodynamics by means of *K-value charts* or *PVT-tables*. Using distribution coefficients, K-values, the partitioning of chemical species among gas and liquid phases could be calculated using the computational procedures that came to be known as the *Rachford-Rice* equations [34, 35]. The development of predictive thermodynamic models gave rise to more thermodynamically rigorous modelling routines. Equations of state followed on the pioneering work of Van der Waals to consistently describe the properties of gas and liquid states and into the critical region. Alternatively, phase-specific models were developed for purely liquid and solid phases.

However, it wasn't until the work of Baker *et al.* [36] that the geometric interpretation of computational thermodynamics in the spirit of Gibbs was revisited for engineering applications. While this work discussed the implications of Gibbs' tangent plane criterion for multicomponent systems only on a conceptual level, Michelsen [37] provided a computational implementation of the tangent plane distance (TPD) using an equation of state. By localizing all minima of the TPD surface, the stability of a mixture could be tested in accordance with the fundamental thermodynamic principles. In case of instability, a flash calculation would have to be performed to find the phase split that minimizes Gibbs free energy [38].

Michelsen's methods have been instrumental in the field of equilibrium thermodynamics and are now standard practice in almost any process or reservoir simulation software. The mathematical framework can be generalized to any number of phases [39], to free-water assumptions, pure phases and selective solubility [40, 41]. Formulations for phase equilibria at other state specifications have been developed, posed as minimization problems of the corresponding state functions. PT- and VTn-equilibria could be formulated as unconstrained minimization procedures [38, 42, 43]. Not all constraints can be directly eliminated for other state specifications and modified objective functions (*Q-functions*) are required [44, 45]. Michelsen suggested a direct substitution method, but a more robust solution procedure was the nested PT-flashes of Agarwal *et al.* [46] with an outer loop that locates the root of the specification equation. Recently, Xu *et al.* [47] presented a hybrid root-finding method for isenthalpic flashes that builds on this

approach, utilizing a robust and efficient combination of derivative-free bracketing and gradient-based update of the specification equation where possible. The nested approach can be applied to solve phase equilibria at the most widely used state specifications, either with a PT- or VTn-based Q-function [45]. An interesting direction here could be the VTn-based PT-flash, as (complex) equations of state are naturally formulated in terms of volume and iterative density solvers can be avoided [48, 49]. Full Newton procedures for the other specifications, on the other hand, require good initial guesses and have been scarce in literature [50, 51]. In fact, Nichita [52] showed that the mathematical structure of TPD optimization at all pressure- and volume-based specifications ultimately results in the same stationary points as the stability test at PT and VTn, respectively, indicating that a robust nested procedure is a valid choice.

With PT- and VTn-computations at the core of most equilibrium calculations, many efforts have been focused on improving these solvers. While successive substitution methods to solve the stability test and phase split are extremely robust, the option to switch to Newton methods highly improves performance by avoiding excessive iterations in difficult regions or close to the solution. For VTn-computations, successive substitution does not even guarantee convergence and Newton solvers must be employed. A standard Newton implementation, however, does not always guarantee a descent direction. Michelsen [38] mentioned the use of a modified Cholesky decomposition to preserve positive definiteness of the Hessian matrix, Petitfrere and Nichita [53] investigated Trust Region methods to find the magnitude of the correction and a line search procedure can be employed to check whether the updated variables lie within the feasible region for a full Newton step and to ensure a decrease in the objective function [43, 49].

The demand for accurate models and increased multiphase complexity in relation to CO_2 storage calls for efficient computational procedures. Modelling the interactions of reservoir mixtures with brine, CO_2 and impurities requires higher accuracy compared to the conventional flash routines. Yet, significant improvements in terms of accuracy, applicability, simplicity and performance may be found by revisiting the geometrical framework as Gibbs had intended.

Thesis outline

The aim of this work is to develop a robust, flexible and efficient thermodynamics-based simulation framework that is primarily intended for modelling of geological CO_2 sequestration. Using a combination of the newly developed DARTS-flash [54] and the existing OBL approach, we can utilize a thermal-compositional formulation and solve complex multiphase physics at only discrete points in the parameter space. The main benefit of the OBL technique for such simulations is that the computational burden of thermodynamic calculations is limited and only required to compute uncomputed supporting points for (multi-)linear interpolation. Furthermore, partial derivatives of all terms are readily obtained by performing interpolation. Hence, the computational load of thermodynamic modelling routines is effectively minimized and the simulation architecture is readily extended to any state specification.

Starting from the fundamentals of equilibrium thermodynamics, Chapter 2 reviews the most important concepts of classical thermodynamics. This serves to obtain the different state functions, conditions for equilibrium and a consistent derivation of thermodynamic properties from thermodynamic models. Chapter 3 presents the models utilized in the simulations. These involve Van der Waals-type cubic equations of state, as well as specific models for aqueous and hydrate phases. The fundamentals and models are brought together in Chapter 4, where the concepts of phase equilibrium computations are outlined and applied to model multiphase equilibria of reservoir mixtures involving brine, gas/liquid and hydrate phases. A geometric approach to the phase equilibrium problem is employed, leading to efficient initialization strategies and flexibility to use different thermodynamic models in the process. The framework is extended to *PH*- and *PS*-specifications, including fully analytical partial derivatives.

Chapter 5 outlines the conservation of mass and energy in porous media in partial differential equations and in discretized form. The strong dependence of fluid flow solvers on thermodynamic and transport properties modelling is emphasized, building a case for the Operator-Based Linearization approach. A generic OBL framework for reservoir cells and well controls is developed, with a special remedy for OBL parametrization of multicomponent systems. Sources of nonlinearities in thermal-compositional are discussed. A generic state specification can resolve some of these nonlinearities and is readily implemented in the OBL framework. In addition, a simplified initialization procedure is described to obtain a (near-)steady-state vertical equilibrium with gravity, capillary and thermal forces. The solution method involves the OBL approach to linearize the system of equations and to use a consistent parameter space with the dynamic simulation.

Finally, the full thermodynamics-based simulation framework is applied to a range of subsurface problems relevant to CO_2 sequestration. Chapter 6 involves simulation of CO_2 sequestration in saline aquifers and depleted hydrocarbon fields. These two types of target reservoirs are typically concerned with rather different conditions. The dominating physical phenomena in each are discussed, after which a set of field-scale models is presented. For saline aquifers, two recently established benchmarks include the *FluidFlower* and *SPE11*. As for depleted hydrocarbon reservoirs, a simplified radial model is employed to mimic the conditions in the highly depleted Porthos field in the North Sea oshore, and explore the challenges for these complex multiphase simulations. Chapter 7 introduces gas hydrates into the simulation model. In recent decades, methane hydrates have gained attention as one of the major sources of hydrocarbons on Earth. In addition to being a target for gas production, destabilizing hydrates and thawing permafrost could potentially pose a threat and exacerbate global warming. Modelling of gas hydrates is also of interest to CO_2 sequestration applications, both as an operational risk and as a possible solution for long-term carbon storage by forming a seal to trap CO_2 or exchange CO_2 with guest molecules, mainly CH_4, in existing hydrate deposits. This chapter presents a kinetic model for single-guest CH_4- and CO_2-hydrates and applies it to a range of core- and reservoir-scale simulation cases, setting the stage for further hydrate research.

2

Fundamental concepts of equilibrium thermodynamics

The framework of classical thermodynamics is the theory that is concerned with the transfer and distribution of energy. It provides the direction of change towards an equilibrium state and analyzes the conversion of energy for systems in equilibrium. Classical thermodynamics was initially developed in a desire to improve the efficiency of mechanical heat engines, but have become fundamental to our understanding of chemical equilibria, phase coexistence, solution properties, electrochemical cells and surface phenomena. Thermodynamics is concerned with equilibrium states, and because power production is a non-equilibrium process, it has been said that thermodynamics gained more from heat engines than heat engines gained from thermodynamics.

Classical thermodynamics is a theory of principle: it is founded in empirically observed general properties of phenomena. This means that any mathematical formula that can be deduced from its principles will apply in every case that presents itself. The two fundamental principles that thermodynamics is built on state that total internal energy is conserved, and that heat cannot spontaneously flow from a colder to a hotter body. These observations have historically given rise to the formulation of the first and second laws of thermodynamics.

The framework of classical thermodynamics in itself does not make any statements about the nature and structure of materials that it applies to. Statistical thermodynamics, on the other hand, has provided models for molecular structure and has supported thermodynamic model development that classical theory does not provide.

This section gives an overview of the mathematical framework that constitutes the basis for the majority of multiphase equilibrium calculations. We start from the first and second laws of thermodynamics and develop the fundamental equation of Gibbs in terms of entropy and internal energy. From there, the fundamental equation can be expressed in terms of other thermodynamic potentials (enthalpy, Helmholtz and Gibbs free energy) and conditions for equilibrium and stability are

introduced. In addition, consistent development and evaluation of thermodynamic models is based on mainly two state functions: Helmholtz and Gibbs energy. The second part of this chapter serves to obtain a consistent framework for thermodynamic property calculations from different branches of thermodynamic models.

2.1. Thermodynamic state functions and equilibrium

Classical thermodynamics is concerned with a system where changes within the system are described by state functions. A thermodynamic system is a physical collection of entities. Entities not belonging to the system are denoted the surroundings. For the thermodynamic state functions, line integrals are independent of the path and consequently, the thermodynamic state of the system is uniquely defined by a set of variables that are time independent and defines the thermodynamic state at equilibrium.

The framework of classical thermodynamics, as formalized by Gibbs, starts from the first and second fundamental laws, introducing the state functions of internal energy and entropy. The formulation of the fundamental equation can then be transformed to other variables through mathematical principles, as these may be more accessible. Conditions for equilibrium and stability can be deduced, which will become the basis of multiphase equilibrium calculations in Section 4.

2.1.1. The first and second laws of thermodynamics

The first law states that the total internal energy of a system and its surroundings is conserved. The equivalence principle, as formulated by Thomson, states that when equal amounts of mechanical work are produced from thermal sources or disappear in thermal effects, equivalent amounts of heat disappear or appear [55].

$$\oint dU = 0 \tag{2.1}$$

Any change in internal energy of a system U can be formulated in differential form as

$$dU = dQ + dW \tag{2.2}$$

where U is defined except an additive constant. Heat Q is defined as the entity that flows between regions of different temperatures solely because of a temperature gradient; work W is the energy that originates from any external force that is applied to the system. The differentials dQ and dW are not exact, meaning that $\int_1^2 dQ$ and $\int_1^2 dW$ depend on the path of integration.

The empirical basis of the second law follows from the observation that it is not possible for heat to flow spontaneously from a colder to a hotter body. It can be shown that any reversible cyclic process may be represented as the sum of infinitesimal so-called Carnot cycles, consisting of two adiabatic ($dQ = 0$, no heat

exchanged between system and surroundings) and two isothermal (T = constant) processes. Then holds

$$\oint \frac{dQ}{T} = 0 \tag{2.3}$$

Introducing a state function entropy S, this constitutes the formulation of the second law for reversible processes:

$$dS = \frac{dQ}{T} \tag{2.4}$$

Entropy is, like the internal energy, defined except for an additive constant. For an adiabatic reversible process, the entropy remains constant, and such processes are therefore referred to as isentropic processes.

For any irreversible process, however, it can be shown that the entropy change can only be positive. Consider an adiabatic isolated system consisting of two phases α and β with $T^\alpha > T^\beta$. The change in entropy of the system is equal to the sum of entropy changes in α and β. If the barrier between the phases allows heat to pass, heat will flow from α to β. If no external work is done ($dW = 0$), the entropy changes can be described by

$$dS = \frac{dQ}{T^\beta} - \frac{dQ}{T^\alpha} \tag{2.5}$$

and thus

$$dS \geq 0 \tag{2.6}$$

More generally,

$$dS \geq \frac{dQ}{T} \tag{2.7}$$

This relationship is known as Clausius' inequality. The entropy of a system can thus never decrease. Furthermore, in thermodynamic equilibrium, when all irreversible processes have been completed, the entropy has achieved its maximum value at current conditions.

2.1.2. The fundamental equation

The contribution of work W to the internal energy originates from external forces that are applied to the system. Work from any external force is usually defined so that the differential of the 'work coordinate' dy_j multiplied by its 'generalized force' Y_j gives the work done during a quasi-static change of the system:

$$dW = \sum_j Y_j dy_j \tag{2.8}$$

Examples of work coordinates are volume work ($Y_j = -P, dy_j = dV$), surface tension ($Y_j = \sigma, dy_j = dA$), electrical and magnetic forces ($Y_j = \mathbf{E}, dy_j = d\mathbf{P}$

for electric field strength and polarization, and $Y_j = \mathbf{H}$, $dy_j = d\mathbf{M}$ for magnetic field strength and magnetization). All of these work coordinates are adiabatically freely adjustable. Contributions of gravitational or centrifugal forces are position-dependent and require specific treatment [55].

On an open system where different chemical substances are free to flow in and out, additional variables are associated with the quantities of each of the chemical species. These coordinates are not adiabatically freely adjustable; for instance, there is work done by compression when one adds molecules to a fixed volume. However, a general formulation of the second law can be deduced from the concept of a contact equilibrium for each of the quantities of state, consisting of an extensive parameter X_i with conjugated intensive parameter:

$$Y_i = \frac{\partial S}{\partial X_i} \tag{2.9}$$

For U, it is thermal equilibrium, for V it is pressure equilibrium (mechanical equilibrium), and for n_i it is chemical equilibrium, with an equilibrium of newly introduced quantity of chemical potentials μ_i. Thus, for every phase α containing c components, there exists a function of state

$$S^\alpha = S^\alpha(U^\alpha, V^\alpha, y_2^\alpha, \ldots, y_m^\alpha, n_1^\alpha, \ldots, n_c^\alpha) \tag{2.10}$$

Substituting into (2.2) and (2.4), it is Gibbs' fundamental equation that gives the differential of the entropy as

$$dS^\alpha = \frac{1}{T^\alpha} dU^\alpha + \frac{P^\alpha}{T^\alpha} dV^\alpha - \sum_{j=2}^{m} \frac{Y_j^\alpha}{T^\alpha} dy_j^\alpha - \sum_i \frac{\mu_i^\alpha}{T^\alpha} dn_i^\alpha \tag{2.11}$$

and the entropy of the total system is given by

$$S = \sum_\alpha S^\alpha \tag{2.12}$$

We find that chemical potential reads

$$\mu_i^\alpha = -T \left(\frac{\partial S^\alpha}{\partial n_i^\alpha} \right)_{U^\alpha, V^\alpha, y_j^\alpha, n_k^\alpha \neq n_i^\alpha} \tag{2.13}$$

If a homogeneous system is not in equilibrium, gradients in the intensive properties will give rise to the transport of extensive properties.

Since entropy constitutes a unique, continuous and differentiable function of the internal energy if all other quantities of state are constant, we can equivalently state the fundamental equation (dropping the α) as

$$dU = TdS - PdV + \sum_{j=2}^{m} Y_j dy_j + \sum_{i=1}^{c} \mu_i dn_i \tag{2.14}$$

or

$$U = U(S, V, y_2, \ldots, y_m, n_1, \ldots, n_c) \tag{2.15}$$

The relation (2.14) is referred to as the energy representation of the fundamental equation; (2.11) is the entropy representation. Note that the intensive parameters in (2.14) are obtained by partial derivatives of the internal energy as $Y_i = \frac{\partial U}{\partial X_i}$, rather than from the entropy.

The variables of state in the fundamental equation belong to either of two classes: *extensive* parameters, for which the quantities of the subsystems are additive, and *intensive* parameters, which are defined by means of contact equilibria. The fundamental equation is, in both representations, a function which depends on extensive parameters only. Extensive parameters are homogeneous functions of the first degree in all independent variables. The intensive parameters can be represented as a function of the same independent variables as the corresponding fundamental equation, and these functions are homogeneous and of the zeroth degree.

In most applications of interest in reservoir engineering, PV-work is the most important work contribution, although surface tension can become significant in tight reservoirs, and (electro)chemical equilibria are involved in many applications. From here onward, however, the expressions will be limited to consider volume work only.

Importantly, the fundamental equation in both entropy and energy representations is a characteristic function. It contains all information to uniquely describe its thermodynamic state. The set of variables for other representations of the fundamental equation, as discussed in the next section, must be chosen such that all information is preserved. Any other representation may be useful, but it is not a characteristic function and thus not equivalent.

Euler's theorem and the Gibbs-Duhem equation

The fundamental equation is, in both entropy and energy representations, a homogeneous function of degree one in all independent variables. A homogeneous function $M(\boldsymbol{\alpha}, \mathbf{b})$ of degree m in the variables $\mathbf{b}$ has the property

$$M(\boldsymbol{\alpha}, \lambda \mathbf{b}) = \lambda^m M(\boldsymbol{\alpha}, \mathbf{b}) \tag{2.16}$$

Euler's theorem states that given this function $M(\boldsymbol{\alpha}, \mathbf{b})$ that is homogeneous of degree m in variables $\mathbf{b}$, then

$$\boxed{mM(\boldsymbol{\alpha}, \mathbf{b}) = \sum_i b_i \left(\frac{\partial M(\boldsymbol{\alpha}, \mathbf{b})}{\partial b_i} \right)_{\boldsymbol{\alpha}}} \tag{2.17}$$

If $\boldsymbol{\alpha}$ is the vector of intensive variables ($m = 0$) and $\mathbf{b}$ is the vector of extensive variables ($m = 1$), the internal energy $M = U$ can be written solely in terms of

extensive properties $\mathbf{b} = (S, V, \mathbf{n})$. From (2.17), we can write

$$U = TS - PV + \sum_{i=1}^{C} \mu_i n_i \tag{2.18}$$

This expression, however, has a major limitation for practical applications, because we cannot calculate an absolute value of the entropy and its derived properties. It is more useful to perform calculations in terms of changes of the thermodynamic functions relative to a reference state.

Upon differentiation of (2.18):

$$dU = TdS + SdT - PdV - VdP + \sum_{i=1}^{C} \mu_i dn_i + \sum_{i=1}^{C} n_i d\mu_i \tag{2.19}$$

Comparison of (2.19) with (2.14) yields the following relationship between the intensive parameters:

$$SdT - VdP + \sum_{i=1}^{C} n_i d\mu_i = 0 \tag{2.20}$$

Analogously, in the entropy representation:

$$Ud\left(\frac{1}{T}\right) - Vd\left(\frac{P}{T}\right) + \sum_{i=1}^{C} n_i d\left(\frac{\mu_i}{T}\right) = 0 \tag{2.21}$$

These relationships are also known as the *Gibbs-Duhem equation*.

2.1.3. Other thermodynamic state functions

The fundamental equation in entropy or energy representation contains the maximum possible information thermodynamics can give about a system. However, due to the fact that only extensive parameters occur as independent variables in these representations, their practical implementation introduces great difficulties. Extensive parameters are generally not easily or not at all measurable or controllable. On the other hand, the intensive parameters can often be conveniently measured and controlled experimentally by their nature of contact equilibria. The transformation of the fundamental equation to one with (some) intensive variables, while preserving all information, is thus desirable.

Such a transformation can be obtained by means of a Legendre transform. A Legendre transform changes the independent variables in a function by application of the product rule. The transformation conserves the 'mathematical content' of the original function; it reversibly and uniquely assigns points in the original space to points in the transformed parameter space. The process of transformation can be performed on a subgroup of primary variables, into a $(k+1)$-dimensional subspace of an $(n+1)$-dimensional space. For a function $y = y(x_1, \ldots, x_k, \ldots, x_n)$ with

partial derivatives $p_i = \frac{\partial y}{\partial x_i}$, its k-fold Legendre transform reads:

$$\psi_k = y - \sum_i^k p_i x_i \tag{2.22}$$

and thus $\psi = \psi(p_1, \ldots, p_k, x_{k+1}, \ldots, x_n)$. The differential $d\psi$ is

$$d\psi = -\sum_i^k x_i dp_i + \sum_{j=k+1}^n p_j dx_j \tag{2.23}$$

and the partial derivatives of ψ are

$$\begin{cases} \frac{\partial \psi}{\partial p_i} = -x_i, & \text{if } i \leq k, \\ \frac{\partial \psi}{\partial x_j} = p_j, & \text{if } j > k. \end{cases} \tag{2.24}$$

The fundamental equation with quantities of state X_i becomes

$$U = U(X_i, \ldots, X_r) \quad r \geq c + 2 \tag{2.25}$$

with the intensive parameters

$$P_i = \left(\frac{\partial U}{\partial X_i} \right)_{X_j} \quad i \neq j \tag{2.26}$$

In differential form,

$$dU = \sum_{i=1}^r P_i dX_i \tag{2.27}$$

The Legendre transforms of the fundamental equation in the energy representation yield the general definition of the thermodynamic potentials:

$$\Psi_k = U - \sum_{i=1}^k P_i X_i = \sum_{j=k+1}^r P_j X_j \tag{2.28}$$

Differentiation of (2.28) and substitution of (2.27) gives

$$d\Psi_k = dU - \sum_{i=1}^k X_i dP_i - \sum_{i=1}^k P_i dX_i = -\sum_{i=1}^k X_i dP_i + \sum_{j=k+1}^r P_j dX_j \tag{2.29}$$

It is with the Legendre transforms of the energy representation that characteristic functions in terms of different sets of variables can be obtained. The most important thermodynamic potentials (enthalpy, Helmholtz free energy and Gibbs free energy) are discussed below. Alternatively, the entropy representation can be used to derive characteristic functions analogous to the thermodynamic potentials, referred to as Massieu-Planck functions. In addition, other potentials can be derived, such as the grand potential $\Omega(T, V, \mu)$, which has great significance for use in statistical thermodynamics in relation to the grand canonical ensemble, but it is not in scope here.

Enthalpy

The enthalpy $H(S, P, \mathbf{n})$ can be obtained as a first-order Legendre transform that replaces volume V with its conjugated intensive variable pressure P, as

$$H = U + PV = TS + \sum_{i=1}^{C} \mu_i n_i \tag{2.30}$$

with differential

$$dH = TdS + VdP + \sum_{i=1}^{C} \mu_i dn_i \tag{2.31}$$

The partial derivatives of enthalpy are

$$\left(\frac{\partial H}{\partial S}\right)_{P,\mathbf{n}} = T, \quad \left(\frac{\partial H}{\partial P}\right)_{S,\mathbf{n}} = V, \quad \left(\frac{\partial H}{\partial n_i}\right)_{S,P,n_j \neq n_i} = \mu_i \tag{2.32}$$

If no work is performed on the system except PV-work, the change in enthalpy equals the heat absorbed by the system at constant pressure. The reversible work done by a closed system at constant entropy and constant pressure is equal to the decrease in its enthalpy. Equivalently, the heat introduced into a closed system at constant pressure is equal to the increase in enthalpy. Enthalpy is a useful quantity for measurement of thermal processes that occur at constant pressure.

Helmholtz free energy

The Helmholtz free energy $A(T, V, \mathbf{n})$ can be obtained as a first-order Legendre transform to replace entropy S with its conjugated variable temperature T, as

$$A = U - TS = -PV + \sum_{i=1}^{C} \mu_i n_i \tag{2.33}$$

with differential

$$dA = -SdT - PdV + \sum_{i=1}^{C} \mu_i dn_i \tag{2.34}$$

The partial derivatives of Helmholtz free energy are

$$\left(\frac{\partial A}{\partial T}\right)_{V,\mathbf{n}} = -S, \quad \left(\frac{\partial A}{\partial V}\right)_{T,\mathbf{n}} = -P, \quad \left(\frac{\partial A}{\partial n_i}\right)_{T,V,n_j \neq n_i} = \mu_i \tag{2.35}$$

In a system that is in thermal equilibrium with a reservoir (constant T), where system and reservoir together are adiabatically isolated, and the reservoir cannot do work, the isothermal reversible work done by the system is equal to the decrease in Helmholtz free energy. The Helmholtz free energy is a useful quantity for systems where volume can be kept constant easily or for problems that are primarily concerned with temperature dependence. In addition, volume and temperature are generally the most accessible fluid properties and therefore often used as primary variables for PVT-modelling of fluids.

Gibbs free energy

The Gibbs free energy $G(T, P, \mathbf{n})$ can be obtained as a two-fold Legendre transform, replacing entropy by temperature and volume by pressure, as

$$G = U - TS + PV = \sum_{i=1}^{C} \mu_i n_i \tag{2.36}$$

with differential

$$dG = -SdT + VdP + \sum_{i=1}^{C} \mu_i dn_i \tag{2.37}$$

The partial derivatives of Gibbs free energy are

$$\left(\frac{\partial G}{\partial T}\right)_{P,\mathbf{n}} = -S, \quad \left(\frac{\partial G}{\partial P}\right)_{T,\mathbf{n}} = V, \quad \left(\frac{\partial G}{\partial n_i}\right)_{T,P,n_j \neq n_i} = \mu_i \tag{2.38}$$

In a system coupled with two reservoirs, one of constant temperature and the other of constant pressure, the reversible isothermal-isobaric work done by the system is equal to the change in Gibbs free energy. In the Gibbs free energy, mole numbers are the only extensive parameters. These are easily measurable and controllable, and thus the Gibbs free energy, as well as the chemical potentials, can be computed completely by means of mole numbers.

Expressing thermodynamic properties in terms of other variables

It must be noted that the thermodynamic properties may be written as a function of any complete set of variables. For instance, the use of internal energy U as a thermodynamic potential requires the use of entropy S as an independent variable. Instead, U may be represented as a function of the variables T, V and $\mathbf{n}$, which gives the differential

$$dU = \left(\frac{\partial U}{\partial T}\right)_{V,\mathbf{n}} dT + \left(\frac{\partial U}{\partial V}\right)_{T,\mathbf{n}} dV + \sum_{i=1}^{C} \left(\frac{\partial U}{\partial n_i}\right)_{T,V,n_j \neq n_i} dn_i \tag{2.39}$$

Such a function $U = U(T, V, \mathbf{n})$ is, however, not a characteristic function, as the intensive parameters - pressure and chemical potential - cannot be obtained from it by differentiation as entropy is not uniquely defined. As a result, the two representations of internal energy are not equivalent.

Expressing quantities as a function of more accessible sets of variables, however, is extremely useful. By means of converting partial derivatives, experimentally measurable quantities such as heat capacity at constant volume ($C_V = \left(\frac{\partial U}{\partial T}\right)_{V,\mathbf{n}}$) or heat capacity at constant pressure ($C_P = \left(\frac{\partial H}{\partial T}\right)_{P,\mathbf{n}}$), can be used to compute partial derivatives that are not straightforward or impossible to measure directly. Table 2.1 summarizes the relationship among partial derivatives of thermodynamic properties with respect to volume, temperature and pressure. Note that some

expressions, such as $\left(\frac{\partial U}{\partial P}\right)_{T,\mathbf{n}}$, are left out; all can be computed, but not all are relevant for our purposes. As will be discussed in Chapter 4, it can be shown that VUN- and VSN- based equilibrium calculations rely on VTN-based core functions, while PHN- and PSN-based flashes utilize PT-based properties.

Table 2.1.: Relationship among partial derivatives of thermodynamic properties with respect to volume, temperature and pressure.

M	$\left(\frac{\partial M}{\partial V}\right)_T$	$\left(\frac{\partial M}{\partial P}\right)_T$	$\left(\frac{\partial M}{\partial T}\right)_V$	$\left(\frac{\partial M}{\partial T}\right)_P$
S	$\left(\frac{\partial P}{\partial T}\right)_V$	$-\left(\frac{\partial V}{\partial T}\right)_P$	C_V/T	C_P/T
U	$T\left(\frac{\partial P}{\partial T}\right)_V - P$		C_V	
A	$-P$		$-S$	
H		$V - T\left(\frac{\partial V}{\partial T}\right)_P$		C_P
G		V		$-S$

2.1.4. Conditions for equilibrium and stability

It was discussed earlier that an isolated system approaches equilibrium by increasing its entropy. If any spontaneous process occurs, the increase in entropy must be larger than the corresponding reversible change done:

$$\delta S > \Delta S_{rev} \tag{2.40}$$

The notation δ indicates a 'virtual displacement': an infinitesimal change of state of the first order, maintaining the general conditions governing the system. The equilibrium state is a stationary point in the entropy that is reached when all irreversible processes have been completed, and entropy has achieved its maximum value at current conditions:

$$(\delta S)_{U,V,\mathbf{n}} \leq 0 \tag{2.41}$$

Equivalently, it can be shown that, to be in equilibrium, it is necessary and sufficient that

$$(\delta U)_{S,V,\mathbf{n}} \geq 0 \tag{2.42}$$

One can also include the secondary conditions into the extremum formulation:

$$\delta U - \sum_{i=1}^{k} P_i \delta X_i \geq 0 \tag{2.43}$$

where X_j = constant for $j > k$. Considering only volume work and mole numbers gives:

$$\delta U - T\delta S + P\delta V - \sum_{i=1}^{c} \mu_i \delta n_i \geq 0 \tag{2.44}$$

The conditions (2.41), (2.42) and (2.43) contain only first-order derivatives and therefore do not provide information about the nature of the extremum. We can distinguish three cases:

- A stable equilibrium, where there are virtual displacements Δ for which $(\Delta S)_{U,V,\mathbf{n}} < 0$ or $(\Delta U)_{S,V,\mathbf{n}} > 0$, as obtained from the second law
- A neutral equilibrium, where $(\Delta S)_{U,V,\mathbf{n}} = 0$ or $(\Delta U)_{S,V,\mathbf{n}} = 0$
- An unstable equilibrium, where $(\Delta S)_{U,V,\mathbf{n}} > 0$ or $(\Delta U)_{S,V,\mathbf{n}} < 0$

A fourth case, metastable equilibrium, would be an equilibrium that is stable with respect to infinitesimally near neighbouring states but unstable with respect to states at a finite difference.

Conditions for equilibrium and stability for other thermodynamic potentials

For a system whose intensive parameters P_i are fixed and constant, it can be shown that the condition for equilibrium in terms of any Legendre transform of the fundamental equation is:

$$(\delta \Psi_k)_{P_i,X_j} \geq 0, \quad i \leq k, j > k \tag{2.45a}$$

For constant pressure, entropy and mole numbers:

$$(\delta H)_{P,S,\mathbf{n}} \geq 0 \tag{2.45b}$$

For constant volume, temperature and mole numbers:

$$(\delta A)_{V,T,\mathbf{n}} \geq 0 \tag{2.45c}$$

For constant pressure, temperature and mole numbers:

$$(\delta G)_{P,T,\mathbf{n}} \geq 0 \tag{2.45d}$$

Furthermore, a stable equilibrium in terms of the thermodynamic potentials requires the stationary value to be a minimum:

$$(\Delta \Psi_k)_{P_i,X_j} > 0 \tag{2.46}$$

A system will thus approach equilibrium when enthalpy, Helmholtz free energy or Gibbs free energy is decreasing and equilibrium is a global minimum of the state function.

These statements are, however, less general than the conditions (2.41), (2.42) and (2.43). The reason for this is that those statements make no assumptions about the contact equilibria, while the other thermodynamic potentials do. The secondary conditions for the extremum principle in terms of δS or δU are expressed fully in terms of extensive parameters, and the intensive parameters have only been defined for each phase separately. The formulation of the equilibrium conditions in terms of other thermodynamic potentials, however, implicitly contains the assumption that the intensive variables have the same value for all coexisting phases. In many applications, however, the assumptions of a system where the individual phases are open systems that can exchange energy, work and matter are valid.

Phase stability

For a homogeneous phase in the absence of chemical reactions, the internal energy can be written as

$$U - TS + PV - \sum_{i=1}^{c} \mu_i n_i = 0 \tag{2.47}$$

For a virtual displacement where two phases coexist, the phases denoted by $'$ and $''$, three possibilities are:

- $U' + U'' = U$. This is a neutral equilibrium, in which the formation of the new phase does not change the internal energy as long as the secondary conditions are obeyed ($S' + S'' = S$, $V' + V'' = V$, $n_i' + n_i'' = n_i$)
- $U' + U'' > U$. The formation of the new phase increases the internal energy, a process that cannot occur spontaneously, and the original phase is stable
- $U' + U'' < U$. The formation of the new phase decreases the internal energy. The original phase cannot exist as such and the system will become heterogeneous

This constitutes Gibbs' stability criterion: if, for all fixed extensive parameters, values of the intensive parameters (T, P, μ_i) exist such that the internal energy is lower for a split into more phases, the original phase state is considered unstable. If the change in internal energy is non-negative, the phase under consideration is in neutral or stable equilibrium.

Nichita [52] and Michelsen and Mollerup [56] derived phase stability criteria for different sets of variables. The independent variables are fixed for the total system, but the formation of a new phase, denoted by $'$, results in the transfer of a quantity δ of the extensive property to the new phase. A stable phase satisfies the inequality corresponding to the independent variables for any virtual displacement:

$$\Delta U(V, S, \mathbf{n}) = (T' - T)\delta S - (P' - P)\delta V + \sum_i (\mu_i' - \mu_i)\delta n_i > 0 \tag{2.48a}$$

$$\Delta A(V, T, \mathbf{n}) = -(P' - P)\delta V + \sum_i (\mu_i' - \mu_i)\delta n_i > 0 \tag{2.48b}$$

$$\Delta S(P, H, \mathbf{n}) = \left(\frac{1}{T'} - \frac{1}{T}\right)\delta H - \sum_i \left(\frac{\mu_i'}{T'} - \frac{\mu_i}{T}\right)\delta n_i < 0 \tag{2.48c}$$

$$\Delta H(P, S, \mathbf{n}) = (T' - T)\delta S + \sum_i (\mu_i' - \mu_i)\delta n_i > 0 \tag{2.48d}$$

$$\Delta G(P, T, \mathbf{n}) = \sum_i (\mu_i' - \mu_i)\delta n_i > 0 \tag{2.48e}$$

2.1.5. Gibbs' phase rule

In an isolated, non-reacting system consisting of several phases, the individual phases can be considered as open systems that can exchange energy, work and matter with one another. If we apply the stability conditions to each of these phases, we have:

$$\begin{cases} \delta U^\alpha = T^\alpha \delta S^\alpha - P^\alpha \delta V^\alpha + \sum_{i=1}^{c} \mu_i^\alpha \delta n_i^\alpha \\ \dots \\ \delta U^\gamma = T^\gamma \delta S^\gamma - P^\gamma \delta V^\gamma + \sum_{i=1}^{c} \mu_i^\gamma \delta n_i^\gamma \end{cases} \tag{2.49}$$

According to the general condition for equilibrium, total internal energy, entropy, volume and number of moles for each component i should be fixed:

$$\sum_{j=1}^{n_p} \delta U^j = 0, \quad \sum_{j=1}^{n_p} \delta S^j = 0, \quad \sum_{j=1}^{n_p} \delta V^j = 0, \quad \sum_{j=1}^{n_p} \delta n_i^j = 0, \quad i = 1, \dots, n_c \tag{2.50}$$

This extremum formulation can be treated by means of Lagrange's multipliers:

$$(T^j - \lambda_1)\delta S^j - (P^j - \lambda_2)\delta V^j + \sum_{i=1}^{c} (\mu_i^j - \lambda_{3i})\delta n_i^j \tag{2.51}$$

If we fix one term in each of the sums such that one bracket vanishes, it follows that the equation can only be satisfied if all the remaining brackets also vanish. For each j and i:

$$\lambda_1 = T^j, \quad \lambda_2 = P^j, \quad \lambda_{3i} = \mu_i^j \tag{2.52}$$

Therefore, T, P and μ_i should be uniform throughout the system, which is then in thermal, mechanical and chemical equilibrium:

$$T^j = T^\alpha, \quad j \neq \alpha \tag{2.53a}$$

$$P^j = P^\alpha, \quad j \neq \alpha \tag{2.53b}$$

$$\mu_i^j = \mu_i^\alpha, \quad j \neq \alpha \text{ and } i = 1, \dots, n_c \tag{2.53c}$$

Under these simplest conditions, we have $(n_c + 2)n_p$ independent variables S^j, V^j and n_i^j and an equal number of equations from (2.53) and secondary conditions of fixed total entropy, volume and moles. Under other assumptions, however, other conditions may arise. It may be, for instance, that not all species can be freely exchanged (semipermeable membranes), which could give rise to osmotic pressures.

A useful concept is that of Gibbs' phase rule, which states how many variables of state can be varied independently for given values of n_c components and n_p phases. Using the result from (2.53), we have $n_c + 2$ variables and an equation for each of the phases. The number of freely adjustable variables F is, therefore:

$$F = n_c + 2 - n_p \tag{2.54}$$

Phase diagrams

The implications of the equilibrium conditions in the form of Gibbs' phase rule can be related to what we can observe in phase diagrams. Where $n_c + 2$ phases coexist at equilibrium, the number of degrees of freedom is equal to $F = 0$ and these conditions can be found only for a particular set of values for P, T and μ_i. This is an *invariant* equilibrium, represented by a point in an $(n_c + 1)$-dimensional phase diagram. A *univariant* equilibrium involves $n_c + 1$ phases, and is represented by a line, or coexistence curve. For conditions where more degrees of freedom are available, the system is *multivariant* and the coexistence "curve" becomes a two- or higher-dimensional shape.

For single-component systems, invariant equilibria correspond to the coexistence of three phases, known as a triple point. Two-phase equilibria are represented by a line in a PT-diagram (Figure 2.1). An important result for the coexistence curve is the *Clausius-Clapeyron equation*. By definition, Gibbs free energies (and thus chemical potentials) are equal between the two phases, and equating the Gibbs-Duhem equations for both phases using (2.53) gives:

$$-S^{\alpha}dT + V^{\alpha}dP = -S^{\beta}dT + V^{\beta}dP \tag{2.55}$$

As a result:

$$\frac{dP}{dT} = \frac{S^{\alpha} - S^{\beta}}{V^{\alpha} - V^{\beta}} \tag{2.56}$$

Substituting $G = H - TS$ gives a more useful relation:

$$\frac{dP}{dT} = \frac{H^{\alpha} - H^{\beta}}{T(V^{\alpha} - V^{\beta})} \tag{2.57}$$

The enthalpy difference is the heat related to the phase change and can be observed as a discontinuity when plotting the total enthalpy along an isobar or isotherm.

For n_c-component systems, invariant equilibria are associated with conditions where $n_c + 2$ phases coexist, such as quadruple points for a binary system. The behaviour of multicomponent mixtures and their phase diagrams is much more complex than in the single-component case, however. In literature, binary systems have been most thorouhly studied to understand the nature of multicomponent systems and general phenomena in phase diagrams [57–59].

Critical phases

Throughout the thermodynamic space, quantities can vary such that two or more phases ultimately become identical. Such phases are called a critical phase. A critical phase that does not coexist with other phases has $n_c - 1$ thermodynamic degrees of freedom.

For single-component systems, critical phases have no degrees of freedom and are therefore represented by a critical point. Vapour-liquid equilibria always have a critical point. At temperatures beyond the critical temperature, a continuous

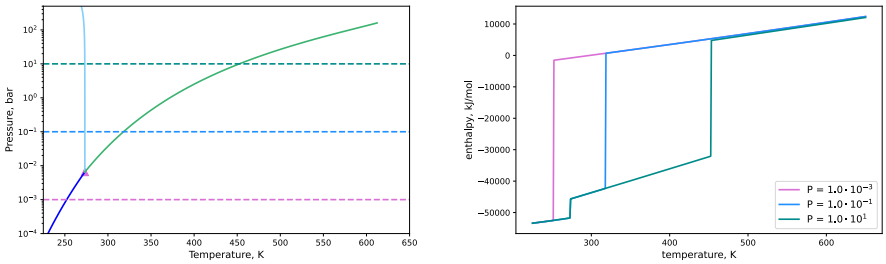

(a) *PT*-diagram (b) Enthalpy along isobars

Figure 2.1.: Pure H_2O phase diagram and isobars.

transition from vapour-like to liquid-like states occurs. No critical point has ever been found for solid-liquid equilibria.

For binary and multicomponent systems, $n_c - 1$ degrees of freedom remain. These degrees of freedom are often used to fix pressure, temperature or composition variables, and then critical conditions are associated with a single point again. An interesting phenomenon that occurs in multicomponent systems is that of retrograde condensation or vaporization, when at temperatures beyond the critical point, further compression causes the amount of liquid to decrease.

From the phase rule, a normal phase has $n_c + 1$ degrees of freedom. A critical phase is thus described by two equations. For single-component systems, the conditions can be easily deduced by considering isotherms on a *PV*-diagram. The critical point corresponds to the conditions where the inflection point has a horizontal tangent:

$$\left(\frac{\partial P}{\partial V}\right)_T = 0 \quad \text{and} \quad \left(\frac{\partial^2 P}{\partial V^2}\right)_T = 0 \tag{2.58}$$

For binary systems, an analogous representation can be obtained from isotherms on a μx-diagram. A more rigorous thermodynamic criterion for critical phases by means of "Gibbs determinants" is rooted in thermodynamic stability theory, but this is of less straightforward direct use [55]. Some efforts have been made to apply equations of state to the determinants-based criteria [60, 61], but the Gibbs determinant conditions were replaced by more efficient procedures [62–64].

2.2. Thermodynamic properties

The concepts of classical thermodynamics are used to relate thermodynamic properties to PVT-behaviour of the system. We discuss ideal and nonideal behaviour of phases and distinguish ideal and residual contributions to thermodynamic properties. Analogous to this, the concept of fugacity is introduced, a property that becomes pivotal in equilibrium calculations. A range of models exists for which pressure, volume and temperature are explicitly related, and all thermodynamic properties can be obtained by means of partial derivatives of the residual Helmholtz function. Conversely, thermodynamic properties can be calculated using the partial derivatives of the fugacity coefficient for models that do not provide a PVT-relation. Lastly, the concepts of activity and activity coefficients provide a different means to correlate fluid behaviour.

2.2.1. Ideal and nonideal behaviour

The hypothetical perfect gas state is described with the ideal gas equation of state

$$P^* = nRT/V \tag{2.59}$$

This is hypothetical state, because even in a gas with no attraction forces, the minimum volume is bounded by the hard-sphere volume of the particles themselves. In addition, all sorts of attraction and repulsion forces add to the nonideality. In the most general sense, the equation of state for a real gas can be described by introducing the compressibility factor Z:

$$P = ZnRT/V \tag{2.60}$$

For an ideal gas, the compressibility factor is equal to one. Figure 2.2 shows the PV-diagram of pure CO_2 from the NIST database [65] compared to the ideal gas curve (a) and the corresponding compressibility factor (b). The gas exhibits increasingly ideal gas behaviour for lower pressures. Note that for high pressures, ideal gas behaviour will yield densities below hard-sphere volumes.

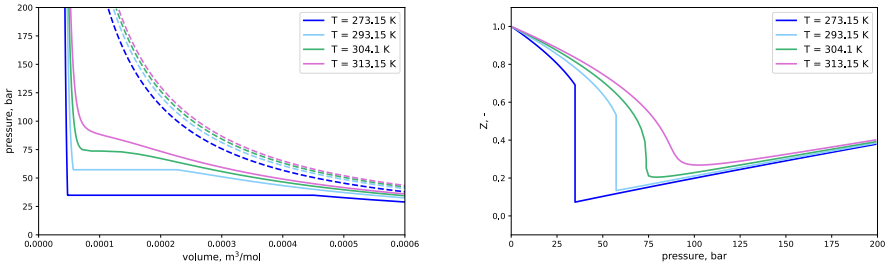

(a) Pressure-volume diagram

(b) Compressibility factor

Figure 2.2.: Ideal and real gas behaviour of CO_2.

Ideal and residual properties

It was discussed that, within the framework of classical thermodynamics, we cannot calculate an absolute value of entropy and chemical potentials. We can, however, measure changes in the extensive properties experimentally, and for most calculations, fortunately, we are only concerned with changes of properties relative to an (arbitrary) zero. Often, the choice of zero is the state of a gas at temperature T_0 and zero density and pressure. The property M at $(V, T, \mathbf{n})$ or $(P, T, \mathbf{n})$ can be calculated by mixing the gases at temperature T_0 and zero density and pressure, then heating the mixture to the temperature T and then compressing it to the volume or pressure of the state:

$$M = \Delta M^* + \int_{T_0}^{T} \left(\frac{\partial M^*}{\partial T}\right)_{V=\infty,n} dT + \int_{\infty}^{V} \left(\frac{\partial M}{\partial V}\right)_{T,n} dV \tag{2.61a}$$

$$M = \Delta M^* + \int_{T_0}^{T} \left(\frac{\partial M^*}{\partial T}\right)_{P=0,n} dT + \int_{0}^{P} \left(\frac{\partial M}{\partial P}\right)_{T,n} dP \tag{2.61b}$$

The right-hand sides of these equations can be rearranged to comprise two terms: one is the property M^* of an ideal gas at the state $(V, T, \mathbf{n})$ or $(P, T, \mathbf{n})$ over the chosen zero, and a second term M^r, which is the difference between the property of the real mixture and that of an ideal gas at the same state. For a property defined at the state $(V, T, \mathbf{n})$,

$$M = M^*(V, T, \mathbf{n}) + M^r(V, T, \mathbf{n}) \tag{2.62a}$$

where

$$M^*(V, T, \mathbf{n}) = \Delta M^* + \int_{T_0}^{T} \left(\frac{\partial M^*}{\partial T}\right)_{V=\infty,n} dT + \int_{\infty}^{V} \left(\frac{\partial M^*}{\partial V}\right)_{T,n} dV \tag{2.62b}$$

and

$$M^r(V, T, \mathbf{n}) = \int_{\infty}^{V} \left(\left(\frac{\partial M}{\partial V}\right)_{T,n} - \left(\frac{\partial M^*}{\partial V}\right)_{T,n}\right) dV \tag{2.62c}$$

For a property defined at the state $(P, T, \mathbf{n})$,

$$M = M^*(P, T, \mathbf{n}) + M^r(P, T, \mathbf{n}) \tag{2.63a}$$

where

$$M^*(P, T, \mathbf{n}) = \Delta M^* + \int_{T_0}^{T} \left(\frac{\partial M^*}{\partial T}\right)_{P=0,n} dT + \int_{0}^{P} \left(\frac{\partial M^*}{\partial P}\right)_{T,n} dP \tag{2.63b}$$

and

$$M^r(P, T, \mathbf{n}) = \int_{0}^{P} \left(\left(\frac{\partial M}{\partial P}\right)_{T,n} - \left(\frac{\partial M^*}{\partial P}\right)_{T,n}\right) dP \tag{2.63c}$$

Ideal gas properties

The ideal gas contribution to total properties, by definition, does not include any interactions between molecules and thus solely depends on internal degrees of freedom within the particles (vibrational and rotational modes). The energy state and partition functions of the different degrees of freedom can be expressed using statistical mechanical models of molecules, but the number of parameters required in such calculations grows quickly with the number of atoms. Only an expression of ideal gas heat capacities at constant volume or pressure is required, commonly expressed in simple power-series form Passut and Danner [66]:

$$C_P^*(T) = A + BT + CT^2 + DT^3 + ET^4 \tag{2.64}$$

Alternatively, Aly and Lee [67] derived a functional form of ideal gas heat capacities that is based on characteristic vibrational and rotational temperatures from statistical thermodynamic theory:

$$C_P^*(T) = A + B\left[\frac{C/T}{\sinh(C/T)}\right]^2 + D\left[\frac{E/T}{\cosh(E/T)}\right]^2 \tag{2.65}$$

Ideal gas heat capacities at constant volume and pressure are related by:

$$C_P^* = C_V^* - R \tag{2.66}$$

Then, other properties can be obtained by applying the thermodynamic relations. If the properties are evaluated at $(V, T, \mathbf{n})$, internal energy can be calculated as:

$$\Delta U^* = \int_{T_0}^{T} C_V^* dT \tag{2.67}$$

The entropy can be deduced from the fundamental equation (2.11), substituting $dU = C_V^* dT$ and $PdV/T = nR/VdV$:

$$\Delta S^* = \int_{T_0}^{T} \frac{C_V^*}{T} dT + \int_{V_0}^{V} \frac{nR}{V} dV = \int_{T_0}^{T} \frac{C_V^*}{T} dT + nR \ln \frac{V}{V_0} \tag{2.68}$$

The Helmholtz free energy follows from the relation:

$$\Delta A^* = \Delta U^* - T\Delta S^* \tag{2.69}$$

If the properties are evaluated at $(P, T, \mathbf{n})$, enthalpy can be calculated as:

$$\Delta H^* = \int_{T_0}^{T} C_P^* dT \tag{2.70}$$

The entropy can be deduced from the fundamental equation (2.31), substituting $dH = C_P^* dT$ and $VdP/T = nR/PdP$:

$$\Delta S^* = \int_{T_0}^{T} \frac{C_P^*}{T} dT - \int_{P_0}^{P} \frac{nR}{P} dP = \int_{T_0}^{T} \frac{C_P^*}{T} dT - nR \ln \frac{P}{P_0} \tag{2.71}$$

The Gibbs free energy follows from the relation:

$$\Delta G^* = \Delta H^* - T\Delta S^* \tag{2.72}$$

The mixture internal energies and enthalpies are calculated by a summation over all the mole fractions:

$$H^*(T) = \sum_i n_i H_i^*(T) \tag{2.73}$$

Entropies, however, contain an additional term that results from (ideal) mixing. As introduced in Section 2.2.3, the activities of an ideal mixture are defined to equal the mole fraction. Chemical potentials then read:

$$\mu_i^{id}(P, T, \mathbf{n}) \equiv \mu_i(P, T) + RT \ln x_i \tag{2.89}$$

Its Gibbs free energy is then

$$G^{id}(P, T, \mathbf{n}) = \sum_i n_i \mu_i(P, T) + RT \sum_i n_i \ln x_i \tag{2.74}$$

and from its partial derivative with respect to temperature, we obtain the entropy:

$$S^{id}(P, T, \mathbf{n}) = -\left(\frac{\partial G^{id}(P, T, \mathbf{n})}{\partial T}\right)_{P,\mathbf{n}} = \sum_i S_i^*(P, T, \mathbf{n}) - R \sum_i n_i \ln x_i \tag{2.75}$$

Residual properties

Residual properties can be obtained from an equation of state describing the PVT-behaviour of a fluid. By means of thermodynamic relations, all residual properties can be obtained from the pressure equation and residual Helmholtz free energy $A^r(V, T, \mathbf{n})$ and partial derivatives. Table 2.2 summarizes the most important residual properties at volume-based and pressure-based specifications. Note the difference between the sets of volume- and pressure-based residual properties. The total properties at $(V, T, \mathbf{n})$ and $(P, T, \mathbf{n})$ are equal, but there exists a difference in integration of the ideal gas state from V_0 to V and P_0 to P [56].

It was discussed that partial derivatives of thermodynamic properties can be expressed in any set of variables, irrespective of the function being a characteristic function, and they can be related to other thermodynamic quantities by means of partial derivatives of the PVT-relation (Table 2.1). The partial derivatives of residual entropy, enthalpy and Gibbs free energy with respect to P and T, therefore, do not need to be calculated, and only the partial derivatives of the residual properties with respect to mole numbers are required. For instance:

$$\left(\frac{\partial S^r}{\partial n_k}\right)_{P,T,n_j \neq n_k} = \left(\frac{\partial^2 A^r}{\partial T \partial n_k}\right)_{V,n_j \neq n_k} + R\left[\ln Z + \frac{n}{Z}\left(\frac{\partial Z}{\partial n_k}\right)_{P,T,n_j \neq n_k}\right] \tag{2.76}$$

Such partial derivatives require careful implementation, as the expressions contain secondary properties (P, V, Z) that are a function of mole numbers. Note that (2.76) does not constitute a chemical potential, as the thermodynamic property is not an intensive property from a characteristic function of the fundamental equation as discussed in Section 2.1.3.

Table 2.2.: Bulk residual properties

	$(V, T, \mathbf{n})$	$(P, T, \mathbf{n})$
S^r	$-\left(\frac{\partial A^r}{\partial T}\right)_{V,\mathbf{n}}$	$S^r(V, T, \mathbf{n}) + nR \ln Z$
A^r	$-\int_{\infty}^{V}\left(P - nRT/V\right)dV$	$A^r(V, T, \mathbf{n}) - nRT \ln Z$
G^r	$A^r(V, T, \mathbf{n}) + PV - nRT$	$G^r(V, T, \mathbf{n}) - nRT \ln Z$
U^r	$A^r(V, T, \mathbf{n}) - TS^r(V, T, \mathbf{n})$	$U^r(V, T, \mathbf{n})$
H^r	$G^r(V, T, \mathbf{n}) - TS^r(V, T, \mathbf{n})$	$H^r(V, T, \mathbf{n})$
C_V^r	$-T\left(\frac{\partial^2 A^r}{\partial T^2}\right)_{V,\mathbf{n}}$	$C_V^r(V, T, \mathbf{n})$
C_P^r	$C_V^r(V, T, \mathbf{n}) + T\left(\frac{\partial P}{\partial T}\right)_{V,\mathbf{n}}\left(\frac{\partial V}{\partial T}\right)_{P,\mathbf{n}} - nR$	$C_P^r(V, T, \mathbf{n})$

2.2.2. Chemical potentials and fugacity

Analogous to the residual properties, the fugacity $\hat{f}_i$ of component i in a mixture is defined as the difference between the chemical potential of component i and that in the hypothetical ideal gas state:

$$RT \ln \hat{\varphi}_i(P, T, \mathbf{n}) = RT \ln \frac{\hat{f}_i(P, T, \mathbf{n})}{P x_i} \tag{2.77}$$

$$= \mu_i(P, T, \mathbf{n}) - \mu_i^*(P, T, \mathbf{n}) \tag{2.78}$$

where $\hat{\varphi}_i = \hat{f}_i / P x_i$ is the fugacity coefficient of component i in the mixture, which is unity for an ideal gas. Note that this expression is equivalent to the partial molar Gibbs free energy of component i. Fugacity has units of pressure, and for an ideal gas, the fugacity of component i in the mixture is equal to its partial pressure.

Fugacity and partial derivatives from *PVT*-relation

Chemical potentials at $\mu_i(V, T, \mathbf{n})$ and $\mu_i(P, T, \mathbf{n})$ are equal. However, similar to the other thermodynamic properties, a difference exists between the chemical potential of a hypothetical ideal gas at two states $(V, T, \mathbf{n})$ and $(P, T, \mathbf{n})$:

$$\mu_i^*(V, T, \mathbf{n}) - \mu_i^*(P, T, \mathbf{n}) = -RT \ln Z \tag{2.79}$$

Utilizing this, we can show that the fugacity coefficient of species i in the mixture and its partial derivatives can be calculated from the expression of the residual Helmholtz free energy and its partial derivatives [68, 69]:

$$\begin{aligned} RT \ln \hat{\varphi}_i(P, T, \mathbf{n}) &= \left(\frac{\partial G^r(P, T, \mathbf{n})}{\partial n_i}\right)_{T,P,n_j} \\ &= \mu_i(P, T, \mathbf{n}) - \mu_i^*(P, T, \mathbf{n}) \\ &= \mu_i(V, T, \mathbf{n}) - \mu_i^*(V, T, \mathbf{n}) - RT \ln Z \\ &= \left(\frac{\partial A^r(V, T, \mathbf{n})}{\partial n_i}\right)_{T,V,n_j} - RT \ln Z \end{aligned} \tag{2.80}$$

The residual Helmholtz function at state $(V, T, \mathbf{n})$ is obtained from the pressure equation $P(V, T, \mathbf{n})$ by

$$A^r(V, T, \mathbf{n}) = -\int_{\infty}^{V} \left(P - \frac{nRT}{V}\right) dV \tag{2.81}$$

and Z is related to P, V and T by (2.60). In many cases, it is more convenient to use the reduced residual Helmholtz function:

$$F = \frac{A^r(V, T, \mathbf{n})}{RT} \tag{2.82}$$

Then:

$$\ln \hat{\varphi}_i = \left(\frac{\partial F}{\partial n_i}\right)_{T,V,n_j} - \ln Z \tag{2.83a}$$

$$\left(\frac{\partial \ln \hat{\varphi}_i}{\partial n_i}\right)_{P,T} = \left(\frac{\partial^2 F}{\partial n_i \partial n_j}\right)_{T,V} + \frac{1}{n} + \frac{1}{RT} \frac{(\frac{\partial P}{\partial n_j})_{T,V,n_i} (\frac{\partial P}{\partial n_i})_{T,V,n_j}}{(\frac{\partial P}{\partial V})_{T,\mathbf{n}}} \tag{2.83b}$$

$$\left(\frac{\partial \ln \hat{\varphi}_i}{\partial T}\right)_{P,\mathbf{n}} = \left(\frac{\partial^2 F}{\partial n_i \partial T}\right)_{V,n_j} + \frac{1}{T} - \frac{\bar{V}_i}{RT}\left(\frac{\partial P}{\partial T}\right)_{V,\mathbf{n}} \tag{2.83c}$$

$$\left(\frac{\partial \ln \hat{\varphi}_i}{\partial P}\right)_{T,\mathbf{n}} = \frac{\bar{V}_i}{RT} - \frac{1}{P} \tag{2.83d}$$

where

$$\left(\frac{\partial P}{\partial n_i}\right)_{T,V,n_i} = -RT\left(\frac{\partial^2 F}{\partial V \partial n_i}\right)_{T,n_j} + \frac{RT}{V} \tag{2.83e}$$

$$\left(\frac{\partial P}{\partial V}\right)_{T,\mathbf{n}} = -RT\left(\frac{\partial^2 F}{\partial V^2}\right)_{T,\mathbf{n}} - \frac{nRT}{V^2} \tag{2.83f}$$

$$\left(\frac{\partial P}{\partial T}\right)_{V,\mathbf{n}} = -RT\left(\frac{\partial^2 F}{\partial T \partial V}\right)_{\mathbf{n}} + \frac{P}{T} \tag{2.83g}$$

$$\bar{V}_i = \left(\frac{\partial V}{\partial n_i}\right)_{T,P,n_j} = -\left(\frac{\partial P}{\partial n_i}\right)_{T,V,n_i} \Big/ \left(\frac{\partial P}{\partial V}\right)_{T,\mathbf{n}} \tag{2.83h}$$

As such, all thermodynamic properties can be obtained by calculating the 1st and 2nd order partial derivatives of F with respect to T, V and n_i, as summarized in Table 2.3.

Table 2.3.: Bulk thermodynamic properties from partial derivatives of F with respect to V, T and n_i

	$(V, T, \mathbf{n})$	$(P, T, \mathbf{n})$
S^r/R	$-T\left(\frac{\partial F}{\partial T}\right)_{V,\mathbf{n}} - F$	$S^r(V,T,\mathbf{n})/R + n\ln Z$
A^r/RT	F	$F - n\ln Z$
G^r/RT	$F + PV/RT - n$	$G^r(V,T,\mathbf{n})/RT - n\ln Z$
U^r/RT	$F - S^r(V,T,\mathbf{n})/R$	$U^r(V,T,\mathbf{n})/RT$
H^r/RT	$G^r(V,T,\mathbf{n})/RT - S^r(V,T,\mathbf{n})/R$	$H^r(V,T,\mathbf{n})/RT$
C_V^r/R	$-T^2\left(\frac{\partial^2 F}{\partial T^2}\right)_{V,\mathbf{n}} - 2T\left(\frac{\partial F}{\partial T}\right)_{V,\mathbf{n}}$	
C_P^r/R	$C_V^r/R - \frac{T}{R}\left(\frac{\partial^2 P}{\partial T^2}\right)^2_{V,\mathbf{n}} / \left(\frac{\partial P}{\partial V}\right)_{T,\mathbf{n}} - n$	

Residual properties and partial derivatives from fugacity

Not all thermodynamic models, however, have an explicit expression for $P(V, T, \mathbf{n})$. For this type of thermodynamic model, residual properties can also be obtained from the fugacity (coefficient) and its partial derivatives. As we do not have a function that is explicit in volume, we limit the use of such models to the residual properties relevant to pressure-based specifications:

$$G^r(P,T,\mathbf{n}) = RT\sum_i n_i \ln\varphi_i \tag{2.84a}$$

$$H^r(P,T,\mathbf{n}) = -RT^2\sum_i n_i\left(\frac{\partial \ln f_i}{\partial T}\right)_{P,\mathbf{n}} = -RT^2\sum_i n_i\left(\frac{\partial \ln \varphi_i}{\partial T}\right)_{P,\mathbf{n}} \tag{2.84b}$$

$$S^r(P,T,\mathbf{n}) = (H^r(P,T,\mathbf{n}) - G^r(P,T,\mathbf{n}))/T \tag{2.84c}$$

It was discussed that partial derivatives of thermodynamic properties with respect to P, V and T can be related by means of the partial derivatives of the pressure function, as presented in Table 2.1. For fugacity models that are not explicitly formulated in terms of a pressure function, however, one cannot directly obtain partial derivatives of the PVT-relation and Helmholtz free energy expression. For such models, partial derivatives of the thermodynamic properties are obtained from the partial derivatives of ideal and residual properties by means of differentiating (2.70)-(2.75) and (2.84). A look at these expressions indicates that this is trivial, provided the expressions for first- and second-order derivatives of $\ln\hat{\varphi}_i$ with respect to the primary variables P, T and n_k.

Note that for thermodynamic models that have mole fractions $\mathbf{x}$ as a primary variable, rather than mole numbers $\mathbf{n}$, a chain rule is required to obtain the partial derivatives with respect to mole numbers:

$$\frac{\partial \ln\varphi_i}{\partial n_k} = \sum_m \frac{\partial \ln\varphi_i}{\partial x_m}\frac{\partial x_m}{\partial n_k} \tag{2.85}$$

Since $x_i = n_i/n_T$ and $n_T = \theta_j$, we can write

$$\frac{\partial x_i}{\partial n_k} = \frac{1}{\theta_j}(\delta_{ik} - x_i) \tag{2.86}$$

and the derivative of the fugacity coefficient with respect to mole numbers becomes

$$\frac{\partial \ln \varphi_i}{\partial n_k} = \frac{1}{\theta_j}\left(\frac{\partial \ln \varphi_i}{\partial x_k} - \sum_m x_m \frac{\partial \ln \varphi_i}{\partial x_m}\right) \tag{2.87}$$

2.2.3. Activity and mixtures

Activity is defined as the ratio of the fugacity of species i in a mixture $\hat{f}_i$ over the corresponding pure component fugacity f_i at the same pressure and temperature:

$$a_i(P, T, \mathbf{n}) \equiv \frac{\hat{f}_i(P, T, \mathbf{n})}{f_i(P, T)} \tag{2.88}$$

For ideal mixtures, a convenient definition is that the activity equals the mole fraction x_i:

$$\mu_i^{id}(P, T, \mathbf{n}) \equiv \mu_i(P, T) + RT \ln x_i \tag{2.89}$$

To account for non-ideality, the activity coefficient is introduced, defined as

$$\gamma_i(P, T, \mathbf{n}) \equiv \frac{a(P, T, \mathbf{n})}{x_i} = \frac{\hat{f}_i(P, T, \mathbf{n})}{x_i f_i(P, T)} = \frac{\hat{\varphi}_i(P, T, \mathbf{n})}{\varphi_i(P, T)} \tag{2.90}$$

where the chemical potential can be calculated by

$$\mu_i(P, T, \mathbf{n}) = \mu_i(P, T) + RT \ln a_i(P, T, \mathbf{n}) = \mu_i(P, T) + RT \ln \gamma_i(P, T, \mathbf{n}) x_i \tag{2.91}$$

For pure components, the fugacity equals the pure component fugacity, and therefore the activity becomes unity. This activity coefficient is commonly referred to as *symmetric activity coefficient*, where:

$$\lim_{n_j \to 0} \gamma_i(P, T, \mathbf{n}) = 1, \quad j \neq i \tag{2.92}$$

The fugacity of species i in a mixture can be calculated by

$$\hat{f}_i(P, T, \mathbf{n}) = f_i(P, T) \gamma_i(P, T, \mathbf{n}) x_i \tag{2.93}$$

In some cases, a highly diluted solute deviates much more from ideality than the solvent does, and the pure solute corresponds to a different phase state. A choice of reference state that includes the partial molar excess Gibbs energy at infinite dilution, instead, is more appropriate. Rewriting (2.91) to include this term gives:

$$\mu_i(P, T, \mathbf{n}) = \mu_i(P, T) + RT \ln \gamma_i^{\infty} + RT \ln \frac{\gamma_i}{\gamma_i^{\infty}} x_i \tag{2.94}$$

where γ_i^∞ is the symmetric activity coefficient at infinite dilution in a solvent of composition n_k, or:

$$\gamma_i^\infty(P,T,n_k) = \lim_{n_i \to 0} \gamma_i(P,T,\mathbf{n}), \quad i \neq k \tag{2.95}$$

The ratio γ_i/γ_i^∞ can be taken as the definition of the *asymmetric activity coefficient*:

$$\tilde{\gamma}_i \equiv \frac{\gamma_i(P,T,\mathbf{n})}{\gamma_i^\infty(P,T,n_k)} = \frac{\hat{\varphi}_i(P,T,\mathbf{n})}{\hat{\varphi}_i^\infty(P,T,n_k)} \tag{2.96}$$

where $\hat{\varphi}_i^\infty(P,T,n_k)$ is the fugacity coefficient of component i at infinite dilution in a solvent of composition n_k. The chemical potential formulated in terms of the asymmetric activity coefficient then reads:

$$\mu_i(P,T,\mathbf{n}) = \mu_i(P,T) + RT\ln\gamma_i^\infty(P,T,n_k) + RT\ln\tilde{\gamma}_i(P,T,\mathbf{n})x_i \tag{2.97}$$

Substituting the asymmetric activity coefficient into (2.93) gives:

$$\hat{f}_i(P,T,\mathbf{n}) = f_i(P,T)\gamma_i^\infty(P,T,n_k)\tilde{\gamma}_i(P,T,\mathbf{n})x_i = h_i^\infty(P,T,n_k)\tilde{\gamma}_i(P,T,\mathbf{n})x_i \tag{2.98}$$

where $h_i^\infty = f_i(P,T)\gamma_i^\infty$ is the definition of Henry's constant. According to this definition, Henry's constants, and their nonlinear pressure-dependent extensions in the Krichevsky-Kasarnovsky-Ilinskaya correlations [70], are a function of the solute-solvent interactions in relation to the pure component reference fugacity $f_i(P,T)$.

It must be noted that the definition of the asymmetric activity coefficient and Henry's constant can be extended to mixed solvents, replacing n_k by $\mathbf{n}_{solvents}$ in (2.96)-(2.98). However, determination of asymmetric activity coefficients and Henry's constants depends on the specific solute-solvent interactions and, therefore, application of asymmetric activity coefficients and Henry's constants to mixtures of different solvent compositions requires re-evaluation of the activity coefficients. Consequently, Henry's constants are often regarded as an adjustable parameter.

Other thermodynamic properties can be obtained from activity coefficient models by means of rewriting the expression of fugacities, calculating their partial derivatives and substituting them into (2.84).

3

Thermodynamic models

Thermodynamic models can be used as a predictive framework to determine physical properties of pure components and their mixtures. Models can be broadly categorized as equations of state (EoS), activity coefficient models, empirical or system-specific. In this chapter, three thermodynamic models will be discussed: classical Van der Waals-type cubic equations of state, Henry's constant models for the aqueous phase (empirical) and the Van der Waals-Platteeuw hydrate equation of state (system-specific). For all models, thermodynamic properties can be obtained by means of the relations presented in Section 2.2.

Equations of state are generally used for modelling vapour and liquid phases, as they are also consistent in the critical region. Classic Van der Waals-type cubic EoS, such as SRK [71] and PR [72], have proven reliable for thermodynamic calculations of nonpolar mixtures, yet they are not adequate for mixtures of like and unlike molecules that occurs in brines. The solubility of CO_2 in pure water and brine is an important consideration in modelling CO_2 sequestration. Given the highly saline brines often encountered in the subsurface and the occurrence of acid and sour gases in these geological reservoirs, the effect of salinity and presence of gases such as CH_4, N_2, H_2S and SO_2 on dissolution cannot be neglected. Furthermore, the accuracy of fugacity calculation becomes important when thermodynamic models are used in a hybrid flash procedure. This is the case for equilibrium calculations involving hydrates, where gas solubility has a large influence on the predicted hydrate equilibria [73].

Cubic models have an attractive and a repulsive term, which together are not sufficient to predict the interaction between associating molecules. Secondly, they fail to describe the behaviour close to infinite dilution, at which solute-solvent interactions dominate. As a result, prediction of gas solubilities in the aqueous phase using conventional mixing rules may deviate by orders of magnitude.

Modifications to the cubic equations of state have been proposed to improve phase behaviour prediction. Activity coefficient models can be applied to model equilibria in aqueous systems; however, the adjustable parameters hold little physical significance. Alternatively, highly specific temperature-dependent or density-dependent binary interaction coefficients to calculate gas solubility in the

water phase have been used, an approach that has even been extended to salinity-dependence [74]. However, it is not easy to accurately fit temperature-dependency for all phases. This forces one to combine different sets of parameters for different fluid types, which is not physically consistent. With density-dependent interaction parameters, quantitative agreement has been obtained for hydrocarbon solubilities, but the representation of the hydrocarbon phases is worse than that obtained with quadratic mixing rules [75].

A more theoretically sound approach for incorporating association and chain-forming into an equation was developed in the SAFT family of equations of state [76–78]. These models have additional terms and use statistical mechanical perturbation theory to quantify the relationship between molecular bonding site interactions and bulk fluid behaviour. Nonetheless, despite the increased complexity of the physical part of the EoS, the mutual solubilities of hydrocarbon-water systems are still very much dependent on the mixing rules used. This led to the development of the CPA EoS [79, 80], where the simple physical terms of a cubic equation of state have been combined with an association term similar to that used in the SAFT EoS. Yet, a significant drawback of using association models in pressure-based simulations is that they are explicit in volume. While cubic equations of state are also volume-based, they can be solved for density analytically. On the contrary, association terms are implicit and require iterative solutions for an internal set of composition-dependent variables [81, 82].

Another option is to use a separate thermodynamic model for the aqueous phase completely. For many polar and strongly non-ideal liquid solutions, activity models provide an alternative to equations of state. A disadvantage of activity models is that they are not consistent in the critical region and are thus limited to application well below the critical temperature of the mixture. This approach introduces a thermodynamic inconsistency that is most pronounced close to critical conditions. However, far from critical conditions for brine systems (which is the case for the conditions of most depleted hydrocarbon fields and aquifers), the approach should be still applicable. An interesting feature of using a separate equation for the aqueous phase is the flexibility of modelling the aqueous phase properties irrespective of the restrictions of the other EoS.

An often used approach for predicting the solubility of gases and hydrocarbons in aqueous solutions is by means of Henry's constants. Li and Nghiem [83] presented multiphase equilibria for mixtures of oil and gas with water and brines based on Henry's constants for the aqueous phase. The nonaqueous fluids were modelled with a cubic equation of state, and Henry's coefficients were correlated against pressure and temperature. Models based on Henry's constants are essentially asymmetric activity coefficient models (Section 2.2.3), where the reference state is related to the solute-solvent interaction at infinite dilution. Considering the unlike nature of solvents and solutes, this is a more appropriate standard state to which solute thermodynamic properties are related. Furthermore, this approach to describe the dissolution of gases and hydrocarbons in the aqueous phase is justified, given their limited solubility. An important assumption with Henry's constants is that the interaction between solutes in solution is negligible.

Using different thermodynamic models for aqueous and other vapour and liquid phases introduces inconsistencies towards the critical region of the brine phase and yields multiple minima of the Gibbs free energy surfaces in water-rich compositions. We illustrate these practical challenges through a Gibbs energy analysis and present strategies for implementing robust and efficient solution procedures in Chapter 4. We validate the approach by comparing our phase equilibrium calculations with an experimental dataset of relevant gas mixtures with water.

In addition to the brine phase, a separate thermodynamic model is certainly needed in case one chooses to include hydrates in the thermodynamic modelling procedure. While this introduces less interference with other thermodynamic models, it stresses the importance of choosing appropriate models for the fluid phases to obtain accurate predictions of phase equilibrium.

3.1. Cubic equations of state

Cubic equations of state have evolved from the initial version as developed by Van der Waals. Two-parameter equations of state that followed mainly introduced temperature-dependent adjustments to the attractive term to improve agreement with experimental data. *VdW*-type EoS can be rearranged into a cubic polynomial in terms of volume and, as such, can be solved for density analytically.

Later developments focused on volume-, temperature- and composition-dependent binary interaction coefficients to correlate mixtures and improved mixing rules by means of activity coefficient models to accommodate equilibria of polar mixtures. Despite the advent of more sophisticated physical models such as SAFT and CPA, cubic equations of state remain relevant in many reservoir and process simulators due to their flexibility and computational efficiency.

Van der Waals-type EoS

In 1873, Van der Waals [84] introduced an equation of state which is most widely known in the form:

$$P = \frac{RT}{v-b} - \frac{a}{v^2} \tag{3.1}$$

The constant b is related to the size of the hard spheres (repulsive term) and parameter a is associated with intermolecular attraction forces.

This form of the *VdW* EoS can, in fact, be directly obtained from statistical thermodynamics. From the partial derivative of Helmholtz free energy, $A = U - TS$, with respect to volume gives pressure:

$$P = -\left(\frac{\partial A}{\partial V}\right)_{T,N} = -\left(\frac{\partial U}{\partial V}\right)_{T,N} + T\left(\frac{\partial S}{\partial V}\right)_{T,N} = P^{eng} + P^{ent} \tag{3.2}$$

In this form, two terms contribute to the pressure: an energetic term with $\partial U/\partial V$ and an entropic term with $\partial S/\partial V$. Both terms can be derived from lattice theory, with a very simple approximation of a fluid as randomly distributed particles

and vacancies on a lattice. In reality, however, the distribution between occupied and unoccupied sites is non-random. If occupied neighbouring sites attract, this affects both entropic and energetic contributions. From statistical thermodynamic principles, there should exist a temperature dependence of both terms, but such theoretical model development quickly becomes increasingly complicated.

For engineering use, the *VdW* EoS is therefore not very accurate. On the other hand, semi-empirical modifications of the EoS with a temperature dependence and appropriate choice of volume parameters, such as those by Redlich and Kwong [85] (*RK*), Soave [71] (*SRK*) and Peng and Robinson [72] (*PR*), have been successful. A general expression of the cubic equations of state reads

$$P = \frac{RT}{v-b} - \frac{a(T)}{(v-\delta_1 b)(v-\delta_2 b)} \tag{3.3}$$

Figure 3.1 shows the *PV*-diagrams and compressibility factors of CO_2 using the *PR* EoS for a range of isotherms close to the critical point. It is inside the mechanical spinodal, denoting the limits of mechanical stability ($\partial P/\partial V < 0$) that *VdW*-type EoS exhibit a non-physical state that can safely be ignored.

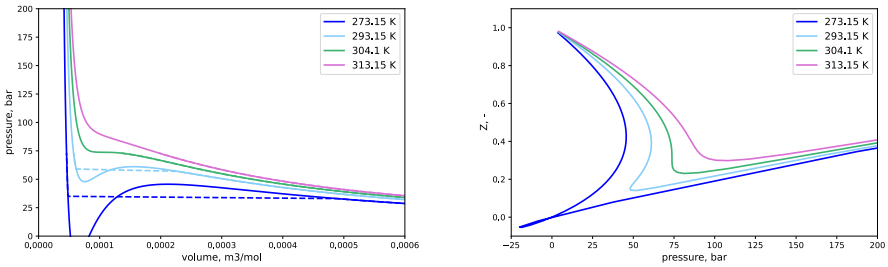

(a) *PV*-diagram (b) Compressibility factor

Figure 3.1.: (a) Pressure-volume diagram and (b) compressibility factors Z (2.60) of CO_2.

In accordance with Section 2.2, thermodynamic properties can be obtained from the residual Helmholtz form of the pressure equation. Substituting (3.3) into (2.81) yields:

$$\begin{aligned} \frac{A^r(T,v)}{RT} &= F\left(b/v, \frac{a(T)}{RTb}\right) \\ &= -\ln(1-b/v) - \frac{a(T)}{RTb(\delta_1-\delta_2)} \ln\left(\frac{1+\delta_1 b/v}{1+\delta_2 b/v}\right) \end{aligned} \tag{3.4}$$

Parametrization of the EoS

At the critical point, the first and second derivatives of pressure with respect to volume must vanish, and expressions can be obtained for a_c and b_c in terms of critical properties:

$$a_c = \frac{\Omega_a}{\Omega_b} b_c R T_c = \Omega_a \frac{(RT_c)^2}{P_c} \tag{3.5a}$$

$$b_c = \Omega_b \frac{v_c}{Z_c} = \Omega_b \frac{RT_c}{P_c} \tag{3.5b}$$

Since the number of unknowns is equal to three (pressure, temperature, volume) and the equation of state has only two adjustable parameters a and b, some of the predicted quantities by the equation of state will likely not match the experimental values [56]. Often, the equation of state shall match experimental critical pressure and temperature at the expense of the prediction of critical compressibility factors Z_c. For pure fluids, the critical compressibility ranges from 0.23 (water) to 0.30 (hydrogen); for the original VdW equations of state, Z_c equals 0.375.

In the original VdW equation of state, a and b are constants and retain their constant values away from the critical point. Based on the temperature dependent term for a for subcritical temperatures suggested by Redlich and Kwong [85], Soave [71] observed a correlation between a/a_c (obtained from hydrocarbon vapour pressure data) and T/T_c:

$$a(T) = a_c \alpha(T_r, \omega) = a_c \left(1 + m(1 - \sqrt{T/T_c})\right)^2 \tag{3.6}$$

where m relates to the compound acentric factor ω, which is associated with the reduced vapour pressure $P_r = 10^{-1-\omega}$ at a reduced temperature of 0.7. Contrary to Soave's procedure, Peng and Robinson [72] did use experimental vapour pressure data to find an expression for m. The model-specific parameters for VdW, SRK and PR EoS are listed in Table 3.1.

Table 3.1.: Parameters of cubic EoS

	VdW	SRK	PR
δ_1, δ_2	$0, 0$	$1, 0$	$1 \pm \sqrt{2}$
Ω_a	$27/64$	$\left(9(\sqrt[3]{2}-1)\right)^{-1} \approx 0.42748$	$(8+40\eta_c)/(49-37\eta_c)$ ≈ 0.45724
Ω_b	$1/8$	$(\sqrt[3]{2}-1)/3 \approx 0.08664$	$\eta_c/(3+\eta_c) \approx 0.0778$
m	1	$0.480 + 1.574\omega - 0.176\omega^2$	$0.37464 + 1.54226\omega$ $-0.26992\omega^2$
Z_c	0.375	0.333	0.307

$$\eta_c = 1/(1 + \sqrt[3]{4+\sqrt{8}} + \sqrt[3]{4-\sqrt{8}})$$

For temperatures above the critical point, experimental data along the critical isochore, which is the natural extension of the vapour pressure curve, could be used. However, cubic equations of state do not match the volume at the critical point, and therefore the correlations for $a(T)$ developed for subcritical temperatures are often extrapolated to supercritical temperatures. As T goes towards infinity, $a(T)$ should go towards zero, but in the expressions developed for SRK and PR, a is equal to zero at a reduced temperature of $T_r = (1 + 1/m)^2$ and goes towards infinity if temperature is increased further [56].

On the other hand, the temperature dependence of the repulsive constant b is thermodynamically inconsistent, as it leads to the crossing of isotherms in a PV-plane [86] and causes negative heat capacities which violate the condition of thermal stability: $T/C_V > 0$ [55, 56]. Therefore, b is often assumed independent of temperature.

Mixtures: quadratic mixing rules

For mixtures, the a and b parameters are replaced by mixture parameters a_{mix} and b_{mix}. In accordance with the quadratic composition dependence of the second virial coefficient for a mixture, the quadratic "Van der Waals mixing rules" have been used widely. For additional flexibility, empirical binary interaction coefficients k_{ij} were added to the expression of a_{mix}. A cross-covolume interaction parameter l_{ij} has also been proposed for b_{mix}, but these are often considered null [87].

With the quadratic mixing rules, the residual Helmholtz energy for n moles of a mixture is formulated as:

$$\frac{A^r(T, V, \mathbf{n})}{RT} = -n \ln(1 - B/V) - \frac{D(T)}{RTB(\delta_1 - \delta_2)} \ln\left(\frac{1 + \delta_1 B/V}{1 + \delta_2 B/V}\right) \tag{3.7}$$

where V is the total mixture volume. The mixture parameters B and D are given by:

$$D = n^2 a_{mix} = \sum_i n_i \sum_j n_j a_{ij} \tag{3.8}$$

with

$$a_{ij} = a_{ji} = \sqrt{a_{ii} a_{jj}}(1 - k_{ij}) \tag{3.9}$$

and

$$nB = n^2 b_{mix} = \sum_i n_i \sum_j n_j b_{ij} \tag{3.10}$$

with

$$b_{ij} = b_{ji} = \frac{1}{2}(b_{ii} + b_{jj})(1 - l_{ij}) \tag{3.11}$$

Derivatives of the residual Helmholtz expression and quadratic mixing rules are given in Michelsen and Mollerup [56] and have been implemented in DARTS-flash [54], see Appendix A.

The cubic nature of cubic EoS

The general form of a cubic EoS (3.3) can be rearranged to be cubic in volume. Commonly, it is expressed as a cubic polynomial of compressibility factor Z as

$$f(Z) = Z^3 + a_2 Z^2 + a_1 Z + a_0 = 0 \tag{3.12a}$$

with

$$\begin{aligned} a_2 &= \left[(\delta_1 + \delta_2 - 1)B - 1\right] \\ a_1 &= \left[A + \delta_1\delta_2 B^2 - (\delta_1 + \delta_2)B(B+1)\right] \\ a_0 &= -\left[AB + \delta_1\delta_2 B^2(B+1)\right] \end{aligned} \tag{3.12b}$$

where $A = \dfrac{a_{mix}P}{R^2T^2}$, $B = \dfrac{b_{mix}P}{RT}$ and $Z = \dfrac{Pv}{RT}$. Locating the roots of this polynomial can be done analytically, which is of significant advantage in terms of performance compared to iterative thermodynamic models. The cubic polynomial (3.12), depicted in Figure 3.2 for a subcritical and a supercritical temperature for pure CO_2, can have either one or three real roots – of which some might be equal. The three cases can be distinguished by a simple criterion. Substituting $Z = x - a_2/3$ eliminates the quadratic term and reduces the cubic polynomial to

$$x^3 + px + q = 0 \tag{3.13}$$

with p and q real numbers. The nature of the roots is then determined by the value of the discriminant D:

$$D = -\frac{p^3}{27} - \frac{q^2}{4} \tag{3.14}$$

If $D > 0$, all roots are real and distinct. If $D < 0$, two roots are complex. If $D = 0$, all roots are real and (at least) two roots are equal [88].

In principle, the roots of a cubic polynomial can be obtained analytically using either Cardano's method or trigonomic functions, depending on the value of D [88]. These methods, however, involve computation of algebraic and trigonomic functions, which may not be very efficient and might suffer from roundoff errors.Instead, Deiters and Macías-Salinas [89] developed an iterative solution that could be more accurate and potentially require less computational effort.

Root identification

For simulation, a consistent interpretation of phase types is required to assign secondary properties such as viscosity, relative permeability and capillary pressure. The cubic polynomial has three roots, of which either one or three are real. It is only inside the mechanical spinodal that three real roots can be obtained, the spinodal denoting the limits of mechanical stability ($\partial P/\partial V < 0$) which coincide at the mechanical critical point [90]. In the case of three real roots, the smallest volume corresponds to the liquid phase, and the largest root represents the vapour phase. For pressures below the mechanical spinodal, the single real root is associated

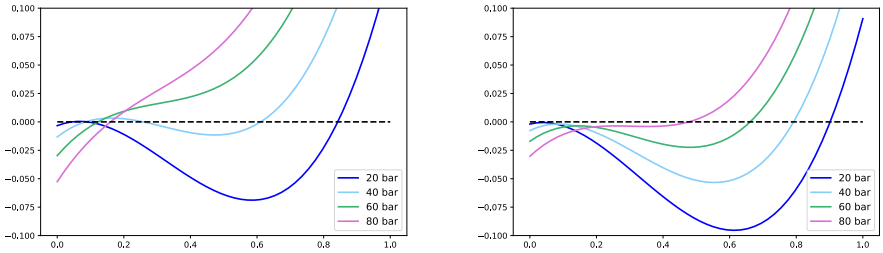

(a) At T = 273.15 K

(b) At T = 313.15 K

Figure 3.2.: Cubic polynomial of *PR* EoS for CO_2 (a) below and (b) above critical temperature. Within the mechanical spinodal (a), limited by the mechanical critical point, three real roots can be obtained. For temperatures above the spinodal (b), only a single real root exists.

with the vapour phase, whereas at higher pressures the phase is a liquid. We can identify these roots using the characteristics of the cubic polynomial [91].

For temperatures above the mechanical spinodal, however, this logic is no longer valid. A completely rigorous method for identifying roots would rely on information about the mixture critical point. Alternatively, vapour and liquid phases are often identified through the use of a two-sided initialization procedure [38]. Here, a vapour-like initial estimate converges to a vapour-like local minimum of the Gibbs free energy (or tangent plane distance, Section 4.1) rich in lighter components, and a liquid-like trial phase locates the denser phase. This procedure can be utilized even outside the two-phase region. Although in this case one of the minima is not part of the equilibrium state, local minima can be obtained for both vapour and liquid phases for conditions within the stability test limit locus (STLL) [92]. The convergence locus of the negative flash, where the negative flash obtains non-trivial solutions, extends further away from the phase boundary and could also be utilized [92, 93].

Improvements to cubic EoS

The introduction of binary interaction coefficients of the attractive term k_{ij} to the quadratic, or Van der Waals, mixing rules could be used to significantly improve agreement between calculated and experimental results. Temperature-dependent, as well as composition-dependent binary interaction coefficients, followed [87].

Other works have applied a volume translation technique proposed by Péneloux *et al.* [94] to improve liquid volumes. The original volume correction was chosen as temperature independent and component specific. Temperature dependence has been investigated in other studies, but the same thermodynamic inconsistency arises that was found in temperature-dependent covolumes [95].

Still, the traditional quadratic mixing rules were not able to accurately model

highly polar systems. Often, activity coefficient models (AC) were chosen to represent liquid mixtures of polar and associating molecules, although their range of applicability being limited to low pressure ranges, and pressure-independence was often assumed. Most activity coefficient models [96–99] were developed based on excess properties of mixing.

Huron and Vidal [100] proposed that improved mixing rules for cubic EoS could be deduced from activity coefficient models, equating the excess Gibbs energies for both EoS and AC:

$$G^{E,EoS}(P_{ref}, T, \mathbf{x}, a/b) = G^{E,\gamma}(T, \mathbf{x}) \tag{3.15}$$

This approach aimed to derive an expression for the unknown parameter a/b. Activity coefficient models were independent of pressure, so a reference pressure had to be specified. Huron and Vidal [100] proposed infinite pressure. Mollerup [101] suggested a zero reference pressure, for which later a number of procedures were developed [102–105]. Alternatively, Wong and Sandler [106] considered the excess Helmholtz energy instead of excess Gibbs energy, which yields different mixing rules for the b parameter.

A significant number of mixing rules have been developed based on these approaches. It is, however, known that both zero and infinite reference pressures have their drawbacks and inconsistencies for equating the separate contributions of $G^{E,EoS}$ [107]. Still, EoS/G^E implementations can provide highly satisfactory results, in many circumstances as accurate for phase equilibrium calculations as modern advanced association models [108].

Meanwhile, improvements to cubic EoS continue to be developed. Lucia [109] presented the multi-scale Gibbs-Helmholtz constrained (GHC) equation, a new approach to incorporate molecular-scale Monte Carlo simulations and upscale them to bulk scale. The method provides an alternative to conventional mixing rules and has been shown to maintain thermodynamic consistency [110].

3.2. Fugacity-activity models for aqueous phase

Cubic equations of state in their most basic form are not adequate for modelling polar mixtures. Models based on Henry's constant for gas solubility and a separate equation for the water component present an attractive alternative. As described in Section 2.2.3, Henry's constants are based on a reference state of infinite dilution, where solvent-solute interactions dominate. As such, Henry's constants can be fitted to experimental data of single solutes accurately and, given the low solubility of the solutes, can be applied to mixed solutes under most conditions. In addition, the equation for water fugacity can be purposefully described using various physical terms.

Clearly, the use of (asymmetric) activity models is limited to describing a liquid aqueous phase. This implies that no consistent description of the (near-)critical region for the brine phase is possible when employing an activity model, and its usage is limited to well below the critical temperature of the mixture. For many applications of interest, however, conditions remain far from it. More problematic,

nonetheless, is the occurrence of multiple local minima of Gibbs free energy surfaces in water-rich compositions. This problem will be addressed in Chapter 4.

In the model employed here, the properties of dissolved gases are calculated from the approach of Ziabakhsh-Ganji and Kooi [111]. Their model combines Henry's constants for nonelectrolyte solutes following Akinfiev and Diamond [112]. Besides, they included an additional term to account for the effect of brine salinity on gas solubilities, which was first proposed by Duan *et al.* [113] and is based on excess Gibbs energies in electrolyte solutions [114]. For the fugacity of the solvent, water, we follow the description of Jager *et al.* [115]. They derive the deviation of the chemical potential of H_2O from the pure water state, including the contributions of all molecular and ionic species to water activity.

Henry's constant asymmetric activity coefficient model for solutes

Using Henry's constants and an asymmetric activity coefficient model, the fugacity of dissolved species can be calculated according to:

$$\hat{f}_i(P, T, \mathbf{n}) = h_i^{\infty}(P, T, n_k)\tilde{\gamma}_i(P, T, \mathbf{n})x_i \tag{2.98}$$

Ziabakhsh-Ganji and Kooi [111] and Zirrahi *et al.* [116] used this approach and adopted the correlation of Akinfiev and Diamond [112]. They developed a virial-EoS-related expression for Henry's constant h_i^{∞} of the dissolved species at infinite dilution:

$$\ln h_i^{\infty} = (1-\eta)\ln f^o_{H_2O} + \eta \ln \frac{RT}{M_w}\rho^o_{H_2O} + 2\rho^o_{H_2O}\Delta B \tag{3.16}$$

The interaction between dissolved gas components in the aqueous phase is effectively neglected.

The asymmetric activity coefficient $\tilde{\gamma}_i$ in this model accounts for the effect of ion interactions with dissolved gases in the brine. The expression used in this model was first proposed by Duan *et al.* [113] and is based on excess Gibbs energies in electrolyte solutions [114]:

$$\ln \gamma_i = \sum_c 2m_c\lambda_{i-c} + \sum_a 2m_a\lambda_{i-a} + \sum_c\sum_a m_c m_a \xi_{i-c-a} \tag{3.17}$$

for cations c and anions a. The parameter λ_{i-a} was assumed equal to zero and the other parameters λ_{i-c} and ξ_{i-c-a} are calculated from:

$$Y(P,T) = c_1 + c_2T + c_3/T + c_4T^2 + c_5/(630-T) + c_6P + c_7P\ln T + c_8P/T + c_9P/(630-T) + c_{10}P^2/(630-T)^2 + c_{11}T\ln P, \quad Y = \{\lambda_{i-c}, \xi_{i-a-c}\} \tag{3.18}$$

Parameters of (3.18) can be found in [111, 113]. The range of models presented here can be readily extended to other (similar) species.

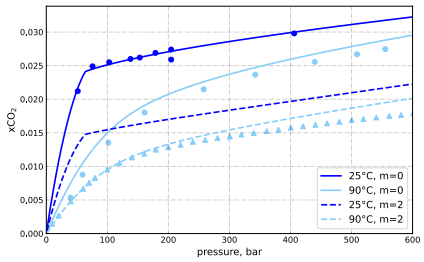

(a) CO_2 solubility in NaCl brine

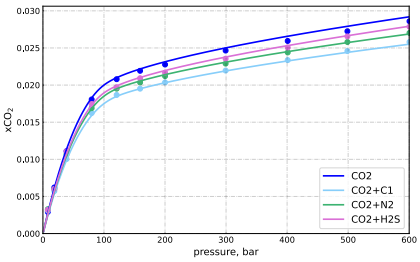

(b) CO_2 solubility in brine with impurities CH_4, N_2 and H_2S at T = 323.15 K

Figure 3.3.: Solubility of CO_2 in brine with salinity (a) and impurities (b). Data points from (a) Spycher *et al.* [117] and Duan and Sun [118] and (b) Ziabakhsh-Ganji and Kooi [111].

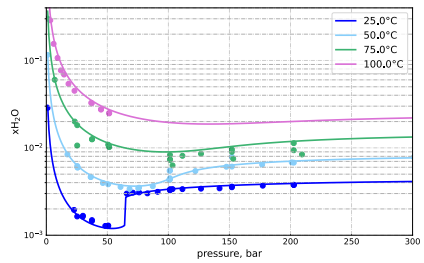

(a) H_2O solubility in CO_2 from pure water

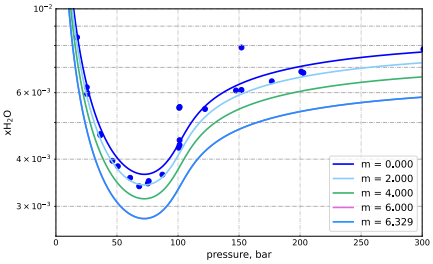

(b) H_2O solubility in CO_2 from NaCl brine at T = 323.15 K

Figure 3.4.: Solubility of H_2O in CO_2 from pure water (a) and NaCl brine with different molalities m [mol/kg] (b). Solubility data from Spycher *et al.* [117].

Fugacity model for solvent

The activity coefficient models for solutes must be accompanied by a separate thermodynamic model for solvent properties. The expression employed by Ziabakhsh-Ganji and Kooi [111] is based on an equilibrium distribution coefficient for the water component proposed by Spycher *et al.* [117]. While these approaches obtain good accuracy for the prediction of mutual solubilities of water and gases, the prediction of water fugacity is rather poor.

The fugacity model from Jager *et al.* [115], which was integrated into the developments around hydrate modelling by Ballard and Sloan, Jr. [119], provides an alternative. The model gives an expression for the chemical potential for each component i in the aqueous phase. Fugacity can then be derived by relating

chemical potential to the ideal gas state of pure component i at 1 bar:

$$f_i^a = f_{io} \exp\left(\frac{\mu_i - g_{io}}{RT}\right) \tag{3.19a}$$

or, in terms of fugacity coefficient:

$$\ln \varphi_i = \frac{\mu_i}{RT} - \frac{g_{io}}{RT} - \ln x_i - \ln P \tag{3.19b}$$

Here, f_{io} is the fugacity of an ideal gas at the reference pressure of 1 bar, which is equal to 1. The deviation from ideality is then accounted for by the difference in chemical potential μ_i and the Gibbs energy of component i in the ideal gas state g_{io}.

The chemical potential of water can be obtained from an expression analogous to (2.61). For water, chemical potential is related to the pure water state with the addition of an activity coefficient $\ln a_w$, which accounts for the effect of dissolved species:

$$\frac{\mu_w}{RT} = \frac{g_{w_0,pure}}{RT_0} - \int_{T_0}^{T} \frac{h_{w,pure}}{RT^2} dT + \int_{P_0}^{P} \frac{v_{w,pure}}{RT} dP + \ln a_w \tag{3.20}$$

where $g_{w_0,pure}$, $h_{w,pure}$ and $v_{w,pure}$ are the Gibbs energy at reference conditions (T_0, P_0), enthalpy and molar volume of pure water, respectively. The activity coefficient accounts for the actual concentration of the solute through short- and long-range interactions between water, solute molecules and ionic species.

Thermal properties from a fugacity-activity model

As discussed in Section 2.2, thermodynamic properties can be obtained from the partial derivatives of the fugacity coefficient. The partial derivatives of the fugacity-activity model presented here are available in DARTS-flash [54].

To apply the fugacity-activity model in simulation, it is important to assess the accuracy and consistency of thermal properties evaluated from the thermodynamic models. The enthalpy and entropy should be monotonically increasing with temperature, or equivalently, heat capacity must be positive at all conditions [55]:

$$\left(\frac{\partial H_j}{\partial T}\right)_{P,\mathbf{n}} = C_{Pj} > 0 \tag{3.21}$$

Figure 3.5 compares aqueous phase enthalpies and enthalpies of mixing with experimental data. The enthalpies of pure H_2O and H_2O-NaCl brines at saturation pressures have been measured by Pitzer *et al.* [120], shown in Figure 3.5a. Molar heat capacities are positive, slightly lowered by the presence of ions and slightly deviating at higher temperatures.

Figure 3.5b shows the molar enthalpy of dissolution for CO_2 at different temperatures. There exists a sharp transition of CO_2 dissolution enthalpy across vapour- and liquid-state CO_2. In addition, note that the process of CO_2 dissolution is exothermic for low temperature and pressure conditions, but becomes endothermic towards higher temperatures and pressures.

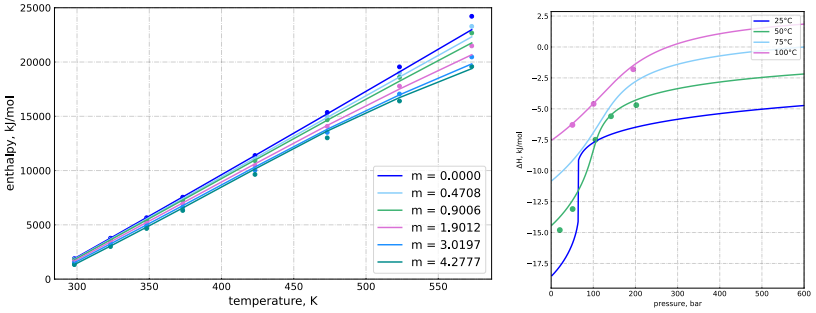

(a) Enthalpy of NaCl brine (b) Enthalpy of dissolved CO_2

Figure 3.5.: Aqueous phase molar enthalpies of (a) solvent at various NaCl molalities m [mol/kg] and (b) solutes. Data from (a) Pitzer *et al.* [120] and (b) Koschel *et al.* [121].

3.3. Hydrate equation of state

Clathrate hydrates are crystalline solids composed of hydrogen-bonded cages of H_2O in which small molecules are trapped. The formation and dissociation of hydrates are phase transitions, not chemical reactions, and the composition of the hydrates is non-stoichiometric. Three types of hydrate structures are generally known. Type sI consists of 46 water molecules and consists of two small and six large cages. The unit cell of type sII contains 136 water molecules, consisting of sixteen small and eight large cages. Hydrates of type sH consist of 34 water molecules, forming three different cage types, two small ones of different types and one very large. Each type typically hosts specific sets of molecules: e.g., CH_4 and CO_2 in sI-type hydrates, gases like O_2 and N_2 in type sII and heavier hydrocarbons in structure H. This is, however, highly dependent on thermodynamic conditions and structural transitions can take place. Typical cage occupancy corresponds to a mole fraction of H_2O of approximately 0.86 [122]. Figure 3.6 depicts a schematic representation of the different hydrate structures.

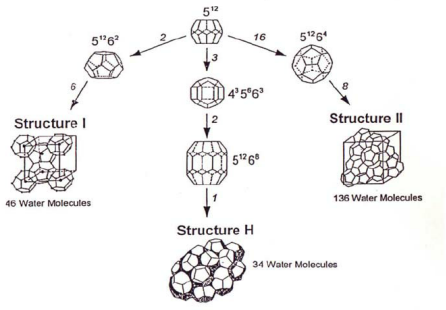

Figure 3.6.: Clathrate structures for sI-, sII- and sH-type hydrates, after [122].

Van der Waals-Platteeuw formulation

Van der Waals and Platteeuw [123] developed a statistical mechanics framework to model clathrate structures. Through a canonical partition function $Q(T, V, \mathbf{n})$ (influence of guests through number of molecules entrapped) and, later, a semi-grand canonical partition function $\Xi(T, V, n_{host}, \mu_{guest})$ (influence of guests by means of chemical potential), they obtained a description of clathrates as a mixed crystal structures with cages of host molecules (H_2O) occupied by a guest compound. The partition functions included a representation of the configurational integral for hosts and guests, analogous to Langmuir adsorption. From there, macroscopic properties could be obtained by means of the semi-grand canonical potential $\Psi(T, V, n_{host}, \mu_{guest})$. This potential corresponds to a Legendre transform of the Helmholtz free energy (2.34), replacing mole numbers of the guest molecules by their chemical potentials [124].

An equilibrium of the hydrate phase with other phases implies an equal chemical potential of host and guests in the hydrate with the coexisting phases. This was assumed implicitly so that cage occupancy could be related to the chemical potential of the guests, which by definition is equal to that in the other phases. The cage occupancy, therefore, also contributes to the chemical potential of the H_2O molecules in the hydrate lattice, the Gibbs free energy change of water from a hypothetical empty lattice β to the hydrate phase being:

$$\frac{\Delta\mu_{w,H}}{RT} = \frac{\mu_{w,H}}{RT} - \frac{g_{w,\beta}}{RT} = \sum_m \nu_m \ln\left(1 - \sum_j \theta_{jm}\right) \tag{3.22}$$

where $g_{w,\beta}$ denotes the chemical potential of water in the empty standard hydrate lattice at a given volume, ν_m is the number of cavities of type m divided by the number of water molecules in the unit cell and θ_{jm} is the fraction of available cages of type m, occupied by component j, or *fractional occupancy*. A statistical thermodynamic description of the empty hydrate lattice was lacking, however. Instead, they avoided explicit calculation of these properties by introducing the chemical potential change from an empty hydrate lattice to a reference phase α:

$$\Delta\mu_w^{\beta-\alpha} = \mu_w^\beta - \mu_w^\alpha \tag{3.23}$$

The reference phase would be an aqueous or ice phase. The change to the reference phase could be quantified through parameter estimation for an expression of the form:

$$d\left(\frac{\Delta\mu_w^{\beta-\alpha}}{RT}\right) = -\frac{\Delta H_w^{\beta-\alpha}}{RT^2}dT + \frac{\Delta V_w^{\beta-\alpha}}{RT}dP \tag{3.24}$$

In the end, the chemical potential change of the hydrate due to cage occupancy and the hypothetical transition from empty lattice to reference phase would be equal at equilibrium. Utilizing this, the chemical potential of the lattice molecules, i.e. H_2O in the hydrate, could be calculated [125].

The chemical potential of water in the hydrate can be equivalently formulated in terms of fugacity:

$$f_{w,H} = f_{w,A} \exp\left[\frac{\Delta\mu_{w,H} - \Delta\mu_{w,A}}{RT}\right] \tag{3.25}$$

Furthermore, by introducing a Langmuir coefficient C_{jm} of component j in cage m to account for the configurational integral, we have an expression for the fractional occupancy of cage m by component j:

$$\theta_{jm} = \frac{C_{jm} f_j}{1 + \sum_k C_{km} f_k} \tag{3.26}$$

where f_j is the fugacity of guest molecule j. Hydrate composition can be derived from (3.26) by:

$$x_{iH} = \frac{\sum_m \nu_m \theta_{im}}{1 + \sum_m \sum_j \nu_m \theta_{jm}} \tag{3.27}$$

and water mole fraction is equal to $x_{wH} = 1 - \sum_j x_{jH}$.

Implementation of the *VdWP* model for use in phase equilibrium calculations, therefore, requires two main ingredients. The first is a description of reference conditions for the empty hydrate lattice and its fugacity. Secondly, Langmuir adsorption constants must be derived from the intermolecular potentials that describe the configurational integral of the hydrate cages. In addition, calculation of properties in terms of conventional variables **(*P, T,* n)** is desirable for use of the model in flash calculations. This can be done by means of an iterative procedure.

Reference fugacity

In the original *VdWP* model, the fugacity of a reference phase, water or ice, must be known. Later works have eliminated this constraint by using an (ideal) gas phase as reference conditions [126, 127]. The formulation of Ballard and Sloan, Jr. [127] is convenient:

$$f_{w,H} = f_{io} \exp\left[\frac{\mu_{w,H} - g_{wo}}{RT}\right] \tag{3.28}$$

Here, f_{io} is equal to 1 bar and g_{wo} is the Gibbs energy of water in the ideal gas state at 1 bar, and the chemical potential of water in the hydrate $\mu_{w,H}$ appears in (3.22). In order to have a standalone expression for hydrate fugacity, they derived the Gibbs energy of the hypothetical empty hydrate lattice using pure component thermodynamics:

$$\frac{g_{w,\beta}}{RT} = \frac{g_{w_0,\beta}}{RT_0} - \int_{T_0}^{T} \frac{h_{w,\beta}}{RT^2}\, dT + \int_{P_0}^{P} \frac{v_{w,\beta}}{RT}\, dP \tag{3.29}$$

Values for $g_{w_0,\beta}$ and expressions have been derived for the standard state. Molar enthalpy and molar volume of water in the hydrate phase are given by:

$$h_{w,\beta} = h_{w_0,\beta} + \int_{T_0}^{T} c_{p_w,\beta}\, dT \quad \text{with} \quad c_{p_w,\beta} = a_0 + a_1 T + a_2 T^2 + a_3 T^3 \tag{3.30a}$$

and

$$v_{w,\beta} = v_0 \exp[\alpha_1(T-T_0) + \alpha_2(T-T_0)^2 + \alpha_3(T-T_0)^3 - \kappa(P-P_0)] \tag{3.30b}$$

In addition, Ballard and Sloan, Jr. [127] considered the non-ideality of the hydrate phase. The inclusion of guest molecules may perturb the cavities from the standard hydrate lattice, and they accounted for this effect through the introduction of an activity coefficient. The expression for chemical potential then becomes:

$$\frac{\mu_{w,H}}{RT} = \frac{g_{w,\beta}}{RT} + \sum_m \nu_m \ln\left(1 - \sum_j \theta_{jm}\right) + \ln \gamma_{w,H} \tag{3.31}$$

where

$$\ln \gamma_{w,H} = \frac{\Delta g_{w_0,\beta}}{RT_0} + \frac{\Delta h_{w_0,\beta}}{R}(1/T - 1/T_0) + \int_{P_0}^{P} \frac{\Delta v^H}{RT}\, dP \tag{3.32}$$

The perturbed Gibbs energy of formation $\Delta g_{w_0,\beta}$ and enthalpy of formation $\Delta h_{w_0,\beta}$ are assumed to be linear in Δv^H, which is the difference in molar volume between the standard hydrate and the real hydrate.

Langmuir constants and cell potentials

The Langmuir adsorption constant describes the potential interaction between the encaged guest molecules and the water molecules surrounding it:

$$C_{jm} = \frac{4\pi}{k_B T} \int_0^{R_{cage}} \exp\Big[-\frac{\omega_{jm}(r)}{k_B T}\Big] r^2 dr \tag{3.33}$$

Van der Waals and Platteeuw [123] originally used a spherically symmetrical Lennard-Jones-type potential, but many modifications have been proposed to this approach. The spherically symmetrical potential yielded better results for more spherical molecules, but poorer performance for non-spherical, rod-like molecules. Some have used a square-well potential [125, 128], but the Kihara potential has been most widely used:

$$\omega_{jm}(r) = 2\epsilon_j z_m \Big[\frac{\sigma_j^{12}}{R_m^{11} r}\Big(\delta_{jm}^{10} + \frac{a_j}{R_m}\delta_{jm}^{11}\Big) - \frac{\sigma_j^{6}}{R_m^{5} r}\Big(\delta_{jm}^{4} + \frac{a_j}{R_m}\delta_{jm}^{5}\Big)\Big] \tag{3.34}$$

with

$$\delta_{jm}^{N} = \frac{1}{N}\Big[\Big(1 - \frac{r}{R_m} - \frac{a_j}{R_m}\Big)^{-N} - \Big(1 + \frac{r}{R_m} - \frac{a_j}{R_m}\Big)^{-N}\Big] \tag{3.35}$$

The model from Ballard and Sloan, Jr. [127] utilizes a multilayered Langmuir coefficient expression (3.33) with three shells to represent the interaction between guest and host molecules more accurately. This accommodates better aspherical molecules.

Figure 3.7 shows the hydrate equilibrium curves for pure CH_4 and CO_2 in brine-gas systems with different salinities. The presence of ions acts as an inhibitor for hydrate formation. Note how the transition between liquid and gaseous CO_2 causes the equilibrium curves to change slope drastically.

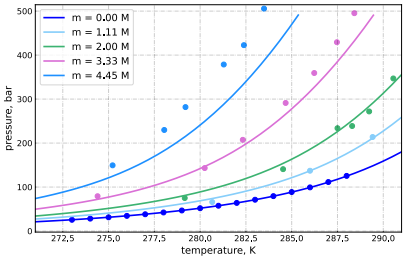

(a) CH_4-hydrate equilibrium pressures

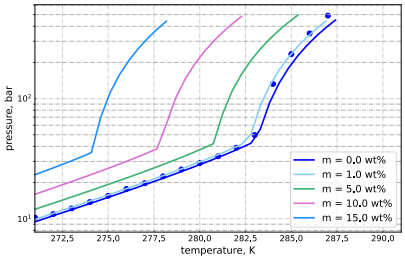

(b) CO_2-hydrate equilibrium pressures

Figure 3.7.: Hydrate equilibrium pressures of (a) CH_4 and (b) CO_2 with NaCl brine of different salinities. Salinity denoted (a) in M [mol/kg] and (b) in weight %. Data from (a) Jager *et al.* [129] and (b) Aghajanloo *et al.* [23].

Calculation of hydrate fugacities

In the form presented here, the equation of state is a function of the fugacity of the guest molecules, rather than composition. The iterative procedures of Cole and Goodwin [130] and Michelsen [131] make it possible to evaluate component fugacities in the hydrate phase as a function of composition, as in ordinary thermodynamic models. Cole and Goodwin [130] rearranged the equations of the *VdWP* model to be able to evaluate component fugacities in a hydrate phase as a function of overall composition. Michelsen [131] simplified this procedure, ultimately solving a single equation.

After obtaining the iterative solution, partial derivatives of the fugacity coefficients to calculate hydrate thermodynamic properties require implicit differentiation of the iterative procedure with respect to the primary variables P, T and x_k. This procedure has been implemented in DARTS-flash [54].

4

Multiphase equilibrium

Phase equilibrium calculations are at the core of reservoir simulation. Accurate physical modelling requires robust multiphase flash routines. For different applications and conditions, the phase equilibrium problem may have to be posed with different specifications. For simulation of CO_2 sequestration problems, specifically, a *PT*-formulation is not adequate for resolving complex thermal effects, and a *PH*-formulation is preferred. Nevertheless, such *PH*-calculations heavily rely on *PT*-flashes, calling for robust and efficient solvers for both specifications.

4.1. The phase equilibrium problem

In Section 2.1, the general conditions for equilibrium and phase stability were obtained for different state specifications. Criteria of phase stability were discussed, where virtual displacements of the independent variables would be transferred from the original phase to a new phase.

4.1.1. A geometric interpretation of phase equilibria

The simplest illustration of phase equilibrium and stability involves a mixture at constant P and T. For this problem, Gibbs free energy is the choice of thermodynamic potential. For any (infinitesimal) transfer of material between phases α and β, the virtual displacement reads:

$$\delta G = (\mu_i^\alpha - \mu_i^\beta)\delta n_i \tag{4.1}$$

At equilibrium, Gibbs free energy must be minimized, and any virtual displacement departing from the equilibrium state can only be non-negative:

$$(\delta G)_{P,T,\mathbf{n}} \geq 0 \tag{2.45d}$$

Equality of chemical potentials, therefore, is a necessary condition for equilibrium. It is, however, only a necessary condition for equilibrium, as the correct solution corresponds to the global minimum of Gibbs free energy.

The more general condition considers the formation of an infinitesimal amount of a new phase δe with composition $\mathbf{y}$, transferred from the original phase with composition $\mathbf{z}$, and then:

$$\delta G = \delta e \sum_{i=1}^{n_c} y_i(\mu_i(\mathbf{y}) - \mu_i(\mathbf{z})) \tag{4.2}$$

Phase stability according to this condition corresponds to the general stability criterion for isothermal-isobaric equilibrium (2.48e).

From the condition of equal chemical potentials, we find that the equilibrium state corresponds to a point on an n_c-dimensional hyperplane that is tangent to the single-phase molar Gibbs free energy surface at the equilibrium compositions. For a binary system, the hyperplane is consequently a line that is tangent to the single-phase surface. The Gibbs free energy surface is a function of the mole fraction z of the first component:

$$g(z) = z\mu_1 + (1-z)\mu_2 \tag{4.3}$$

The molar Gibbs energy of mixing is an equivalent but more convenient choice for graphical interpretation (Figure 4.1):

$$g^{mix}(z) = z(\mu_1 - \mu_{1,pure}) + (1-z)(\mu_2 - \mu_{2,pure}) \tag{4.4}$$

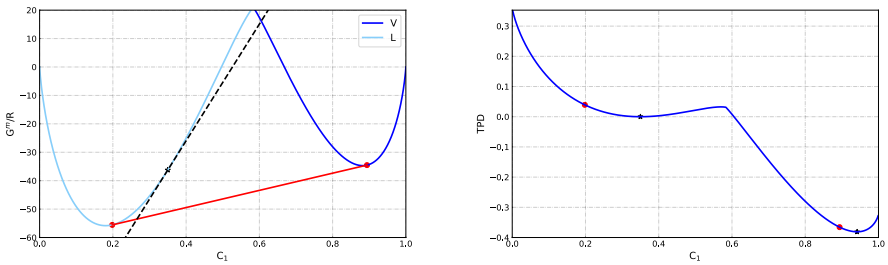

(a) Gibbs free energy (b) Tangent plane distance

Figure 4.1.: (a) Gibbs free energy surface and (b) tangent plane distance function for binary mixture C_1-nC_4 at P = 40 bar and T = 300 K. Tangent plane distance is evaluated from a feed composition of $x_{C_1} = 0.35$.

Figure 4.1a depicts the hypothetical single-phase surface for a binary mixture of C_1-nC_4. For a feed composition of $x_{C_1} = 0.35$, the tangent plane to the single-phase surface (black) intersects the blue vapour-phase curve, which is an indication that the feed is not stable as a single-phase state. Figure 4.1b represents the tangent plane distance, the distance of the Gibbs energy curve to the tangent plane at the feed composition. A negative minimum exists around $x_{C_1} = 0.93$,

which gives an appropriate estimate of the equilibrium phase at $x_{C_1} = 0.90$. In the two-phase region, the red line tangent to the Gibbs free energy curve can be constructed between the two points on the surface that denote the compositions of the equilibrium phases. Any point on this line corresponds to a linear combination of the two phases, a linear combination that results in the lowest possible Gibbs free energy for any composition in consideration. Solutions that are located outside of the region bounded by the two equilibrium compositions, however, would result in at least one of the two phases being present in negative quantities. Hence, these compositions correspond to a single-phase equilibrium state.

Tangent plane criterion

The stability of a phase state can be assessed by constructing a tangent hyperplane to the Gibbs free energy surface at the particular feed composition $\mathbf{z}$. If this tangent hyperplane intersects anywhere the single-phase surface, we are certain that the tested phase state does not correspond to the global minimum of Gibbs free energy. The same holds for testing the stability of a multiphase state consisting of a linear combination of points on the tangent hyperplane that touch the single-phase Gibbs free energy surface.

The tangent plane distance function represents the vertical distance from the tangent hyperplane to the Gibbs free energy surface at the tested composition $\mathbf{z}$ to the Gibbs energy curve at composition $\mathbf{y}$. For any point $\mathbf{y}$, the tangent plane distance (tpd), becomes

$$tpd(\mathbf{y}) = g(\mathbf{y}) - t_z(\mathbf{y}) = \sum_i y_i(\mu_{i,y} - \mu_{i,z}) \tag{4.5}$$

If the tpd is non-negative for all $\mathbf{y}$, this means that the tangent line does not intersect the Gibbs energy for any $\mathbf{y}$, indicating that the investigated phase is stable. If it is negative somewhere, it means that the Gibbs energy can be reduced by forming another phase. This yields the same condition as equation (2.48e). The tangent plane criterion is thus a sufficient condition for stability.

Writing chemical potential in terms of fugacity and substituting in (4.5), we can obtain the stability criterion from the reduced tangent plane distance:

$$tpd(\mathbf{y}) = \sum_i y_i\big(\ln y_i + \ln \hat{\phi}_i(\mathbf{y}) - d_i\big) \geq 0 \tag{4.6}$$

with $d_i = \ln z_i + \ln \hat{\phi}_i(\mathbf{z})$. Stationary points of the tpd-function are found where the tangent hyperplane to the Gibbs energy curve is parallel to the tangent at $\mathbf{z}$. Equivalently, the stationary points are characterized by a constant difference between chemical potential or fugacity at the compositions $\mathbf{y}$ and $\mathbf{z}$ [56].

Tangent plane criteria have also been formulated for other state specifications based on the fundamental equation [52, 56]. Nichita [52] discussed in detail the implications of stability testing at other state specifications, which were shown to ultimately reduce to the stationary points of either PT-stability for pressure-based specifications and VTn-stability [42, 43] for volume-based stability testing.

A geometric interpretation of Gibbs' phase rule

Gibbs' phase rule was introduced in Section 2.1.5, dictating that at any equilibrium state, the number of degrees of freedom follows $F = n_c + 2 - n_p$. This implies that a pure-component system exhibits:

- $n_p = 1$: two degrees of freedom (a region in a PT-diagram)
- $n_p = 2$: one degree of freedom (a line in a PT-diagram)
- $n_p = 3$: zero degrees of freedom (a point in a PT-diagram)

Equality of Gibbs energies of two phases at fixed pressure (or temperature) can thus only occur for certain temperatures (pressures). Three-phase equilibrium exists at a single point of pressure and temperature.

As analysed by Baker *et al.* [36], we can observe these conditions in compositional Gibbs energy diagrams as well. Let us analyze a binary mixture first, as depicted in Figure 4.2. For two-phase conditions in the PTx-space, we are free to vary two out of pressure, temperature and composition. The system can be in equilibrium with a third phase if the hyperplane is tangent to three local minima of the Gibbs energy surface. Such conditions leave only a single quantity of state to be varied independently. Alignment of four local minima occurs only at specific values of P, T and x at the quadruple point.

The number of local minima is thus not necessarily limited to two, as the phase equilibrium problem may involve any number of phase types: vapour and multiple liquid phases (VLE, VLLE and more), as well as other phases such as ice, minerals and hydrates. The same principles for tangent plane criteria apply as discussed before, but non-negativity of all local minima must be confirmed to verify stability.

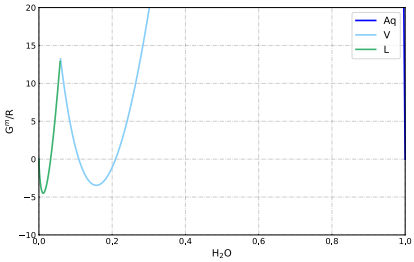

Figure 4.2.: Gibbs energy surfaces or binary system H_2O-nC_5 system at P = 10 bar and T = 387.8 K. Local minima are located at nC_5-rich (V), H_2O-rich compositions (Aq) and an intermediate composition for the L phase.

Generalizing for any number of components n_c, a PT-flash exhibits a maximum number of $n_p = n_c$ phases. Any solution with $n_p = n_c$ phases is located within a *tie-simplex*, which is the n_c-dimensional equivalent of a tie-line. For any phase state for which $n_p < n_c$, the tangent hyperplane is no longer uniquely described by the fixed equilibrium compositions and tie-simplices reduce to lower-dimensional

shapes. For instance, in a ternary system (Figure 4.3), three phases coexist inside the tie-triangle and tie-lines exist in two-phase regions outside of the tie-triangle.

The tangent hyperplane must be found that does not intersect the hypothetical single-phase surface anywhere. A false solution of the phase equilibrium problem may be obtained by a tangent hyperplane to a wrong set of phase compositions. The false solution does satisfy the material balance and equifugacity conditions, but is intersected by the single-phase surface in some places, and thus a lower minimum of the Gibbs free energy can be obtained.

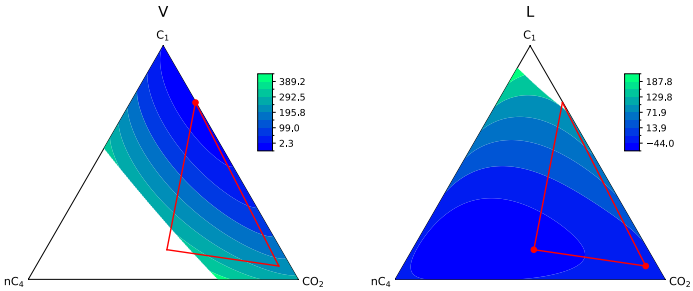

Figure 4.3.: Gibbs energy surfaces for ternary system nC_4-CO_2-C_1 at P = 10 bar and T = 200 K. The two diagrams represent the vapour-like and liquid-like roots of the cubic EoS, respectively.

Critical phases

The occurrence of critical phases can also be observed in Gibbs energy diagrams. At a critical point, equilibrium phase compositions and densities of two or more phases become identical. As the critical point is approached, equilibrium phase properties become increasingly similar. The local minima of the *tpd*-function move together until they degenerate into one local minimum at the critical point [56].

4.1.2. State specifications and state function minimization

It was discussed in Section 2.1 that thermodynamic equilibrium corresponds to a maximization of entropy S at the given extensive parameters (U, V, $\mathbf{n}$, ...), or minimization of internal energy U. By means of defining other thermodynamic potentials, the state of a system is also completely and uniquely described by any of the other surfaces $(H, S, P, \mathbf{n})$, $(G, T, P, \mathbf{n})$ and $(A, T, V, \mathbf{n})$. A phase equilibrium problem can thus be specified with different state variables, as listed in Table 4.1. Equilibrium can be found by minimizing the corresponding state function. For instance, for a *PH*-flash, find H_j and n_{ij} for which:

$$\max S(P, H, \mathbf{n}) \equiv \sum_j S_j(P, H_j, \mathbf{n}_j) \tag{4.7a}$$

Table 4.1.: State specifications and state function to be minimized

State specification	V, S	V, U	V, T	P, S	P, H	P, T
Minimized state function	U	$-S$	A	H	$-S$	G

subject to

$$P = P^{spec}, \quad \sum_j H_j - H^{spec} = 0, \quad \sum_{k=0}^{n_p-1} \mathbf{n}_k = \mathbf{z} \tag{4.7b}$$

However, thermodynamic models are solved at $(P, T, \mathbf{n})$ or $(V, T, \mathbf{n})$, and not at $(P, H, \mathbf{n})$. The constraint of specified enthalpy is not linear in the independent variables and therefore cannot be eliminated explicitly. It is only with PT- and VTn-specifications that we can perform the flash as an unconstrained minimization problem [38, 43]. Other state specifications can be solved as a constrained optimization. For PH-flashes specifically, direct maximization of entropy has been investigated by Brantferger *et al.* [7] and Sun *et al.* [50]. Paterson *et al.* [51] performed a constrained optimization and a partial Newton approach.

Recall that, from the second law (Section 2.1), it follows that in open systems between which heat is allowed to flow, entropy can be increased by redistributing energy such that the temperature of each phase is equal. This result was also obtained from (2.53). At the global minimum for a PH-flash, the phases are thus in thermal equilibrium. The phase equilibrium calculations may then be formulated with temperature as an independent variable. Michelsen [44] introduced a modified objective function that involves the Gibbs energy, which can formally eliminate the enthalpy constraint. Similarly, modified objective functions have been defined for the isentropic (PS) flash, as well as for volume-based UV- and SV-specifications [45]. In fact, it has been shown by Nichita [52] that by solving the nonlinear equation in temperature, the stationary points of the tpd-functions for $(P, H, \mathbf{n})$- and $(P, S, \mathbf{n})$-specifications are equivalent to those obtained in PT, while $(V, U, \mathbf{n})$- and $(V, S, \mathbf{n})$-based stability testing reduces to $(V, T, \mathbf{n})$-stability.

Minimization of Gibbs free energy

For a PT-flash specification with any number of phases, the minimization formulation can be expressed as:

$$\min G(P, T, \mathbf{n}) \equiv \sum_j G_j(P, T, \mathbf{n}_j) \tag{4.8a}$$

subject to

$$P = P^{spec}, \quad T = T^{spec}, \quad \sum_{k=0}^{n_p-1} \mathbf{n}_k = \mathbf{z} \tag{4.8b}$$

The material balance constraint can be eliminated by using the relation $\mathbf{n}_{n_p-1} = \mathbf{z} - \sum_{k \neq n_p-1} \mathbf{n}_k$ such that the calculation can be performed as an

unconstrained minimization. The dimensionless Gibbs free energy is given by:

$$\overline{G} = G/RT = \sum_{k=1}^{n_p} \sum_{i=1}^{n_c} n_{ik} \ln \hat{f}_{ik} \tag{4.9}$$

with n_{ik} the number of moles of species i in phase k. Minimizing (4.9) with respect to mole numbers, we have that the chemical potential for each component is the same throughout all phases, or, equivalently, that the fugacities of the individual components are equal. Denoting one reference phase by using the material balance constraint, the mole numbers in one phase are dependent variables, and this gives n_c relations for all but one phase:

$$\ln \hat{f}_{ij}(T, P, \boldsymbol{n}_j) - \ln \hat{f}_{iR}(T, P, \boldsymbol{n}_k) = 0, \quad i = 1, \ldots, n_c \tag{4.10}$$

Any tangent hyperplane to one or more phase compositions that does not correspond to any negative phase fractions obeys the equal fugacity and material balance relations. The system is, however, at equilibrium if and only if the total Gibbs energy is at its global minimum We are therefore required to find the specific combination of phases for which no further reduction in Gibbs energy can be realized.

Modified objective functions

Michelsen [44] introduced modified objective functions Q for PH- and PS-flashes that eliminate the enthalpy or entropy constraint. For an isenthalpic flash,

$$Q^H(P, T, \mathbf{z}) = \frac{G(P, T, \mathbf{z}) - H^{spec}}{T} \tag{4.11a}$$

The independent variables are T and $\mathbf{n}_j$. The gradient vector of Q then reads

$$\frac{\partial Q^H}{\partial n_{ij}} = \frac{1}{T}(\mu_{ij} - \mu_{i0}) \tag{4.11b}$$

$$\frac{\partial Q^H}{\partial T} = -\frac{1}{T^2}(H - H^{spec}) \tag{4.11c}$$

Note that the gradient of Q^H with respect to temperature essentially reduces to the enthalpy specification equation. Similarly, for the isentropic specification:

$$Q^S(P, T, \mathbf{z}) = G(P, T, \mathbf{z}) + TS^{spec} \tag{4.12a}$$

with the gradient vector

$$\frac{\partial Q^H}{\partial n_{ij}} = \mu_{ij} - \mu_{i0} \tag{4.12b}$$

$$\frac{\partial Q^S}{\partial T} = \left(\frac{\partial G}{\partial T}\right)_{P,\mathbf{z}} + S^{spec} = -S + S^{spec} \tag{4.12c}$$

At the solution, the gradient of Q with respect to the independent variables are zero. However, the second derivative of Q with respect to temperature is negative:

$$\frac{\partial^2 Q^H}{\partial T^2} = \frac{2}{T^3}(H - H^{spec}) - \frac{1}{T^2}\left(\frac{\partial H}{\partial T}\right)_{P,\mathbf{z}} = \frac{2}{T^3}(H - H^{spec}) - \frac{C_P}{T^2} \tag{4.13a}$$

$$\frac{\partial^2 Q^S}{\partial T^2} = -\left(\frac{\partial S}{\partial T}\right)_{P,\mathbf{z}} = -\frac{C_P}{T} \tag{4.13b}$$

As a result, the solution corresponds to a saddle point, and the Hessian matrix is not positive definite. Michelsen [44] modified the Q-functions by adding a quadratic term that transforms the problem to an unconstrained minimization, but it was reported that this is not entirely unproblematic. Later, Michelsen [45] extended the set of Q-functions to formulate any of the state specifications with Gibbs energy G or Helmholtz energy A as core functions (Table 4.2). It is only for the PT- and VT-specifications that the solution corresponds to a minimum in the Q-function. For other specifications, the stationary points of the Q-functions at the solution are saddle points. They have a positive curvature in the composition directions and a negative curvature in the pressure and/or temperature direction.

The volume-based PT-flash [48, 49] could be an attractive option for PT-flashes, as volume is an independent variable in most (complex) thermodynamic models and no explicit volume root calculation is required. Volume-based thermodynamics have been used in critical point calculations as well [62].

Table 4.2.: Modified objective functions with G and A as core functions

State specification	G-based Q	A-based Q
P, T	G	$A + VP^{spec}$
P, H	$(G - H^{spec})/T$	$(A + VP^{spec} - H^{spec})/T$
P, S	$G + TS^{spec}$	$A + TS^{spec} + VP^{spec}$
T, V	$G - PV^{spec}$	A
U, V	$(G - U^{spec} - PV^{spec})/T$	$(A - U^{spec})/T$
S, V	$G + TS^{spec} - PV^{spec}$	$A + TS^{spec}$

A nested approach for PT- and VTn-based state specifications

It is possible to optimize the Q-function using second-order methods. By nesting a PT-flash calculation with a maximization with respect to the remaining one or two independent variables (T and, in some cases, P), we can solve the specification by maximizing Q. For instance, for the PH-flash, $Q^H = Q^H(T)$ becomes a function that can be optimized for temperature:

$$\max\left((G_{min} - H^{spec})/T\right) \tag{4.14}$$

where G_{min} is the minimum Gibbs energy at current $(P, T, \mathbf{n})$. Then, the gradient $g(T)$ (4.11c) and Hessian $g'(T)$ (4.13a) are required for the determination of the

maximum. The maximum of Q can be obtained by locating the zero gradient $g(T)$ using a root-finding method [46, 47]. This approach can be executed for any number of phases, which requires only multiphase *PT*-procedures. Evaluation of $g'(T)$ of the specific Q-function with respect to temperature requires partial derivatives of the *PT*-flash procedure. These derivatives will be developed in 4.2.3.

Alternatively, derivative-free root-solving methods have been applied to find the solution of temperature to the specification equation [47]. Along an isobar, the enthalpy and entropy increase monotonously with temperature. Therefore, bisection or more clever derivative-free methods, such as Brent's method [132], are very robust. Moreover, these methods can be combined with gradient-based updates of temperature for the specification equation. Under difficult conditions, the inner loop of *PT*-flashes may take many iterations to converge, and therefore, a Newton step for temperature can greatly reduce the number of *PT*-flash calls.

4.2. Computational methods for multiphase equilibrium at *PT*

In this section, we develop methods for solving phase equilibrium problems at *PT*-specification. It was discussed that the isothermal flash can be performed as an unconstrained minimization. Most implementations of a Gibbs energy minimization procedure involve a sequential approach of stability testing, indicating whether or not a mixture is stable at specified conditions, and a multiphase split algorithm, where material balance and fugacity relations are solved. In this section, we explore computational methods for phase stability testing, phase split calculation, and solving the Rachford-Rice equations to satisfy the material balance.

4.2.1. Phase stability testing

The stability criterion for a *PT*-specification was obtained in terms of the reduced tangent plane distance:

$$tpd(\mathbf{y}) = \sum_i y_i\big(\ln y_i + \ln \hat{\varphi}_i(\mathbf{y}) - d_i\big) \geq 0 \tag{4.6}$$

with $d_i = \ln z_i + \ln \hat{\varphi}_i(\mathbf{z})$. The optimization of the reduced tangent plane distance is subject to the constraint that $\mathbf{y}$ represents a valid phase composition ($y_i \geq 0$) and mole fractions y_i sum to 1. To find the stationary points of the tpd-function, the optimization can be formulated by means of a Lagrange multiplier λ [56]:

$$\mathcal{L}(\mathbf{y}, \lambda) = \sum_i y_i\big(\ln y_i + \ln \hat{\varphi}_i(\mathbf{y}) - d_i\big) - \lambda\Big(\sum_i y_i - 1\Big) \tag{4.15}$$

At all stationary points (i.e., minima, maxima, saddle points):

$$\frac{\partial \mathcal{L}}{\partial y_i} = \ln y_i + \ln \hat{\varphi}_i(\mathbf{y}) - d_i + 1 - \lambda = 0, \quad i = 1, \ldots, n_c \tag{4.16}$$

Based on this result, Michelsen [37] introduced variables $Y_i = \exp(-k)y_i$, where $k = \lambda - 1$. The stationarity criterion then becomes:

$$\ln Y_i + \ln \hat{\varphi}_i(\mathbf{Y}) - d_i = 0, \quad i = 1, \ldots, n_c \tag{4.17}$$

The Y_i can formally be treated as mole numbers ($y_i = Y_i / \sum_j Y_j$), with $\hat{\varphi}_i(\mathbf{Y}) = \hat{\varphi}_i(\mathbf{y})$. Then, the different but equivalent stability criterion based on the variables Y_i reads:

$$tpd^*(\mathbf{Y}) = 1 + \sum_i Y_i \big(\ln Y_i + \ln \hat{\varphi}_i(\mathbf{Y}) - d_i - 1 \big) \geq 0 \tag{4.18}$$

where no constraints on the Y_i except $Y_i > 0$ are required. At the stationary points, tpd^* satisfies

$$\frac{\partial tpd^*}{\partial Y_i} = \ln Y_i + \ln \hat{\varphi}_i(\mathbf{Y}) - d_i = 0, \quad i = 1, \ldots, n_c \tag{4.19}$$

The stationary points of the modified tangent plane distance, as well as their sign, are the same as those of the original function. Stability of a mixture is therefore indicated by non-negative values of tpd^* for any trial phase composition $\mathbf{Y}$. Equivalently, $k \geq 0$ or $\sum_i Y_i \leq 1$.

The composition $\mathbf{z}$ also represents a stationary point of the tangent plane distance function, referred to as a trivial solution. A trivial solution is a minimum of the tpd-function if the curvature is positive in all directions of composition (indicated by a positive-definite Hessian matrix, i.e., all eigenvalues are positive). If, on the other hand, the tangent plane distance can become negative arbitrarily to $\mathbf{z}$, the mixture is intrinsically unstable. The trivial solution is not a minimum but a local maximum or a saddle point (Hessian matrix has one or more negative eigenvalues). In case of a maximum, at least two minima in the Gibbs free energy surface exist, corresponding to compositions other than the feed.

Successive substitution

The gradient vector reads:

$$g_i = \frac{\partial tpd^*}{\partial Y_i} = \ln Y_i + \ln \hat{\varphi}_i(\mathbf{Y}) - d_i \tag{4.20}$$

A successive substitution iteration (SSI) is obtained from $\boldsymbol{\Delta} \ln \mathbf{Y} = -\mathbf{g}(\mathbf{n})$ and therefore [133]:

$$\ln Y_i = d_i - \ln \hat{\varphi}_i(\mathbf{Y}) \tag{4.21}$$

This procedure will converge to a local minimum of the modified tangent plane distance if the eigenvalues of the Hessian are smaller than 1, which is the case in the vast majority of applications. When the fugacity coefficients are weakly dependent on composition, convergence is rapid. In the vicinity of a mixture critical point, however, one eigenvalue will approach 1. The rate of convergence of

successive substitution iterations may become extremely slow [37, 56]. In addition, divergence of the SSI procedure has been observed in certain cases that exhibit strong negative deviations from ideal solution behaviour, such as polymer solutions and gas hydrates [134]. In such cases, improved methods are required.

Newton's method with mole numbers Y or $\ln Y$

To calculate a Newton iteration $\mathbf{H\Delta Y} = -\mathbf{g}$, the Hessian matrix is [37]:

$$H_{ij} = \frac{\partial g_i}{\partial Y_j} = \frac{\delta_{ij}}{Y_i} + \frac{\partial \ln \varphi_i}{\partial Y_j} \tag{4.22}$$

If the nonlinear system of equations $\mathbf{g(Y)} = \mathbf{0}$ is solved with $\ln Y_i$ as independent variables, the Newton iterations are [133]:

$$\mathbf{J\Delta} \ln \mathbf{Y} = \mathbf{HU^{-1}\Delta} \ln \mathbf{Y} = -\mathbf{g} \tag{4.23}$$

where

$$J_{ij} = \frac{\partial g_i}{\partial \ln Y_j} = \delta_{ij} + \frac{\partial \ln \varphi_i}{\partial Y_j} \tag{4.24}$$

The elements of matrix $\mathbf{U}$ and its inverse are $U_{ij} = \delta_{ij}/Y_i$ and $U_{ij}^{-}1 = \delta_{ij}Y_i$, and $\mathbf{\Delta} \ln \mathbf{Y} = \mathbf{U\Delta Y}$. The Jacobian matrix is non-symmetric, but the system can be solved by applying a Cholesky decomposition of $\mathbf{H}$, such that $\mathbf{\Delta} \ln \mathbf{Y} = -\mathbf{UL}^{-T}\mathbf{L}^{-1}\mathbf{g}$ [133]. It was found that this is the best choice of independent variables [135].

Newton's method with α

Alternatively, Michelsen [37] proposed the use of $\alpha_i = 2\sqrt{Y_i}$ as independent variables. Newton's method normally converges relatively fast, but in cases where the Hessian matrix is near-singular or has negative eigenvalues, the desired solution may take several steps to converge or may not be found. From (4.22), it is clear that when the variable Y_i reaches lower values, the diagonal of the Hessian matrix may have significantly high values. This makes the condition number not proper for the solution search. In a Newton procedure with α as independent variable, the Hessian matrix will have its diagonal elements close to one for small values of Y_i. The matrix will thus be well-conditioned, since the best condition for a matrix is achieved when it is close to an identity matrix. In this method, the gradient is given by:

$$\overline{g}_i = \frac{\partial D}{\partial \alpha_i} = g_i\sqrt{Y_i} \tag{4.25}$$

The Hessian matrix:

$$\overline{H}_{ij} = \frac{\partial^2 D}{\partial \alpha_i \partial \alpha_j} = \delta_{ij} + \frac{1}{4}\alpha_i\alpha_j\frac{\partial \ln \varphi_i}{\partial Y_i} + \frac{1}{2}\delta_{ij}\overline{g}_i \tag{4.26}$$

The last term can be neglected without any effect on the rate of convergence since it vanishes at the solution.

Advanced computational methods for stability testing

In case the Hessian is not positive definite, a descent direction of the objective function is not guaranteed by the Newton step and Cholesky factorization will fail. A switch back to SSI can be performed instead, which leads to a decrease of the objective function in the vast majority of cases. More advanced methods involve the application of a correction to the Hessian to yield a positive-definite matrix and ensure a descent direction of the objective function:

$$(\mathbf{H} + \mathbf{E})\mathbf{\Delta}\xi = -\mathbf{g} \tag{4.27}$$

where $\mathbf{E}$ is a diagonal matrix. Michelsen [38] mentioned the use of a modified Cholesky decomposition [136]. Petitfrere and Nichita [53] investigated Trust Region methods to find the magnitude of the correction. In addition, a line search procedure can be employed to check whether the updated variables lie within the feasible region for a full Newton step and to ensure a decrease in the objective function [43, 49].

4.2.2. Multiphase split

The aim of multiphase split calculations is to satisfy the material balance and equifugacity constraints. For this, the dimensionless Gibbs energy (4.9) is minimized with respect to mole numbers n_{ik}. The gradient vector reads:

$$\begin{aligned}(g_i)_k = \frac{\partial G}{\partial n_{ik}} = \ln f_{ik} - \ln f_{iR} &= \ln x_{ik} + \ln \varphi_{ik} - \ln x_{iR} - \ln \varphi_{iR} \\ &= \ln K_{ik} + \ln \varphi_{ik} - \ln \varphi_{iR}\end{aligned} \tag{4.28}$$

The solution procedure is initialized with a set of initial guesses for equilibrium constants $\ln \mathbf{K}$. Phase fractions and compositions can be calculated by means of the Rachford-Rice equations, which are obtained by substituting the material balance constraints. Subsequently, fugacities can be obtained from the thermodynamic models to instantiate the Gibbs energy minimization procedure.

Material balance: the Rachford-Rice equations

A material balance for each component yields

$$\sum_{j=0}^{n_p} \theta_j x_{ij} = z_i, \quad i = 1, \ldots, n_c \tag{4.29}$$

Finally, mole fractions in the different phases j must sum to unity, yielding

$$\sum_{i=1}^{n_c} x_{ij} = 1 \tag{4.30a}$$

or

$$\sum_{i=1}^{n_c}(x_{ij}-x_{i0})=0, \quad j=1,\ldots,n_p-1 \tag{4.30b}$$

Utilizing $\theta_0 = 1-\sum_{j=1}^{n_p-1}\theta_j$ and introducing $K_{ij}=x_{ij}/x_{i0}$, (4.29) can be written as

$$x_{i0}\left(1+\sum_{j=1}^{n_p-1}\theta_j(K_{ij}-1)\right)=z_i, \quad i=1,\ldots,n_c \tag{4.31}$$

Substituting (4.31) into (4.30) gives a generalized Rachford-Rice equation [34, 35]:

$$f_j(\theta)=\sum_{i=1}^{n_c}\frac{z_i(K_{ij}-1)}{1+\sum_{k=1}^{n_p-1}\theta_k(K_{ik}-1)}=0, \quad j=1,\ldots,n_p-1 \tag{4.32}$$

The solution to the *RR* equation yields the set of independent phase fractions θ_j. The phase compositions can subsequently be obtained from (4.31) and the equilibrium constants K_{ij}. Note that at a solution of equal fugacities, by definition

$$K_{ij}=x_{i0}/x_{ij}=\varphi_{ij}/\varphi_{i0} \tag{4.33}$$

For two phases, equation (4.32) represents a monotonically decreasing function within the negative flash window, that is, the region characterized by all non-negative phase compositions [137]. Alternatively, the two-phase RR equation can be solved using convex transformations and restricted solution windows, leading to a significant increase in solution speed [138, 139].

For multiphase systems, recursive equation solving approaches have been developed [140, 141]. However, the minimization approach from Michelsen [39], which was later extended to negative flashes [142–144], is preferred.

Successive substitution

A successive substitution iteration is obtained from $\boldsymbol{\Delta}\ln\mathbf{K}=-\mathbf{g(n)}$ [133], which corresponds to updating the equilibrium constants $\ln K_{ik}$ by:

$$\ln K_{ik}=\ln\varphi_{iR}-\ln\varphi_{ik} \tag{4.34}$$

With the updated equilibrium factors, the material balance is satisfied by solving the RR equation (4.32) for the set of independent phase fractions θ_k.

The SSI method is extremely robust, but it might require large numbers of iterations in the vicinity of phase boundaries and critical regions [38]. The use of a Newton procedure can obtain quadratic convergence near the solution, but this requires a good initial guess. Generally, calculations are initialized with a number of SSI iterations and switch to the second-order method close to the solution. When second-order Newton-Raphson methods are used, either component mole numbers n_{ik} or equilibrium constants $\ln K_{ik}$ are selected as independent variables.

Newton's method with mole numbers n

Taking the component mole numbers as independent variables, the Newton step is $\mathbf{H\Delta n} = -\mathbf{g}$ [53]. For an arbitrary number of phases, the Hessian reads:

$$\begin{aligned}\left(H_{ij}\right)_{kp} = \frac{\partial^2 G}{\partial n_{ik}\partial n_{jp}} &= \frac{\partial}{\partial n_{jp}}\left(\ln K_{ik} + \ln\varphi_{ik} - \ln\varphi_{iR}\right) \\ &= \left(U_{ij}\right)_{kp} + \left(\Phi_{ij}\right)_{kp}\end{aligned} \tag{4.35a}$$

This can be expressed as the sum of two symmetric matrices $\mathbf{H} = \mathbf{U} + \mathbf{\Phi}$ [38, 145]. With $x_{ik} = n_{ik}/\theta_k$, the elements of $\mathbf{U}$ (which is always positive semi-definite) read:

$$\begin{aligned}\left(U_{ij}\right)_{kp} = \frac{\partial \ln K_{ik}}{\partial n_{jp}} &= \frac{\partial}{\partial n_{jp}}\left(\ln n_{ik} - \ln\theta_k - \ln n_{iR} + \ln\theta_R\right) \\ &= \delta_{kp}\left(\frac{\delta_{ij}}{n_{ik}} - \frac{1}{\theta_k}\right) + \frac{\delta_{ij}}{n_{iR}} - \frac{1}{\theta_R}\end{aligned} \tag{4.35b}$$

The non-ideal contribution $\mathbf{\Phi}$:

$$\begin{aligned}\left(\Phi_{ij}\right)_{kp} = \frac{\partial^2 G_E}{\partial n_{ik}\partial n_{jp}} &= \delta_{kp}\frac{\partial \ln\varphi_{ik}}{\partial n_{jp}} - \frac{\partial \ln\varphi_{iR}}{\partial n_{jR}}\frac{\partial n_{jR}}{\partial n_{jp}} \\ &= \delta_{kp}\frac{\partial \ln\varphi_{ik}}{\partial n_{jp}} + \frac{\partial \ln\varphi_{iR}}{\partial n_{jR}}\end{aligned} \tag{4.35c}$$

The dimensionality of the problem is $n_c \times (n_p - 1)$ and the Hessian has a block structure of $(n_p - 1) \times (n_p - 1)$. For two phases, the reference phase fraction can be expressed as $\theta_0 = 1 - \theta_1$. Substituting $n_{ik} = \theta_k x_{ik}$, matrix $\mathbf{U}$ reduces to [133]:

$$\begin{aligned}U_{ij} = \frac{\partial \ln K_i}{\partial n_{j1}} &= \delta_{ij}\left(\frac{1}{\theta_1 x_{i1}} + \frac{1}{(1-\theta_1)x_{i0}}\right) - \left(\frac{1}{\theta_1} + \frac{1}{1-\theta_1}\right) \\ &= \frac{1}{\theta_1(1-\theta_1)}\left(\frac{\delta_{ij} z_i}{x_{i1}x_{i0}} - 1\right)\end{aligned} \tag{4.36}$$

We can use the symmetry of $\mathbf{H}$ efficiently by solving the Newton step with a Cholesky factorization of the Hessian $\mathbf{H} = \mathbf{L}\mathbf{L}^T$ (or $\mathbf{H} = \mathbf{L}\mathbf{D}\mathbf{L}^T$), such that $\mathbf{\Delta n} = -\mathbf{L}^T\mathbf{L}^{-1}\mathbf{g}$ [38, 145]. In addition, Michelsen [38] suggested selecting for each component the phase with the largest molar amounts as reference phase such that the Hessian is better conditioned.

Newton's method with equilibrium constants $\ln K$

Taking $\ln K_{ik}$ as primary variables instead, the Newton iteration becomes $\mathbf{J\Delta}\ln\mathbf{K} = -\mathbf{g}$, where $\mathbf{\Delta}\ln\mathbf{K} = \mathbf{U\Delta n}$ and $\mathbf{J} = \mathbf{H}\mathbf{U}^{-1} = \mathbf{I} + \mathbf{\Phi}\mathbf{U}^{-1}$. For two-phase equilibrium, the inverse of matrix $\mathbf{U}$ (4.36) is given by Petitfrere and Nichita [133]:

$$U_{ij}^{-1} = \frac{\partial n_{iV}}{\partial \ln K_j} = VLu_i\left(\delta_{ij} + \frac{u_j}{s}\right) \tag{4.37}$$

where $s = 1 - \sum_i u_i$ and $u_i = x_i y_i / z_i$. For multiphase equilibria, it is less straightforward to invert matrix $\mathbf{U}$ (4.35b) analytically. The elements of $\mathbf{U^{-1}}$ are given by Petitfrere and Nichita [145].

The variables $\ln K_{ik}$ are much better scaled than the mole numbers n_{ik}, improving the condition number of $\mathbf{J}$ as compared to $\mathbf{H}$, and unlike n_{ik}, they are unbounded. The Jacobian matrix $\mathbf{J}$ is non-symmetric, but we can take advantage of the symmetry of matrices $\mathbf{\Phi}$ and $\mathbf{U^{-1}}$ in constructing it. The Newton step can be performed using an LU decomposition. The use of $\ln K_{ik}$ does, however, require the solution of the RR material balance equations (4.32). Alternatively, one can solve the system $\mathbf{H\Delta n} = -\mathbf{g}$ with a Cholesky decomposition of the Hessian, and then update the equilibrium factors through $\mathbf{\Delta} \ln \mathbf{K} = \mathbf{U\Delta n}$.

Petitfrere and Nichita [146] developed a linear system structure to update the equilibrium ratios $\ln \mathbf{K}$ and phase fractions θ simultaneously, whilst making use of symmetry such that a Cholesky decomposition can be used. In this way, the solution of the RR equations in the inner loop can be avoided.

Choice of variables

In constructing the matrices for each of the independent variables discussed above, one can make use of symmetry. In addition, in Newton iterations with mole numbers $\mathbf{n}$ or when solving $\mathbf{\Delta} \ln \mathbf{K} = \mathbf{U\Delta n}$, one can perform a Cholesky decomposition in $n^3/3$ floating point operations, while an LU decomposition requires $2/3n^3$ flops. This difference becomes increasingly large with the number of components and phases. The Jacobian, however, is much better conditioned than the Hessian, especially near phase boundaries (and mole numbers become small). Therefore, Petitfrere and Nichita [145] recommended using $\ln \mathbf{K}$ using the Cholesky decomposition, and switching to $\ln \mathbf{K}$ whenever any value of $\mathbf{n}$ becomes small or if phase compositions become similar, which indicates one is in the vicinity of a critical point.

Analogous to phase stability calculations, advanced methods are available to improve the robustness of the phase split algorithm and ensure descent direction of the objective function in case of a non-positive definite Hessian matrix. A switch back to SSI, modified Cholesky decomposition [38, 136], Trust Region methods [53], and line search [43, 49] can be applied.

4.2.3. Partial derivatives of phase equilibrium at *PT*

To use gradient-based methods of the nested *P*-based phase equilibrium algorithm, evaluation of the partial derivatives of the *PT*-flash is required. Furthermore, in case the phase equilibrium calculations are integrated into a compositional flow and transport or process simulator, the partial derivatives of the flash procedure with respect to the primary variables in the simulation may be required. The partial derivatives can be obtained by implicit differentiation of the thermodynamic and material balance relations (4.10), (4.29), and (4.30), which comprise the multiphase isothermal-isobaric equilibrium procedure. The partial derivatives for isenthalpic and isentropic flashes can be calculated by applying the chain rule.

Partial derivatives of *PT*-flash

The thermodynamic and material balance relations read:

$$\ln \hat{f}_{ij}(T,P,\boldsymbol{n}_j) - \ln \hat{f}_{i0}(T,P,\boldsymbol{n}_0) = 0, \quad i = 1,\dots,n_c, \quad j = 1,\dots,n_p-1 \tag{4.10}$$

$$\sum_{j=0}^{n_p-1} \theta_j x_{ij} = z_i, \quad i = 1,\dots,n_c \tag{4.29}$$

$$\sum_{i=1}^{n_c} (x_{ij} - x_{i0}) = 0, \quad j = 1,\dots,n_p-1 \tag{4.30}$$

Together, these make up for $n_p(n_c+1)$ equations for the n_p phase fractions and $n_p n_c$ phase compositions. The primary variables of this set of equations are P, T and z_i.

Implicit differentiation of the fugacity relations with respect to state variable $\omega = \{P, T, z_k\}$ yields:

$$\frac{\partial \ln \varphi_{i0}}{\partial \omega_k} + \frac{1}{x_{i0}}\frac{\partial x_{i0}}{\partial \omega_k} - \frac{\partial \ln \varphi_{ij}}{\partial \omega_k} + \frac{1}{x_{ij}}\frac{\partial x_{ij}}{\partial \omega_k} = 0, \quad i = 1,\dots,n_c, \quad j = 1,\dots,n_p-1 \tag{4.38}$$

The derivative of the fugacity coefficient is calculated by using the chain rule:

$$\frac{\partial \ln \varphi_{ij}}{\partial \omega_p} = \Big(\frac{\partial \ln \varphi_{ij}}{\partial \omega_p}\Big)_{\omega_k \neq \omega_p} + \sum_{k=1}^{n_c} \Big(\frac{\partial \ln \varphi_{ij}}{\partial n_{kj}}\Big)_{P,T} \frac{\partial n_{kj}}{\partial \omega_p} \tag{4.39}$$

where $\frac{\partial n_{ij}}{\partial \omega_k} = \frac{\partial \theta_j}{\partial \omega_k} x_{ij} + \frac{\partial x_{ij}}{\partial \omega_k}\theta_j$. The first term on the right-hand side in (4.39) defaults to zero for partial derivatives with respect to overall composition z_k.

Implicit differentiation of the overall mass balance gives:

$$\sum_{j=0}^{n_p} \frac{\partial \theta_j}{\partial \omega_k} x_{ij} + \frac{\partial x_{ij}}{\partial \omega_k}\theta_j = \frac{\partial z_i}{\partial \omega_k}, \quad i = 1,\dots,n_c \tag{4.40}$$

where the right-hand side equals zero for pressure and temperature derivatives, and

$$\frac{\partial z_i}{\partial z_k} = \begin{cases} 1 - z_i, & \text{if } i = k \\ -z_i, & \text{otherwise} \end{cases}$$

Finally, the contribution of the mole fraction relations (4.30) to the system of equations is:

$$\sum_{i=1}^{n_c} \Big(\frac{\partial x_{i0}}{\partial \omega_k} - \frac{\partial x_{ij}}{\partial \omega_k}\Big) = 0, \quad j = 1,\dots,n_p-1 \tag{4.41}$$

Following Nichita and Leibovici [147], the expressions (4.39)-(4.40) can be reorganized such that the left-hand side of the system of equations is expressed

as a set of linear combinations of all terms $\Delta\mathbf{n} = \{\Delta\mathbf{n_0}^T, \ldots, \Delta\mathbf{n_{n_p-1}}^T\}$ making up system $\mathbf{J}\cdot\Delta\mathbf{n} = \mathbf{f}$:

$$\mathbf{J} = \begin{pmatrix} J_{A,00} & \cdots & J_{A,0n} \\ \vdots & \ddots & \vdots \\ J_{A,m0} & \cdots & J_{A,mn} \\ J_{Bi0} & \cdots & J_{Bin} \end{pmatrix} \tag{4.42a}$$

where A denotes the fugacity relation and B is the overall mole fraction relation.

$$J_{Aijk} = \frac{\partial \ln \hat{f}_{ij}}{\partial n_{kp}} - \frac{\partial \ln \hat{f}_{i0}}{\partial n_{kp}} \tag{4.42b}$$

$$J_{Bij} = \frac{\partial n_{ij}}{\partial n_{kp}} \tag{4.42c}$$

The right-hand side:

$$\mathbf{f} = \begin{pmatrix} f_A \\ f_B \end{pmatrix} \tag{4.43a}$$

$$f_{Aij} = \frac{\partial \ln \hat{f}_{ij}}{\partial \omega_k} - \frac{\partial \ln \hat{f}_{i0}}{\partial \omega_k} \tag{4.43b}$$

$$f_{Bi} = \frac{\partial z_i}{\partial \omega_k} \tag{4.43c}$$

For pressure and temperature derivatives, this comprises vector f where $f_{Bi} = 0$ and for composition, it is matrix $\mathbf{F}$ with $F_{jk} = \frac{\partial F_j}{\partial z_k}$. This matrix contains mostly zeros as $F_{Aij} = 0$.

Using this approach to obtain the derivatives for a *PT*-flash, we can solve partial derivatives of the flash using the same matrix $\mathbf{A}$ irrespective of which set of partial derivatives with respect to P, T or z_k is chosen.

Partial derivatives of secondary properties from *PT*-flash

The derivative $\left(\frac{\partial M}{\partial \omega_k}\right)_{\omega_j \neq \omega_k}$ of any secondary property M at equilibrium with respect to any of the primary *PT*-flash variables $\omega = \{P, T, \mathbf{z}\}$ can be formulated by means of a chain rule of the primary variables of the property $\psi = \{P, T, \mathbf{n}\}$:

$$\left(\frac{\partial M}{\partial \omega_p}\right)_{\omega_j \neq \omega_p} = \left(\frac{\partial M}{\partial \omega_p}\right)_{\psi_j \neq \omega_p} + \sum_k \left(\frac{\partial M}{\partial n_k}\right)_{P,T,n_j \neq n_k} \left(\frac{\partial n_k}{\partial \omega_p}\right)_{\omega_j \neq \omega_p} \tag{4.44}$$

The first term vanishes for any derivatives with respect to z_k as it is not a primary variable for the property calculation. The summation term reflects the dependency of the property to composition changes and therefore involves derivatives of the flash.

4.3. Strategies for multiphase equilibrium at *PT*

In general, one does not know in advance how many phases coexist at thermodynamic equilibrium, and a sequence of stability testing and phase split procedures has to be performed to find the equilibrium phases.

If it is known how many phases can coexist and good initial guesses are available, a negative flash procedure can be used to determine the phase state [93]. The domain of the Rachford-Rice equations (4.32) is bounded by the set of phase fractions θ_k that yield all non-negative phase compositions, which is larger than the physical domain. While the material balance and equifugacity equations may be satisfied in a negative flash, the solution clearly doesn't yield physically valid phase fractions. More importantly, a negative flash corresponds to a saddle point in the Gibbs energy surface, rather than a minimum [137].

Nonetheless, the negative flash can be useful for phase-state identification in a multiphase flash. In a two-phase system, θ can take any value between the asymptotes $\theta_{min} = 1/(1 - K_{max})$ and $\theta_{max} = 1/(1 - K_{min})$. In systems that are known to form two phases at maximum, converging to a non-trivial solution with a negative flash indicates the single-phase stability of the feed with the same certainty as a traditional phase stability test [137].

In multiphase systems, however, phase-state identification based on negative flash is not sufficient. If one knows the maximum number of phases, the solution of the flash procedure can only be confirmed for all positive phase fractions, i.e., it cannot confirm the phase state of a single- or two-phase mixture with a three-phase negative flash. Additional two-phase negative flash computations would be required to identify the equilibrium state, because the phase behaviour outside the three-phase region may be different from the results of the negative flash [140, 148]. Complemented with the parametrization technique, the negative flash approach can still be used for robust evaluation of complex multiphase systems [149].

For some applications of interest, such as subsurface gas production and storage, sequestration of supercritical CO_2 in saline aquifers and geothermal energy production, the assumption of a maximum of two phases is reasonable. In these cases, a two-phase negative flash approach initialized with K-values based on Henry's constants may be an appropriate choice. This approach is limited to liquid water conditions and cannot handle the transition from liquid water to steam. In addition, this simplification is not valid in more complex multiphase systems, and a full Gibbs energy minimization procedure is required.

4.3.1. A systematic approach to phase equilibrium problems

When knowledge of the number of phases at equilibrium is not available, most strategies to find the compositions of coexisting phases at equilibrium rely on a sequential combination of stability testing and phase split calculations [37, 38, 150]. If a phase state is not at the global minimum of Gibbs energy, a stability test will indicate its thermodynamic instability. Starting from various points in the thermodynamic parameter space to ensure a high degree of certainty, all stationary

points (local minima) of the tangent plane distance function are located. Stability of a phase is indicated by a non-negative value in all stationary points of the tangent plane function. In addition, the stationary points can be used to provide an initial guess for further phase split calculations [37].

For vapour-liquid systems, Michelsen [37] suggested initial estimates that are located on opposite sides of the feed composition. These initial estimates of trial phase compositions $\mathbf{Y}$ were based on ideal equilibrium constants from Raoult's law (at low pressures) or Wilson's correlation [151]:

$$\{Y_i^{stab}\} = \{x_i \cdot K_i^{Wilson}, x_i/K_i^{Wilson}\} \tag{4.45}$$

This approach works well for a two-phase vapour-liquid system, but it is less adequate for liquid-liquid or three- and multiphase equilibria. Li and Firoozabadi [152] proposed a general strategy for vapour-liquid (VLE), liquid-liquid (LLE) and vapour-liquid-liquid equilibria (VLLE) in particular. They suggested an extended set of initial guesses as

$$\{Y_i^{stab}\} = \left\{x_i \cdot K_i^{Wilson}, x_i/K_i^{Wilson}, x_i \cdot \sqrt[3]{K_i^{Wilson}}, x_i/\sqrt[3]{K_i^{Wilson}}, Y_{ij}^{pure}\right\} \tag{4.46a}$$

Here, Y_{ij}^{pure} are defined as 'pure' phases of component j according to:

$$Y_{i=j}^{pure} = y_{pure}, \quad Y_{i\neq j} = (1 - y_{pure})/(n_c - 1) \tag{4.46b}$$

with $y_{pure} = 0.9$. In their approach, they generally pick the lowest tpd from a stability test over each of the phases to initialize phase split calculations, and repeat this cycle until no instabilities of the reference phase(s) occur.

In principle, however, the information about the local minima of Gibbs free energy in the compositional space is readily available from the tangent plane distance evaluation. This information can be used to initialize multiphase split calculations directly and skip an unnecessary multi-stage procedure. In addition, while non-negativity is important to indicate whether or not a mixture is at an equilibrium state, none of the stationary points (tpd negative or positive) can, in principle, be neglected. It may be the case that the equilibrium compositions can be found by starting split calculations, including the stationary point that exhibits a tpd that is not the most negative or even positive. Thus, in principle, all feasible sets of stationary points must be considered for a phase split.

A geometric approach to initialization

Generally, we can distinguish a few outcomes from a stability test:

1. All minima of the tpd function are non-negative
2. The trivial solution is a minimum (or in the edge case, a saddle point), and at least one negative minimum exists
3. The trivial solution is a maximum, and at least two negative minima exist

This does not imply anything for the nature of the stationary points that correspond to the equilibrium phases. These could equally exhibit positive *tpd*.

The implications of this geometric approach are most easily illustrated for a binary system. Consider the binary mixture of CH_4-H_2S at T = 190 K [37], in Figure 4.4. At P = 40 atm (b), three distinct phases could be stable: an H_2S-rich liquid phase, a vapour phase rich in CH_4 and an 'intermediate' liquid phase around 10% H_2S. It was discussed in Section 4.1 that the equilibrium state in a binary system corresponds to a one-dimensional tangent hyperplane (i.e., a line) that is below the hypothetical single-phase Gibbs energy surface everywhere.

An evaluation of stationary points for the *tpd*-function at P = 40 atm indicates there are three local minima, i.e., two liquid and one vapour. In the conventional approach [152], the lowest *tpd* value and feed composition are used to initialize phase split calculations. Along the composition axis, however, the global minimum of the *tpd*-function does not necessarily correspond to an equilibrium phase. Moreover, equilibrium phases do not always exhibit a negative *tpd* value during initialization. In addition, the single-phase Gibbs energy surface is concave for a large range of compositions [153]. Initialization of the flash calculations with two local minima instead is inherently closer to any solution.

Michelsen [37] analyzed this particular problem for another reason. With a poor selection of trial phase compositions, it may be difficult to detect the two local minima in methane-rich compositions. The utilization of additional initial guesses, e.g. (4.45) in combination with a few "pure" component trial phases, may lead to convergence to such "shielded" compositions as well. Michelsen and Mollerup [56] mention that choosing pure trial phases for lightest and heaviest components is usually sufficient to locate all minima.

The logic can be easily extended to multicomponent systems. Figure 4.5 shows the Gibbs energy surfaces of the ternary mixture nC_4-CO_2-C_1. The green point indicates the stationary points of the tangent plane distance relative to a feed composition of $z = \{0.4, 0.5, 0.1\}$, while the red line denotes the tie-line of the

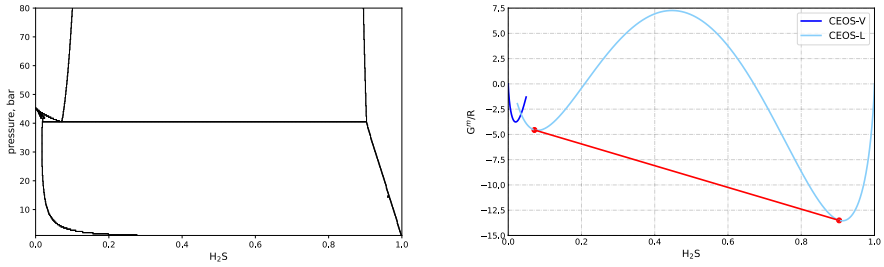

(a) Pressure-composition diagram

(b) Gibbs energy surfaces at P = 40 atm

Figure 4.4.: Binary mixture H_2S-CH_4 at T = 190 K. (a) Pressure-composition diagram. (b) represents Gibbs energy surfaces at P = 40 atm.

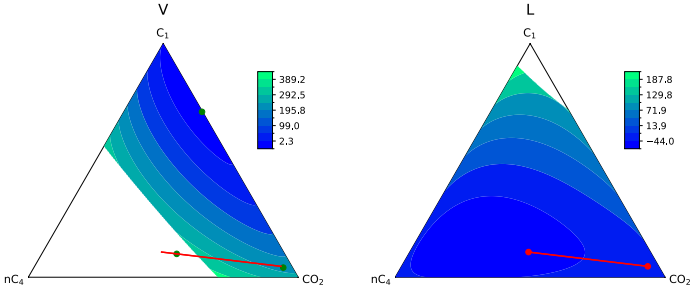

Figure 4.5.: Gibbs energy surfaces of vapour-like and liquid-like roots of cubic EoS and stationary points (green) of ternary mixture nC_4-CO_2-C_1 at P = 10 bar and T = 200 K. These are the same conditions as depicted in Figure 4.3. Notice how three stationary points are obtained from the reference composition $z = \{0.4, 0.5, 0.1\}$, but two equilibrium phases (red) exist. The third stationary point has a positive *tpd* in this example, but is associated with one of the equilibrium phases in the three-phase region.

equilibrium phases. Note that these are the same conditions that were displayed in Figure 4.3, in which the tie-triangle was plotted. The third stationary point corresponding to the vapour phase is found in the stability test, but it is not one of the equilibrium phases for this particular feed composition.

An improved initialization strategy based on stationary points

Assuming the set of initial guesses for stability testing leads to all of the stationary points of the *tpd*-function and the stability test indicates instability, one can proceed to generate initial estimates for the phase split calculations. From the total set of stationary points that present a minimum, any feasible combination satisfies two basic conditions: the number of trial phases is not larger than the number of components ($n_p \leq n_c$) and at least one stationary point exhibits a negative *tpd*.

Any feasible combination must, in principle, be considered, but in specific cases, one can make a good judgment about which of the combinations is most likely leading to the equilibrium state. When the number of stationary points is larger than the number of components, the compositions that make up a tie-simplex within which the feed composition is located are good candidates. This can be evaluated by means of barycentric coordinates. Any combination for which the feed composition is not inside its tie-simplex is likely to yield negative flashes. Secondly, a negative flash of a higher-dimensional flash can generally be used to select the proper initial guess for a subsequent lower-dimensional flash.

Huang *et al.* [154] presented an initialization strategy for multiphase flashes of CO_2-hydrocarbon mixtures based on the use of multiple stationary points of the *tpd*-function. They used all compositions of minima with negative *tpd*

to identify a possible three-phase equilibrium, leading to the elimination of a number of two-phase splits and stability analyses. This approach leads to some improvements, but we can improve it further by using all information available from the stability test [155]. Firstly, the feed composition is only considered as a feasible composition for a phase split if it represents a local minimum (i.e., Hessian is positive definite). After all, the equilibrium phases at the global minimum all correspond to local minima. Secondly, stationary points with a positive tpd can, as long as at least one negative minimum is included, equally lead to the global minimum and can therefore also be considered. The phase split can be terminated after a few iterations in case a negative flash is obtained, avoiding high computational cost. The improved multiple initialization (IMI) algorithm that we propose (Figure 4.6, Heringer *et al.* [155]) follows the sequential stability and phase split logic using all information available from the stability test. Algorithm 1 describes how to generate K-values for multiphase split calculation using the IMI approach.

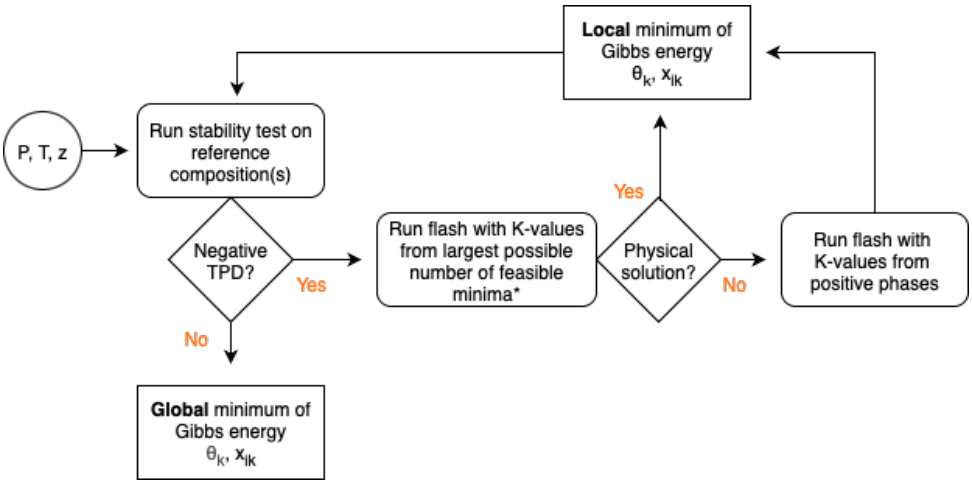

Figure 4.6.: Flow chart of general flash algorithm with IMI initialization.

(Augmented) free-water flash methods and partial solubility

The occurrence of pure phases or phases where the solubility of certain components is very small or even zero requires specific treatment in phase equilibrium calculations. The former is encountered for many equilibria with solids, such as ice, minerals or wax precipitation, while the latter is commonly found in equilibria with aqueous or hydrate phases. Michelsen [38] discussed the simplification of linear systems for flash calculations in the case of partial solubility, a simplification that requires reformulation of the material balance and objective functions. Many subsequent works have developed procedures to handle the water phase using the *Free-Water Flash* (FWF, H_2O is the only component in the water

Algorithm 1 Improved multiple initialization (IMI) strategy

while global minimum not confirmed **do**
  if reference phase composition corresponds to a minimum **then**
    Add reference phase composition(s) to set of stationary points
  end if
  For each trial phase $\mathbf{x}_j$, run stability test. Append distinct stationary points.
  if negative tpd **then**
    Sort n_{sp} stationary points according to tpd from most negative value.
    if $n_{sp} \leq n_c$ **then**
      Generate K-values from all stationary points.
    else
      Generate K-values from n_c most negative stationary points.
    end if
    Solve n_p-split. If negative phases, perform $(n_p - 1)$-split.
  else
    Global minimum found. Exit.
  end if
end while

phase) and *Augmented Free-Water Flash* concepts (AFWF, selected number of components dissolved). In Heringer *et al.* [156], we presented a general method for AFWF using both SSI and Newton iterations.

The implications of a reduction in dissolved components are easily translated into geometry. All present components correspond to one compositional dimension, and therefore, the Gibbs energy extends along the full space if all components are dissolved. For components that are not present, the dimension reduces to $n_{ij} = 0$. For instance, if we consider a ternary system with a phase that only contains two components, the Gibbs energy reduces from ternary to binary surface. For pure phases, the Gibbs energy always reduces to a single point. From this perspective, it is straightforward to develop an algorithm for phase stability testing using the AFWF concept and extend the geometrical initialization strategy to a general method for any phase equilibrium with partial solubility.

Robust and efficient *PT*-flash algorithms for use in simulation

Many works in literature validate their presented computational methods using a familiar set of benchmark mixtures. A dynamic simulation, however, requires an efficient and, most importantly, consistent solution to the flash for all (unexpected) states and compositions. With regard to flash calculations for simulation, common techniques involve a bypass of stability testing for states that are (likely) single-phase and the use of results of a previous or nearby two-phase state to initialize the two-phase flash directly [157]. While this is good practice for reservoir cells far away from wells, most things can go wrong close to the well. Here, the transient effects are most pronounced and composition changes are large.

More so, injected fluids of high purity imply dealing with trace compositions of certain components that are tedious for numerical implementation. Discussion of such flash problems is limited in literature [47, 158]. From experience, however, finding the equilibrium phases in these conditions consistently is vital to obtain convergence in simulations. The following techniques have been applied in DARTS-flash to increase robustness, consistency and performance:

- Run flash with compositions that are above a certain threshold (e.g., $z_i > 10^{-4}$) to generate an initial guess of equilibrium phases for the full composition. By evaluating the global minimum of Gibbs energy in the reduced compositional space, we obtain a state that is located very near the global minimum for the full composition. This improves the condition number of the problem, which can be very large for near-zero compositions.
- Set lower bound to compositions (e.g., $z_{min} = 10^{-8}$) and normalize compositions to run flash with. After convergence to the global minimum, recalculate the phase fractions and compositions with the actual composition, using the K-values of the final state. The minimum composition value should be low enough that it can be assumed that K-values do not change noticeably below this composition. This logic takes away the smallest compositions from the flash procedure and guarantees conservation of mass.
- Use trial compositions of strict vapour and liquid roots for stability test. This enables the stability test to locate two local minima in case V- and L- minima are of similar composition. Such conditions may occur close to a phase boundary of a near-pure phase, where all initial guesses may otherwise converge to a trivial solution, and the flash mistakenly misses the phase split.

4.3.2. A hybrid-EoS implementation

In their most basic form, cubic equations of state have proven to be reliable for thermodynamic calculations of nonpolar mixtures, but are not adequate to predict the interaction between associating molecules in aqueous solutions and fail to describe the behaviour close to infinite dilution. Using a hybrid-model approach, thermodynamic models can be combined to represent different phase types. The implementation of a separate model for the aqueous phase (Section 3.2) maintains the simplicity of solving phase equilibrium problems with cubic EoS while obtaining an accurate thermodynamic description of the aqueous phase.

The cubic equation of state is valid for all compositions, but the aqueous fugacity model is limited to a H_2O-rich phase. For a practical implementation of mixed models for aqueous systems, it is important to distinguish the vapour- and liquid-like roots of the cubic EoS to correctly identify the minima of the Gibbs energy surfaces in water-rich compositions. We can identify these roots using the characteristics of the cubic polynomial [91]. Furthermore, one can take advantage of the convexity of the Gibbs energy surface that the aqueous phase model exhibits

Parts of this chapter have been submitted to Gas Science and Engineering

throughout the relevant range of compositions. We therefore have only a single local minimum of the Gibbs energy, which allows the use of a specific initial guess for the aqueous model. The hybrid-model approach introduces a thermodynamic inconsistency that is mostly pronounced close to critical conditions. Far from brine criticality, however, we obtain robust, accurate, and efficient solution procedures.

The hybrid-EoS approach is best illustrated by utilizing Gibbs energy diagrams with surfaces for each of the different equations of state. In Figure 4.7, the Gibbs energy surfaces for a binary system H_2O-CO_2 at given pressure and temperature of the vapour(-like) root, liquid(-like) root and aqueous fugacity model are shown. The cubic EoS is valid for all compositions, but the fugacity model for the aqueous phase is limited to H_2O-rich compositions.

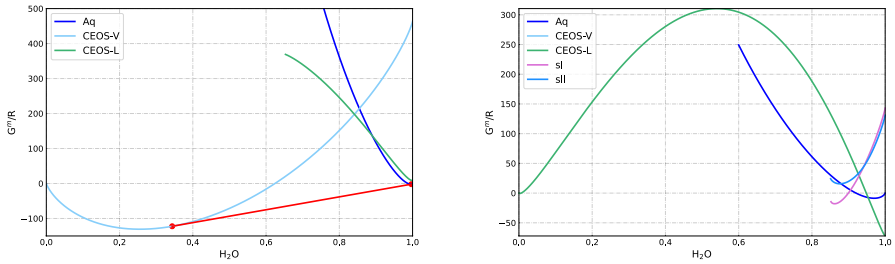

(a) P = 30 bar, T = 450 K

(b) P = 80 bar, T = 280 K

Figure 4.7.: Gibbs energy of mixing surfaces of H_2O-CO_2 mixture at (a) P = 30 bar and T = 450 K and (b) P = 80 bar and T = 280 K. *Aq* is aqueous phase fugacity model, $CEOS-V$ and $-L$ denote the vapour- and liquid-like roots (if present) of the cubic EoS, *sI* and *sII* are the hydrate EoS. The red line in (a) is tangent to the Gibbs energy surface at the equilibrium phases. Feed compositions between the red dots split into two phases.

Root selection and range of validity

From Figure 4.7, it can be observed that at H_2O-rich compositions, there can be a minimum of both the liquid(-like) root of the cubic EoS and aqueous fugacity model. Nonetheless, they both describe the liquid water phase. We thus need to identify the root types of the cubic EoS, ignore any water-rich liquid(-like) root and select the vapour-like root instead.

From a consistency point of view, a thermodynamically consistent equation of state is capable of describing the continuity of fluid between gas and liquid phase states beyond the critical point. When choosing different thermodynamic models for aqueous and other fluid phase types, however, there is no such continuous transition, and no critical point exists. Therefore, it is not possible to identify the criticality of water-rich phases, and the accuracy of the hybrid-EoS approach decreases in the vicinity of solvent criticality and beyond.

Stability test and phase split

Contrary to the equation of state, the fugacity model for the aqueous phase has been developed only to describe a water-rich liquid phase. Furthermore, the model's Gibbs energy surface is convex throughout the relevant range of compositions. We therefore have only a single local minimum of the Gibbs energy, which allows us to use a specific initial guess. In addition, for problems where fugacity coefficients are only weakly dependent on the phase composition, the SSI procedures for stability testing and phase split converge rapidly [38]. The use of a Newton procedure may not even improve performance, as the computational cost of evaluating derivatives and solving the linear system is relatively large. In addition, it is important for both the stability test and phase split updates to check if aqueous composition remains within the specified range.

4.3.3. Results of *PT*-flash calculations

The models considered in this study have been extensively validated with experimental data for binary systems of water or brines with a single solute at moderate temperatures [111, 113]. We apply the hybrid-EoS framework to gas mixtures of interest to extend this range of conditions: H_2O-CO_2 at near-critical conditions [159], and a set of gas mixtures in contact with brine [160–162].

H_2O-CO_2 mixture

Tödheide and Franck [159] measured phase equilibria of the H_2O-CO_2 system at near-critical conditions for the solvent. Although it is known that the hybrid-model approach is not able to describe criticality, Figure 4.8 shows that we can reproduce experimental results accurately up to conditions relatively close to critical conditions. The colour scheme indicates aqueous phase fractions, and the data points are measured dew- and bubble point curves. Notice that at temperatures too close to the critical temperature, the logic for root selection is no longer adequate.

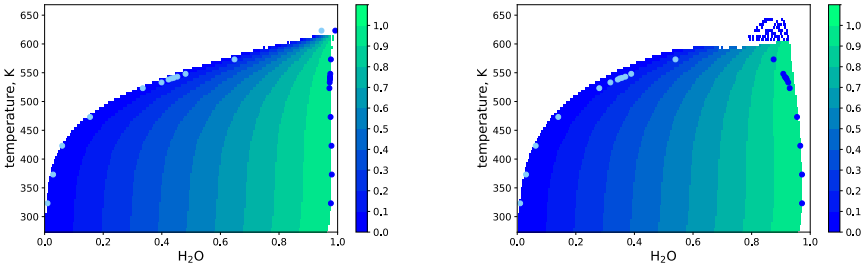

(a) P = 200 bar (b) P = 500 bar

Figure 4.8.: *Tx*-diagram for H_2O-CO_2 mixture. Colour scheme indicates the aqueous phase fraction in the two-phase region. Data from [159].

H_2O-CO_2-CH_4 mixture

Qin *et al.* [160] measured vapour-liquid equilibria of the H_2O-CO_2-CH_4 ternary system at temperatures of 324 K and 375 K and pressures from 100 to 500 bar. They reported solubility data of the pure gases and mixtures of CO_2 and CH_4. Figure 4.9 displays the results of the hybrid-EoS approach for gas solubility at 375 K and a range of pressures. The ternary diagrams show only the water-rich end of compositions, from 97% to 100% H_2O. The dots indicate the solubilities, and the tie-lines represent feed compositions for which the same equilibrium phases will be obtained.

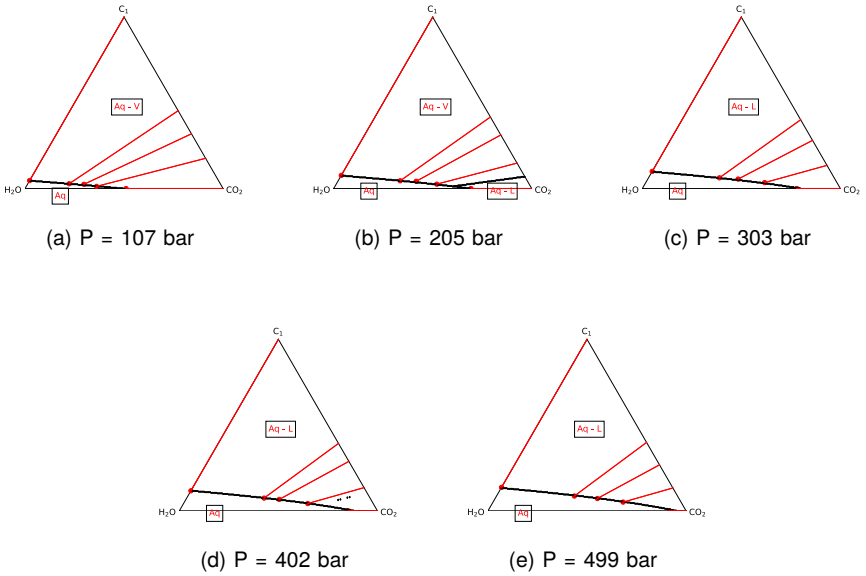

(a) P = 107 bar (b) P = 205 bar (c) P = 303 bar

(d) P = 402 bar (e) P = 499 bar

Figure 4.9.: Ternary diagram for H_2O-CH_4-CO_2 mixtures at 375.6 K, zoomed in to 97-100% H_2O. Black lines are phase boundaries, red lines are tie-lines. Solubility data from Qin *et al.* [160].

H_2O-CH_4-CO_2-H_2S mixture

Huang *et al.* [161] reported solubility and phase boundary data of two CH_4-CO_2-H_2S mixtures with water over a wide range of temperatures and pressures. Two gas compositions are considered, the first rich in CO_2 and the second rich in H_2S. This results in the appearance of a three-phase region with a dense CO_2-rich and H_2S-rich phase, respectively. The *PT*-diagrams of the mixtures (Figure 4.10a and e) show the single-, two- and three-phase regions with *Aq*, *V* and *L* phases. Note that the change from vapour-like to liquid-like phases beyond the three-phase envelope is not an actual phase change, but originates from phase labelling.

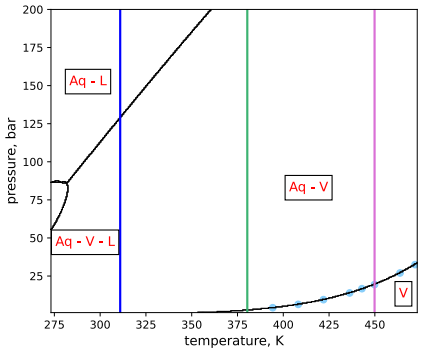

(a) Mixture 1: 0.50/0.15/0.30/0.05

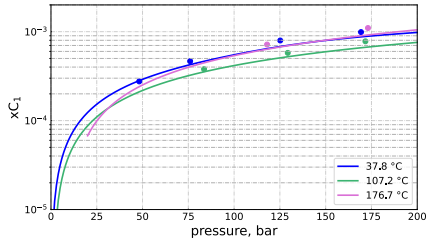

(b) CH_4 solubility for mixture 1

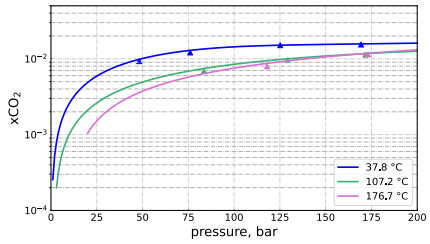

(c) CO_2 solubility for mixture 1

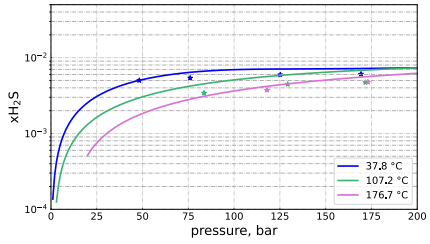

(d) H_2S solubility for mixture 1

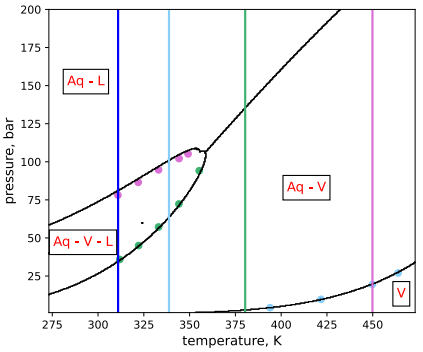

(e) Mixture 2: 0.50/0.05/0.05/0.40

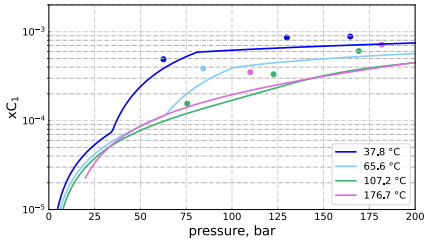

(f) CH_4 solubility for mixture 2

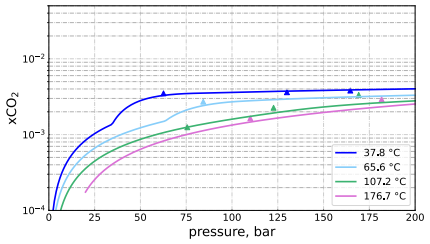

(g) CO_2 solubility for mixture 2

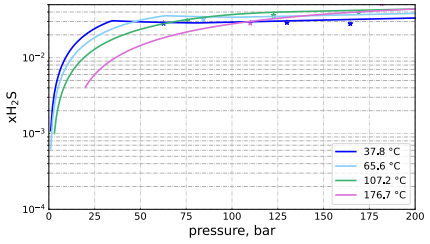

(h) H_2S solubility for mixture 2

Figure 4.10.: *PT*-diagram and solute solubility in aqueous phase for H_2O-CH_4-CO_2-H_2S mixtures. Dew point (V/Aq, blue), three-phase boundary (L/L_{H_2S}, pink, and V/L_{H_2S}, green) and solubility data from [161].

Figure 4.10 also shows the solubility curves of the two mixtures along the isotherms indicated in each of the *PT*-diagrams. The solubility of gases heavily depends on gas composition. The y-axes for each of the components are equal between mixtures 1 and 2, but the variation in gas composition creates a difference in solubility of up to an order of magnitude. This effect may play a significant role in the dynamics of subsurface applications. Furthermore, note that the slopes of the solubility curves are altered across phase boundaries. This occurs along the isotherms of 37.8 °C (311 K) and 65.6 °C (339 K) for mixture 2, at pressures where the three-phase boundary with the H_2S-rich liquid is crossed.

Brine-CO_2-H_2S mixture

Savary *et al.* [162] studied the solubility of CO_2-H_2S mixtures in pure water and 2 molal NaCl solution (moles of solute per kg of pure solvent, denoted *M*) at a temperature of 393.15 K. The results of the hybrid-EoS approach for gas solubility in 0M and 2M brines of gas mixtures with different compositions, indicated by the ratios, are shown in Figure 4.11. Under these high temperature conditions, no three-phase conditions occur. The experimental study reported difficulties with measurements of ternary mixtures at high pressures, leading to uncertainties, in part due to the toxicity of H_2S. Nonetheless, the data and results clearly show a salting-out effect of the gases as a result of brine salinity.

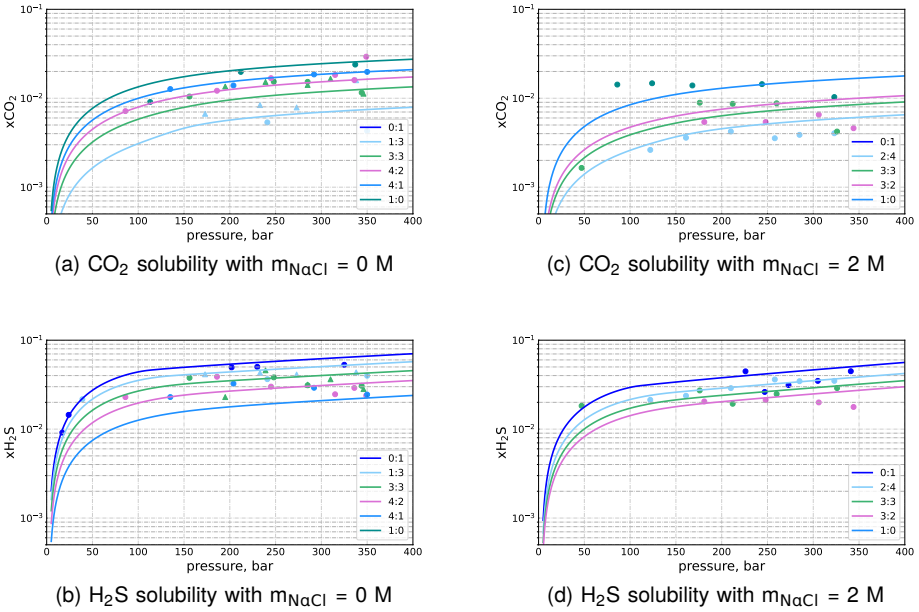

(a) CO_2 solubility with m_{NaCl} = 0 M

(c) CO_2 solubility with m_{NaCl} = 2 M

(b) H_2S solubility with m_{NaCl} = 0 M

(d) H_2S solubility with m_{NaCl} = 2 M

Figure 4.11.: Solubility of CO_2 and H_2S in brine for H_2O-NaCl-CO_2-H_2S mixtures with different NaCl molalities [mol/kg] at T = 393.15 K. Ratios indicate mole fraction ratios of CO_2 to H_2S in the feed. Data from [162].

4.4. Multiphase equilibrium at *PH* and *PS*

In many cases, enthalpy or entropy is a better choice than temperature for use as a nonlinear unknown in reservoir simulation [163]. This requires thermodynamic equilibrium to be performed at isenthalpic or isentropic conditions. While a *PT*-flash can be performed as an unconstrained minimization, the constraints of specified state variables cannot all be eliminated explicitly in the case of an isenthalpic or isentropic state specification [44, 45].

4.4.1. A nested approach for *P*-based specifications

As discussed in Section 4.1, it is possible to optimize the Q-function using second-order methods. Agarwal *et al.* [46] suggested nesting a *PT*-flash calculation with a maximization with respect to T. For the *PH*-flash, $Q^H = Q^H(T)$ becomes a function that can be optimized for temperature:

$$\max\left((G_{min} - H^{spec})/T\right) \tag{4.14}$$

where G_{min} is the minimum Gibbs energy at current $(P, T, \mathbf{n})$. The maximum of Q can then be obtained by locating the zero gradient $g(T) = \left(\frac{\partial Q}{\partial T}\right)$ using a root-finding method.

Root-finding methods for solving the state specification equation

The outer loop of the nested algorithm consists of solving the temperature for which the state specification equation is satisfied. By definition, the enthalpy or entropy increases monotonically with temperature. In case of a phase transition, $H(T)$ or $S(T)$ may exhibit a sharp nonlinearity that is difficult to capture in the *PT*-domain. However, consistent bracketing of the lower and upper temperature bounds for the solution, combined with a robust *PT* flash in the inner loop, guarantees the location zero of (4.11c) or (4.12c), even in the limiting case of a discontinuity at a singular transition temperature T^* in the objective function [163]. These conditions occur when an n_c-component mixture encounters an $(n_c + 1)$-phase state. Gibbs' phase rule dictates that at such a phase boundary, only one degree of freedom remains, and either temperature or pressure becomes a dependent variable. A *PT*-flash may find either of two states α and b with equal Gibbs free energies [50]:

$$G^{\alpha}(P, T^*, \mathbf{z}) = G^{b}(P, T^*, \mathbf{z}). \tag{4.47}$$

Along an isobar (or isotherm), the total enthalpy or entropy of the system exhibits a discontinuity due to the transition from state α to state b. The temperature (or pressure) of the system is invariant and can only change when the energy variable has sufficiently increased or decreased. The phase state that does satisfy the specified state X^{spec} is described by a linear combination of two *PT*-flashes at values X^{α} and X^{b} with weights β and $(1 - \beta)$:

$$X^{spec} = \beta X^{\alpha} + (1 - \beta) X^{b}, \tag{4.48a}$$

where

$$\beta = \frac{X^{spec} - X^b}{X^a - X^b}. \tag{4.48b}$$

In this work, we follow the procedure for nested isenthalpic flashes by Xu *et al.* [47], using a hybrid approach of derivative-free and Newton methods. Under difficult conditions, both the inner loop of *PT*-flashes, as well as the outer loop of temperature updates, may take many iterations to converge and therefore a gradient-based update of temperature can improve performance. To do this, they combined Brent's method [132] and, if the curvature of the objective function allows, a Newton step can be safely performed to improve convergence. The convergence criterion for a Newton step is given by

$$g(T) \cdot g''(T) > 0, \tag{4.49}$$

where the second derivative of the objective function $g''(T)$ is approximated using numerical derivatives.

Evaluation of $g'(T)$ of the specific Q-function with respect to temperature requires the derivatives of the *PT*-flash procedure:

$$\left(\frac{\partial H}{\partial T}\right)_{P,\mathbf{z}} = \left(\frac{\partial}{\partial T}\sum_j H_j\right)_{P,\mathbf{z}} = \sum_j \left(\left(\frac{\partial H_j}{\partial T}\right)_{P,\mathbf{n}_j} + \sum_i \left(\frac{\partial H_j}{\partial n_{ij}}\right)_{P,T,n_k} \frac{\partial n_{ij}}{\partial T}\right) \tag{4.50a}$$

$$\left(\frac{\partial S}{\partial T}\right)_{P,\mathbf{z}} = \left(\frac{\partial}{\partial T}\sum_j S_j\right)_{P,\mathbf{z}} = \sum_j \left(\left(\frac{\partial S_j}{\partial T}\right)_{P,\mathbf{n}_j} + \sum_i \left(\frac{\partial S_j}{\partial n_{ij}}\right)_{P,T,n_k} \frac{\partial n_{ij}}{\partial T}\right) \tag{4.50b}$$

In addition, Xu *et al.* [47] suggested an extrapolation method to estimate compositions for *PT*-flash initialization after a temperature update, using the partial derivatives of the previous *PT*-flash with respect to temperature:

$$\mathbf{n}_{est} \approx \mathbf{n} + \frac{\partial \mathbf{n}}{\partial T} s_{try}. \tag{4.51}$$

The value of s_{try} should be determined iteratively.

Robust and efficient *PH*- and *PS*-flash algorithms for use in simulation

It was discussed in the previous section that smooth convergence of simulations relies on a robust flash algorithm. Most importantly, states with near-zero compositions are often encountered in near-well cells, states that require careful numerical implementation. In the inner loop of *PT*-flashes, we can use the techniques discussed earlier. In addition, the specification equation for *PH*- and *PS*-specifications can be tricky for near-zero compositions. Temperature is a secondary variable in these specifications, but it must be determined to high accuracy to ensure smoothness of the properties for simulation. This is especially crucial at transition temperatures or near phase boundaries. Near-zero compositions, however, introduce additional degrees of freedom to the system. As

a result, transition temperatures are extended to occur over a small temperature interval in which the flash has to distinguish between two almost identical phases. To improve robustness and performance for all conditions, DARTS-flash employs a few techniques:

- Run flash with compositions that are above a certain threshold (e.g., $z_i > 10^{-2}$) to determine an initial guess of temperature for the full composition. Brent's root-finding method is generally able to quickly bracket the final temperature within a few iterations. In addition, phase compositions from the reduced composition evaluation can be utilized to initialize the new PT-iteration.
- Switch to locate the phase boundary when temperature bounds have converged to within a certain tolerance (e.g., $T_{max} - T_{min} < 10^{-1}$) to prevent excessive bracketing. This can be done by solving (4.47). In case of a transition temperature (i.e., two different $(n_c + 1)$-phase states are found on both sides), the solution corresponds to the condition of equal Gibbs energies and can be quickly located by a root-finding algorithm. In case of a disappearing phase, locating the phase boundary temperature improves the root-finding procedure by ensuring a smooth function within the temperature bounds. The temperature of the phase boundary can be located by applying Brent's method with an inner loop of negative flashes.

4.4.2. Partial derivatives of phase equilibrium at *PH* and *PS*

Away from transition temperatures

The partial derivatives of the primary quantities of isenthalpic and isentropic phase equilibrium calculations with respect to primary variables ψ, as well as any secondary properties, can be calculated by applying the chain rule to the PT-results ω:

$$\left(\frac{\partial M}{\partial \psi_k}\right)_{\psi_j \neq \psi_k} = \left(\frac{\partial M}{\partial \omega_k}\right)_{\omega_j \neq \omega_k} + \left(\frac{\partial M}{\partial T}\right)_{P,T,\mathbf{z}} \left(\frac{\partial T}{\partial \psi_k}\right)_{\psi_j \neq \psi_k} \tag{4.52}$$

For this, one needs to calculate the derivative of temperature T with respect to the primary variable of the PH- or PS-flash ψ: $\left(\frac{\partial T}{\partial \psi_k}\right)_{\psi_j \neq \psi_k}$. For any function $F(x, y, z) = 0$, the following relationship between the partial derivatives holds:

$$\left(\frac{\partial z}{\partial x}\right)_y \left(\frac{\partial x}{\partial y}\right)_z \left(\frac{\partial y}{\partial z}\right)_x = -1 \tag{4.53}$$

Consequently, one can formulate the function $F(P, T, X, \mathbf{z}) = 0$ with $X = \{H, S\}$ and use the relationship in (4.53) to obtain the partial derivatives required for the chain rule (4.52). For instance:

$$\left(\frac{\partial T}{\partial P}\right)_{H,\mathbf{z}} = -\left(\frac{\partial H}{\partial P}\right)_{T,\mathbf{z}} \Big/ \left(\frac{\partial H}{\partial T}\right)_{P,\mathbf{z}} \tag{4.54}$$

At transition temperatures

At a transition temperature, the phase split is described by (4.48a). As described by Sun *et al.* [50], one needs to find the partial derivatives of the weighted flash results M (4.48a) with respect to the primary flash variables ψ to obtain the derivatives of the isenthalpic or isentropic flash at transition temperatures:

$$\left(\frac{\partial M}{\partial \psi_k}\right)_{\psi_j \neq \psi_k} = \beta\left(\frac{\partial M^a}{\partial \psi_k}\right)_{\psi_j \neq \psi_k} + (1-\beta)\left(\frac{\partial M^b}{\partial \psi_k}\right)_{\psi_j \neq \psi_k} + (M^a - M^b)\left(\frac{\partial \beta}{\partial \psi_k}\right)_{\psi_j \neq \psi_k} \tag{4.55}$$

In the partial derivatives of flashes at a and b, the derivative of temperature with respect to the primary variables in (4.52) is replaced by the partial derivative of the transition temperature. This partial derivative is obtained by evaluating the sensitivity of the equilibrium conditions (4.47):

$$\left(\frac{\partial T}{\partial \omega_k}\right)_{\omega_j \neq \omega_k} = -\left[\frac{\partial G^a - G^b}{\partial \omega_k}\right]_{\omega_j \neq \omega_k} \Big/ \left[\frac{\partial G^a - G^b}{\partial T}\right]_{P,\mathbf{z}} \tag{4.56}$$

In addition, the partial derivatives of the weight β with respect to the primary variables ψ are required:

$$\left(\frac{\partial \beta}{\partial \psi_k}\right)_{\psi_j \neq \psi_k} = -\frac{1}{X^a - X^b}\left[\beta\left(\frac{\partial X^a}{\partial \psi_k}\right)_{\psi_j \neq \psi_k} + (1-\beta)\left(\frac{\partial X^b}{\partial \psi_k}\right)_{\psi_j \neq \psi_k}\right] \tag{4.57}$$

The partial derivatives of X^a and X^b are also obtained by applying the chain rule:

$$\left(\frac{\partial X^a}{\partial \psi_k}\right)_{\psi_j \neq \psi_k} = \left(\frac{\partial X^a}{\partial \psi_k}\right)_{\omega_j \neq \psi_k} + \left(\frac{\partial X^a}{\partial T}\right)_{P,\mathbf{z}} \left(\frac{\partial T}{\partial \psi_k}\right)_{\psi_j \neq \psi_k} \tag{4.58}$$

4.4.3. Extension of hybrid-EoS approach to *P*-based specifications

The hybrid EoS approach is an interesting candidate for nested *PH*- and *PS*-flashes of mixtures with brine. Firstly, the thermodynamic models considered in this work are evaluated at P, T and composition at low computational cost during *PT*-flash calls, while they maintain their accuracy for phase equilibrium calculations. In addition, we demonstrate that the use of the models considered in our approach is consistent and accurate for the evaluation of thermal properties, thus validating the extension of the hybrid-EoS approach to any *P*-based state specification.

Accuracy and consistency of the hybrid-EoS approach for *P*-based equilibrium calculations

To apply the hybrid-EoS framework to *PH*- and *PS*-specifications, it is important to assess the accuracy and consistency of thermal properties evaluated from the

thermodynamic models. Enthalpy and entropy should monotonically increase with temperature. Equivalently, heat capacity must be positive at all conditions [55]:

$$\left(\frac{\partial H_j}{\partial T}\right)_{P,\mathbf{n}} = C_{Pj} > 0 \tag{4.59}$$

Standalone thermal properties from the fugacity-activity model have been shown in Figure 3.5 in Section 3.2. Enthalpies of CO_2 dissolution into the aqueous phase were reported by Koschel *et al.* [121], shown here for a temperature of 323.15 K in Figure 4.12b. The y-axis has been inverted; a negative enthalpy of mixing for CO_2 dissolution indicates the exothermic nature of the process. The enthalpy of mixing reaches a plateau at the solubility limit of CO_2 into H_2O at the specific pressure, and any additional CO_2 does not dissolve into the aqueous phase. Total enthalpies of mixing across the entire composition range have been measured by Chen *et al.* [164], Figure 4.12c. The distinct linear shapes of these curves, compared to smooth enthalpies of mixing for gas mixtures, result from the two-phase behaviour.

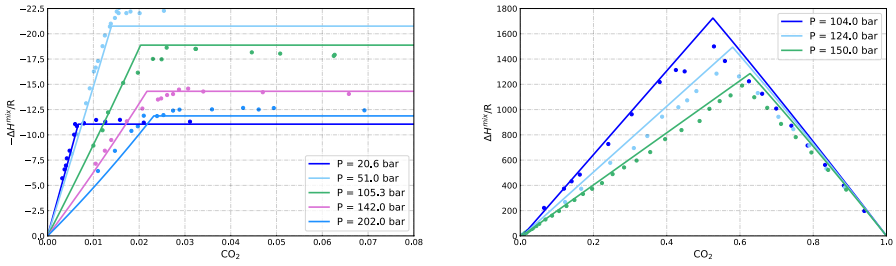

(a) Enthalpy of dissolution at T = 323.15 K

(b) Enthalpy of mixing at T = 523.15 K

Figure 4.12.: Enthalpies of dissolution and mixing for CO_2-H_2O systems. Data from (a) Koschel *et al.* [121] and (b) Chen *et al.* [164].

4.4.4. Results of *PH*- and *PS*-flash calculations

We extend the application of the hybrid-EoS framework to *PH*- and *PS*-flashes. It is not straightforward to validate isenthalpic and isentropic phase equilibria with experimental data, and, as a result, not many experimental benchmarks are available. We compare the results of two-phase envelopes in *PH*- and *PS*-domains for pure H_2O with those obtained from the IAPWS-95 reference EoS for water and steam [165]. In addition, we reproduce the numerical benchmark of the H_2O-nC_5 (pentane) mixture [46, 166] and investigate its behaviour throughout the compositional domain. Finally, we explore the nature of isenthalpic phase equilibria to a ternary mixture of H_2O-CO_2-CH_4, which is pivotal for modern

H_2O phase envelopes

Figure 4.13 shows the two-phase envelopes where liquid water and steam coexist in the *PH*- and *PS*-space, as modelled with the IAPWS-95 reference EoS for pure water and steam [165]. At enthalpies below and above the two-phase region, the system is in a single-phase liquid water and steam state, respectively. Using a consistent equation of state such as IAPWS-95, the saturation curves coincide at the critical point, which for H_2O is around 220 bar and 647 K. As stated before, the use of different thermodynamic models for aqueous and vapour phases introduces an inconsistency towards the critical point, and that is evident towards higher pressures and temperatures.

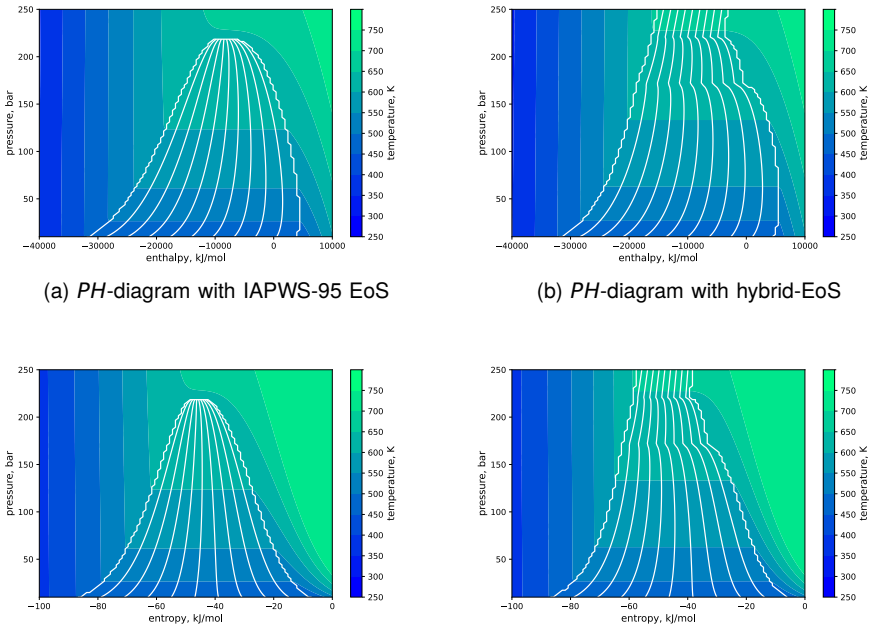

(a) *PH*-diagram with IAPWS-95 EoS

(b) *PH*-diagram with hybrid-EoS

(c) *PS*-diagram with IAPWS-95 EoS

(d) *PS*-diagram with hybrid-EoS

Figure 4.13.: Comparison of pure H_2O *PH*- and *PS*-diagrams from hybrid-EoS approach with IAPWS-95 EoS [165].

H_2O-nC_5 mixture

Agarwal *et al.* [46] and Zhu and Okuno [166] investigated isenthalpic flashes of an equimolar mixture of water and pentane along an isobar of 10 bar. The results for this binary mixture using the proposed approach are shown in Figure 4.14. From the temperature-composition diagram (Figure 4.14a), it is evident that the isobars cross different phase states for different compositions. The nC_5-rich mixture starts

from $Aq-L$ conditions, then crosses a small $V-L$ region and then enters the single-phase vapour state. The other compositions cross a region of $Aq-V$, rather than $V-L$. In all cases depicted here, the three-phase boundary of $Aq-V-L$ states is crossed. By definition, such a three-phase transition for a binary system occurs at a single transition temperature T^*.

The phase transitions also appear in the total enthalpies along the isobars (Figure 4.14b). Within regions, enthalpies increase smoothly, but at any phase transition, the slopes are discontinuous. At the transition temperature of 387 K, total enthalpy jumps from $Aq-L$ to $V-L/Aq-V$ states, as prescribed by (4.47).

Figure 4.14c shows the phase equilibria for the H_2O-nC_5 mixture under the same conditions, but now in the enthalpy-composition domain. The isobars represent the same temperature ranges, but because reference enthalpies for each component are different, such a diagram is skewed and less straightforward to analyze. Still, the same phase regions can be observed while moving along the enthalpy axis. Contrary to the temperature-composition diagram, however, the three-phase boundary now appears as a region of constant temperature that must be crossed for temperature to change again.

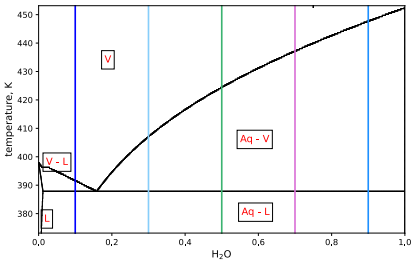

(a) Temperature-composition diagram

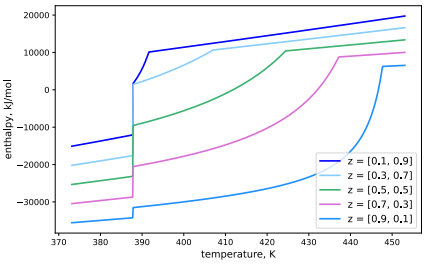

(b) Total enthalpy along isobar for a range of compositions

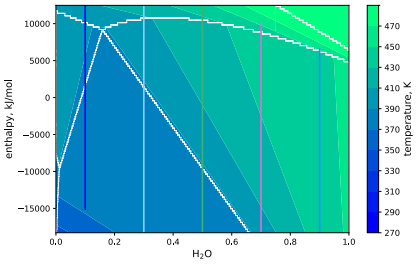

(c) Enthalpy-composition diagram

Figure 4.14.: Isothermal and isenthalpic flashes for H_2O-nC_5 mixture at 10 bar.

H_2O-CH_4-CO_2 mixture

A simple representation of CO_2 sequestration in depleted gas fields involves a ternary mixture of H_2O-CH_4-CO_2. In such CO_2 injection operations, high-purity CO_2 is injected into a depleted gas reservoir, often at relatively low pressure conditions with large saturations of CH_4 gas.

Figure 4.15a-c present ternary diagrams of this mixture at a pressure of 70 bar and three different temperatures (280-290-300 K), close to the critical point of pure CO_2. Under these conditions, which are not unlikely in CO_2 injection processes into depleted gas reservoirs, a three-phase region of $Aq - V - L_{CO_2}$ exists. It is under these circumstances that simulation models which employ a *PT*-formulation will struggle to converge.

This is, again, illustrated by the shape of the total enthalpies along isobars. Figure 4.15d is a quasi-binary temperature-composition diagram with mole fractions of H_2O-CH_4 at a constant ratio – along the blue dotted lines in Figures 4.15a-c. This can be thought of as being the original composition of the depleted gas reservoir, into which pure CO_2 is injected. The temperature-composition diagram clearly shows the presence of the three-phase envelope that degenerates at the critical point for pure CO_2. Notice that the blue dotted line crosses the three-phase region at very different feed compositions throughout the increase from 280 to 300 K, which indicates how sensitive this system is to changes in thermodynamic state.

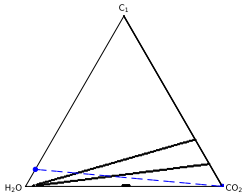

(a) T = 280 K

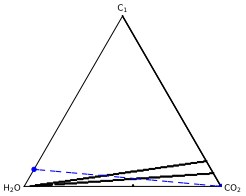

(b) T = 290 K

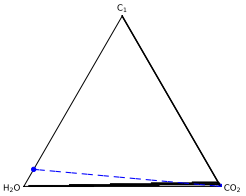

(c) T = 300 K

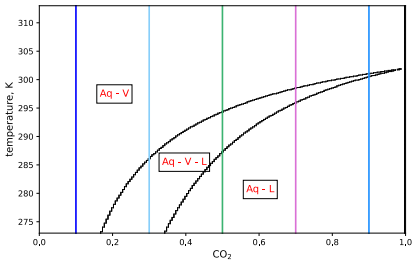

(d) Temperature-composition diagram

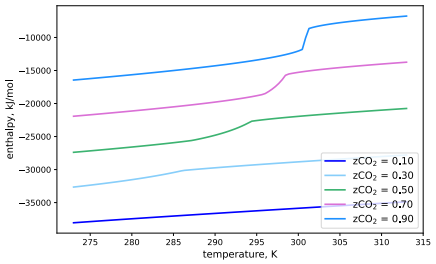

(e) Total enthalpy along isobar for a range of compositions

Figure 4.15.: Isothermal flashes for H_2O-CH_4-CO_2 mixture at 70 bar.

The phase transitions also appear in the total enthalpies along the isobars (Figure 4.15e). The curves are shown for different compositions, corresponding to the lines in Figure 4.15d. In this ternary mixture, we do not observe phase transitions where an $(n_c + 1)$-state would occur, and thus no transition temperatures exist as such. Yet, the curves show an increasingly nonlinear trend when approaching pure CO_2 conditions, which will reduce to the $V - L$ transition at pure CO_2. These nonlinearities are problematic for PT-based simulation models.

Hydrate systems

Figure 4.16a shows the temperature-composition diagram of a binary system containing H_2O and CO_2 at a pressure of 100 bar. Under these conditions and with sufficient CO_2 in the system, a hydrate phase is stable for temperatures up to 284 K. The total enthalpy along isobars (Figure 4.16b) clearly exhibits the transition temperature at the hydrate equilibrium temperature, where the three phases coexist. Note that the jump is largest near the small region of single-phase hydrate state around $x_{H_2O} = 0.86$. This is where the largest ratio of gas and brine is converted to form hydrates.

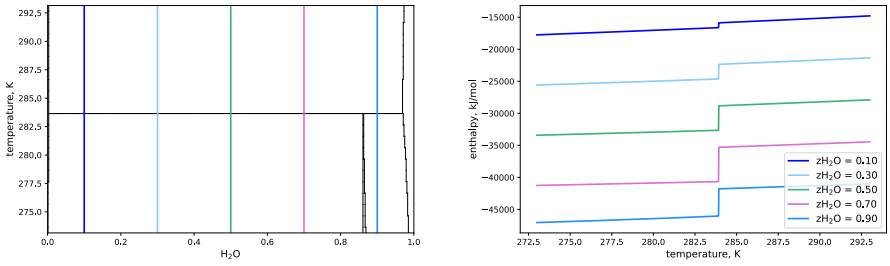

(a) Temperature-composition diagram

(b) Total enthalpy along isobars

Figure 4.16.: Isothermal flashes for a binary mixture of H_2O-CO_2 at P = 100 bar.

5

Reservoir simulation

Reservoir simulators are an essential tool in any reservoir engineering project. With only limited information available about the subsurface, reservoir simulation aims to describe the flow of mass and energy throughout a geological model over time. Over a discrete mesh in space, we approximate the conservation of mass and energy. These differential equations account for how much matter and energy is flowing in and out of a volume and how much is accumulating inside over time. Generally, no analytical solution exists for these equations. Compositional models commonly solve the conservation equations in a fully implicit manner for reasons of numerical stability. This approach relies on variables from the future state that is being solved and therefore requires an iterative solution.

In this chapter, the thermal-compositional framework is outlined. In DARTS [33], we utilize the Operator-Based Linearization technique, an approximation of the continuous physical parameter space that allows straightforward implementation of complex physical modelling. Consistent implementation of the OBL framework will be discussed, including extrapolation at the edge of the compositional domain, a generic state specification and approximate equilibrated initialization procedures.

5.1. Compositional simulation

5.1.1. Governing equations

For a domain with volume Ω, bounded by surface Γ, the mass and energy conservation can be expressed in a uniformly integral way, as

$$\frac{\partial}{\partial t}\int_{\Omega} M^c d\Omega + \int_{\Gamma} \mathbf{F}^c \cdot \mathbf{n} d\Gamma = \int_{\Omega} Q^c d\Omega \tag{5.1}$$

Here, M^c denotes the accumulation term for the c^{th} component ($c = 1, \ldots, n_c$, indexing for the mass components and $c = n_c + 1$ for the energy quantity); $\mathbf{F}_c$ refers to the flux term of the c^{th} component; $\mathbf{n}$ refers to the unit normal pointing outward to the domain boundary; Q_c denotes the source/sink term of the c^{th} component.

In this formulation, fluid flow is governed by advective and diffusive fluxes and the source term contains source/sink terms for wells and kinetic reactions. The energy accumulation term contains both the fluids and rock, and the flux term for energy accounts for the energy fluxes that result from advective and diffusive mass fluxes as well as conduction.

The mass accumulation term collects each component distribution over n_p fluid phases in a summation form,

$$M^c = \phi \sum_{j=1}^{n_p} x_{cj} \rho_j s_j, \quad c = 1, \ldots, n_c \tag{5.2}$$

where ϕ is porosity, s_j is phase saturation, ρ_j is phase density $[\mathrm{kmol/m^3}]$ and x_{cj} is molar fraction of c component in j phase.

The energy accumulation term contains the internal energy of fluid and rock,

$$M^{n_c+1} = \phi \sum_{j=1}^{n_p} \rho_j s_j U_j + (1-\phi) U_r \tag{5.3}$$

where U indicates specific fluid internal energy [kJ/kmol], U_r indicates the rock internal energy [kJ/m^3]. The rock is assumed compressible and represented by the change of porosity through:

$$\phi = \phi_0 \big(1 + c_r (p - p_{\mathrm{ref}})\big) \tag{5.4}$$

where ϕ_0 is the initial porosity, c_r is the rock compressibility [1/bar] and p_{ref} is the reference pressure [bar].

The mass flux of each component is represented by the summation over n_p fluid phases,

$$\mathbf{F}^c = \sum_{j=1}^{n_p} \big(x_{cj} \rho_j \mathbf{u_j} + s_j \mathbf{J}_{cj} \big), \quad c = 1, \ldots, n_c \tag{5.5}$$

Here the velocity $\mathbf{u_j}$ follows the extension of Darcy's law to multiphase flow, including gravitational and capillary effects,

$$\mathbf{u_j} = -\mathbf{K} \frac{k_{rj}}{\mu_j} (\nabla p_j - \gamma_\mathbf{j} \nabla z) \tag{5.6}$$

where $\mathbf{K}$ is the permeability tensor $[\mathrm{mD}]$, k_{rj} is the relative permeability of phase j, μ_j is the viscosity of phase j $[\mathrm{mPa \cdot s}]$, p_j is the pressure of phase j [bar], $\gamma = \rho^T \mathbf{g}$ is the specific weight $[\mathrm{N/m^3}]$ and z is the depth vector [m]. Due to capillary forces, a pressure difference arises between wetting and non-wetting phases j and k as a function of (non-wetting phase) saturation. If hysteresis effects are not present, the capillary pressure curve often is a function of the form:

$$p_{c,jk}(S_k) = p_k - p_j \tag{5.7}$$

The $\mathbf{J}_{cj}$ is the diffusion flux of component c in phase j, which is described by Fick's law as

$$\mathbf{J}_{cj} = -\phi \mathbf{D}_{cj} \nabla(\rho_j x_{cj}) \tag{5.8}$$

where $\mathbf{D}_{cj}$ is the diffusion coefficient [m^2/day].

The energy flux includes the thermal fluxes associated with advection and diffusion, and conduction terms

$$\mathbf{F}^{n_c+1} = \sum_{j=1}^{n_p} \left(H_j \rho_j \mathbf{u_j} + \phi \kappa_j s_j \nabla T \right) + (1-\phi)\kappa_r \nabla T \tag{5.9}$$

where H_j is phase enthalpy [kJ/kmol] and κ_j is thermal conductivity for phase j [kJ/m.day.K].

Note that the energy accumulation term consists of the total internal energy in a control volume and the energy fluxes has enthalpy contributions. From Chapter 2, the first law of thermodynamics states that a change in internal energy in a closed system equals the heat absorbed by the system and the work done on the system:

$$dU = dQ + dW = TdS - PdV + \sum_i \mu_i dn_i \tag{2.14}$$

The enthalpy equals the internal energy minus the PV-work contribution:

$$H = U - V\left(\frac{\partial U}{\partial V}\right)_{S,\mathbf{n}} = U + PV \tag{2.30}$$

The advective energy fluxes therefore only account for the flow of heat and do not include PV-work.

Combining all terms, the mass and energy conservation equations can be written in residual form as

$$\frac{\partial}{\partial t}\left(\phi \sum_{j=1}^{n_p} \rho_j s_j x_{cj}\right) + \nabla \cdot \left(\sum_{j=1}^{n_p} x_{cj} \rho_j \mathbf{u}_j + s_j \rho_j \mathbf{J}_{cj} \right) + \sum_{j=1}^{n_p} x_{cj} \rho_{mj} q_j + \sum_{k=1}^{n_k} \nu_{ck} r_k = 0 \quad c = 1, \ldots, n_c \tag{5.10}$$

and

$$\frac{\partial}{\partial t}\left(\phi \sum_{j=1}^{n_p} \rho_j s_j U_j + (1-\phi) U_r\right) + \nabla \cdot \left(\sum_{j=1}^{n_p} H_j \rho_j \mathbf{u}_j - \kappa \nabla T \right) + \sum_{j=1}^{n_p} h_j \rho_j \hat{q}_j = 0 \tag{5.11}$$

The nonlinear equations (5.10)-(5.11) are discretized using finite volume discretization with a two-point flux approximation and upstream weighting in space and a backward Euler approximation in time [29]. For each reservoir block i:

$$R_i^c = V_i\left(M_i^c(\omega_i) - M_i^c(\omega_i^n)\right) - \Delta t\left(\sum_l A_l F_l^c(\omega) + V_i Q_i^c(\omega)\right) = 0, \quad c = 1, \ldots, n_c+1 \tag{5.12}$$

Fluid thermodynamic and transport properties

At each timestep and for each grid cell, a consistent evaluation of thermodynamic equilibrium and phase properties is required. The thermodynamic modelling procedure is used as input to evaluate the fluid properties in the different terms of the conservation equations. Phase densities, viscosities and enthalpies are calculated based on the phase compositions. Some of these properties are available directly from the equations of state.

In multiphase systems, consistent phase identification is important to assign flow properties (relative permeabilities, capillary pressure curves, etc.) and keep track of the different possible phases during simulation. In the hybrid-EoS approach, the identification of the aqueous phase is straightforward. For the non-aqueous phases, however, one needs to distinguish vapour(-like) and potentially multiple liquid(-like) phases. In our approach, we can take advantage of the characteristics of the cubic polynomial to determine the phase type at a given composition [91].

For phases that are calculated with an equation of state that has an expression for $P = (V, T, \mathbf{n})$, densities can be obtained directly from the EoS. It was described in Section 2.2 how thermodynamic properties are calculated from the residual Helmholtz free energy $A^r(V, T, \mathbf{n})$ [56, 68, 69]. For cubic EoS (Section 3.1), the expression for $A^r(V, T, \mathbf{n})$ can be derived from the pressure equation. For other phases, enthalpies can be calculated from their respective thermodynamic models (Section 2.2.2). In some cases, density can also be obtained from the thermodynamic model. Alternatively, correlations can be employed.

By conserving phase enthalpies and internal energies consistently, the simulation implicitly accounts for energy and temperature changes related to mixing and dissolution, phase transitions, and isenthalpic compression and expansion (also referred to as Joule-Thomson effect). Figure 5.1a shows the enthalpy of pure CO_2 in the PT-domain. The phase boundary (white line) separates liquid and vapour states of the CO_2. Beyond the critical point, there is no noticeable transition between liquid-like and vapour-like states. The three curves describe isenthalpic pressure drops, conditions where no heat is exchanged with surrounding cells. Such a

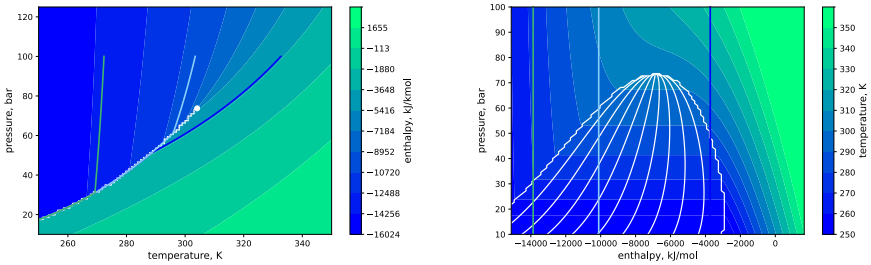

(a) PT-diagram (b) PH-diagram

Figure 5.1.: Isenthalpic expansion of pure CO_2 in PT- and PH-diagrams.

pressure drop is accompanied by a significant decrease in temperature. This is the result of a combined effect of expansion cooling in single-phase conditions and a phase transition when the phase boundary is reached. Notice how the initial conditions of the three curves correspond to very different initial temperatures, but drop to the same values upon encountering the phase boundary. Furthermore, observe that across the phase transition, a small change in temperature causes a large change in enthalpy. A pressure-enthalpy diagram (Figure 5.1b) can capture the discontinuity across the two-phase region. As discussed in Section 4.4, the isotherms in the *PH*-diagrams are nearly horizontal (exactly horizontal for any $(n_c + 1)$-phase state). While these conditions are generally slightly smoothed in multicomponent systems, near-pure phases are common in well modelling and injection processes. Such phase transitions can exhibit sharp nonlinearities in the parameter space. Such *narrow-boiling conditions* introduce difficulties in the *PT*-domain and an energy-based formulation is preferred [51, 158].

5.1.2. Operator-based linearization

The Operator-Based Linearization (OBL) approach significantly simplifies the solution of a discretized nonlinear system of equations (5.10)-(5.11) by introducing algebraic operators that capture all complex physics and nonlinear terms. Instead of keeping track of each property and its derivatives with respect to nonlinear unknowns, abstract algebraic operators representing the physics can be constructed and assembled into the set of Jacobian and residuals defined at each iteration [28, 167]. In the described approximation method, pressure, temperature and overall composition are taken as the state variables in a given control volume. Upstream weighting of the physical state is used to determine the flux-related fluid properties determined at the interface l. The discretized mass conservation equation in operator form for each grid block reads

$$V\phi_0[\alpha_c(\omega)-\alpha_c(\omega_n)]-\Delta t\sum_{l\in L(i)}\sum_{j=1}^{n_p}\left[\Gamma^l\beta^l_{cj}(\omega^u)\Delta\psi^l_j+\Gamma^l_d\gamma^l_j(\omega)\Delta\chi_{cj}\right] + \Delta tV\delta_c(\omega)=0, \quad c=1,\ldots,n_c \tag{5.13}$$

Here we define the following state-dependent operators:

$$\alpha_{cf}(\omega) = \Big(1+c_r(p-p_{ref})\Big)\sum_{j=1}^{n_p}x_{cj}\rho_j s_j,\ c=1,\ldots,n_c \tag{5.14a}$$

$$\beta_{cj}(\omega) = x_{cj}\rho_j k_{rj}/\mu_j,\ c=1,\ldots,n_c,\ j=1,\ldots,n_p \tag{5.14b}$$

$$\gamma_j(\omega) = \Big(1+c_r(p-p_{ref})\Big)s_j,\ j=1,\ldots,n_p \tag{5.14c}$$

$$\chi_{cj}(\omega) = D_{cj}\rho_j x_{cj},\ c=1,\ldots,n_c,\ j=1,\ldots,n_p \tag{5.14d}$$

$$\delta_c(\omega) = \sum_{j=1}^{n_p}v_{cj}r_j(\omega),\ c=1,\ldots,n_c \tag{5.14e}$$

The phase-potential-upwinding (PPU) strategy for OBL parametrization is applied to model the gravity and capillary effect [30, 167]. The potential difference of phase j on the interface l between block 1 and 2 can be written as:

$$\Delta\psi_j^l = p_1 - p_j^c(\omega_1) - (p_2 - p_j^c(\omega_2)) - \frac{\rho_j(\omega_1) + \rho_j(\omega_2)}{2} g(z_2 - z_1) \tag{5.15}$$

where p_j^c is the capillary pressure.

The discretized energy conservation equation in operator form can be written as:

$$\begin{aligned} V\phi_0[\alpha_{ef}(\omega) - \alpha_{ef}(\omega_n)] - \Delta t \sum_{l\in L(i)} \sum_{j=1}^{n_p} [\Gamma^l \beta_{ej}^l(\omega^u)\Delta\psi_j^l + \Gamma_d^l \gamma_j(\omega)\Delta\chi_{ej}] + \Delta t V \delta_e(\omega) \\ + (1-\phi_0)[V[\alpha_{er}(\omega) - \alpha_{er}(\omega_n)] - \Delta t \sum_l \Gamma_d^l \kappa_r \alpha_{er}(\omega)\Delta\chi_{er}] = 0 \end{aligned} \tag{5.16}$$

where:

$$\alpha_{ef}(\omega) = \Big(1 + c_r(p - p_{ref})\Big) \sum_{j=1}^{n_p} \rho_j s_j U_j \tag{5.17a}$$

$$\beta_{ej}(\omega) = h_j \rho_j k_{rj}/\mu_j,\ j = 1, \ldots, n_p \tag{5.17b}$$

$$\chi_{ej}(\omega) = \kappa_j T_j,\ j = 1, \ldots, n_p \tag{5.17c}$$

$$\delta_e(\omega) = \sum_{j=1}^{n_j} \nu_{ej} r_{ej}(\omega) \tag{5.17d}$$

In this form, most nonlinear parts of the system are defined only in terms of physical state-dependent functions. The values of these functions are uniquely determined in the parameter space of the simulation problem with the set of primary unknowns.

Importantly, operator values are calculated only in supporting points comprising the discretized parameter space and stored in $(n_c + 1)$-dimensional tables. Operator values for a specific state are obtained by multi-linear interpolation of tabulated values of the operator. Partial derivatives, required for the assembly of the Jacobian matrix, can be evaluated directly as interpolation coefficients. However, to delineate the nonlinear behavior in the system, especially strong nonlinearity, it is necessary to select a reasonable OBL resolution to characterize the physical space. Too coarse OBL resolution may lead to large errors in the solutions [28].

Rather than calculating at the pre-processing stage, Khait and Voskov [30] modified the original approach to adaptively evaluate the approximation interpolants at each required point in the discrete parameter space. In addition, caching of previously generated operator tables potentially improves simulation performance greatly, especially for simulations involving complex physics.

Operator-based well controls

In reservoir operations, the only control one has over the dynamics of the reservoir is by injecting or removing fluids through wells. In general, the options to control the conditions at the wellbore are limited to *BHP*- (bottom-hole pressure) and *rate*-controlled, where an injection well also has the freedom to control the temperature and composition of the injected fluid. A production well has no control over the temperature and composition of the produced fluid.

At the connection between the wellhead and the wellbore, the mass balance is specified to converge to the exact conditions that constitute the prescribed well control. The composition of the injected or produced fluids is specified and taken from the upstream well block, respectively, while the thermodynamic state must comply with pressure or rate controls. For a pressure-controlled well, a control equation is defined at the ghost well block:

$$P - P^{spec} = 0. \tag{5.18}$$

For a rate-controlled well, another control is defined:

$$\Gamma^{l} \zeta_j^{wctrl}(\omega) \Delta P - Q^{spec} = 0. \tag{5.19}$$

Injection temperature:

$$T - T^{spec} = 0 \tag{5.20}$$

Analogous to the governing equations in reservoir blocks, the specification equations for well controls can be formulated in operator form. Introducing operators ζ^{wctrl} for BHP-, and phase mass-, volume- and molar-rate controlled specifications:

$$\zeta^{bhp} = P \tag{5.21a}$$

$$\zeta_j^{mass} = \frac{\rho_j(\omega) k_{r,j}(\omega)}{\mu_j(\omega)} \tag{5.21b}$$

$$\zeta_j^{volume} = \frac{k_{r,j}(\omega)}{\mu_j(\omega)} \tag{5.21c}$$

$$\zeta_j^{molar} = \frac{\rho_j^m(\omega) k_{r,j}(\omega)}{\mu_j(\omega)} \tag{5.21d}$$

In addition, an operator is required for temperature control:

$$\zeta^{bht} = T \tag{5.21e}$$

The pressure and temperature operators are trivial when they are in the state specification, but for other state specifications, this operator serves to translate injection pressure and temperature to the OBL parameter space. It may be possible to control the enthalpy of injected fluid at constant pressure. However, as enthalpy is an extensive parameter, this won't work for rate-controlled wells, and temperature is a more accessible (intensive) variable.

A similar set of operators is used to initialize the well head state.

A note on OBL parametrization for multicomponent systems

In multicomponent systems, a multilinear interpolation strategy for OBL may require evaluation of supporting points for which the composition of the last component is negative. This is the case for compositions that are located in an interpolation hypercube that is intersected by the edge of the compositional space where $z_{n_c} = 0$. For these compositions, one supporting point corresponds to a coordinate where the $n_c - 1$ independent mole fractions sum up to a value greater than unity. Such a state is non-physical, and therefore a different approach must be used to evaluate operator values at these supporting points. Figure 5.2 shows how the $(n_c - 1)$-dimensional compositional domain of the OBL discretization at the edge of the physical parameter space for (a) three- and (b) four-component simulations. In the hypercubes that are intersected by $z_{n_c} = 0$, some of the supporting points correspond to $z_{n_c} > 0$ (blue), some are located exactly on the edge (green) and a few lie outside of the physical space (red, orange, yellow).

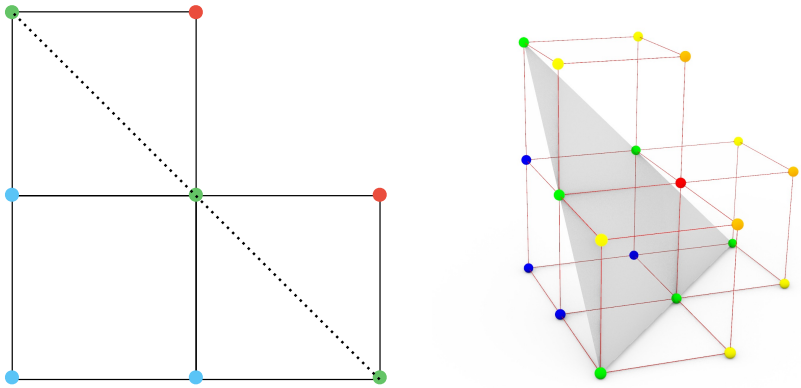

(a) Three-component space (b) Four-component space

Figure 5.2.: Hypercubes in multicomponent compositional space.

A solution to obtain consistent values for interpolation lies in the linear nature of the parameter space within each hypercube. Using this property, the OBL implementation for these hypercubes requires extrapolation of the operator values in the physical coordinates to calculate the corresponding operator values in the non-physical supporting point. Mathematically, this is described as a hyperplane that goes through the physical supporting points. In the $(n_c - 1)$-dimensional compositional subspace with the additional dimension of operator value, this corresponds to the set of points $\mathbf{y} = (x_1, \ldots, x_N)$ in $\mathbb{R}^N$ with $N = n_c$. The equation

for a hyperplane in $\mathbb{R}^N$ through point $\mathbf{p}$ with normal vector $\mathbf{n}$ is given by

$$\sum_n^N a_n(y_n - p_n) = 0 \tag{5.22}$$

or

$$\sum_n^N a_n y_n = -d \tag{5.23}$$

where $d = -\mathbf{n} \cdot \mathbf{p}$.

One can extrapolate the operator values at the physical points to the non-physical coordinate by determining the equation of the hyperplane. This can be done by finding the null vector $\mathbf{h}$ of matrix $\mathbf{P}$ that contains the coordinates of the N known coordinates $\mathbf{p}_N$ and operator values α_N:

$$\begin{pmatrix} z_{11} & \dots & z_{1,n_c-1} & \alpha_1 & 1 \\ \vdots & \ddots & & & \\ z_{N1} & \dots & z_{N,n_c-1} & \alpha_N & 1 \end{pmatrix} \tag{5.24}$$

After performing a Gaussian elimination of the matrix (5.24), the extrapolated operator value can be found by substituting the non-physical coordinate into the obtained equation of the hyperplane.

By definition of the linear nature of the hyperplane, interpolated values at the edge of the physical domain are linearly interpolated between the supporting points that correspond to $z_{n_c} = 0$. As a result, any interpolated states at a composition with $z_{n_c} = 0$ that should be zero by being located at the edge of the composition domain, are indeed zero.

For the three-component problem (Figure 5.2a), extrapolation always occurs in the three-dimensional subspace. In the four-component space (and up), however, more varieties of cases exist. In case all $n_c - 1$ compositions are nonzero, the extrapolation relies on a different set of supporting points in the red and orange states (Figure 5.2b). If the extrapolation concerns a state where one or more of the compositions are zero, one of the axes degenerates and an the problem reduces to $n_c - 1$ dimensional extrapolation (yellow).

5.1.3. Reservoir simulation at generic state specification

The primary variables in the compositional formulation described in the previous section are often straightforwardly chosen P, T and composition, which are simple with regard to thermodynamic equilibrium modelling. It was shown in Chapter 4 that a PT-flash is an inherently simpler problem than an isenthalpic or isentropic flash, which cannot be performed as an unconstrained minimization.

For many applications, however, alternative state specifications may be preferred. It is the case for solving the governing equations for reservoir simulation, where the conserved quantity is total energy, and the choice of temperature as a primary variable is inferior to using an enthalpy-based formulation. In certain regions of the

thermodynamic space, small changes in pressure, temperature and/or composition may result in large changes in thermodynamic behaviour. Most notably, under narrow-boiling conditions and in the vicinity of phase boundaries or mixture critical points, severe convergence problems may arise for *PT*-based formulations.

The governing equations can be solved using any thermodynamically consistent state specification. In an energy-based formulation, the discontinuities and nonlinearities encountered in the *PT*-domain are naturally captured. The main consequence of such formulation is that the complexities now have to be resolved in the flash calculations, which have to be performed at the given state specification. For instance, a *PH*-formulation needs an isenthalpic flash routine. Earlier developments in single-component geothermal reservoir simulation had already employed formulations based on different state specifications, including *PH* and *UV* [168–170]. The single-component formulation encounters some of the challenges posed to thermal-compositional simulation, but additional nonlinearities of a full compositional simulation require more careful heuristics and analysis.

Nonlinearities in thermal-compositional simulation

The fully implicit scheme that is employed in DARTS is unconditionally stable with regard to timestep selection. However, it requires an iterative approach to solving the nonlinear system of equations. Heuristics are available to improve convergence of Newton's method in fully implicit simulation by locally and/or globally damping large jumps in primary variables [10, 171, 172]. Nonlinearities associated with complex multiphase flow can introduce inflection points [173]. Compositional changes, gravitational effects, and countercurrent flow, resulting from capillarity, can severely increase complexity for the nonlinear solver [174, 175].

In thermal simulations, complex thermodynamics related to condensation and phase changes represent additional sources of nonlinearity. Negative compressibility effects have been reported in geothermal and steam flooding simulators [3, 4, 176]. This occurs when liquid flows into a gas-saturated grid block, triggering a temperature and pressure drop in the cell while vaporizing the liquid. In addition, narrow-boiling behaviour introduces large sensitivity of enthalpies with pressure, temperature and composition. By using enthalpy as a primary variable, however, this complexity is handled by the thermodynamic modelling procedure and does not hinder nonlinear convergence [177].

Operators for generic state specification

Pressure and temperature are involved in many physical terms in the governing equations, both directly (e.g., potential difference, capillary pressure, rock compressibility, rock energy and heat conduction terms) and by means of secondary properties calculated at the current P, T and composition. In addition, well controls are commonly specified in terms of pressure and temperature.

A small adjustment to the OBL approach prepares the simulation framework to be used at any state specification. Pressure and temperature are always primary or secondary variables of the phase equilibrium. For the generic state specification,

two additional operators are required to keep track of pressure and temperature. For the assembly of the linear system, pressure and temperature are evaluated from these interpolated operators, rather than taking the values from the solution vector directly.

5.2. Vertical equilibrium

A simulation can be initialized from a previous run or from an initial equilibrium state of the reservoir. For the latter case, an initialization procedure is required. Over geological time, a balance between gravity and chemical forces with thermal gradients may have been established along vertical and lateral directions in a reservoir, resulting in heterogeneous fluid distributions [178]. Composition variation can be the result of many factors, such as gravity segregation of lighter and heavier components, thermal diffusion (which generally has the opposite effect), thermally induced convection or background aquifer flow, solid precipitation, biogenic activity or regional variations.

A full thermodynamic equilibrium procedure could include the effects of gravitational field (sedimentation equilibrium), capillary forces and thermal gradients [55, 179–181]. Compositional grading algorithms have been proposed to solve (thermo)diffusive equilibrium for reservoir simulation of hydrocarbon fields [178, 182, 183]. Nonetheless, equilibrium may not have been reached as the time required for diffusive fluxes to equilibrate over large distances could require millions of years. Moreover, vertical and lateral distributions often exhibit seemingly uncorrelatable variations, and modelling of the complex equilibria is impossible due to a lack of physical and chemical understanding of the problem, unknown boundary conditions or a lack of physical and geological data to build appropriate models [178].

For simulation purposes, however, it is important that the initial state is sufficiently close to a stationary state. If it is not, the system will quickly equilibrate and redistribute its mass, and defining features such as a liquid-gas contact or the bottom of hydrate stability zone may change their position. A stationary state implies that the partial derivatives of (5.10)-(5.11) with respect to time are zero. Depending on the boundary conditions, this corresponds to a balanced in- and outflow of mass and heat in each cell in the discretized spatial domain. It is with some simplifying assumptions that we can find an initial state for which mass fluxes are near steady state. Note that the procedure holds only for simple two-phase systems; a more sophisticated setup is required for more advanced multicomponent systems with complex capillary transition zones. This topic covers decades of reservoir simulator development [2].

A simplified gravity-capillary-thermal equilibrium

Generally, gravity, capillary and thermal equilibrium have established relatively rapidly, but diffusive fluxes require much larger timescales to be in full chemical equilibrium. Ignoring diffusive fluxes and background in- and outflow, a gravity-capillary-thermal equilibrium with zero convective mass fluxes can be fully defined

for a system that contains $n_c = n_p$ components. In the end, the diffusive fluxes in depleted hydrocarbon fields have most likely not equilibrated fully, and this simplified procedure could suffice.

From the discretized mass conservation equations (5.13), the convective and diffusive fluxes at a stationary state would result in net zero mass fluxes. Ignoring the diffusive fluxes, the convective flux q of phase j through connection l is described by:

$$q_{j,l} = T_l \left(\frac{\rho_j k_{rj}}{\mu_j} \right)_l \Delta\psi_j^l \tag{5.25}$$

The condition of zero convective flux can be satisfied by at least one of the conditions:

$$T_l = 0, \quad k_{r,j}^l = 0, \quad \text{or} \quad \Delta\psi_j^l = 0 \tag{5.26}$$

In case of zero transmissibility, there is no flow for any of the phases and potential differences $\Delta\psi_j$ can exist even if relative permeabilities are nonzero. For nonzero transmissibilities, conditions must be so that phases are not flowing. In other words, either phase mobility or the potential difference, which obeys gravitational and capillary forces, must be zero:

$$\Delta\psi_j^l = p_1 - p_j^c(\omega_1) - (p_2 - p_j^c(\omega_2)) - \frac{\rho_j(\omega_1)\rho_j(\omega_2)}{2} g(z_2 - z_1) \tag{5.15}$$

It must be noted that the pressure gradient only depends on continuous phases, i.e., phases that are able to exert a hydrostatic gradient and are not residually trapped. Therefore, the specific gravity term in the potential difference only includes contributions from phases for which $S_j > S_{j,r}$. Note also that, in the presence of capillarity, a phase saturation below residual values is not favorable, and capillary backflow is strong. Convective heat fluxes also reduce to zero when convective mass fluxes are absent. In addition, energy is transported along with molecular diffusive fluxes. Furthermore, geothermal gradients arise from (steady state) conductive heat flux from below, but this is often simplified to a linear temperature gradient.

Cell-wise initialization

To solve the stationary state, one must know the thermodynamic conditions at a reference depth. At the reference depth, the thermodynamic state of $n_c + 1$ primary variables is described by providing an equal number of equations. Given initial values of primary variables (state specification, overall composition) and/or secondary variables (phase saturations, phase composition, etc.), the thermodynamic state ω at the reference depth can be determined. Specification equations must be provided to account for the number of primary variables. For a completely defined state, $n_c + 1$ linearly independent specifications must be defined:

$$\text{res} = \{X_i - X_i^{spec}, \ldots, Y_j - Y_j^{spec}, \ldots\}^T \tag{5.27}$$

where X_i denotes the i^{th} primary and Y_j the j^{th} secondary specification.

As implied by Gibbs' phase rule (2.54), pressure and temperature are independent variables if the number of phases does not exceed the number of components. One degree of freedom remains if the number of phases equals $n_c + 1$, and such conditions can only occur at the $(n_c + 1)$-phase boundary. Thus, for a state where $n_p \leq n_c$, both state specifications can be specified, while for $n_p = n_c + 1$, only one of pressure or temperature is independent. In fact, resolving such a state requires an isenthalpic flash. The set of equations is solved similarly to the conservation equations during simulation. Using the OBL technique, assembly of the Jacobian and residuals is done through interpolation of (5.27) in the same discrete parameter space.

From the reference depth, the entire vertical column can be solved in a cell-wise manner. There is one equation (5.25) for each phase, and the geothermal gradient provides an additional relation, adding up to $n_p + 1$ equations. This means that in a system for which $n_c > n_p$, the vertical equilibrium is not uniquely described if we do not consider a full thermodynamic modelling procedure. We can close the system of equations by providing additional primary or secondary specifications, such as saturations or phase compositions, which are not fully in equilibrium from a thermodynamic perspective, but it does allow for solving zero convective flux conditions.

Initialization of a hydrate-bearing system

In addition to the gravity-capillary-thermal equilibrium, correct initialization for the simulation of hydrate systems requires equilibrium of the hydrate phase with the fluid phases. Failure to initialize properly will drive the system to redistribute rapidly upon simulation, resulting in different equilibrium conditions elsewhere on the hydrate equilibrium curve. Given initial distributions of pressure, temperature and phase saturations, the initial conditions for (5.27) can be determined by solving a set of specification equations, with the addition of equality of fugacity between fluid and hydrate phases. As implied by the Gibbs phase rule, all three phases can only coexist at the three-phase boundary. Thus, either P or T is a dependent variable, whereas both are independent in brine-hydrate or vapour-hydrate conditions. For the three-phase conditions, this gives:

$$\begin{cases} X & = X^{spec} \\ S_1 & = S_1^{spec} \\ S_2 & = S_2^{spec} \\ f_{w,j} & = f_{w,H} \end{cases} \tag{5.28}$$

with X either P or T. Alternatively, for two-phase conditions:

$$\begin{cases} P & = P^{spec} \\ T & = T^{spec} \\ S_1 & = S_1^{spec} \\ f_{w,j} & = f_{w,H} \end{cases} \tag{5.29}$$

6

Simulation of CO_2 sequestration applications

Geological carbon sequestration (GCS) is considered one of the principal options for mitigating excessive emissions of greenhouse gases into the atmosphere and the associated negative impacts on climate change. Field pilots of CO_2 sequestration in sedimentary formations, such as saline aquifers or depleted oil and gas reservoirs, have been operating for a few decades [184, 185]. While saline aquifers globally offer the greatest potential for carbon sequestration in terms of capacity, targeting depleted gas reservoirs for CO_2 sequestration in particular has major advantages. Injected CO_2 can replace the volumes of hydrocarbons still in place, and, due to the compressibility of gas in particular, pressures required to maintain injection flow rates are lower than in aquifers [186]. The injection of supercritical CO_2 has been applied in enhanced oil and gas recovery processes (EOR/EGR) to displace the fluids in place in full or partial miscibility [186, 187]. To date, most CO_2-EOR projects have used CO_2 produced from natural sources and have been optimized for oil production rather than CO_2 sequestration volumes, which could unveil large additional storage potential [184]. In addition to the technical aspects of depleted hydrocarbon fields in comparison to aquifers, the ability to re-use a field's existing facilities and knowledge of its geological settings and containment integrity for gas storage gives a significant cost advantage [188].

The injection of CO_2 into depleted hydrocarbon reservoirs poses some challenges related to the thermodynamic properties of CO_2. Typically, the injected CO_2 is in a supercritical, liquid-like state. However, adiabatic expansion in the wellbore and into the lower-pressured reservoir can result in significant cooling. Temperatures can drop by more than 20 °C, which may result in sub-zero conditions [189]. In addition, the combined pressure and temperature decrease may be sufficient to enter the two-phase region, where the reduction in temperature is even more pronounced due to phase transitions [22, 190]. Such low temperatures could be sufficient to trigger ice and hydrate formation, limiting well injectivity, and thermal stresses could damage the near-wellbore region.

Furthermore, upon CO_2 injection into a formation, connate water will slowly evaporate into the CO_2-stream. Even though the solubility of H_2O into the CO_2-rich phase is relatively low, a continuous injection stream of dry CO_2 can lead to almost complete dry-out in the near-wellbore region. As a result, dissolved solids in the saline residual brine may start to precipitate [24, 25]. This effect is even more pronounced in heterogeneous rock due to capillary back-flow [191, 192].

This section explores the main characteristics of CO_2 sequestration in saline aquifers and depleted hydrocarbon fields with regard to thermodynamic interactions. The two recent studies of *FluidFlower* and *SPE11*, which will be covered in Section 6.1, have established important benchmarks for numerical modelling of CO_2 sequestration in saline aquifers. The topic of numerical simulation for CO_2 sequestration in depleted hydrocarbon fields, on the other hand, has been less widely resolved to date. More advanced physical modelling capabilities are required to handle such problems. A set of simple test cases for depleted fields is presented in Section 6.2.

6.1. CO_2 sequestration in saline aquifers

Permanent subsurface storage of CO_2 relies on a range of trapping mechanisms, which involve different physical aspects related to the characteristics of reservoirs and fluids: structural trapping, residual trapping of immobile free gas CO_2 due to capillary forces, dissolution trapping in brine and mineral trapping.

Several analytical models and semi-analytical approaches were developed to quantify some of these effects [193–195]. Riaz and Tchelepi [196] presented an analysis based on perturbation theory, which predicts the convective instability of dissolved CO_2 and enhanced dissolution rates for a small-scale homogeneous domain. This model was further improved and validated against experimental results by Neufeld *et al.* [197]. Another attempt to connect simulation with experiments has been performed by Farajzadeh *et al.* [198]. Subsequently, the analytical model was enhanced to account for capillary transition effects [199], realistic density [200], and viscosity variations [201]. Moreover, the influence of a simplified layer cake heterogeneity was addressed by Ghorbani *et al.* [202].

These models attempt to address the important geological and residual trapping mechanisms linked to CO_2 sequestration at relatively short time scales after injection (tens to hundreds of years) but have been hampered to date by the lack of geologically realistic input models that capture key heterogeneities of interest across length-scales. Furthermore, it is infeasible that any combined analytical model will be capable of representing all phenomena together for a range of realistic parameters relevant to industrial CO_2 sequestration projects with realistic geological heterogeneity. Numerical modeling is essential for such representation. At longer time scales (hundreds to thousands of years), however, numerical models, too, only approximately represent the dissolution trapping that dominates in the reservoir. This is a concern given the discrepancies between different modern simulation approaches, as reported in the benchmark study by Nordbotten *et al.* [203]. This benchmark study also illustrates the high sensitivity of the existing

models to the physical assumptions, even under conditions of simplified geological properties.

Recently, attempts to assess the predictive capabilities of simulation models have been made. The *FluidFlower* benchmark [204, 205] was carried out as a blind study for numerical simulation groups to model CO_2 sequestration based on physical experiments. Although conducted at atmospheric conditions, the performance, accuracy and numerical convergence of simulators could be tested against a physical ground truth. The SPE11 Comparative Solution Project [206, 207] was initiated as a subsequent simulation study in which reservoir conditions were considered. This study presents a benchmark that is by now well established for numerical investigation of CO_2 storage problems in aquifers.

6.1.1. Description of the physics in saline aquifers

Trapping mechanisms for storage of CO_2

Permanent subsurface storage of CO_2 relies on a range of trapping mechanisms, which involve different physical aspects related to the characteristics of reservoirs and fluids. Structural trapping, analogous to the trapping of oil and gas, occurs when buoyant CO_2 is held in place by geological structures, overlain by a low-permeability layer [185, 208]. In addition, the low-permeability rock can create a capillary barrier to further invasion of the non-wetting CO_2. Residual trapping occurs when the CO_2 plume migrates due to buoyancy. In this process, CO_2 at the tail of the plume is immobilized due to capillary forces at the pore scale as the wetting phase is imbibed back into the pores [209, 210].

In the shorter time scale, structural and residual trapping mechanisms are expected to dominate, while dissolution and mineral trapping occur over longer time scales [211]. During solubility trapping, CO_2 dissolves into the aquifer water. This molecular diffusion process occurs slowly and is enhanced by the convective mixing of brine and CO_2 [197]. Convective mixing starts at the interface between CO_2 and water. Density-driven currents are induced as CO_2 dissolves into the brine. This, in turn, increases the dissolution rate. In the slow process of mineral trapping, CO_2 reacts with other chemical species to form solids [19, 212, 213].

Density-driven enhanced dissolution

At the interface between a CO_2 gas cap and aquifer, CO_2 slowly diffuses into the undersaturated brine. As CO_2 dissolves into the brine, density-driven flow is induced. With the growing contact area of density-driven currents, the process of dissolution trapping accelerates. The onset of convective mixing, however, can occur over thousands of years [212, 214, 215]. To accurately capture this process, numerical convergence of CO_2 storage simulations should be obtained with grid resolutions in the range of analytic wavelengths and approached onset times [214, 216]. Figure 6.1 shows the results of density-driven enhanced dissolution from a stationary gas cap of pure CO_2 into pure water.

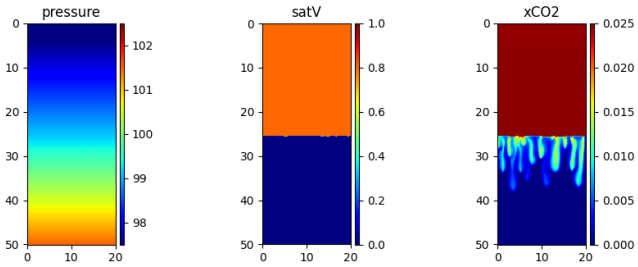

Figure 6.1.: Density-driven enhanced dissolution of CO_2 into aquifer.

Salinity and impurities

The formation water in geological reservoirs generally contains minerals, electrolytes and small quantities of thermogenic methane that have dissolved into the brine over geological time. Brine composition and salinity have a significant impact on CO_2 dissolution, which cannot be ignored in predictions of the reservoir dynamics in GCS operations. Figure 6.2 shows how the presence of salt reduces the capacity to dissolve CO_2 and, as a result, delays the onset and relative magnitude of enhanced dissolution.

In addition, CO_2 is often co-injected with small fractions of other gases, such as methane and hydrogen sulfide [217, 218]. The injection of such impurities can have significant implications for phase behaviour and fluid properties that control CO_2-plume dynamics and storage capacity [219].

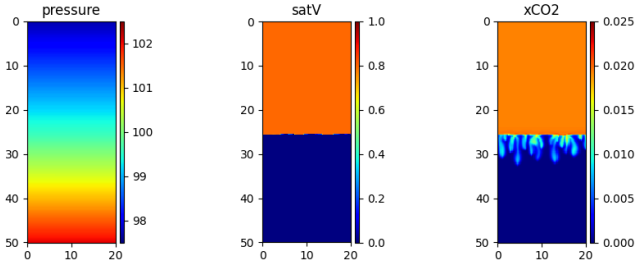

Figure 6.2.: Enhanced dissolution with NaCl brine salinity of 2 mol/kg H_2O.

Formation dry-out

Drying out of saline formations upon dry gas injection, accompanied by precipitation of salt dissolved in brines, is another important phenomenon in CO_2 sequestration applications [24, 25]. Ott *et al.* [191, 192] have addressed this issue in a series of experimental and numerical studies. Following their experiments, we illustrate the mechanism of salt precipitation from residual brine, which is vaporized by the

dry CO_2 injection stream. The approach taken in Figure 6.3 has been simplified to exclude the effect of counter-current capillary backflow, which could allow accumulation of solid salt beyond the brine's original local salt content and lead to severe reductions in pore volume available for fluids. All parameters in the simulation follow the experimental setup from Ott *et al.* [191].

The importance of accurate treatment of salinity in the activity model for the aqueous phase should be emphasized, as this affects the solubility of H_2O in the CO_2-rich phase. This ultimately controls evaporation and thus the propagation of the trailing shock.

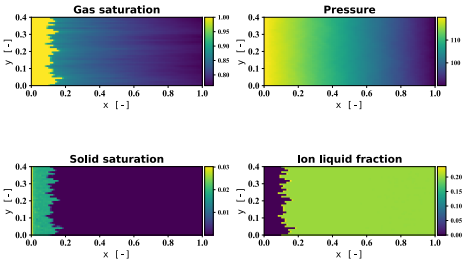

Figure 6.3.: Simulation of formation dryout and NaCl precipitation in sandstone core.

6.1.2. FluidFlower benchmark

The FluidFlower study [205] considers the injection of CO_2 into brine-saturated formations at atmospheric conditions. The dominating trapping mechanisms under these conditions rely to a large extent on capillary effects and properties related to a mutual dissolution of CO_2 and water: solubility, density differences, and diffusion. The accuracy of the modeling of these physical phenomena and the corresponding computational grid determines to what extent the dynamics of the FluidFlower can be captured in simulation.

One of the aims of the benchmark study was to assess the predictive capabilities of the reservoir simulation community. The workflow we put up for making such predictions was threefold. From the tracer test data provided by the experimental group [204], we performed a history-matching procedure in order to populate the different sand facies with permeabilities and anisotropy [221]. Then, a most representative model run, with best estimates of physical properties and (relatively) fine resolution, had to be defined and reported through a series of spatial distributions and other metrics over the course of the simulation, and finally, an estimate of the uncertainty around the reported metrics had to be given.

Parts of this chapter have been published in Transport in Porous Media **151** (2024) [220].

The high nonlinearity and unconventional conditions for reservoir simulation, however, introduced challenges for linear and nonlinear solvers. Most notably, the failure of the CPR preconditioner for the benchmark conditions, related to a large contrast between densities and viscosities, and permeable layers in the benchmark, is a main factor significantly increasing the computational cost of benchmark simulation. We have discussed issues related to solvers and numerical convergence, discretization and uncertainty quantification in detail [220].

Physical properties at atmospheric conditions

We considered a binary system with H_2O and CO_2 that distributes between a vapor and an aqueous phase using the hybrid-EoS approach (Section 4.3.2), in which the effect of salinity is neglected. We have validated the properties of the separate fluid phases at atmospheric conditions against experimental data [220]. A remark on the use of the OBL technique under these conditions; with the low solubility of CO_2 in water, it is crucial to apply an OBL resolution that is sufficiently fine to capture the solubility limit of CO_2 in brine [32].

For capillary pressure curves, data on entry pressures at residual water saturation were provided for the different sand facies. The model response is extremely sensitive to capillary pressure curves, as the injected gas rapidly migrates upwards due to large density differences, leading to low gas saturation reaching the capillary barrier. The coarse resolution of the grid is then unable to impose the capillary trapping mechanism, leading to a CO_2 plume that is crossing the capillary barriers. In our initial submission, we applied a constant capillary pressure function, equal to the reported values of entry pressure [204], and we keep the same strategy in this study.

Lastly, diffusion is an important driver behind gravitational instabilities at the interface between CO_2-saturated brine and pure brine, followed by the development of density-driven fingering. Consequently, diffusion coefficients are a determining factor for finger onset time and wavelength [214]. However, data on binary diffusion coefficients for CO_2 and water in the aqueous phase under atmospheric conditions is not well studied. We included the uncertainties around reported binary diffusion coefficients into the uncertainty quantification.

Computational grid

The FluidFlower rig comprises a heterogeneous sand pack assembled within a thin, slightly curved filled Hele-Shaw cell of 2.8m wide by 1.3m high. Figure 6.4 presents a digitized version of the geometry, constructed from high-resolution images [204]. The setup contained variations in thickness from the intended constant 25mm, as reported by the experimental group. The boundaries of the rig are closed on the bottom, left, and right sides, and the top is open and in contact with the atmosphere, with a free water table at a fixed level.

Two ports for CO_2 injection, referred to as *I1* and *I2*, are installed in the reservoir. The location of the injection ports, as well as that of two pressure sensors and three boxes, which are related to the comparison metrics related to CO_2 distribution

used in the benchmark study, are marked in Figure 6.4. The rig has been filled with six different sand types, from finest to coarsest, labeled as ESF, C, D, E, F, and G, subdivided into four regions with specific Corey-related parameters (Table 6.1). During the experimental runs, CO_2 was injected from the first injection port for 5:00 hours at a constant rate of 10 mL/min; injection from the second well starts after a 2:15 hours delay and runs for 2:45 hours, at the same volumetric rate.

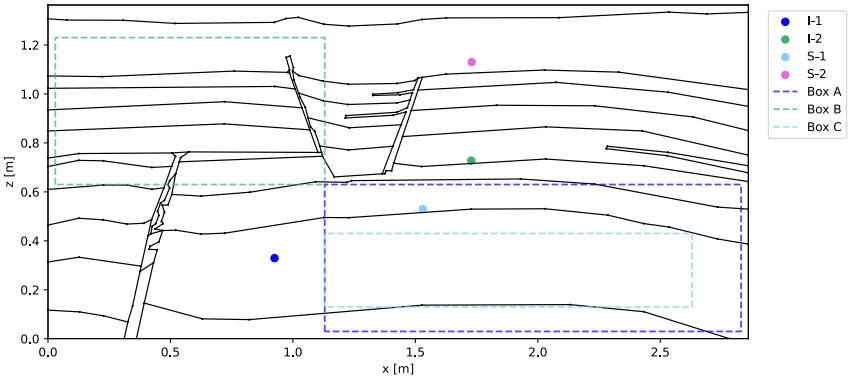

Figure 6.4.: Digitized FluidFlower geometry from high-resolution images [204]. *I* refers to injection ports, *S* refers to pressure sensors, and the boxes are used in the reporting of various comparison metrics.

Table 6.1.: Petrophysical properties for different sand types

Type	ESF	C	D	E	F	G
ϕ [-]	0.43	0.44	0.44	0.45	0.45	0.44
k [D]	44	473	1110	2005	4259	9580
n_w [-]	2.0	2.0	2.0		2.0	
n_g [-]	1.5	1.5	1.5		1.5	
s_{wc} [-]	0.11	0.12	0.14		0.32	
s_{gc} [-]	0.06	0.08	0.10		0.14	
k_{rwe} [-]	0.80	0.93	0.93		0.71	
k_{rge} [-]	0.85	0.95	0.95		0.75	
p_e [mbar]	15	3	1		-	
k_z/k_x [-]	0.75	0.8	0.9		1	

From the digitized geometry, we generated unstructured grids of different resolutions, with refinement around the well locations. A thickness correction was applied to the mesh according to a spline interpolation of the provided thickness map in the benchmark description. The constant pressure boundary condition at the top was mimicked by placing a production well connected to the top cells at atmospheric pressure. In addition, we accounted for the anisotropy in some layers (ESF, C, and D) for which internal layering, due to the manual filling of the rig, is observable in the images. The properties of the separate layer types are estimated through a history matching and uncertainty quantification procedure [220, 221].

Effects of discretization

While Cartesian grids are often used in enhanced dissolution studies with certain convergence in the numerical results achieved [216], it is still unclear how the structured nature of the grid affects the numerical results of enhanced dissolution problems. On one side, the Two-Point Flux Approximation (TPFA) applied on a structured grid is fully consistent and K-orthogonal. However, a structured grid introduces a strong orientation grid effect, which may in turn affect the numerical results. More importantly, Cartesian grids are not suitable for capturing the complex geometry of the FluidFlower rig. For a non-K-orthogonal unstructured grid, a multi-point flux approximation (MPFA) is a fully consistent choice. However, MPFA is usually more expensive to solve and can significantly add to the already prohibitive time of the simulation. In addition, the simulation conditions of the benchmark posed some further challenges to the use of MPFA, which has been discussed [220]. Finally, it was found that performing simulations under the atmospheric benchmark conditions required one to adjust the linear solver and time-stepping strategies [220].

We compared Cartesian and unstructured grids using the conventional TPFA at different resolutions. We use grids with characteristic mesh size and a number of grid cells shown in Table 6.2, such that the number of degrees of freedom at the two resolutions is comparable. Finer resolution demonstrates a prohibitive run time, and we decided not to include it in this study. It must be noted that, for all unstructured models, we keep a locally refined mesh near injection ports with a characteristic mesh size of 0.003 m. The Cartesian grids cannot provide this refinement.

Table 6.2.: Grids and resolutions for comparison

Resolution	Grid type	Mesh, m	# DOF
Coarse	Cartesian	0.019×0.018	11,250
Fine	Cartesian	0.0095×0.0091	45,000
Coarse	Unstructured	0.03	11,250
Fine	Unstructured	0.015	47,731

The results of simulation after 1 and 5 days on the Cartesian and unstructured grids for coarse and fine resolutions are shown in Figure 6.5. It can be observed that on the unstructured grids, the coarse resolution is not able to capture the distribution from the fine grid, the CO_2 plume extending less far into the domain. Remarkably, the final distribution of CO_2 for the fine resolution resembles more closely the outcomes of the experimental runs, although we assumed a constant thickness for this setup as opposed to our efforts in the main benchmark, where a variable thickness has been applied. On Cartesian grids, the distribution of CO_2 deviates significantly from the results obtained on unstructured grids and from reported experimental outcomes. Coarse and fine resolutions show similar spatial distributions, and a much finer resolution is required to converge to accurate results.

Another source of differences between unstructured and Cartesian grids is the pattern of gravity-driven fingers. On the unstructured meshes, the onset time of convective mixing and the wavelength of the fingers show less sensitivity to the resolution. On the other hand, there exists a notable difference in the fingering patterns between coarse and fine resolutions for the Cartesian grids, which is most evident in wavelength. In Figure 6.6, the temporal evolution of the total quantities of CO_2 in different forms (free gas and dissolved in brine) in Boxes A and B are shown. The amounts of CO_2 accumulating in both boxes is often higher in the structured models. Furthermore, the inflow and outflow of CO_2, either through flow or dissolution of free gas into the brine, exhibits a smooth pattern in unstructured grids, while it is much less smooth in structured ones. This resembles the grid-dependent numerical effect reported by some groups that used a Cartesian grid in the benchmark study when the water-gas contact coincides with cell faces and bursts the dissolution [205].

The significant differences in spatial and temporal quantities in the results arise from several factors. They include grid type, mesh resolution, and thickness of the rig for the benchmark problem. That explains a significant divergence of reported values between different groups in the main simulation benchmark [205]. Notice that these results do not even consider uncertainties in the physical modeling.

A study on the resolution and comparison of unstructured and Cartesian gridding reveals a high sensitivity of the overall distribution of CO_2 throughout the domain to gridding choices. Based on these modeling decisions alone, large differences occur in the main benchmark's reporting metrics, especially for Box B. Overall, the physical phenomena associated with the main trapping mechanisms for CO_2 sequestration can be captured relatively well. However, the wavelength of gravity-driven instabilities shows deviations between Cartesian grids of different resolutions. Furthermore, the shape of the fingers illustrates the grid orientation effect of the Cartesian grid, at least at early times. Concluding, it can be seen that the grid resolution plays quite an important role in FluidFlower modeling, and a finer grid is needed for a fully numerically converged solution. This conclusion is also supported by an analytic evaluation of the first unstable wavelength mode at the benchmark parameters.

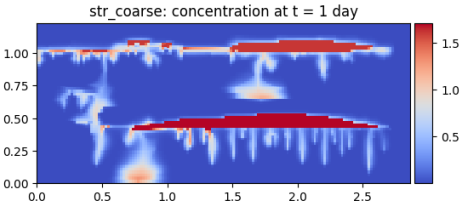

(a) Cartesian coarse at t = 1 day

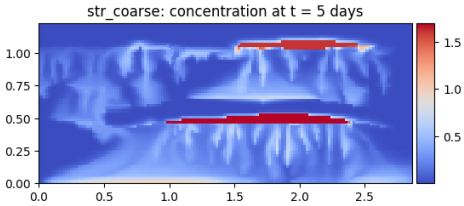

(e) Cartesian coarse at t = 5 days

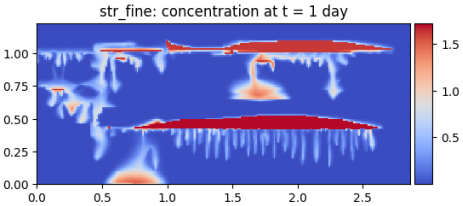

(b) Cartesian fine at t = 1 day

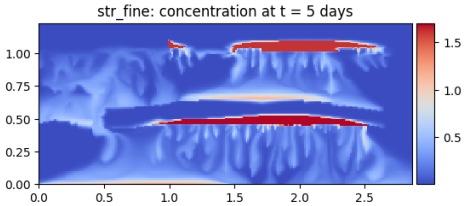

(f) Cartesian fine at t = 5 days

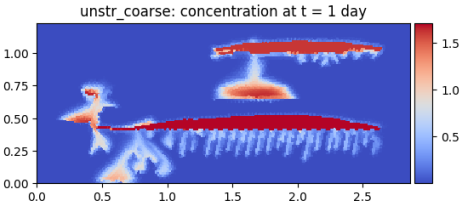

(c) Unstructured coarse at t = 1 day

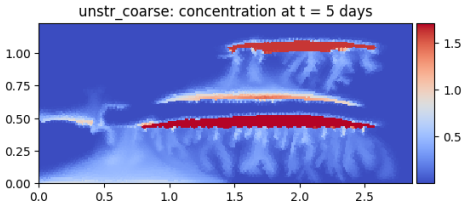

(g) Unstructured coarse at t = 5 days

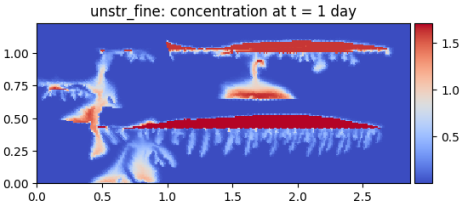

(d) Unstructured fine at t = 1 day

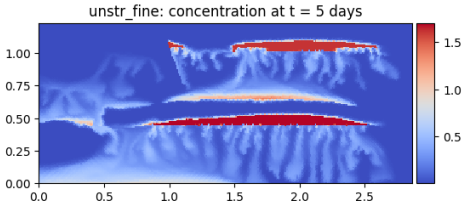

(h) Unstructured fine at t = 5 days

Figure 6.5.: Spatial distribution of CO_2 concentration in brine [kg/m^3] on Cartesian and unstructured grids for coarse and fine resolutions, at t = 1 day and t = 5 days.

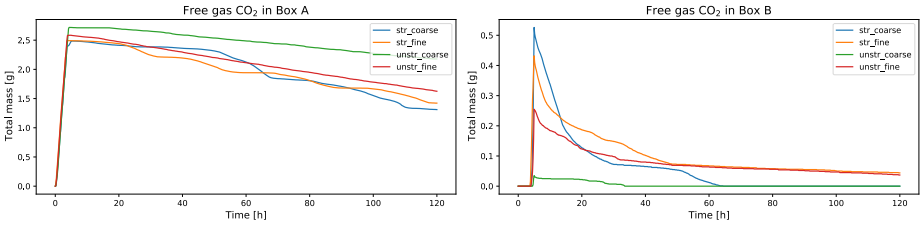

(a) Free gas CO_2 in Box A (b) Free gas CO_2 in Box B

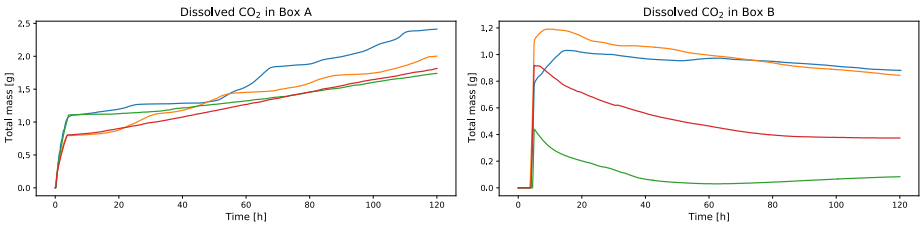

(c) CO_2 dissolved in brine in Box A (d) CO_2 dissolved in brine in Box B

Figure 6.6.: Evolution of total mass [g] of free gas CO_2 and CO_2 dissolved in brine in Box A (left) and Box B (right) for Cartesian and unstructured grids for coarse and fine resolutions over time.

6.1.3. SPE11 benchmark

The SPE11 Comparative Solution Project [206, 207] followed up on the FluidFlower benchmark. This study consisted of three modelling scenarios that resembled the FluidFlower geometry. SPE11a assumed atmospheric conditions, while SPE11b and -c comprised subsurface conditions and a realistic reservoir-scaled grid. Furthermore, SPE11c extended into three dimensions, with an anticlinal structure. In addition, while FluidFlower was assumed to be isothermal, thermal effects were taken into account in SPE11 to consider realistic field-scale GCS operations. We will discuss the results of our benchmark submission for SPE11b. Hadjisotiriou *et al.* [222] went into more detail with a convergence study and assessed the impact of impurities (C_1, H_2S) that are often present in the CO_2 injection stream.

Table 6.3 lists the seven different facies that are defined in the 11b reservoir models. Facies 1 represents the storage complex and serves as a capillary barrier to migrating CO_2. Facies 2 through 5 consist of permeable reservoir sands, while Facies 6 corresponds to fault infill. Finally, Facies 7 forms an impermeable barrier. The spatial distribution of facies for the 11b model is shown in Figure 6.7. The vertical permeability of each of the facies is one-tenth of its horizontal permeability. For all simulations, a structured mesh is constructed and populated according to the facies descriptions.

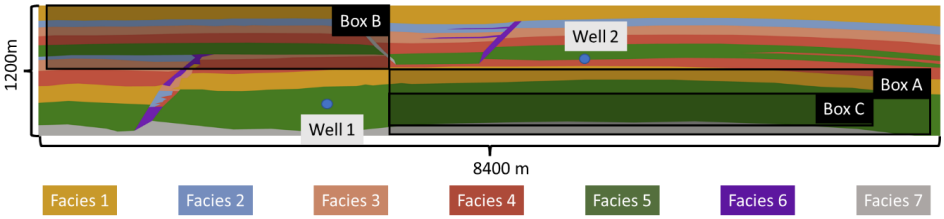

Figure 6.7.: SPE11b geometry with reporting boxes and well locations [206].

Table 6.3.: Facies properties of 11b.

Facies no.	Permeability k_x, mD	Porosity ϕ	$s_{w,\mathrm{imm}}$	κ_s, $\mathrm{W\,m^{-1}\,K^{-1}}$
1	0.101	0.10	0.32	1.90
2	101	0.20	0.14	1.25
3	202	0.20	0.12	1.25
4	507	0.20	0.12	1.25
5	1013	0.20	0.12	0.92
6	2027	0.25	0.12	0.26
7	0	0	0.10	2.00

SPE11b

Temperatures are fixed at the top and bottom boundaries, while all boundaries are impermeable and the boundary volumes are increased to $5 \times 10^4 \Delta z$. No CO_2 is present in the system before injection. A geothermal gradient of $25\,^{\circ}\mathrm{C\,km^{-1}}$ is applied along with a temperature of $70\,^{\circ}\mathrm{C}$ maintained at the bottom boundary. The initial reservoir pressure is hydrostatic and measured from datum. Injection starts in well 1 at t = 0 and continues for 50 years. Well 2 starts injection after 25 years, lasting for 25 years. The injection rate is equal to 3024 kg/day at a temperature of $10\,^{\circ}\mathrm{C}$. In the post-injection period, the simulation continues until 1000 years. We used a 600K-cell grid for simulation of the SPE11b scenario.

The spatial distributions of temperature and gas saturation after 300 years are shown in Figure 6.8. Interestingly, the colder injected CO_2 initially moves downward due to its higher density compared to the surrounding reservoir water. However, as the CO_2 equilibrates with the reservoir temperature, it migrates upwards due to buoyancy. Subsequently, the majority of CO_2 accumulates beneath the capillary barrier and begins lateral migration, while a portion migrates via the adjacent fault to the upper sand units. As the CO_2 plume migrates upwards to Box B, residual trapping takes place. Figure 6.9 shows that in Box A, CO_2 diffuses into the capillary barrier and enhanced dissolution into the aquifer below initiates (Section 6.1.1).

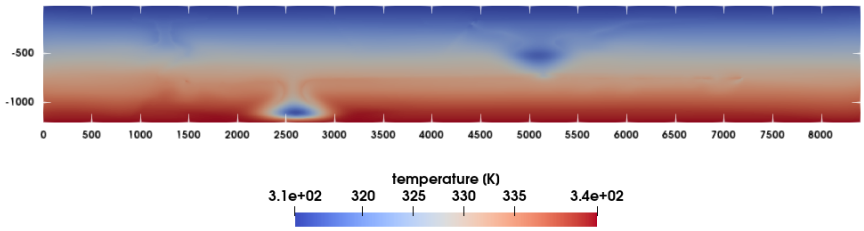

(a) Temperature

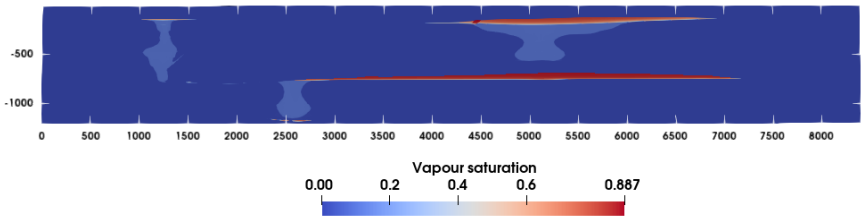

(b) Gas saturation

Figure 6.8.: Temperature and gas saturation after 300 years.

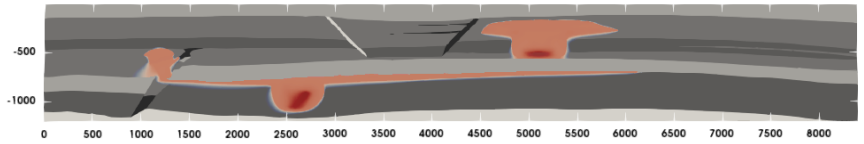

(a) 50 years

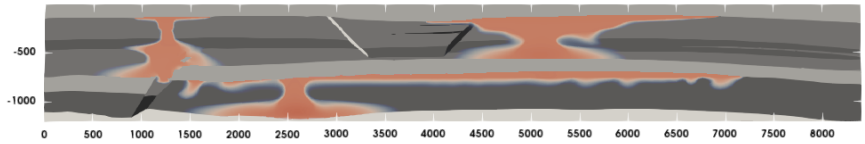

(b) 300 years

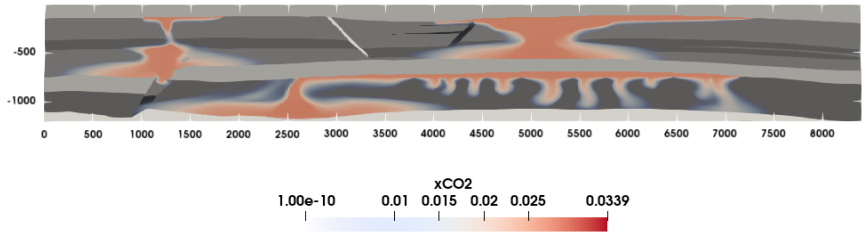

(c) 600 years

Figure 6.9.: CO_2 fraction in aqueous phase post-injection.

6.2. CO_2 sequestration in depleted hydrocarbon fields

Depleted oil and gas reservoirs are often regarded as the primary candidates for large-scale CO_2-storage. They offer several benefits over saline aquifers, allowing the re-use of infrastructure, facilities and existing knowledge of geological conditions and sealing capacity. In addition, the fluids in place are compressible and, therefore, lower injection pressures are needed to maintain reasonable flow rates.

The complexity of thermal-compositional effects upon injection of CO_2 into a depleted hydrocarbon field, however, is much larger compared to aquifers. Depleted fields are often at conditions close to the critical point of CO_2 or at lower pressures, where densities and enthalpies of the injected CO_2-rich phase can change rapidly. At the onset of injection, rapid expansion of injected CO_2 into the well and reservoir causes severe cooling near the wellhead [189]. As such, the temperature of the injected fluid into the reservoir may be much lower than desired, leading to the risk of hydrate formation and freezing in the wellbore and near-wellbore region. A good understanding of these dynamics is therefore vital for planning and operating a field for CO_2 injection.

6.2.1. Description of the physics in depleted fields

Adiabatic expansion

Often referred to as the Joule-Thomson effect, an adiabatic expansion refers to a pressure drop in which no heat is exchanged with the surroundings (i.e., at constant enthalpy). This expansion and pressure decrease are typically accompanied by a significant temperature change. It can occur upon the injection and expansion of CO_2 into the lower-pressure surroundings of a well. The temperature change accompanied by the pressure drop is often quantified in terms of the Joule-Thomson coefficient

$$\frac{\Delta T}{\Delta P} \approx \left(\frac{\partial T}{\partial P}\right)_H = \mu_{JT} \tag{6.1}$$

For most common gases at conditions of interest, μ_{JT} is positive, and consequently, the temperature decreases with a pressure drop. The Joule-Thomson coefficient is not used directly in the governing equations, but it indicates the significance of an adiabatic pressure drop on temperature. The single-phase Joule-Thomson coefficient is calculable from partial derivatives of the reduced residual Helmholtz energy [56, 69]. It can be calculated for multiphase states as well, using the partial derivatives of the flash calculation [147].

Figure 6.10 shows the results of the four-cell simulation setup proposed by Oldenburg [22] for pure CO_2 and various mixtures of CO_2-C_1. In this simulation, a pressure drop occurs across a low-permeability block in between two large volumes such that gas flows from left to right, and the temperature change is recorded. We use a cubic EoS [72]. Experimental values are obtained from the NIST database [65]. Note that the temperature drop is most pronounced for systems under vapour-like conditions.

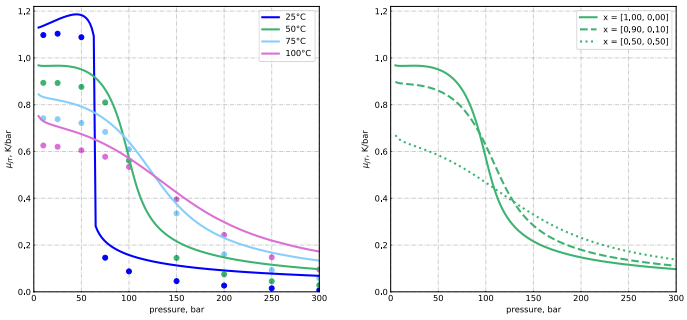

(a) Pure CO_2 (b) Mixture CO_2-C_1

Figure 6.10.: Joule-Thomson coefficient measured using four-cell simulation [22].

Phase transitions and narrow-boiling behaviour

In addition, operational conditions may be such that phase boundaries can be encountered. Upon a pressure drop under adiabatic assumptions, the enthalpy change associated with the phase transition induces a temperature decrease. Figure 6.11 shows the *PH*-diagrams of (a) pure CO_2 and (b) a mixture of 90%-10% CO_2-C_1. Outside of the two-phase region, cooling follows the Joule-Thomson coefficient. Moving into the two-phase region, the slope of the isotherms changes, and any state change is associated with a gradual mass transfer between vapour and liquid phases. The strongly nonlinear thermodynamic behaviour under such conditions is commonly referred to as narrow-boiling behaviour. Total enthalpy exhibits large changes for small changes in pressure and temperature, with the limiting case of a discontinuity at transition temperatures (Section 4.4).

The thermal effects of CO_2 expansion into the surroundings can be observed in sandstone core experiments. Figure 6.12 shows the results of liquid CO_2 injection (64 bar, 296 K) into a gaseous CO_2-saturated core (20 bar, 296 K, close to the

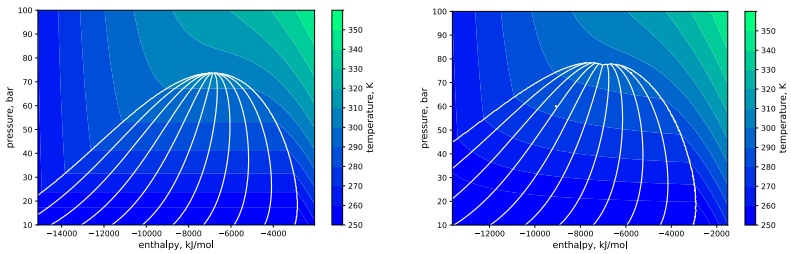

(a) Pure CO_2 (b) Mixture 90%-10% CO_2-C_1

Figure 6.11.: Phase envelopes of CO_2-rich gas mixtures in the *PH*-domain.

vapour-liquid boundary). The liquid, displacing the gas initially in place, slightly expands, and at some distance into the core, it reaches the vapour-liquid boundary. Temperature along the front follows the phase boundary along the pressure drop and some of the liquid at the tip of the front starts to evaporate. Simulation of these conditions requires the *PH*-specification.

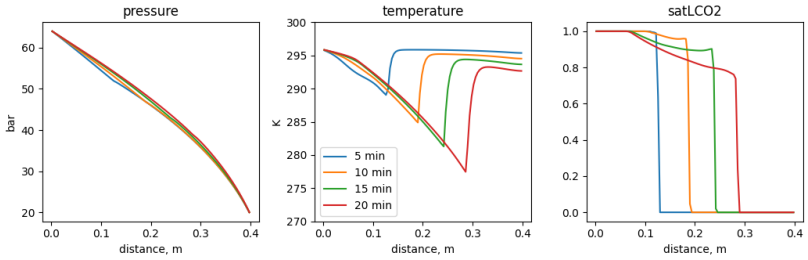

Figure 6.12.: Injection of liquid CO_2 into core saturated with gaseous CO_2.

Multiphase flow

For mixtures involving CO_2, conditions close to the critical point of CO_2 potentially give rise to a separate CO_2-rich liquid phase. Depending on the reservoir and injection conditions, sufficient cooling can bring the system to three-phase conditions (Figure 6.13). Due to the complex coupled thermal processes, this phenomenon could be triggered even at gas conditions for CO_2. In such systems, the CO_2-rich phase should be modeled using a three-phase relative permeability model and other phase-related properties. As such, the displacement front will follow more complex three-phase characteristics [223, 224]. In literature, many works have focused on the mathematics of three-phase displacement in porous media for oil-gas-water systems, as well as CO_2-EOR applications [225–228].

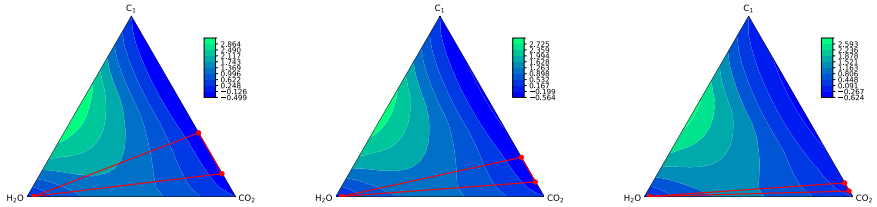

(a) T = 270 K (b) T = 280 K (c) T = 290 K

Figure 6.13.: Gibbs energy of mixing surfaces for H_2O-CO_2-C_1 mixtures at 60 bar. The red lines indicate the three-phase region (Aq-V-L_{CO_2}), which degenerates with increasing temperature.

6.2.2. CO_2 sequestration in depleted gas field

In this model, we investigate typical conditions for CO_2 injection into depleted fields. We consider a depleted gas reservoir saturated with CH_4 and residual brine. This model is inspired by the Porthos project in the Netherlands offshore of the North Sea [229]. A simple radial reservoir model with a high-permeable strike (100 mD) and a lower-permeable zone (20 mD) is considered, with impermeable over- and underburden. We simulate the injection of CO_2 into the reservoir at different temperatures to compare the characteristics of the injection process under vapour(-like) and liquid conditions. In addition, we use two scenarios: a simplified binary model when in-situ methane is represented by gaseous CO_2 and a ternary representation (H_2O-CO_2-CH_4) of the fluids with CH_4-H_2O originally in place.

Injection of gaseous CO_2 into depleted gas field

In this example, we inject gaseous CO_2 into the depleted field. The reservoir is depleted to 20 bar and uniformly saturated with brine at a residual saturation of 25%. Pure CO_2 is injected with a pressure of 60 bar. The 3D radial plots of pressure and temperature in the ternary model after one year of injection with a temperature of 310 K are presented in Figure 6.14. The expansion of CO_2 and corresponding cooling below the injection temperature can clearly be observed.

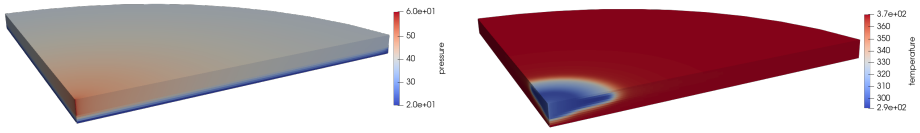

(a) 3D view of pressure profile (b) 3D view of temperature profile

Figure 6.14.: 3D view of pressure and temperature profile after one year of simulation (lower half of the reservoir).

Figure 6.15 shows the 2D profiles in logarithmic scale for the binary and ternary system simulation after one year of injection with an injection temperature of 305 K. The simulation shows a pronounced cooling front in the reservoir due to the CO_2 expansion seen in the density plot. A temperature drop of more than 20 °C can be observed with most of the cooling at the tip of the thermal front. The saturation profile reflects non-uniform distribution due to the layer heterogeneity structure. Despite the significant temperature drop along the CO_2-plume, the injected fluids remain in a vapour-like state. Surprisingly, the simulation results in the binary representation (Figure 6.15a) are remarkably similar to the ternary system (Figure 6.15b) with only insignificant changes in the saturation profiles. This is due to the similar properties of the gas mixtures at these extremely depleted conditions. In a less depleted state, this difference will become more pronounced.

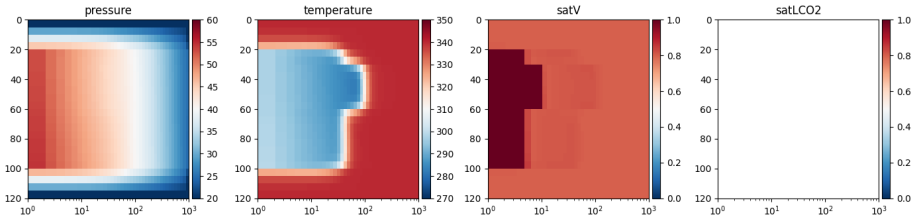

(a) Binary representation H_2O-CO_2

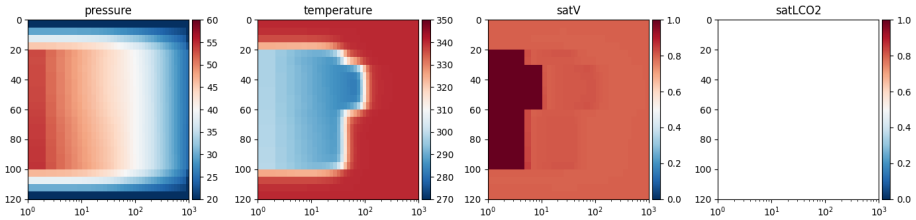

(b) Ternary system H_2O-CO_2-CH_4

Figure 6.15.: Simulation results after one years of pure CO_2 injection at 60 bar into radial depleted gas reservoir with $T_{inj} = 305$ K.

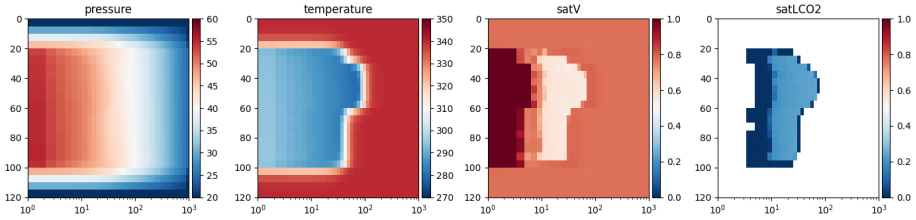

(a) Binary representation H_2O-CO_2

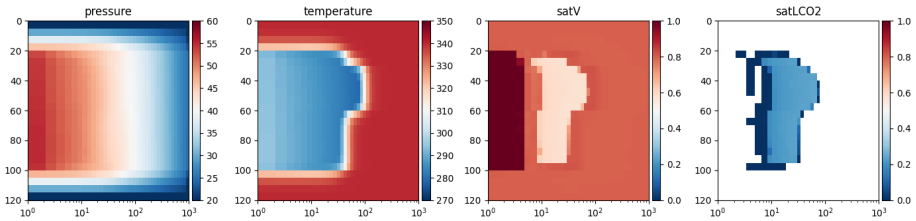

(b) Ternary system H_2O-CO_2-CH_4

Figure 6.16.: Simulation results after one years of pure CO_2 injection at 60 bar into radial depleted gas reservoir with $T_{inj} = 300$ K.

Figure 6.16 shows the 2D profiles for the binary and ternary system simulation after one year of injection with an injection temperature of 300 K. These conditions are close enough to the phase boundary and some of the injected CO_2 is converted to liquid. This phase transition occurs some distance into the reservoir, after it has sufficiently expanded and cooled down to reach the transition temperature. Not all CO_2 is turned to liquid, but it is enough to have an impact on phase mobility. Although the displacement fronts reach roughly the same distance out into the reservoir here compared to Figure 6.15, more rigorous multiphase flow models must be implemented to appropriately characterize the effect of condensed CO_2. In addition, the plume migration of binary and ternary representations starts to deviate more significantly. This is expected, because the methane content alters the phase envelope of the gas mixture.

Injection of liquid CO_2 into depleted gas field

If the temperature of the injected CO_2 is slightly lower compared to previous examples, it is injected in a liquid state. Figure 6.17 shows the results of CO_2 injection at a temperature of 295 K after one year. The injection stream takes a distinct liquid form, driving an efficient displacement of the in-situ gas, and any compositional effects within the CO_2-plume are less pronounced. This results in relatively small differences between binary and ternary systems. In addition, notice how density contrasts between liquid and gas phases are reflected in density profiles over depth.

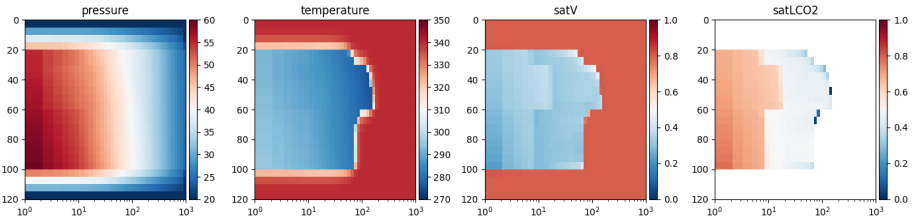

(a) Binary representation H_2O-CO_2

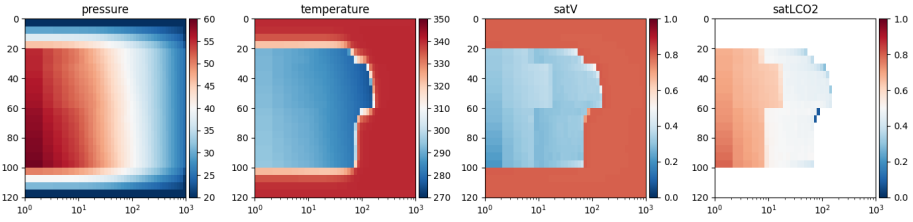

(b) Ternary system H_2O-CO_2-CH_4

Figure 6.17.: Simulation results after one years of pure CO_2 injection at 60 bar into radial depleted gas reservoir with $T_{inj} = 295$ K.

Considerations for a realistic field-scale simulation model

It must be noted that the simulations presented here merely serve as a proof-of-concept for the *PH*-specification within the OBL framework. This is an important step towards a simulation model that can handle narrow-boiling conditions and capture the complex coupled thermal and multiphase effects. However, there are a few important considerations for future work in order to establish a realistic field-scale simulation model for this application.

The characteristics of three-phase flow has not been investigated much in relation to CO_2 sequestration applications. Besides, the cooling of the field depends on the particular reservoir geometry and structure, which need to be considered for a practical dynamic simulation. Laboratory experiments could provide insights into the complex thermal-compositional multiphase flow dynamics on Darcy scale. In addition, the experiments can be used to validate the predictive capabilities of the simulation model with regard to these conditions. Furthermore, the thermodynamic conditions that we can encounter upon CO_2 injection into depleted gas fields may introduce gas hydrates and precipitated salt, further complicating the flow characteristics.

Finally, a simulation model of CO_2 sequestration is not complete without an accurate model for flow inside the wellbore. Most transient effects and nonlinear behaviour take place inside and in the vicinity of the wellbore. Some simulations have indicated strong thermal effects and sub-zero temperatures that span timescales in the order of seconds [189], yet these are enough to cause significant damage to the wellbore and near-well reservoir.

7

A kinetic model for hydrate formation and dissociation

Gas hydrates are crystalline solids, composed of hydrogen-bonded water, stabilized by small non-polar guest molecules [122]. The hydrate cages exist in a stable thermodynamic state at sufficient pressure and low-temperature conditions, yet above the freezing point of water. Hydrates are a well-known challenge in subsurface engineering, hydrocarbon production, and pipeline transport [230]. With the advent of carbon sequestration in depleted or low-pressure oil and gas fields, the potential for CO_2-hydrate formation has become an operational concern. Injection of dense-phase CO_2 into depleted reservoirs introduces additional hydrate risks. A temperature decrease due to JouleThomson cooling and phase transitions during expansion in combination with the availability of water in the reservoir can drive near-well CO_2-hydrate formation, severely impairing injectivity [22, 23].

Methane (CH_4) is the most commonly occurring guest molecule in natural hydrate deposits, found typically in continental margin sediments and shallow permafrost [232]. Estimates of gas in place in the form of hydrates range over a few orders of magnitude, but even in the most modest estimates, they represent a substantial portion of mobile carbon on the earth [233]. Perturbations of hydrate stability and thawing of permafrost caused by ocean and atmospheric warming may lead to CH_4 being released into overlying sediments or water columns, which could exacerbate greenhouse warming. There is no conclusive evidence that hydrate-derived CH_4 is reaching the atmosphere now, but more observational data and improved numerical models will better characterize the climate-hydrate synergy in the future [234].

From another perspective, naturally occurring hydrate deposits are also recognized as a vast potential energy resource [235]. Recovery of natural gas from hydrate reservoirs relies on common production technologies such as depressurization, thermal stimulation, inhibitor injection and guest molecule

This chapter has been published in Energy Conversion and Management: X **30** (2026) [231].

exchange. The first three methods are aimed at destabilizing the hydrate by prohibiting hydrate formation conditions. The latter is rooted in the improved thermodynamic stability of a mixed hydrate phase over single-component hydrates and has the benefit of maintaining the structural integrity of the hydrate-bearing geological formation [236]. Furthermore, this process offers potential for carbon sequestration in hydrate deposits.

The interest in CO_2-hydrates, on the contrary, has primarily emerged from operational concerns in CO_2 sequestration [23]. Beyond operational risks, however, the formation of CO_2-hydrates in subsurface environments has attracted increasing attention as a promising pathway for long-term carbon storage. Hydrate-based CO_2 sequestration takes advantage of the fact that under sufficient pressure and low-temperature conditions, CO_2 can form thermodynamically stable hydrates in marine and permafrost sediments [237, 238]. Compared to conventional supercritical CO_2 storage at higher temperatures and depths, hydrate-based storage offers additional safety through solid-phase trapping and reduced leakage potential [122, 239]. Geological assessments have indicated that the hydrate stability zone (HSZ) in marine sediments can extend several hundred meters below the seafloor, providing a large volume for potential CO_2 immobilization [240].

Field data from geological surveys aimed at identifying the occurrence and properties of gas hydrate reservoirs have provided a wealth of information regarding CH_4-hydrates in porous media. Furthermore, several short-term field pilots have been carried out in permafrost- and marine hydrate deposits, such as the Ignik-Sikumi field trials at the Alaska North Slope [241]. These particular tests involved depressurization, as well as the guest molecule exchange of CH_4 with the injected CO_2-N_2 mixture. However, controlling operating conditions in hydrate reservoirs is challenging due to complexity of interpretation of the field tests. Moreover, the dynamics of hydrate dissociation and formation, heat exchange due to the endothermic nature of hydrate phase behaviour and potential formation of ice upon hydrate production add to the operational complexities and have restricted short-termed field tests to typically days or weeks [242]. Therefore, numerical investigation of hydrate systems is essential to evaluate the production potential and develop strategies for the commercial use of hydrate reservoirs. This will lead to a better understanding of the dynamics of hydrate-bearing geologic media.

The majority of the existing literature on hydrates in porous media focuses on CH_4-hydrates. Historically, it has been the most common type of guest species, in oil and gas production and as a naturally occurring carbon source. As a consequence, the comparison and benchmarking of a numerical model for gas hydrates in porous media is limited to mostly single-component CH_4-hydrates. Nevertheless, single-component hydrates of CH_4 and CO_2 share a common thermodynamic basis. Therefore, only a few adjustments allow the use of the numerical model presented in this study for CO_2-hydrates as well.

Numerical studies on the simulation of gas hydrate systems in porous media are limited. The TOUGH+HYDRATE (T+H) simulator [243] is capable of simulating CH_4-hydrate formation and dissociation under kinetic and equilibrium conditions, involving the various production techniques destabilizing the hydrate. Other

simulators that use a kinetic description of CH_4-hydrate formation and dissociation include CMG STARS [244] and MH21-HYDRES Konno *et al.* [245]. Furthermore, with the STOMP-HYDT-KE simulator [246], an attempt has been made to develop and demonstrate kinetic models representing the CH_4-CO_2-N_2 guest molecule exchange process that is presumed to have occurred during field tests [241]. More recently, the Full Implicit Simulator of Hydrate (FISH) has implemented a fully coupled thermal-hydraulic-chemical (THC) framework specifically for CO_2-hydrates and reproduces core-scale pressure, temperature, and hydrate-mass profiles within 10% deviation [247]. However, most models mentioned here assume that hydrate formation and dissociation are driven by a pressure difference relative to the hydrate equilibrium curve, rather than a thermodynamic (non-)equilibrium state. This assumption is limited to regions in the thermodynamic space where three phases (vapour-aqueous-hydrate) can coexist. Without excess water or with low gas concentrations, hydrate formation is still possible, but the required pressure can be above the equilibrium curve. Furthermore, the modelling of the hydrate phase equilibria under equilibrium assumptions in T+H is based on tabulated equilibrium constants [243].

This chapter is structured as follows. First, we develop the workflow for thermodynamic calculations for hydrate systems under kinetic assumptions. We analyze the Gibbs energy surfaces of each of the fluid and hydrate phases to confirm that, in the limit, kinetic assumptions would yield the same conditions as equilibrium thermodynamics. Then, we benchmark the simulation model for formation and dissociation of CH_4- and CO_2-hydrates against T+H through several test cases Yin *et al.* [235], Li *et al.* [247] and Kowalsky and Moridis [248].

7.1. Thermodynamic description of hydrate systems

Hydrates can form in any system that contain water and the presence of small, non-polar guest molecules, either undersaturated in aqueous solution or as a free phase. The hydrate pseudo-reaction is given by:

$$G + n_H H_2O \longleftrightarrow G \cdot n_H H_2O \tag{7.1}$$

The hydration number n_H corresponds to the number of water molecules bound to each guest molecule G. Hydrates are non-stoichiometric substances, i.e., they have no set chemical composition. Full cage occupancy of sI-hydrate corresponds to 8 guest molecules per 46 H_2O molecules and would yield a hydration number of 5.75. In reality, full cage occupancy is not a thermodynamically favourable state, and the composition of the hydrate phase varies with thermodynamic conditions.

The conditions for hydrates to exist then require rather low temperatures, though not necessarily sub-zero, and sufficiently high pressures. However, formation conditions, (non-stoichiometric) composition, and structure type (sI, sII, sH) of hydrates are highly dependent on fluid composition. As a result, mixed guest hydrates introduce a very nonlinear thermodynamic behaviour which cannot be easily understood without considering a full thermodynamic equilibrium approach including hydrate phases.

For single-guest hydrates, such as nearly-pure CH_4-hydrates in natural hydrate deposits or natural gas pipelines or CO_2-hydrates in carbon sequestration operations, a thermodynamic model using a kinetic description for the hydrate phase is, in many cases, a better approximation of the dynamics. This holds especially for hydrate systems in porous media, where nucleation highly depends on local conditions and pore-scale geometry limits transport of matter to the hydrate surface and governs the ability to sustain the growth process [248].

In this section, we discuss the thermodynamic model for single-component CH_4- and CO_2-hydrates. We limit ourselves to a two-component system containing H_2O and CH_4 or CO_2, which are limited to partition into non-aqueous (V/L), aqueous (Aq) or sI-hydrate (H) phases. According to Gibbs' phase rule, the degrees of freedom at equilibrium amount to $F = C - P + 2$. This implies that a three-phase equilibrium can only occur at the phase boundary (the hydrate equilibrium curve), where pressure (or temperature) behaves as a dependent variable. By means of a Gibbs energy analysis, we demonstrate that both kinetic and equilibrium approaches yield the same equilibrated conditions given enough time. In the mass balance equations (5.10), however, the hydration number is often fixed. An aspect that is not easily captured using a kinetic model with a set hydrate composition is the variability in gas 'stoichiometry' throughout the equilibration process. This phenomenon is relatively harmless for single-component hydrates, but becomes crucial for modelling of mixed hydrates [249].

Thermodynamic description of kinetic model

A kinetic description of the hydrate phase requires a flash procedure for solving thermodynamic equilibrium only between the fluid phases. The assumption of instantaneous thermodynamic equilibrium is not applied to the hydrate phase, and a separate mass balance equation for the hydrate pseudo-component is added. The kinetic pseudo-reaction of the hydrate phase is then driven by the difference in fugacities of water between fluid and hydrate phases:

$$r_k \propto \Delta f_w \tag{7.2}$$

The process of formation or dissociation results in a net exchange of mass between hydrate and non-hydrate phases to minimize Gibbs energy and restore thermodynamic equilibrium between all phases.

The proposed thermodynamic framework for kinetics consists of two stages. Firstly, a two-phase flash procedure yields the thermodynamic equilibrium between the fluid phases. Secondly, the hydrate reaction rate is determined from the fugacity difference between the fluid and hydrate phases. We demonstrate that the conditions of the equilibrated system obtained with kinetic assumptions are, in the limit, equivalent to those obtained from equilibrium assumptions.

For the fluid phases, we rely on the hybrid-EoS framework with the fugacity-activity model for the aqueous phase and cubic EoS for non-aqueous fluid phases from Chapters 3 and 4. In practice, hydrate calculations are limited to a narrow range of temperature and a wide range of pressure, and the inconsistencies toward

critical conditions of the brine phase by using separate equations of state are therefore not a concern [115]. An accurate evaluation of aqueous phase properties is particularly important for hydrate modelling, where gas solubility and component fugacities have a large influence on predicted hydrate equilibria [73].

It must furthermore be noted that, albeit the Peng-Robinson EoS [72] is often preferred because of improved (critical) compressibility factors, predictions of hydrate structures and equilibrium pressures obtained with the Soave-Redlich-Kwong EoS [71] are more satisfactory. This is due to the fact that the improvement in volumes is at the expense of the (critical) fugacity coefficient [73].

To calculate hydrate fugacity and determine the magnitude of the thermodynamic driving force (7.2), the common procedure in the literature relates to the hydrate equilibrium curve. In this work, however, we evaluate the fugacity of water in the hydrate phase from the modified Van der Waals-Platteeuw hydrate equation of state [123] following Ballard and Sloan, Jr. [127] (Section 3.3).

Gibbs energy analysis of kinetic assumptions

Contrary to equilibrium assumptions, where the hydrate phase is incorporated into a multiphase flash procedure, the kinetic model assumes a thermodynamic non-equilibrium between the fluid and hydrate phases. In the limit, however, both tend to the direction of minimum Gibbs energy. We demonstrate this by analyzing the Gibbs energy surfaces of the three phases. Figure 7.1 shows the dimensionless Gibbs energy of mixing for the H_2O-CH_4 system at a temperature of 277.6 K, typically encountered at the sea floor [122]. Note that the surfaces are only plotted for relevant ranges of composition (i.e., CH_4-rich for the vapour, H_2O-rich for the aqueous phase). The composition of the hydrate phase is physically limited to the range between empty ($z_{H_2O} = 1$) and full cage occupancy ($z_{H_2O} \approx 0.85$).

The fugacity of each separate component can be calculated from its intersection with the y-axis at pure composition. The guest molecule fugacity is taken from the fluid-phase equilibrium. The stability of the hydrate at specified conditions is indicated by whether the hydrate fugacity is above or below fluid-phase equilibrium.

Three different pressures are considered: below hydrate equilibrium pressure (P = 10.0 bar), exactly at the three-phase coexistence curve (P = 40.79 bar) and above equilibrium pressure (P = 70.0 bar). At thermodynamic equilibrium between any number of phases, the chemical potential of each component is equal throughout all equilibrium phases. In the Gibbs energy diagram, this corresponds to a common tangent to the surface at each of the equilibrium phase compositions. Observe that the Gibbs energy surface of the hydrate phase for the three pressures is above, exactly at and below the Gibbs energy surface for two-phase equilibrium, respectively. Using the fugacity of CH_4 in the fluid phases to calculate the hydrate fugacity, the tangent to the hydrate surface indicates that total Gibbs energy would be decreased by either hydrate formation ($P > P_{eq} : f_k > f_H$) or dissociation ($P < P_{eq} : f_k < f_H$). Through the consumption or release of gas upon formation or dissociation, respectively, the system decreases or increases its pressure accordingly to return to equilibrium.

From the Gibbs energy analysis, we find that, as was implied by Gibbs' phase rule, three-phase equilibrium in a binary system occurs only at the phase boundary between the three phases, which corresponds to the hydrate equilibrium curve. In single-phase fluid conditions – either when the brine is undersaturated with dissolved methane or all water is evaporated – we would find that increasingly large pressures are necessary to sustain a stable hydrate phase.

Aside from finding equilibrium conditions of the hydrate phase, note that the phase equilibrium conditions also determine the composition of the hydrate phase. It corresponds to the tangent line to the hydrate surface, which varies from low cage occupancy in brine-hydrate conditions to high concentrations of CH_4 in the vapour-hydrate region.

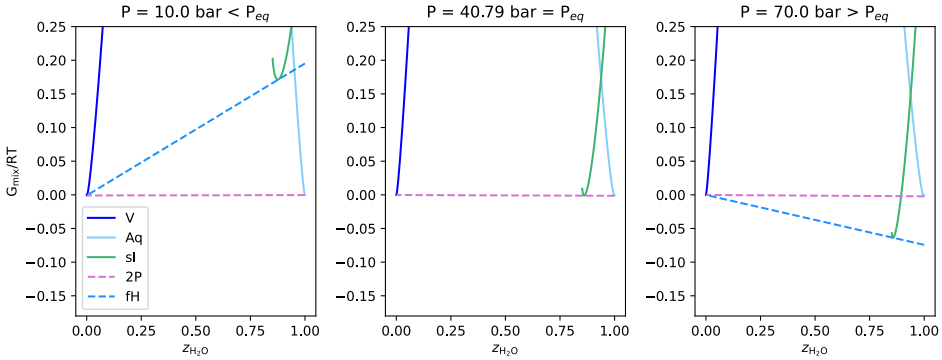

Figure 7.1.: Gibbs energy surfaces of mixing of H_2O-CH_4 mixture at T = 277.6 K for conditions below equilibrium pressure (P = 10.0 bar), at the three-phase boundary (P = 40.79 bar) and above equilibrium pressure (P = 70.0 bar). The solid lines are the Gibbs energy of mixing surfaces for hypothetical single-phase mixtures and the dashed lines are the Gibbs energy of mixing of two-phase equilibrium, and of the hydrate phase at the given two-phase equilibrium.

7.2. Results

In this section, we apply the modelling framework to simulate gas hydrates in porous media. We first reproduce hydrate formation the numerical experiments for CH_4 [235] and CO_2 [247]. Then, we investigate test cases for dissociation of natural CH_4-hydrate deposits as studied by [248]. The reaction models for each case have been summarized in Table 7.1. Note that we adopt the same kinetic rate parameters, porosity-permeability relationships, spatial grids and boundary conditions as in the original publications, since the primary goal here is to reproduce the reported behavior.

Table 7.1.: Hydrate formation/dissociation kinetic models and parameters employed in numerical studies.

Study	Kinetic model and parameters
CH_4-hydrate formation [235]	$r = K_f A_s \exp\left(-\frac{E_a}{RT}\right)\left(f_w^H - f_w^k\right)$ $K_f = 3.6 \times 10^4\ \text{mol}\,\text{Pa}^{-1}\,\text{m}^{-2}\,\text{s}^{-1}$ $E_a = 8.1 \times 10^4\ \text{J}\,\text{mol}^{-1}$ $n_H = 6.1$ $A_s = 0.879\, F_A(t)\, \frac{1-\phi}{r_p}\, S_H^{2/3}$ $r_p = \left[\frac{45\,k}{(1-\phi)^2\,\phi^3}\right]^{1/2}$ $F_A = 0.23$
CO_2-hydrate formation [247]	$r = 3K_{f0} \exp\left(-\frac{E_a}{RT}\right) S_A^{\beta}(1-S_H)^{\beta}\, \frac{1-\phi}{r_p}\, S_G^{2/3}\left(f_w^H - f_w^k\right)$ $K_{f0} = 8.4 \times 10^{11}\ \text{kg}\,\text{m}^{-2}\,\text{Pa}^{-1}\,\text{s}^{-1}$ $E_a = 1.0288 \times 10^5\ \text{J}\,\text{mol}^{-1}$ $\beta = 5.3$ $n_H = 6.0$ No separate A_s; geometric factor is inside the rate. $r_p = 1.645 \times 10^{-4}\ \text{m}$
CH_4-hydrate dissociation [248]	$r = K_d A_s \exp\left(-\frac{E_a}{RT}\right)\left(f_w^H - f_w^k\right)$ $K_{d0} = 3.6 \times 10^4\ \text{kg}\,\text{Pa}^{-1}\,\text{m}^{-2}\,\text{s}^{-1}$ $E_a = 8.1 \times 10^4\ \text{J}\,\text{mol}^{-1}$ $n_H = 6.1$ A_s and r_p same as CH_4-hydrate formation study $F_A = 1.0$

7.2.1. Formation of CH_4- and CO_2-hydrates

Authors of Yin *et al.* [235, 250] analysed numerically earlier experimental studies that involved CH_4-hydrate formation and dissociation in a small reactor filled with a sandy porous medium. Their study aimed to investigate the hydrate reaction kinetics and phase distribution heterogeneity throughout core samples in such laboratory studies. In a similar setup, we simulate a CO_2-hydrate formation experiment under a semi-batch, constant-pressure configuration [247]. The core properties for both experiments are summarized in Table 7.2.

Table 7.2.: Reactor and porous medium properties for formation experiments.

Parameter	CH_4	CO_2
Internal height of reactor	120.0 mm	160.0 mm
Internal diameter of reactor	102.0 mm	101.6 mm
External height of reactor	170.0 mm	164.0 mm
External diameter of reactor	132.0 mm	116.0 mm
Thickness of reactor wall	15 mm	7.2 mm
Porosity ϕ	0.44	0.312
Permeability k	3.83 D	30.0 D
Density of rock ρ_r	2650 kg/m^3	2075.5 kg/m^3
Thermal conductivity of dry rock κ_d	0.30 W/m.K	2.2 W/m.K
Thermal conductivity of wet rock κ_w	1.65 W/m.K	N.A.
Heat capacity of rock $c_{p,r}$	1400 J/kg.K	745 J/kg.K
Thermal conductivity of Steel κ_s	16.0 W/m.K	13.4 W/m.K
Heat capacity of Steel $c_{p,s}$	500 J/kg.K	468 J/kg.K

CH_4-hydrate formation

The CH_4-hydrate formation experiment describes a 1.0L cylindrical reactor, blanketed by a cooling jacket that circulates a heat exchange fluid. A stainless-steel wall surrounds the porous medium and is used for cooling via the external bath; in the model, the wall is treated as an impermeable layer with zero porosity (no mass flow through the wall). A water injection point is located at the top of the reactor. Pressure sensors record pressure at the top and bottom, and thermal sensors a and b are installed at radii of 25 and 38 mm.

The core is initially pressurized by pure CH_4. Then, three sequences of water injection (I), stabilization (S) and hydrate formation (F) stages followed, allowing the system to equilibrate. We model the first stage of hydrate formation $F1$. The bath temperature and pressure initially measure 288.2 K and 95.0 bar and are practically uniform. The cooling fluid starts circulating the boundary, its temperature slowly reduced to 274.5 K (reached at $t = 0.66$ hr). The temperature at the boundaries is maintained constant for the remainder of 24 hours. This is sufficiently low to create hydrate formation conditions. The rate of hydrate formation is described in Table 7.1.

Figure 7.2 shows the temporal and spatial evolution of pressure (a), temperature (c) and phase distributions (e). The high porosity and permeability of the sand result in a practically uniform pressure distribution at all times. The temperature distribution is heterogeneous at early times, caused by the combined effect of the cooling boundary and the exothermic nature of hydrate formation. The temperature drop at the boundary spreads into the core by means of thermal conduction, then increases due to the heat released upon hydrate formation and becomes uniform after 4 hours. A similar heterogeneous distribution of hydrates to Yin *et al.* [235] can be observed. They recorded a hydrate saturation of 0.49 at the cooling boundary and a saturation of only 0.10 at the center of the core. In our simulations, the distributions are slightly different. Notice that the pattern of hydrate distribution heavily depends on the kinetic parameters and thermal properties of the medium.

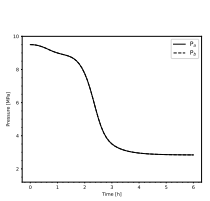

(a) Pressure vs. time

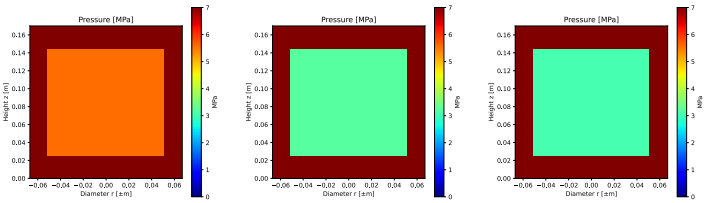

(b) Pressure – spatial distributions at 2 h, 3 h, 5 h

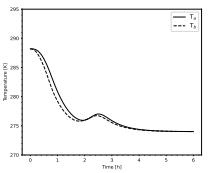

(c) Temperature vs. time

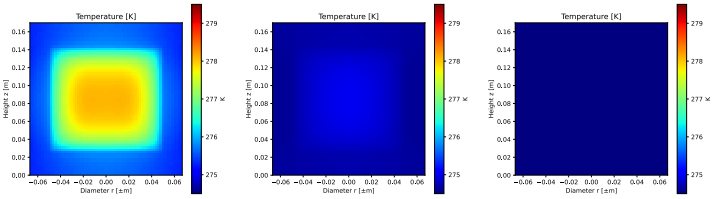

(d) Temperature – spatial distributions at 2 h, 3 h, 5 h

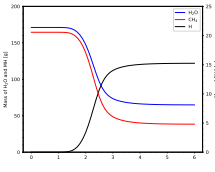

(e) Hydrate mass vs. time

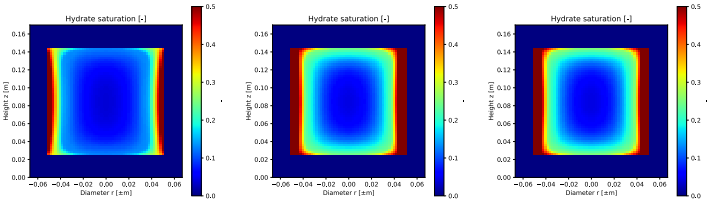

(f) Hydrate saturation – spatial distributions at 2 h, 3 h, 5 h

Figure 7.2.: Results for CH_4-hydrate formation experiment after 6 hours of simulation. (Left) Time evolution of (a) pressure, (c) temperature at sensors a and b and (e) total mass of H_2O, CH_4 and MH components. (Right) Spatial distributions of (b) pressure, (d) temperature and (f) hydrate saturation. Markers show reference points from [235].

Under hydrate-forming conditions, the system pressure and temperature gradually decrease as the boundary cools. The pressure-temperature trajectories at sensors A and B (Figure 7.3) show that both locations follow a cooling path that progressively departs from the equilibrium curve as hydrates begin to form. The deviation below the equilibrium line indicates the consumption of free gas and water for hydrate generation, while the subsequent pressure stabilization reflects the slowing of formation as the system approaches equilibrium.

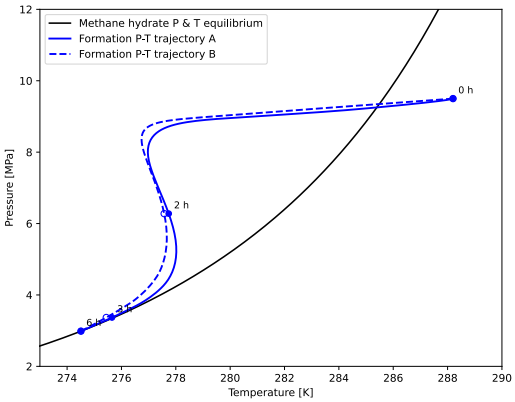

Figure 7.3.: Pressure-temperature trajectories at sensors *a* and *b* during hydrate formation, compared with the CH_4-hydrate equilibrium curve. Markers indicate system conditions at 0, 2, 3, and 6 hours.

CO_2-hydrate formation

We reproduce the semi-batch/constant-pressure configuration (run 3) of the CO_2-hydrate formation experiment reported by Li *et al.* [247]. Initial conditions correspond to a uniform $T = 1.95\,°C$ and $P = 3.20\,MPa$. In the sand bed, $S_A = 0.25$, $S_G = 0.75$. The gas cap is void ($\phi = 0.99$) that is saturated with nearly pure CO_2. All steel walls (side, top, bottom) are impermeable to flow and held isothermal at the external bath temperature ($T_b = 1.0\,°C$). The core is pressurized from the gas cap by pressure-controlled CO_2 injection at $P_{inj} = 3.20\,MPa$ and $T_{inj} = 1.0\,°C$. The rate of formation follows the CO_2-specific kinetic law [251] mentioned in Table 7.1. Capillary pressure, relative permeability, and porosity-permeability relationships are taken from Li *et al.* [247].

Figure 7.4 shows the evolution of pressure and temperature at different locations in the core. While pressure remains virtually constant, the temperature strongly increases at early stages due to the exothermic process of hydrate formation. The temperature increase is more pronounced at the top and middle sensors, indicating that the amount of hydrate formed in these regions is larger than in the bottom, where no cooling is applied. After equilibration, a uniform temperature distribution is restored due to conductive fluxes from the cooling bath inward.

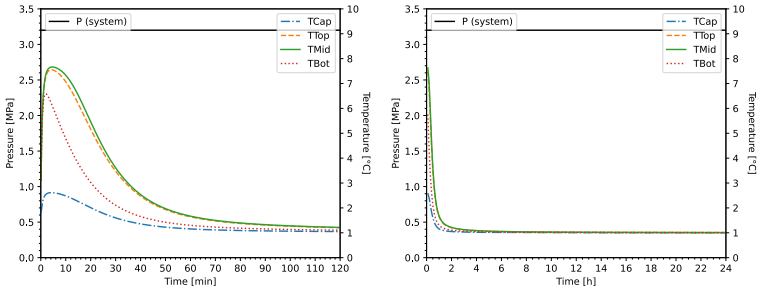

(a) After 2 hours (b) After 24 hours

Figure 7.4.: Pressure and temperature at sensors at bottom, middle, top and gas cap over time from simulation of CO_2-hydrate formation experiment.

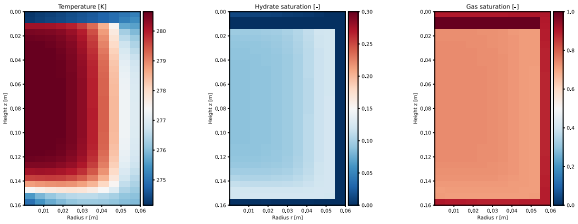

(a) t = 3 min

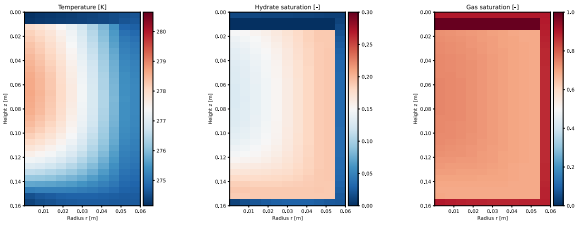

(b) t = 20 min

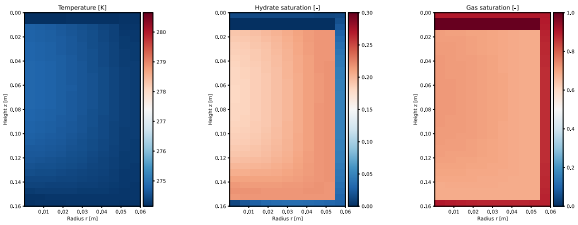

(c) t = 60 min

Figure 7.5.: Spatial distribution of pressure, temperature and gas/hydrate saturations from simulation of CO_2-hydrate formation experiment.

The features that show up in the time data can be recognized in the spatial maps from Figure 7.5. In addition, it can be observed that the cooling bath enforces low temperatures from the outside, and the temperature increase that accompanies the formation process is suppressed in the outer region. The strongest driving force for hydrate formation is thus induced at the outermost cells, resulting in a non-uniform final hydrate saturation.

7.2.2. Dissociation of CH_4-hydrates

Here, we run test cases of hydrate dissociation in hydrate-bearing sedimentary layers. We follow two scenarios from Kowalsky and Moridis [248]. Both cases are concerned with so-called Class 3 type radial reservoirs, hydrate accumulations that are underlain and overlain by impermeable layers [252]. Case A considers thermal stimulation to induce hydrate dissociation by providing a heat source at the well at the centre of the reservoir to bring the temperature above hydrate equilibrium conditions. In case B, hydrate dissociation is driven by depressurization, where the pressure at the well is reduced below the hydrate equilibrium pressure. We use 1D radial domains for both cases in which the size of the grid blocks increases in the radial direction, starting from 5 cm at the well radius $r_w = 7.5$ cm, to 100 m at the outer radius. Table 7.3 lists the specifics. The dissociation of CH_4-hydrates follows a similar kinetic model as the formation case listed in Table 7.1.

Table 7.3.: Parameters for simulation of dissociation test cases A and B.

Parameter	Case A	Case B
Thickness	10 m	10 m
Radius	1000 m	10000 m
P_{init}	40 bar	90 bar
T_{init}	1.0 °C	11.0 °C
P_{well}	40 bar	27 bar
T_{well}	45.0 °C	N/A
$S_{h,init}$	0.5	0.5
$S_{a,init}$	0.5	0.5
Porosity ϕ	0.30	
Permeability k	296 mD	
Thermal conductivity of dry/wet rock κ_d/κ_w	0.5-3.1 W/m.K	
Heat capacity of rock $c_{p,r}$	1000 J/kg.K	

Case A: thermal stimulation

Initially, two-phase brine-hydrate equilibrium exists with $S_h = S_a = 0.50$, T = 274.15 K and P = 40.0 bar, uniform throughout the domain. The pressure at the well is kept at the initial pressure, and production is initialized by increasing the temperature at the well to the specified $T_w = 45$ °C.

The results of test case A after 30 days of simulation time are displayed in Figure 7.6. A fine OBL resolution of 4000 points has been used. Figures (a) and (b) show the spatial distributions of pressure and temperature and phase saturations, respectively. A temperature front propagates into the reservoir, resulting in a small zone behind which the hydrates have completely dissociated. In the simulations, the temperature rapidly decreases from well temperature $T_w = 45°C$ into the near-well region, in part due to the endothermic nature of hydrate dissociation and the increasingly large area of dissociating hydrates outwards. The largest pressure can be found in the dissociation zone, leading to fluid flow in both the inward and outward directions. The amount of gas produced in the early stages, however, is insignificant. Ahead of the dissociation front, secondary hydrate formation occurs as a result of the increased pressure associated with gas release from dissociation.

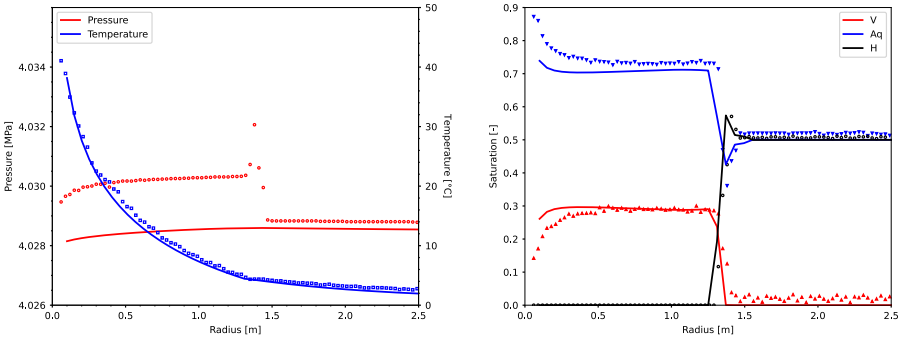

(a) (b)

Figure 7.6.: Results for case A after 30 days of simulation. Spatial distributions of (a) pressure and temperature and (b) saturations of V, Aq and H phases. Markers show reference points from [248].

Case B: depressurization

The second test case is very similar to case A, but now dissociation is triggered by constant pressure at the well. Initial saturations are again uniformly distributed $S_h = S_a = 0.50$ with T = 284.15 K and P = 90.0 bar. Production is initialized with a constant pressure control at 27.0 bar.

The spatial distributions of pressure and temperature (a) and phase saturations (b) after 30 days of simulation time are displayed in Figure 7.7. An OBL resolution of 400 points has been used. It can be observed that depressurization results in a wide region of dissociating hydrates, unlike in case A. Temperature drops due to the effect of endothermic dissociation and expansion cooling of the released gas.

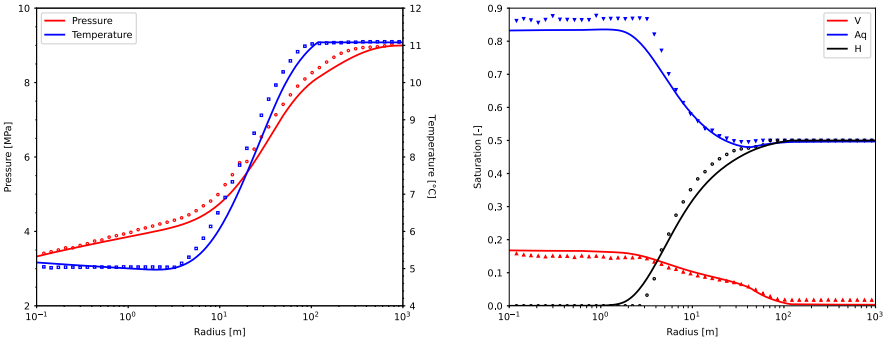

(a) (b)

Figure 7.7.: Results for case B after 30 days of simulation. Spatial distributions of (a) pressure and temperature and (b) saturations of V, Aq and H phases. Markers show reference points from [248].

7.2.3. Discussion on simulation results

A simulation model for hydrate formation and dissociation must be able to capture the competing physical phenomena – a sharp decrease in temperature due to the boundary conditions, adiabatic cooling, exothermic hydrate formation reaction, and a reaction rate highly sensitive to hydrate surface area – which result in highly nonlinear simulation problems. This requires an appropriate resolution of the OBL mesh. A coarse resolution of the OBL mesh is not fully able to resolve the nonlinearities introduced by the kinetic reaction. A very fine resolution would be a limiting performance factor, thereby losing the advantages of the OBL approach.

In our paper, we go into more detail on the advantages and trade-offs of an OBL implementation for complex physics such as the hydrate model. We illustrate how OBL- and grid resolution affect scaling and performance. In general, OBL statistics show that Jacobian assembly increasingly dominates the runtime with finer OBL resolution. This is due to a higher amount of points to be generated, while the number of interpolations remains of the same order of magnitude. In addition, a grid convergence study indicated a good scalability of the OBL technique with grid resolution. This is due to the fact that the number of interpolations increases rapidly with the number of primary unknowns, while the amount of points generated remains orders of magnitude less. This presents a significant computational advantage over conventional simulators that utilize analytical or numerical derivatives for Jacobian assembly, which scale poorly with the number of unknowns. A similar conclusion was drawn from a comparison between TOUGH2 and open-DARTS for modeling of fractured reservoirs [253].

8

Conclusion

This work aimed to develop a robust, flexible and efficient thermodynamics-based simulation framework for modelling of geological CO_2 sequestration. The existing open-DARTS simulation software was provided with robust and accurate thermodynamic modelling routines. The integration of DARTS-flash into the Operator-Based Linearization framework for physical modelling extended its applicability to model complex multiphase mixtures involving brine, reservoir fluids, CO_2 and impurities. By the nature of the OBL technique, the computational load of thermodynamic calculations is limited and only required to compute missing supporting points for interpolation. As partial derivatives of all terms are readily obtained by performing interpolation, an extension of the OBL framework to solve with any state variables is straightforward and greatly improves simulation robustness.

CO_2 sequestration processes involve a wide range of physical interactions at different scales. Accurate and consistent thermodynamic modelling, coupled with the mass and energy conservation equations, is able to capture effectively the interplay of thermal-compositional phenomena. Through a thorough review of fundamental thermodynamics, computational techniques and available branches of thermodynamic models, a computational framework was established to solve phase equilibria of reservoir mixtures with brine and CO_2. Starting from a geometrical interpretation of the phase equilibrium problem, efficient initialization procedures were formulated to perform two- and three-phase equilibrium calculations that is readily extended to a higher number of phases. In addition, the approach allows for the straightforward use of multiple thermodynamic models together.

A hybrid-EoS model that uses a specific fugacity-activity model for the aqueous phase and a cubic equation of state for the non-aqueous fluid phases was introduced and validated against experimental data of multiphase mixtures of brine and reservoir fluids. Similarly, the hydrate equation of state was added in the same setup to include different hydrate types into the model. Moreover, the flash procedures were extended to calculate phase equilibria in *PH*- and *PS*-specifications in line with state-of-the-art computational methods for inner and outer loops of the nested algorithms.

The thermal-compositional framework was applied to a set of simulation scenarios relevant to geological CO_2 sequestration. Two conventional targets for CO_2 injection – saline aquifers and depleted hydrocarbon fields – have been investigated in terms of typical conditions and dominating physical phenomena. By means of two recent benchmark studies for CO_2 storage in aquifers, the *FluidFlower* and *SPE11*, the combination of DARTS and DARTS-flash has been demonstrated to capture plume migration and capillary trapping, as well as enhanced dissolution and impurity impacts that is in accordance with experimental data and modelling efforts throughout the community. Simulation of CO_2 sequestration in depleted hydrocarbon reservoirs was modelled here in a simplified radial model that mimics the conditions of the highly depleted Porthos project in the North Sea offshore. It is, however, a less resolved field of study, as thermal-compositional effects related to expansion cooling and phase changes are much more pronounced. This introduces additional nonlinearities to the simulation from thermodynamic, as well as multiphase flow points of view. While a *PH*-formulation was developed to resolve the former, this matter requires thorough investigation of all coupled processes and nonlinearities to come up with appropriate heuristics. Additionally, the OBL framework was extended to include gas hydrates into the simulation model. By use of a kinetic description of hydrate formation and dissociation, a set of core-scale methane- and carbon-dioxide-hydrate formation experiments and field-scale dissociation scenarios for gas production could be reproduced from literature.

Recommendations for further research

With the efficient coupling of thermodynamic modelling and fluid flow solvers using the OBL approach, improvements to the thermal-compositional simulation framework can still be sought in both areas. By means of a *PH*-specification, most thermodynamic nonlinearities for fluid flow can be effectively resolved. However, an investigation of the nonlinear solver behaviour with respect to the change of variables from temperature to enthalpy is required to develop appropriate heuristics for the Newton solver. This may be particularly important in relation to multicomponent systems, where mixture enthalpy is highly influenced by the pure component enthalpies.

The nonlinearities associated with multiphase dynamics are another source of convergence problems. It has been reported that complex multiphase flow introduces inflection points, which can be amplified by compositional changes, gravitational effects and capillarity. Advanced numerical techniques to improve the robustness of the nonlinear solver, such as Trust-Region-based methods, may provide a robust solution.

From the thermodynamic modelling point of view, improvements can be made in terms of computational efficiency and physical complexity of the mixtures. By utilizing a generalized selective solubility, which is in essence an extension of the augmented free-water flash concept to any phase, nonlinearity of solution procedures for the flash, as well as linear system sizes, can be significantly reduced. In addition, it opens up possibilities to efficiently handle complex

thermodynamics related to pure phases, hydrates, ions and aqueous chemistry to model bio- and geochemical processes.

Finally, with the option of OBL to use any state specification, it may be worth investigating if the simulation performs well with a volume-based formulation. Simulation of unsteady-state pipeline flow, for instance, is often solved using internal energy and volume. Most complex thermodynamic models, in the end, are formulated in terms of volume.

An outlook for modelling and understanding CO_2 sequestration processes

The path towards sustainable future relies heavily on safe and efficient usage of the subsurface. Given that the available data for exploration, operation and monitoring for any project is very limited, numerical simulation provides an important tool to understand the ongoing dynamics.

Numerical simulation of CO_2 sequestration, in particular, involves the modelling of complex physical processes at multiple scales. In order to gain an understanding of the physics, it is important to develop models that are able to reproduce observations from core-scale laboratory experiments and extrapolate their applicability to field-scale operations. Yet, on an intermediate scale, such as in the *FluidFlower*, it nonetheless proved to be challenging to capture all dynamics accurately, and such benchmark studies can help to advance in the right direction. Only when a converged solution to these problems is obtained, we can be sufficiently confident in our ability to design, monitor and intervene in such complex operations appropriately.

Furthermore, the ability to convincingly demonstrate to the public what subsurface processes look like by means of such benchmark studies will help to build trust and support pragmatic decision-making in the combat of climate change and energy security. While political pragmatism and economic incentives have not yet reached the desired urgency, the first field-scale pilots have been undertaken, technologies have started to mature, and, most of all, the time to make the right decisions to continue to support research and act appropriately is now.

Bibliography

[1] T. M. Lenton *et al. The Global Tipping Points Report 2025*. Tech. rep. University of Exeter, 2025. URL: https://global-tipping-points.org/resources-gtp/.

[2] K. Aziz and A. Settari. *Petroleum Reservoir Simulation*. Society of Petroleum Engineers, 1979. ISBN: 978-1-61399-964-6. URL: 10.2118/9781613999646.

[3] K. H. Coats. 'A Highly Implicit Steamflood Model'. In: *Advances in Water Resources* 18.5 (1978), pp. 369–383. DOI: 10.2118/6105-PA.

[4] K. H. Coats. 'An Equation of State Compositional Model'. In: *SPE Journal* 20.5 (1980), pp. 363–376. DOI: 10.2118/8284-PA.

[5] M. C. H. Chien, S. T. Lee and W. H. Chen. 'A new fully implicit compositional simulator'. In: *SPE Reservoir Simulation Symposium, Dallas, Texas*. 1985, SPE-13385–MS. DOI: 10.2118/13385-MS.

[6] M. C. H. Chien, H. E. Yardumian, E. Y. Chung and W. W. Todd. 'The Formulation of a Thermal Simulation Model in a Vectorized, General Purpose Reservoir Simulator'. In: *SPE Symposium on Reservoir Simulation, Houston, Texas*. 1989, SPE-18418–MS. DOI: 10.2118/18418-MS.

[7] K. M. Brantferger, G. A. Pope and K. Sepehrnoori. 'Development of a Thermodynamically Consistent, Fully Implicit, Equation-of-State, Compositional Steamflood Simulator'. In: SPE Reservoir Simulation Conference. Feb. 1991, SPE-21253–MS. DOI: 10.2118/21253-MS.

[8] W. W. Monroe, M. K. Silva, L. L. Larsen and F. M. Orr, Jr. 'Composition Paths in Four-Component Systems: Effect of Dissolved Methane on 1D CO_2 Flood Performance'. In: *SPE Res Eng* 5.3 (1990), pp. 423–432. DOI: 10.2118/16712-PA.

[9] R. Zaydullin, D. Voskov and H. Tchelepi. 'Nonlinear formulation based on an equation-of-state free method for compositional flow simulation'. In: *SPE Journal* 18.2 (2013), pp. 264–273. DOI: 10.2118/146989-PA.

[10] D. V. Voskov and H. A. Tchelepi. 'Comparison of nonlinear formulations for two-phase multi-component EoS based simulation'. In: *Journal of Petroleum Science and Engineering* 82 (2012), pp. 101–111. DOI: 10.1016/j.petrol.2011.10.012.

[11] J. R. Wallis, R. P. Kendall and T. E. Little. 'Constrained Residual Acceleration of Conjugate Residual Methods'. In: *SPE Reservoir Simulation Symposium*. 1985. DOI: 10.2118/13536-MS.

[12] Y. Saad and M. Schultz. 'A Generalized Minimal Residual Algorithm for Solving Nonsymmetric Linear Systems'. In: *SIAM Journal on Scientific and Statistical Computing* 7 (1986), pp. 856–869. DOI: 10.1137/0907058.

[13] D. Collins, L. Nghiem, Y.-K. Li and J. Grabenstetter. 'Efficient approach to adaptive-implicit compositional simulation with an equation of state'. In: *SPEJ* 7.2 (1992), pp. 259–264.

[14] H. Cao, H. A. Tchelepi, J. Wallis and H. Yardumian. 'Parallel Scalable Unstructured CPR-Type Linear Solver for Reservoir Simulation'. In: *SPE Annual Technical Conference and Exhibition, Dallas, Texas*. 2005, SPE-96809–MS. DOI: 10.2118/96809-MS.

[15] M. Heidari. 'Equation of State Based Thermal Compositional Reservoir Simulator for Hybrid Solvent/Thermal Processes'. PhD thesis. University of Calgary, 2014. URL: https://prism.ucalgary.ca/server/api/core/bitstreams/fe070bb5-8026-441f-acc6-742e7092837d/content.

[16] R. Zaydullin, D. Voskov and H. Tchelepi. 'Phase-state identification bypass method for three-phase thermal compositional simulation'. In: *Computational Geosciences* 20 (2016), pp. 461–474. DOI: 10.1007/s10596-015-9510-y.

[17] A. Settari and D. A. Walters. 'Advances in Coupled Geomechanical and Reservoir Modeling With Applications to Reservoir Compaction'. In: *SPE Journal* 6.3 (2001), pp. 334–342. DOI: 10.2118/74142-PA.

[18] T. T. Garipov, P. Tomin, R. Rin, D. V. Voskov and H. A. Tchelepi. 'Unified thermo-compositional-mechanical framework for reservoir simulation'. In: *SPE Journal* 22 (2018), pp. 1039–1057. DOI: 10.1007/s10596-018-9737-5.

[19] Y. Fan, L. J. Durlofsky and H. A. Tchelepi. 'A fully-coupled flow-reactive-transport formulation based on element conservation, with application to CO_2 storage simulations'. In: *Advances in Water Resources* 42 (2012), pp. 47–61. DOI: 10.1016/j.advwatres.2012.03.012.

[20] R. Zaydullin, D. Voskov, S. James, H. Henley and A. Lucia. 'Fully compositional and thermal reservoir simulation'. In: *Computers & Chemical Engineering* 63 (2014), pp. 51–65. DOI: 10.1016/j.compchemeng.2013.12.008.

[21] K. Kala and D. V. Voskov. 'Element balance formulation in reactive compositional flow and transport with parameterization technique'. In: *Computational Geosciences* 24.2 (2020), pp. 609–624. DOI: 10.1007/s10596-019-9828-y.

[22] C. M. Oldenburg. 'Joule-Thomson cooling due to CO_2 injection into natural gas reservoirs'. In: *Energy Conversion and Management* 48 (2007), pp. 1808–1815. DOI: 10.1016/j.enconman.2007.01.010.

[23] M. Aghajanloo, L. Yan, S. Berg, D. Voskov and R. Farajzadeh. 'Impact of CO_2 hydrates on injectivity during CO_2 storage in depleted gas fields: A literature review'. In: *Gas Science and Engineering* 123 (2024), p. 205250. DOI: 10.1016/j.jgsce.2024.205250.

[24] K. Pruess and N. Müller. 'Formation dry-out from CO_2 injection into saline aquifers: 1. Effects of solids precipitation and their mitigation'. In: *Water Resources Research* 45 (Mar. 2009), W03402. DOI: 10.1029/2008WR007101.

[25] K.-Y. Kim, W. S. Han, J. Oh, T. Kim and J.-C. Kim. 'Characteristics of Salt-Precipitation and the Associated Pressure Build-Up during CO_2 Storage in Saline Aquifers'. In: *Transport in Porous Media* 92 (Mar. 2011), pp. 397–418. DOI: 10.1007/s11242-011-9909-4.

[26] H. Cao. 'Development of techniques for general purpose simulators'. PhD thesis. Stanford University, Stanford, CA, 2002. URL: https://pangea.stanford.edu/ERE/pdf/pereports/PhD/Cao02.pdf.

[27] D. Voskov and H. Tchelepi. 'Compositional space parametrization for miscible displacement simulation'. In: *Transport in Porous Media* 75.1 (2008), pp. 111–128. DOI: 10.1007/s11242-008-9212-1.

[28] D. V. Voskov. 'Operator-based linearization approach for modeling of multiphase multi-component flow in porous media'. In: *Journal of Computational Physics* 337 (2017), pp. 275–288. DOI: 10.1016/j.jcp.2017.02.041.

[29] M. Khait and D. V. Voskov. 'Operator-based linearization for general purpose reservoir simulation'. In: *Journal of Petroleum Science and Engineering* 157 (2017), pp. 990–998. DOI: 10.1016/j.petrol.2017.08.009.

[30] M. Khait and D. V. Voskov. 'Adaptive parameterization for solving of thermal/compositional nonlinear flow and transport with buoyancy'. In: *SPE Journal* 23.02 (2018), pp. 522–534. DOI: 10.2118/182685-PA.

[31] Y. Wang, D. Voskov, M. Khait and D. Bruhn. 'An efficient numerical simulator for geothermal simulation: A benchmark study'. In: *Applied Energy* 264 (2020). DOI: 10.1016/j.apenergy.2020.114693.

[32] X. Lyu and D. Voskov. 'Advanced modeling of enhanced CO_2 dissolution trapping in saline aquifers'. In: *International Journal of Greenhouse Gas Control* 127 (2023), p. 103907. ISSN: 1750-5836. DOI: 10.1016/j.ijggc.2023.103907.

[33] D. Voskov *et al.* 'open Delft Advanced Research Terra Simulator (open-DARTS)'. In: *Journal of Open Source Software* 9.99 (2024), p. 6737. DOI: 10.21105/joss.06737.

[34] M. Muskat and J. M. McDowell. 'An Electrical Computer for Solving Phase Equilibrium Problems'. In: *Journal of Petroleum Technology* 1.11 (1949), pp. 291–298. DOI: 10.2118/949291-G.

[35] H. H. Rachford Jr. and J. D. Rice. 'Procedure for use of electronic digital computers in calculating flash vaporization hydrocarbon equilibrium'. In: *Petr. Trans. AIME* 195 (1952), pp. 327–328. DOI: 10.2118/952327-G.

[36] L. E. Baker, A. C. Pierce and K. D. Luks. 'Gibbs Energy Analysis of Phase Equilibria'. In: *SPE Journal* 22.5 (1982), pp. 731–742. DOI: 10.2118/9806-PA.

[37] M. L. Michelsen. 'The isothermal flash problem. Part I. Stability'. In: *Fluid Phase Equilibria* 9 (1982), pp. 1–19. DOI: 10.1016/0378-3812(82)85001-2.

[38] M. L. Michelsen. 'The isothermal flash problem. Part II. Phase split calculation'. In: *Fluid Phase Equilibria* 9 (1982), pp. 21–40. DOI: 10.1016/0378-3812(82)85002-4.

[39] M. L. Michelsen. 'Calculation of multiphase equilibrium'. In: *Computers & Chemical Engineering* 18.7 (1994), pp. 545–550. DOI: 10.1016/0098-1354(93)E0017-4.

[40] Y. Tang and S. Saha. 'An Efficient Method to Calculate Three-Phase Free-Water Flash for WaterHydrocarbon Systems'. In: *Industrial & Engineering Chemistry Research* 42.1 (2003), pp. 189–197. DOI: 10.1021/ie010785x.

[41] A. Lapene, D. V. Nichita, G. Debenest and M. Quintard. 'Three-phase free-water flash calculations using a new Modified Rachford-Rice equation'. In: *Fluid Phase Equilibria* 297.1 (2010), pp. 121–128. DOI: 10.1016/j.fluid.2010.06.018.

[42] D. V. Nichita. 'Fast and robust phase stability testing at isothermal-isochoric conditions'. In: *Fluid Phase Equilibria* 447 (2017), pp. 107–124. DOI: 10.1016/j.fluid.2017.05.022.

[43] D. V. Nichita. 'New unconstrained minimization methods for robust flash calculations at temperature, volume and moles specifications'. In: *Fluid Phase Equilibria* 466 (2018), pp. 31–47. DOI: 10.1016/j.fluid.2018.03.012.

[44] M. L. Michelsen. 'Multiphase isenthalpic and isentropic flash algorithms'. In: *Fluid Phase Equilibria* 33 (1987), pp. 13–27. DOI: 10.1016/0378-3812(87)87002-4.

[45] M. L. Michelsen. 'State function based flash specifications'. In: *Fluid Phase Equilibria* 158-160 (1999), pp. 617–626. DOI: 10.1016/S0378-3812(99)00092-8.

[46] R. Agarwal, Y. Li, L. Nghiem and D. Coombe. 'Multiphase Multicomponent Isenthalpic Flash Calculations'. In: *Journal of Canadian Petroleum Technology* 30.03 (1991), pp. 69–75. DOI: 10.2118/91-03-07.

[47] L. Xu, A. Moncorgé and D. V. Nichita. 'Efficient nested three-phase isenthalpic flash calculations with a hybrid Newton and Brent algorithm for water-CO_2-hydrocarbon mixtures in CO_2 storage simulations'. In: *Chemical Engineering Science* 308 (2025), p. 121379. DOI: 10.1016/j.ces.2025.121379.

[48] N. Nagarajan, A. Cullick and A. Griewank. 'New strategy for phase equilibrium and critical point calculations by thermodynamic energy analysis. Part I. Stability analysis and flash'. In: *Fluid Phase Equilibria* 62.3 (1991), pp. 191–210. DOI: 10.1016/0378-3812(91)80010-S.

[49] D. V. Nichita. 'A volume-based approach to phase equilibrium calculations at pressure and temperature specifications'. In: *Fluid Phase Equilibria* 461 (2018), pp. 70–83. DOI: 10.1016/j.fluid.2017.12.021.

[50] H. Sun, A. Raghavan, K. Haugen and S. Chempath. 'An improved isenthalpic flash algorithm based on maximization of entropy'. In: *Fluid Phase Equilibria* 438 (2017), pp. 18–28. DOI: 10.1016/j.fluid.2017.01.007.

[51] D. Paterson, W. Yan, M. L. Michelsen and E. H. Stenby. 'Multiphase isenthalpic flash: General approach and its adaptation to thermal recovery of heavy oil'. In: *Advances in Chemical Engineering* 65.1 (2019), pp. 281–293. DOI: 10.1002/aic.16371.

[52] D. V. Nichita. 'A unified presentation of phase stability analysis including all major specifications'. In: *Fluid Phase Equilibria* 578 (2024), p. 113990. DOI: 10.1016/j.fluid.2023.113990.

[53] M. Petitfrere and D. Nichita. 'Robust and efficient trust-region based stability analysis and multiphase flash calculations'. In: *Fluid Phase Equilibria* 362 (2014), pp. 51–68. DOI: 10.1016/j.fluid.2013.08.039.

[54] **M. Wapperom**, D. Voskov and J. D. dos Santos Heringer. *open DARTS-flash*. Version 0.12.0. Mar. 2026. DOI: 10.5281/zenodo.18923584.

[55] A. Münster. *Classical Thermodynamics*. 1st ed. Wiley Interscience, 1970.

[56] M. L. Michelsen and J. M. Mollerup. *Thermodynamic Models: Fundamentals & Computational Aspects*. 2nd ed. Holte, Denmark: Tie-Line Publications, 2007.

[57] P. H. van Konynenburg and R. L. Scott. 'Critical lines and phase equilibria in binary van der Waals mixtures'. In: *Philosophical Transactions of the Royal Society of London A* 298.1442 (1980), pp. 495–540. DOI: 10.1098/rsta.1980.0266.

[58] M. Cismondi and M. L. Michelsen. 'Global phase equilibrium calculations: Critical lines, critical end points and liquidliquidvapour equilibrium in binary mixtures'. In: *The Journal of Supercritical Fluids* 39.3 (2007), pp. 287–295. DOI: 10.1016/j.supflu.2006.03.011.

[59] R. Privat and J.-N. Jaubert. 'Classification of global fluid-phase equilibrium behaviors in binary systems'. In: *Chemical Engineering Research and Design* 91.10 (2013), pp. 1807–1839. DOI: 10.1016/j.cherd.2013.06.026.

[60] D.-Y. Peng and D. B. Robinson. 'A rigorous method for predicting the critical properties of multicomponent systems from an equation of state'. In: *AIChE Journal* 23.2 (1977), pp. 137–144. DOI: 10.1002/aic.690230202.

[61] L. E. Baker and K. D. Luks. 'Critical Point and Saturation Pressure Calculations for Multipoint Systems'. In: *SPE Journal* 20.1 (1980), pp. 15–24. DOI: 10.2118/7478-PA.

[62] R. A. Heidemann and A. M. Khalil. 'The calculation of critical points'. In: *AIChE Journal* 26.5 (1980), pp. 769–779. DOI: 10.1002/aic.690260510.

[63] M. L. Michelsen. 'Calculation of critical points and phase boundaries in the critical region'. In: *Fluid Phase Equilibria* 16 (1984), pp. 57–76. DOI: 10.1016/0378-3812(84)85021-9.

[64] M. L. Michelsen and R. A. Heidemann. 'Calculation of tri-critical points'. In: *Fluid Phase Equilibria* 39.1 (1988), pp. 53–74. DOI: 10.1016/0378-3812(88)80003-7.

[65] E. W. Lemmon, I. H. Bell, M. L. Huber and M. O. McLinden. 'Thermophysical Properties of Fluid Systems'. In: *NIST Standard Reference Database Number 69*. Gaithersburg (MD): National Institute of Standards and Technology, 2022. DOI: 10.18434/T4D303.

[66] C. A. Passut and R. P. Danner. 'Correlation of Ideal Gas Enthalpy, Heat Capacity and Entropy'. In: *Industrial & Engineering Chemistry Process Design and Development* 11.4 (1972), pp. 543–546. DOI: 10.1021/i260044a016.

[67] F. A. Aly and L. L. Lee. 'Self-consistent equations for calculating the ideal gas heat capacity, enthalpy, and entropy'. In: *Fluid Phase Equilibria* 6.3-4 (1981), pp. 169–179. DOI: 10.1016/0378-3812(81)85002-9.

[68] M. L. Michelsen and J. M. Mollerup. 'Partial derivatives of thermodynamic properties'. In: *AIChE Journal* 32.8 (1986), pp. 1389–1392. DOI: 10.1002/aic.690320818.

[69] J. M. Mollerup and M. L. Michelsen. 'Calculation of thermodynamic equilibrium properties'. In: *Fluid Phase Equilibria* 74 (1992), pp. 1–15. DOI: 10.1016/0378-3812(92)85049-E.

[70] J. Prausnitz, E. Gomes de Azevedo and R. Lichtenthaler. *Molecular Thermodynamics of Fluid-Phase Equilibria*. 3rd ed. New Jersey: Pearson, 1998.

[71] G. Soave. 'Equilibrium constants from a modified Redlich-Kwong equation of state'. In: *Chemical Engineering Science* 27 (1972), pp. 1197–1203. DOI: 10.1016/0009-2509(72)80096-4.

[72] D.-Y. Peng and D. B. Robinson. 'A new two-constant equation of state'. In: *Ind. Eng. Chem., Fundam.* 15.1 (1976), pp. 59–64. DOI: 10.1021/i160057a011.

[73] L. Lundgaard and J. M. Mollerup. 'The influence of gas phase fugacity and solubility on correlation of gas-hydrate formation pressure'. In: *Fluid Phase Equilibria* 70.2-3 (1991), pp. 199–213. DOI: 10.1016/0378-3812(91)85034-R.

[74] I. Søreide and C. H. Whitson. 'Peng-Robinson predictions for hydrocarbons, CO_2, N_2, and H_2S with pure water and NaCl brine'. In: *Fluid Phase Equilibria* 77 (1992), pp. 217–240. DOI: 10.1016/0378-3812(92)85105-H.

[75] S. Michel, H. H. Hooper and J. M. Prausnitz. 'Mutual solubilities of water and hydrocarbons from an equation of state. Need for an unconventional mixing rule'. In: *Fluid Phase Equilibria* 45.2-3 (1989), pp. 173–189. DOI: 10.1016/0378-3812(89)80256-0.

[76] M. S. Wertheim. 'Fluids with highly directional attractive forces. I. Statistical thermodynamics'. In: *Journal of Statistical Physics* 35.1-2 (1984), pp. 19–34. DOI: 10.1007/BF01017362.

[77] W. G. Chapman, K. E. Gubbins, G. Jackson and M. Radosz. 'SAFT: Equation-of-State Solution Model for Associating Fluids'. In: *Fluid Phase Equilibria* 52 (1989), pp. 31–38. DOI: 10.1016/0378-3812(89)80308-5.

[78] W. G. Chapman, K. E. Gubbins, G. Jackson and M. Radosz. 'New reference equation of state for associating liquids'. In: *Industrial and Engineering Chemistry Research* 29.8 (1990), pp. 1709–1721. DOI: 10.1021/ie00104a021.

[79] G. M. Kontogeorgis, E. C. Voutsas, I. V. Yakoumis and D. P. Tassios. 'An Equation of State for Associating Fluids'. In: *Industrial & Engineering Chemistry Research* 35.11 (1996), pp. 4310–4318. DOI: 10.1021/ie9600203.

[80] G. M. Kontogeorgis and G. K. Folas. *Thermodynamic Models for Industrial Applications: From Classical and Advanced Mixing Rules to Association Theories*. 2009. DOI: 10.1002/9780470747537.

[81] M. L. Michelsen and E. M. Hendriks. 'Physical properties from association models'. In: *Fluid Phase Equilibria* 180.1-2 (2001), pp. 165–174. DOI: 10.1016/S0378-3812(01)00344-2.

[82] M. L. Michelsen. 'Robust and Efficient Solution Procedures for Association Models'. In: *Industrial and Engineering Chemistry Research* 45 (2006), pp. 8449–8453. DOI: 10.1021/ie060029x.

[83] Y.-K. Li and L. X. Nghiem. 'Phase Equilibria of Oil, Gas and Water/Brine Mixtures from a Cubic Equation of State and Henrys Law'. In: *Canadian Journal of Chemical Engineering* 64.3 (1986), pp. 486–496. DOI: 10.1002/cjce.5450640319.

[84] J. D. van der Waals. ‘Over de continuïteit van den gas- en vloeistoftoestand’. PhD thesis. University of Leiden, 1873. URL: http://hdl.handle.net/1887.1/item:3669504.

[85] O. Redlich and J. N. S. Kwong. ‘On the Thermodynamics of Solutions. V. An Equation of State. Fugacities of Gaseous Solutions’. In: *Chemical Reviews* 44.1 (1949), pp. 233–244. DOI: 10.1021/cr60137a013.

[86] O. Pfohl. ‘Letter to the editor: evaluation of an improved volume translation for the prediction of hydrocarbon volumetric properties’. In: *Fluid Phase Equilibria* 163 (1999), pp. 157–159. DOI: 10.1016/S0378-3812(99)00199-5.

[87] R. Privat and J.-N. Jaubert. ‘The state of the art of cubic equations of state with temperature-dependent binary interaction coefficients: From correlation to prediction’. In: *Fluid Phase Equilibria* 567 (2023), p. 113697. DOI: 10.1016/j.fluid.2022.113697.

[88] J. McNamee and V. Pan. ‘Chapter 12 - Low-Degree Polynomials’. In: *Numerical Methods for Roots of Polynomials - Part II*. Ed. by J. McNamee and V. Pan. Vol. 16. Studies in Computational Mathematics. Elsevier, 2013, pp. 527–556. DOI: 10.1016/B978-0-444-52730-1.00006-0.

[89] U. K. Deiters and R. Macías-Salinas. ‘Calculation of Densities from Cubic Equations of State: Revisited’. In: *Industrial and Engineering Chemistry Research* 53 (2014), pp. 2529–2536. DOI: 10.1021/ie4038664.

[90] A. R. Imre and T. Kraska. ‘Stability limits in binary fluids mixtures’. In: *Journal of Chemical Physics* 122 (2005), p. 064507. DOI: 10.1063/1.1847651.

[91] R. S. Kamath, L. T. Biegler and I. E. Grossmann. ‘An equation-oriented approach for handling thermodynamics based on cubic equation of state in process optimization’. In: *Computers & Chemical Engineering* 34 (2010), pp. 2085–2096. DOI: 10.1016/j.compchemeng.2010.07.028.

[92] D. V. Nichita, D. Broseta and F. Montel. ‘Calculation of convergence pressure/temperature and stability test limit loci of mixtures with cubic equations of state’. In: *Fluid Phase Equilibria* 261 (2007), pp. 176–184. DOI: 10.1016/j.fluid.2007.07.041.

[93] A. Iranshahr, D. Voskov and H. Tchelepi. ‘A negative-flash tie-simplex approach for multiphase reservoir simulation’. In: *SPE Journal* 18.6 (2013), pp. 1140–1149. DOI: 10.2118/141896-PA.

[94] A. Péneloux, E. Rauzy and R. Fréze. ‘A consistent correction for Redlich-Kwong-Soave volumes’. In: *Fluid Phase Equilibria* 8.1 (1982), pp. 7–23. DOI: 10.1016/0378-3812(82)80002-2.

[95] J.-N. Jaubert, R. Privat, Y. L. Guennec and L. Coniglio. ‘Note on the properties altered by application of a Pénelouxtype volume translation to an equation of state’. In: *Fluid Phase Equilibria* 419 (2016), pp. 88–95. DOI: 10.1016/j.fluid.2016.03.012.

[96] G. M. Wilson. ‘Vapor-Liquid Equilibrium. XI. A New Expression for the Excess Free Energy of Mixing’. In: *Journal of the American Chemical Society* 86.2 (1964), pp. 127–130. DOI: 10.1021/ja01056a002.

[97] H. Renon and J. M. Prausnitz. ‘Local compositions in thermodynamic excess functions for liquid mixtures’. In: *AIChE Journal* 14.1 (1968), pp. 135–144. DOI: 10.1002/aic.690140124.

[98] D. S. Abrams and J. M. Prausnitz. ‘Statistical thermodynamics of liquid mixtures: A new expression for the excess Gibbs energy of partly or completely miscible systems’. In: *AIChE Journal* 21.1 (1975), pp. 116–128. DOI: 10.1002/aic.690210115.

[99] A. Fredenslund, R. L. Jones and J. M. Prausnitz. ‘Group-contribution estimation of activity coefficients in nonideal liquid mixtures’. In: *AIChE Journal* 21.6 (1975), pp. 1086–1099. DOI: 10.1002/aic.690210607.

[100] M.-J. Huron and J. Vidal. ‘New mixing rules in simple equations of state for representing vapour-liquid equilibria of strongly non-ideal mixtures’. In: *Fluid Phase Equilibria* 3.4 (1979), pp. 255–271. DOI: 10.1016/0378-3812(79)80001-1.

[101] J. Mollerup. ‘A note on the derivation of mixing rules from excess Gibbs energy models’. In: *Fluid Phase Equilibria* 25.3 (1986), pp. 323–327. DOI: 10.1016/0378-3812(86)80007-3.

[102] M. L. Michelsen. ‘A method for incorporating excess Gibbs energy models in equations of state’. In: *Fluid Phase Equilibria* 60.1-2 (1990), pp. 47–58. DOI: 10.1016/0378-3812(90)85042-9.

[103] M. L. Michelsen. ‘A modified Huron-Vidal mixing rule for cubic equations of state’. In: *Fluid Phase Equilibria* 60.1-2 (1990), pp. 213–219. DOI: 10.1016/0378-3812(90)85053-D.

[104] S. Dahl and M. L. Michelsen. ‘High-pressure vapor-liquid equilibrium with a UNIFAC-based equation of state’. In: *AIChE Journal* 36.12 (1990), pp. 1829–1836. DOI: 10.1002/aic.690361207.

[105] S. Dahl, A. Fredenslund and P. Rasmussen. ‘The MHV2 model: a UNIFAC-based equation of state model for prediction of gas solubility and vapor-liquid equilibria at low and high pressures’. In: *Industrial & Engineering Chemistry Research* 30.8 (1991), pp. 1936–1945. DOI: 10.1021/ie00056a041.

[106] D. S. H. Wong and S. I. Sandler. ‘A theoretically correct mixing rule for cubic equations of state’. In: *AIChE Journal* 38.5 (1992), pp. 671–680. DOI: 10.1002/aic.690380505.

[107] R. Privat, J.-N. Jaubert and G. M. Kontogeorgis. ‘Let us rethink advanced mixing rules for cubic equations of state’. In: *Fluid Phase Equilibria* 596 (2025), p. 114455. DOI: 10.1016/j.fluid.2025.114455.

[108] G. M. Kontogeorgis, R. Privat and J.-N. Jaubert. 'Taking Another Look at the van der Waals Equation of StateAlmost 150 Years Later'. In: *Journal of Chemical & Engineering Data* 64.11 (2019), pp. 4619–4637. DOI: 10.1021/acs.jced.9b00264.

[109] A. Lucia. 'A Multiscale Gibbs-Helmholtz Constrained Cubic Equation of State'. In: *Journal of Thermodynamics* (2010), p. 238365. DOI: 10.1155/2010/238365.

[110] A. Lucia. 'Thermodynamic consistency of the multi-scale GibbsHelmholtz constrained equation of state'. In: *Chemical Engineering Research and Design* 91.9 (2013), pp. 1748–1759. DOI: 10.1016/j.cherd.2013.03.009.

[111] Z. Ziabakhsh-Ganji and H. Kooi. 'An Equation of State for thermodynamic equilibrium of gas mixtures and brines to allow simulation of the effects of impurities in subsurface CO_2 storage'. In: *International Journal of Greenhouse Gas Control* 11S (2012), S21–S34. DOI: 10.1016/j.ijggc.2012.07.025.

[112] N. N. Akinfiev and L. W. Diamond. 'Thermodynamic description of aqueous nonelectrolytes at infinite dilution over a wide range of state parameters'. In: *Geochimica et Cosmochimica Acta* 67.4 (2003), pp. 613–629. DOI: 10.1016/S0016-7037(02)01141-9.

[113] Z. Duan, N. Møller, J. Greenberg and J. H. Weare. 'The prediction of methane solubility in natural waters to high ionic strength from 0 to 250 C and from 0 to 1600 bar'. In: *Geochimica et Cosmochimica Acta* 56.4 (1992), pp. 1451–1460. DOI: 10.1016/0016-7037(92)90215-5.

[114] K. S. Pitzer. 'Thermodynamics of electrolytes. I. Theoretical basis and general equations'. In: *Journal of Physical Chemistry* 77.2 (1973), pp. 268–277. DOI: 10.1021/j100621a026.

[115] M. D. Jager, A. L. Ballard and E. D. Sloan, Jr. 'The next generation of hydrate prediction II. Dedicated aqueous phase fugacity model for hydrate prediction'. In: *Fluid Phase Equilibria* 211 (2003), pp. 85–107. DOI: 10.1016/S0378-3812(03)00155-9.

[116] M. Zirrahi, R. Azin, H. Hassanzadeh and M. Moshfeghian. 'Mutual solubility of CH_4, CO_2, H_2S, and their mixtures in brine under subsurface disposal conditions'. In: *Fluid Phase Equilibria* 324 (2012), pp. 80–93. DOI: 10.1016/j.fluid.2012.03.017.

[117] N. Spycher, K. Pruess and J. Ennis-King. 'CO_2-H_2O mixtures in the geological sequestration of CO_2. I. Assessment and calculation of mutual solubilities from 12 to 100°C and up to 600 bar'. In: *Geochimica et Cosmochimica Acta* 67.16 (2003), pp. 3015–3031. DOI: 10.1016/S0016-7037(03)00273-4.

[118] Z. Duan and R. Sun. 'An improved model calculating CO_2 solubility in pure water and aqueous NaCl solutions from 273 to 533 K and from 0 to 2000 bar'. In: *Chemical Geology* 193.3–4 (2003), pp. 257–271. DOI: 10.1016/S0009-2541(02)00263-2.

[119] A. L. Ballard and E. D. Sloan, Jr. 'The next generation of hydrate prediction: an overview'. In: *Journal of Supramolecular Chemistry* 2.4–5 (2002), pp. 385–392. DOI: 10.1016/S1472-7862(03)00063-7.

[120] K. S. Pitzer, J. C. Peiper and R. H. Busey. 'Thermodynamic Properties of Aqueous Sodium Chloride Solutions'. In: *Journal of Physical and Chemical Reference Data* 13.1 (1984), pp. 1–102. DOI: 10.1063/1.555709.

[121] D. Koschel, J.-Y. Coxam, L. Rodier and V. Majer. 'Enthalpy and solubility data of CO_2 in water and NaCl (aq) at conditions of interest for geological sequestration'. In: *Fluid Phase Equilibria* 247 (2006), pp. 107–120. DOI: 10.1016/j.fluid.2006.06.006.

[122] E. D. Sloan, Jr. *Clathrate Hydrates of Natural Gases*. 2nd ed. New York: Marcel Dekker, Inc., 1998.

[123] J. H. Van der Waals and J. C. Platteeuw. 'Clathrate solutions'. In: *Advances in Chemical Physics* 2 (1958). DOI: 10.1002/9780470143483.ch1.

[124] F. de Azevedo Medeiros, I. S. V. Segtovich, F. W. Tavares and A. K. Sum. 'Sixty Years of the van der Waals and Platteeuw Model for Clathrate HydratesA Critical Review from Its Statistical Thermodynamic Basis to Its Extensions and Applications'. In: *Chemical Reviews* 120.24 (2020), pp. 13349–13381. DOI: 10.1021/acs.chemrev.0c00494.

[125] W. R. Parrish and J. M. Prausnitz. 'Dissociation Pressures of Gas Hydrates Formed by Gas Mixtures'. In: *Industrial & Engineering Chemistry Process Design and Development* 11.1 (1972), pp. 26–35. DOI: 10.1021/i260041a006.

[126] J. B. Klauda and S. I. Sandler. 'A Fugacity Model for Gas Hydrate Phase Equilibria'. In: *Industrial and Engineering Chemistry Research* 39.9 (2000), pp. 3377–3386. DOI: 10.1021/ie000322b.

[127] A. L. Ballard and E. D. Sloan, Jr. 'The next generation of hydrate prediction I. Hydrate standard states and incorporation of spectroscopy'. In: *Fluid Phase Equilibria* 194-197 (2002), pp. 371–383. DOI: 10.1016/S0378-3812(01)00697-5.

[128] J. Munck, S. Skjold-Jørgensen and P. Rasmussen. 'Computations of the formation of gas hydrates'. In: *Chemical Engineering Science* 43.10 (1988), pp. 2661–2672. DOI: 10.1016/0009-2509(88)80010-1.

[129] M. D. Jager, A. L. Ballard and E. D. Sloan, Jr. 'Comparison between experimental data and aqueous-phase fugacity model for hydrate prediction'. In: *Fluid Phase Equilibria* 232 (2005), pp. 25–36. DOI: 10.1016/j.fluid.2005.02.011.

[130] W. A. Cole and S. P. Goodwin. 'Flash calculations for gas hydrates: a rigorous approach'. In: *Chemical Engineering Science* 45.3 (1990), pp. 569–573. DOI: 10.1016/0009-2509(90)87001-9.

[131] M. L. Michelsen. 'Calculation of hydrate fugacities'. In: *Chemical Engineering Science* 46.4 (1991), pp. 1192–1193. DOI: 10.1016/0009-2509(91)85113-C.

[132] R. P. Brent. 'An Algorithm with Guaranteed Convergence for Finding a Zero of a Function'. In: *The Computer Journal* 14.4 (1971), pp. 422–425. DOI: 10.1093/comjnl/14.4.422.

[133] M. Petitfrere and D. Nichita. 'A comparison of conventional and reduction approaches for phase equilibrium calculations'. In: *Fluid Phase Equilibria* 386 (2015), pp. 30–46. DOI: 10.1016/j.fluid.2014.11.017.

[134] R. A. Heidemann and M. L. Michelsen. 'Instability of Successive Substitution'. In: *Industrial & Chemical Engineering Research* 34.3 (1995), pp. 958–966. DOI: 10.1021/ie00042a032.

[135] M. Petitfrere and D. Nichita. 'Phase stability analysis using a reduction method'. In: *Fluid Phase Equilibria* 358 (2013), pp. 27–39. DOI: 10.1016/j.fluid.2013.08.006.

[136] P. Gill and W. Murray. 'Newton-type Methods for Linearly Constrained Optimization'. In: *Numerical Methods for Constrained Optimization*. Ed. by P. Gill and W. Murray. London: Academic Press, 1974.

[137] C. H. Whitson and M. L. Michelsen. 'The negative flash'. In: *Fluid Phase Equilibria* 53 (1989), pp. 51–71. DOI: 10.1016/0378-3812(89)80072-X.

[138] D. V. Nichita and C. F. Leibovici. 'A rapid and robust method for solving the Rachford-Rice equation using convex transformations'. In: *Fluid Phase Equilibria* 353 (2013), pp. 38–49. DOI: 10.1016/j.uid.2013.05.030.

[139] D. V. Nichita and C. F. Leibovici. 'Improved solution windows for the resolution of the Rachford-Rice equation'. In: *Fluid Phase Equilibria* 452 (2017), pp. 69–73. DOI: 10.1016/j.fluid.2017.08.020.

[140] A. Iranshahr, D. Voskov and H. A. Tchelepi. 'Generalized negative-flash method for multiphase multicomponent systems'. In: *Fluid Phase Equilibria* 299 (2010), pp. 272–284. DOI: 10.1016/j.uid.2010.09.022.

[141] Z. Li and A. Firoozabadi. 'Initialization of phase fractions in Rachford-Rice equations for robust and efficient three-phase split calculation'. In: *Fluid Phase Equilibria* 332 (2012), pp. 21–27. DOI: 10.1016/j.uid.2012.06.021.

[142] C. F. Leibovici and D. V. Nichita. 'A new look at multiphase Rachford-Rice equations for negative ashes'. In: *Fluid Phase Equilibria* 267 (2008), pp. 127–132. DOI: 10.1016/j.uid.2008.03.006.

[143] R. Okuno, R. T. T. Johns and K. Sepehrnoori. 'A New Algorithm for Rachford-Rice for Multiphase Compositional Simulation'. In: *SPE Journal* 15.02 (2010), pp. 313–325. DOI: 10.2118/117752-PA.

[144] W. Yan and E. H. Stenby. 'On multiphase negative ash for ideal solutions'. In: *Fluid Phase Equilibria* 322-323 (2012), pp. 41–47. DOI: 10.1016/j.uid.2012.03.004.

[145] M. Petitfrere and D. Nichita. 'Multiphase equilibrium calculations using a reduction method'. In: *Fluid Phase Equilibria* 401 (2015), pp. 110–126. DOI: 10.1016/j.fluid.2015.05.006.

[146] M. Petitfrere and D. Nichita. 'On a choice of independent variables in Newton iterations for multiphase flash calculations'. In: *Fluid Phase Equilibria* 427 (2016), pp. 147–151. DOI: 10.1016/j.fluid.2016.06.050.

[147] D. V. Nichita and C. F. Leibovici. 'Calculation of Joule-Thomson inversion curves for two-phase mixtures'. In: *Fluid Phase Equilibria* 246.1-2 (2006), pp. 167–176. DOI: 10.1016/j.fluid.2006.05.025.

[148] C. F. Leibovici and J. Neoschil. 'A solution of Rachford-Rice equations for multiphase systems'. In: *Fluid Phase Equilibria* 112 (1995), pp. 217–221. DOI: 10.1016/0378-3812(95)02797-I.

[149] A. Iranshahr, D. Voskov and H. Tchelepi. 'Tie-simplex based compositional space parameterization: Continuity and generalization to multiphase systems'. In: *AIChE Journal* 59.5 (2013), pp. 1684–1701. DOI: 10.1002/aic.13919.

[150] H. Li. *Multiphase Equilibria of Complex Reservoir Fluids: An Equation of State Modeling Approach*. 1st ed. Petroleum Engineering. Cham, Switzerland: Springer, 2021. DOI: 10.1007/978-3-030-87440-7.

[151] G. M. Wilson. 'Vapor-Liquid Equilibria, Correlation by Means of a Modified Redlich-Kwong Equation of State'. In: *Advances in Cryogenic Engineering* 9 (1964), pp. 168–176. DOI: 10.1007/978-1-4757-0525-6_21.

[152] Z. Li and A. Firoozabadi. 'General Strategy for Stability Testing and Phase-Split Calculation in Two and Three Phases'. In: *SPE Journal* 17.04 (2012), pp. 1097–1107. DOI: 10.2118/129844-PA.

[153] A. Iranshahr, D. Voskov and H. Tchelepi. 'Gibbs energy analysis: Compositional tie-simplex space'. In: *Fluid Phase Equilibria* 321 (2012), pp. 49–58. DOI: 10.1016/j.fluid.2012.02.001.

[154] G. Huang *et al.* 'A novel method to accelerate the three-phase flash calculation of the hydrocarbon-CO_2 system'. In: *Fluid Phase Equilibria* 585 (2024), p. 114127. DOI: 10.1016/j.fluid.2024.114127.

[155] J. Heringer, **M. Wapperom**, C. Secuianu, D. Voskov and D. V. Nichita. 'New initialization procedures from phase stability testing in three-phase flash calculations for CO_2-hydrocarbon mixtures'. In: *Fluid Phase Equilibria* 604 (2026), p. 114653. DOI: 10.1016/j.fluid.2025.114653.

[156] J. Heringer, **M. Wapperom**, C. Secuianu, D. Voskov and D. V. Nichita. 'A robust and efficient augmented free-water flash method for CO_2-water-hydrocarbon mixtures'. In: *Fluid Phase Equilibria* 594 (2025), p. 114378. DOI: 10.1016/j.fluid.2025.114378.

[157] C. P. Rasmussen, K. Krejbjerg, M. L. Michelsen and K. E. Bjurstrøm. 'Increasing the Computational Speed of Flash Calculations With Applications for Compositional, Transient Simulations'. In: *SPE Reservoir Evaluation & Engineering* 9.1 (2006), pp. 32–38. DOI: 10.2118/84181-PA.

[158] D. Zhu and R. Okuno. 'A robust algorithm for isenthalpic flash of narrow-boiling fluids'. In: *Fluid Phase Equilibria* 379 (2014), pp. 26–51. DOI: 10.1016/j.fluid.2014.07.003.

[159] K. Tödheide and E. U. Franck. 'Das Zweiphasengebiet und die kritische Kurve im System KohlendioxidWasser bis zu Drucken von 3500 bar'. In: *Zeitschrift für Physikalische Chemie* 37.5-6 (1963), pp. 387–401. DOI: 10.1524/zpch.1963.37.5_6.387.

[160] J. Qin, R. J. Rosenbauer and Z. Duan. 'Experimental Measurements of Vapor-Liquid Equilibria of the H_2O+CO_2+CH_4 Ternary System'. In: *Journal of Chemical & Engineering Data* 53.6 (2008), pp. 1246–1249. DOI: 10.1021/je700473e.

[161] S. S.-S. Huang, A.-D. Leu, H.-J. Ng and D. B. Robinson. 'The phase behavior of two mixtures of methane, carbon dioxide, hydrogen sulfide, and water'. In: *Fluid Phase Equilibria* 19.1-2 (1985), pp. 21–32. DOI: 10.1016/0378-3812(85)85033-0.

[162] V. Savary *et al.* 'The solubility of CO_2+H_2S mixtures in water and 2 M NaCl at 120 C and pressures up to 35 MPa'. In: *International Journal of Greenhouse Gas Control* 10 (2012), pp. 123–133. DOI: 10.1016/j.ijggc.2012.05.021.

[163] A. Moncorgé, M. Petitfrère and S. Thibeau. 'Complete Equation of State Thermal Formulation for Simulation of CO_2 Storage'. In: *SPE Journal* 27.1 (2022), pp. 914–928. DOI: 10.2118/205447-PA.

[164] X. Chen, S. E. Gillespie, J. L. Oscarson and R. M. Izatt. 'Calorimetric determination of thermodynamic quantities for chemical reactions in the system CO_2-NaOH-H_2O from 225 to 325°C'. In: *Journal of Solution Chemistry* 21 (1992), pp. 825–848. DOI: 10.1007/BF00651511.

[165] W. Wagner and A. PruSS. 'The IAPWS Formulation 1995 for the Thermodynamic Properties of Ordinary Water Substance for General and Scientific Use'. In: *Journal of Physical and Chemical Reference Data* 31 (2002), pp. 387–535. DOI: 10.1063/1.1461829.

[166] D. Zhu and R. Okuno. 'Robust Isenthalpic Flash for Multiphase Water/Hydrocarbon Mixtures'. In: *SPE Journal* 20.6 (2015), pp. 1350–1365. DOI: 10.2118/170092-PA.

[167] X. Lyu, M. Khait and D. Voskov. 'Operator-Based Linearization Approach for Modelling of Multiphase Flow with Buoyancy and Capillarity'. In: *SPE Journal* (2021), pp. 1–18. DOI: 10.2118/205378-PA.

[168] S. Garg and J. Pritchett. 'On pressure-work, viscous dissipation and the energy balance relation for geothermal reservoirs'. In: *Advances in Water Resources* 1.1 (1977), pp. 41–47. DOI: 10.1016/0309-1708(77)90007-0.

[169] C. R. Faust and J. W. Mercer. 'Geothermal reservoir simulation: 1. Mathematical models for liquid- and vapor-dominated hydrothermal systems'. In: *Water Resources Research* 15.1 (1979), pp. 23–30. DOI: 10.1029/WR015i001p00023.

[170] G. F. Pinder. *State-of-the-art review of geothermal reservoir modelling*. Tech. rep. Lawrence Berkeley Laboratory, California University, Berkeley (USA), 1979. DOI: 10.2172/5606003.

[171] J. R. Appleyard, I. M. Cheshire and R. Pollard. 'Special techniques for fully implicit simulators'. In: *European Symposium on Enhanced Oil Recovery, Bournemouth, England*. 1981, pp. 395–408.

[172] J. R. Appleyard and I. M. Cheshire. 'The Cascade Method for Accelerated Convergence in Implicit Simulators'. In: *European Petroleum Conference, London, United Kingdom*. 1982. DOI: 10.2118/12804-MS.

[173] P. Jenny, H. A. Tchelepi and S. H. Lee. 'Unconditionally convergent nonlinear solver for hyperbolic conservation laws with S-shaped flux functions'. In: *Journal of Computational Physics* 228.20 (2009), pp. 7497–7512. DOI: 10.1016/j.jcp.2009.06.032.

[174] X. Wang and H. A. Tchelepi. 'Trust-region based solver for nonlinear transport in heterogeneous porous media'. In: *Journal of Computational Physics* 253 (2013), pp. 114–137. DOI: 10.1016/j.jcp.2013.06.041.

[175] B. Li and H. A. Tchelepi. 'Nonlinear analysis of multiphase transport in porous media in the presence of viscous, buoyancy, and capillary forces'. In: *Journal of Computational Physics* 297 (2015), pp. 104–131. DOI: 10.1016/j.jcp.2015.04.057.

[176] M. A. Grant and M. L. Sorey. 'The compressibility and hydraulic diffusivity of a water-steam flow'. In: *Water Resources Research* 15.3 (1979), pp. 684–686. DOI: 10.1029/WR015i003p00684.

[177] M. Connolly. 'An isenthalpic-based compositional framework for nonlinear thermal simulation'. PhD thesis. Stanford University, Stanford, CA, 2018. URL: https://purl.stanford.edu/vr209gh5661.

[178] L. Høier and C. H. Whitson. 'Compositional Grading Theory and Practice'. In: *SPE Reservoir Evaluation & Engineering* 4.6 (2001), pp. 525–535. DOI: 10.2118/74714-PA.

[179] A. A. Shapiro and E. H. Stenby. 'Kelvin equation for a non-ideal multicomponent mixture'. In: *Fluid Phase Equilibria* 134.1-2 (1997), pp. 87–101. DOI: 10.1016/S0378-3812(97)00045-9.

[180] A. A. Shapiro and E. H. Stenby. 'Mathematical Simulation of Phase Behavior of Natural Multicomponent Systems at High Pressures With an Equation of State'. In: *Fluid Phase Equilibria* 178.1-2 (2001), pp. 17–32. DOI: 10.1016/S0378-3812(00)00403-9.

[181] D. R. Sandoval, W. Yan, M. L. Michelsen and E. H. Stenby. 'The Phase Envelope of Multicomponent Mixtures in the Presence of a Capillary Pressure Difference'. In: *Industrial & Engineering Chemistry Research* 55.22 (2016), pp. 6530–6538. DOI: 10.1021/acs.iecr.6b00972.

[182] A. Firoozabadi, K. Ghorayeb and K. Shukla. 'Theoretical model of thermal diffusion factors in multicomponent mixtures'. In: *AIChE Journal* 46.5 (2000), pp. 892–900. DOI: 10.1002/aic.690460504.

[183] F. Montel, H. Hoang and G. Galliero. 'Linking up pressure, chemical potential and thermal gradients'. In: *The European Physical Journal E* 42.65 (2019). DOI: 10.1140/epje/i2019-11821-0.

[184] P. Kelemen, S. M. Benson, H. Pilorgé, P. Psarras and J. Wilcox. 'An Overview of the Status and Challenges of CO_2 Storage in Minerals and Geological Formations'. In: *Frontiers in Climate* 1 (2019), p. 9. DOI: 10.3389/fclim.2019.00009.

[185] P. Ringrose. *How to Store CO_2 Underground: Insights from early-mover CCS Projects*. Cham, Switzerland: Springer, 2020. DOI: 10.1007/978-3-030-33113-9.

[186] A. Hamza *et al.* 'CO_2 enhanced gas recovery and sequestration in depleted gas reservoirs: A review'. In: *Journal of Petroleum Science & Engineering* 196 (2021), p. 107685. DOI: 10.1016/j.petrol.2020.107685.

[187] M. Blunt, F. J. Fayers and F. M. Orr. 'Carbon dioxide in enhanced oil recovery'. In: *Energy Conversion and Management* 34.9-11 (1993), pp. 1197–1204. DOI: 10.1016/0196-8904(93)90069-M.

[188] A. Peter, D. Yang, K. I.-I. I. Eshiet and Y. Sheng. 'A Review of the Studies on CO_2BrineRock Interaction in Geological Storage Process'. In: *Geosciences* 12.4 (2022), p. 168. DOI: 10.3390/geosciences12040168.

[189] S. Moslehi and D. Voskov. 'DARTS-well: An Open-Source Coupled Wellbore-Reservoir Numerical Model for Energy Transition Applications'. In: *Sixth EAGE Global Energy Transition Conference & Exhibition (GET 2025)*. 2025. DOI: 10.3997/2214-4609.202521225.

[190] C. Chesnokov *et al.* 'Analytical model for Joule-Thomson cooling under heat exchange during CO_2 storage'. In: *Advances in Water Resources* 190 (2024), p. 104758. DOI: 10.1016/j.advwatres.2024.104758.

[191] H. Ott, S. Roels and K. de Kloe. 'Salt precipitation due to supercritical gas injection: I. Capillary-driven flow in unimodal sandstone'. In: *International Journal of Greenhouse Gas Control* 22 (Jan. 2015). DOI: 10.1016/j.ijggc.2015.01.005.

[192] H. Ott, J. Snippe and K. de Kloe. 'Salt precipitation due to supercritical gas injection:II. Capillary transport in multi porosity rocks'. In: *International Journal of Greenhouse Gas Control* 105 (2021), p. 103233. ISSN: 1750-5836. DOI: 10.1016/j.ijggc.2020.103233.

[193] J. M. Nordbotten and M. A. Celia. 'Similarity solutions for fluid injection into confined aquifers'. In: *Journal of Fluid Mechanics* 561 (2006), pp. 307–327. DOI: 10.1017/S0022112006000802.

[194] M. Hesse, F. Orr and H. Tchelepi. 'Gravity currents with residual trapping'. In: *Journal of Fluid Mechanics* 611 (2008), pp. 35–60. DOI: 10.1017/S002211200800219X.

[195] R. Juanes, C. W. MacMinn and M. L. Szulczewski. 'The footprint of the CO_2 plume during carbon dioxide storage in saline aquifers: Storage efficiency for capillary trapping at the basin scale'. In: *Transport in Porous Media* 82.1 (2010), pp. 19–30. DOI: 10.1007/s11242-009-9420-3.

[196] A. Riaz and H. A. Tchelepi. 'Linear stability analysis of immiscible two-phase flow in porous media with capillary dispersion and density variation'. In: *Physics of Fluids* 16.12 (2004), pp. 4727–4737. DOI: 10.1063/1.1812511.

[197] J. A. Neufeld *et al.* 'Convective dissolution of carbon dioxide in saline aquifers'. In: *Geophysical Research Letters* 37.22 (2010). DOI: 10.1029/2010GL044728.

[198] R. Farajzadeh, P. L. J. Zitha and J. Bruining. 'Enhanced mass transfer of CO_2 into water: Experiment and modeling'. In: *Industrial and Engineering Chemistry Research* 48.13 (2009), pp. 6423–6431. DOI: 10.1021/ie801521u.

[199] M. T. Elenius, J. M. Nordbotten and H. Kalisch. 'Convective mixing influenced by the capillary transition zone'. In: *Computational Geosciences* 18.3-4 (2014), pp. 417–431. DOI: 10.1007/s10596-014-9415-1.

[200] M. A. Nomeli, N. Tilton and A. Riaz. 'A new model for the density of saturated solutions of CO_2-H_2O-NaCl in saline aquifers'. In: *International Journal of Greenhouse Gas Control* 31 (2014), pp. 192–204. DOI: 10.1016/j.ijggc.2014.10.006.

[201] D. Daniel and A. Riaz. 'Effect of viscosity contrast on gravitationally unstable diffusive layers in porous media'. In: *Physics of Fluids* 26.11 (2014). DOI: 10.1063/1.4900843.

[202] Z. Ghorbani, A. Riaz and D. Daniel. 'Convective mixing in vertically-layered porous media: The linear regime and the onset of convection'. In: *Physics of Fluids* 29.8 (2017). DOI: 10.1063/1.4996049.

[203] J. Nordbotten *et al.* 'Uncertainties in practical simulation of CO_2 storage'. In: *International Journal of Greenhouse Gas Control* 9 (2012), pp. 234–242. DOI: 10.1016/j.ijggc.2012.03.007.

[204] J. M. Nordbotten, M. Fernø, B. Flemisch, R. Juanes and M. Jørgensen. *Final Benchmark Description: FluidFlower International Benchmark Study*. July 2022. DOI: 10.5281/zenodo.6807102.

[205] B. Flemisch *et al.* 'The FluidFlower Validation Benchmark Study for the Storage of CO_2'. In: *Transport in Porous Media* 151 (2023), pp. 865–912. DOI: 10.1007/s11242-023-01977-7.

[206] J. M. Nordbotten, M. A. Fernø, B. Flemisch, A. R. Kovscek and K.-A. Lie. 'The 11th Society of Petroleum Engineers Comparative Solution Project: Problem Definition'. In: *SPE Journal* 29.05 (2024), pp. 2507–2524. DOI: 10.2118/218015-PA.

[207] J. M. Nordbotten *et al.* 'Benchmarking CO_2 Storage Simulations: Results from the 11th Society of Petroleum Engineers Comparative Solution Project'. In: (2024). DOI: 10.48550/arXiv.2507.15861.

[208] T. Ajayi, A. Awolayo, J. S. Gomes, H. Parra and J. Hu. 'Large scale modeling and assessment of the feasibility of CO_2 storage onshore Abu Dhabi'. In: *Energy* 185 (2019), pp. 653–670. DOI: 10.1016/j.energy.2019.07.052.

[209] S. Krevor *et al.* 'Capillary trapping for geologic carbon dioxide storage–From pore scale physics to field scale implications'. In: *International Journal of Greenhouse Gas Control* 40 (2015), pp. 221–237. DOI: 10.1016/j.ijggc.2015.04.006.

[210] Y. Wang, C. Vuik and H. Hajibeygi. 'Analysis of hydrodynamic trapping interactions during full-cycle injection and migration of CO_2 in deep saline aquifers'. In: *Advances in Water Resources* 159 (2022). DOI: 10.1016/j.advwatres.2021.104073.

[211] B. Metz, O. Davidson, H. DeConinck, M. Loos and L. Meyer. 'IPCC Special Report on Carbon dioxide Capture and Storage'. In: *Policy Stud.* (2005).

[212] K. Pruess and J. Nordbotten. 'Numerical Simulation Studies of the Long-term Evolution of a CO_2 Plume in a Saline Aquifer with a Sloping Caprock'. In: *Transport in Porous Media* 90 (2011), pp. 135–151. DOI: 10.1007/s11242-011-9729-6.

[213] M. Delshad, X. Kong, R. Tavakoli, S. A. Hosseini and M. F. Wheeler. 'Modeling and simulation of carbon sequestration at Cranfield incorporating new physical models'. In: *International Journal of Greenhouse Gas Control* 18 (2013), pp. 463–473. DOI: 10.1016/j.ijggc.2013.03.019.

[214] A. Riaz, M. Hesse, H. Tchelepi and F. Orr Jr. 'Onset of convection in a gravitationally unstable diffusive boundary layer in porous media'. In: *Journal of Fluid Mechanics* 548 (2006), pp. 87–111. DOI: 10.1017/S0022112005007494.

[215] G. S. Pau *et al.* 'High-resolution simulation and characterization of density-driven flow in CO_2 storage in saline aquifers'. In: *Advances in Water Resources* 33.4 (2010), pp. 443–455. DOI: 10.1016/j.advwatres.2010.01.009.

[216] M. Elenius, D. Voskov and H. Tchelepi. 'Interactions between gravity currents and convective dissolution'. In: *Advances in Water Resources* 83 (2015), pp. 77–88. DOI: 10.1016/j.advwatres.2015.05.006.

[217] O. Eiken *et al.* 'Lessons learned from 14 years of CCS operations: Sleipner, In Salah and Snøhvit'. In: *Energy Procedia* 4 (2011), pp. 5541–5548. ISSN: 18766102. DOI: 10.1016/j.egypro.2011.02.541.

[218] S. Whittaker *et al.* 'IEA GHG Weyburn CO_2 monitoring and storage project summary report 2000-2004'. In: 7th International Conference on Greenhouse Gas Control Technologies. 2004, pp. 15–72.

[219] S. Bachu and D. B. Bennion. 'Chromatographic partitioning of impurities contained in a CO_2 stream injected into a deep saline aquifer: Part 1. Effects of gas composition and in situ conditions'. In: *International Journal of Greenhouse Gas Control* 3.4 (2009), pp. 458–467. ISSN: 1750-5836. DOI: 10.1016/j.ijggc.2009.01.001.

[220] **M. Wapperom**, X. Tian, A. Novikov and D. Voskov. 'FluidFlower Benchmark: Lessons Learned from the Perspective of Subsurface Simulation'. In: *Transport in Porous Media* 151 (2024), pp. 1033–1052. DOI: 10.1007/s11242-023-01984-8.

[221] X. Tian *et al.* 'A History Matching Study for the FluidFlower Benchmark Project'. In: *Transport in Porous Media* 151 (2024), pp. 1113–1139. DOI: 10.1007/s11242-023-02048-7.

[222] G. Hadjisotiriou, J. Sass, **M. Wapperom**, A. Novikov and D. Voskov. 'Impact Assessment of Injection Impurities in the SPE11 Geological Carbon Sequestration Benchmark'. In: *SPE Journal* 1-16 (2026). DOI: 10.2118/223922-PA.

[223] T. LaForce and R. T. Johns. 'Composition routes for three-phase partially miscible flow in ternary systems'. In: *SPE Journal* 10.2 (2005), pp. 161–174. DOI: 10.2118/89438-PA.

[224] F. M. Orr, Jr. *Theory of Gas Injection Processes*. 1st ed. Holte, Denmark: Tie-Line Publications, 2007.

[225] J. Gardner, F. Orr and P. Patel. 'The Effect of Phase Behavior on CO_2-Flood Displacement Efficiency'. In: *Journal of Petroleum Technology* 33.11 (1981), pp. 2067–2081. DOI: 10.2118/8367-PA.

[226] A. H. Falls and W. M. Schulte. 'Features of three-component, three-phase displacement in porous media'. In: *SPE Reservoir Engineering* 7.3 (1992), pp. 377–384. DOI: 10.2118/19387-PA.

[227] R. E. Guzman and F. John Fayers. 'Mathematical Properties of Three-Phase Flow Equations'. In: *SPE Journal* 2.3 (1997), pp. 291–300. DOI: 10.2118/35154-PA.

[228] T. LaForce and R. T. Johns. 'Analytical Theory for Three-Phase Partially Miscible Flow in Ternary Systems'. In: SPE/DOE Symposium on Improved Oil Recovery, Tulsa, Oklahoma. Apr. 2004, SPE-21253–MS. DOI: 10.2118/89438-MS.

[229] F. Neele *et al.* *CO_2 storage feasibility in the P18-6 depleted gas field*. TNO, 2019. URL: https://www.commissiemer.nl/projectdocumenten/00007538.pdf.

[230] J. Sayani, S. Pedapati and B. Lal. 'Phase behavior study on gas hydrates formation in gas dominant multiphase pipelines with crude oil and high CO_2 mixed gas'. In: *Scientific Reports* 10 (2020), p. 14748. DOI: 10.1038/s41598-020-71509-6.

[231] **M. Wapperom**, S. M. Taghinejad, X. Lyu, R. Farajzadeh and D. Voskov. 'A thermodynamically consistent simulation of gas hydrates in porous media using Operator-Based Linearization'. In: *Energy Conversion and Management: X* 30 (2026), p. 101616. DOI: 10.1016/j.ecmx.2026.101616.

[232] J. B. Klauda and S. I. Sandler. 'Global Distribution of Methane Hydrate in Ocean Sediment'. In: *Energy & Fuels* 19.2 (2005), pp. 459–470. DOI: 10.1021/ef049798o.

[233] R. Boswell and T. S. Collett. 'Current perspectives on gas hydrate resources'. In: *Energy & Environmental Science* 4 (2011), pp. 1206–1215. DOI: 10.1039/C0EE00203H.

[234] C. Ruppel and J. Kessler. 'The interaction of climate change and methane hydrates'. In: *Reviews of Geophysics* 55.1 (2017), pp. 126–168. DOI: 10.1002/2016RG000534.

[235] Z. Yin, G. J. Moridis, H. Kiang Tan and P. Linga. 'Numerical analysis of experimental studies of methane hydrate formation in a sandy porous medium'. In: *Applied Energy* 220 (2018), pp. 681–704. DOI: 10.1016/j.apenergy.2018.03.075.

[236] J. Zhao *et al.* 'A Review on Research on Replacement of CH_4 in Natural Gas Hydrates by Use of CO_2'. In: *Energies* 5.2 (2012), pp. 399–419. DOI: 10.3390/en5020399.

[237] T. Dance. 'Assessment and geological characterisation of the CO2CRC Otway Project CO2 storage demonstration site: From prefeasibility to injection'. In: *Marine and Petroleum Geology* 46 (2013), pp. 251–269. DOI: 10.1016/j.marpetgeo.2013.06.008.

[238] C. M. Oldenburg and S. M. Benson. 'CO2 Injection for Enhanced Gas Production and Carbon Sequestration'. In: *SPE International Petroleum Conference and Exhibition in Mexico* (Feb. 2002). DOI: 10.2118/74367-MS.

[239] K. Z. House, D. P. Schrag, C. F. Harvey and K. S. Lackner. 'Permanent carbon dioxide storage in deep-sea sediments'. In: *Proceedings of the National Academy of Sciences* 103.33 (Aug. 2006), pp. 12291–12295. DOI: 10.1073/pnas.0605318103.

[240] V. Soloviev and G. D. Ginsburg. 'Formation of submarine gas hydrates'. In: *Bulletin of the Geological Society of Denmark* 41 (Mar. 1994), pp. 86–94. DOI: 10.37570/BGSD-1995-41-09. URL: https://www.researchgate.net/publication/242259825_Formation_of_submarine_gas_hydrates.

[241] B. J. Anderson *et al.* 'Review of the findings of the Ignik Sikumi CO_2-CH_4 gas hydrate exchange field trial'. In: *8th International Conference on Gas Hydrates (ICGH8-2014)*. 2014.

[242] K. Yamamoto, R. Boswell, T. S. Collett, S. R. Dallimore and H. Lu. 'Review of Past Gas Production Attempts from Subsurface Gas Hydrate Deposits and Necessity of Long-Term Production Testing'. In: *Energy & Fuels* 36 (2022), pp. 5047–5062. DOI: 10.1021/acs.energyfuels.1c04119.

[243] G. Moridis. *User's manual for the HYDRATE v1.5 Option of TOUGH+ v1.5: a code for the simulation of system behaviour in hydrate-bearing geologic media*. University of California, Berkeley, California: Earth Sciences Division, Lawrence Berkeley National Laboratory, 2014. URL: https://tough.lbl.gov/assets/files/02/documentation/TH_Manual_v1.5s.pdf.

[244] *CMG STARS. Computer Modeling Group Ltd, Calgary, Alberta, Canada, 2007*. https://www.cmgl.ca/stars. Accessed: 2023-07-23.

[245] Y. Konno, Y. Masuda, H. Oyama, M. Kurihara and H. Ouchi. 'SS - Gas Hydrate:Numerical Analysis on the Rate-Determining Factors of Depressurization-Induced Gas Production from Methane Hydrate Cores'. In: (May 2010). DOI: 10.4043/20591-MS.

[246] C. M. Yonkofski, J. A. Horner and M. D. White. 'Experimental and numerical investigation of hydrate-guest molecule exchange kinetics'. In: *Journal of Natural Gas Science and Engineering* 35 (2016), pp. 1480–1489. DOI: 10.1016/j.jngse.2016.03.080.

[247] G. Li *et al.* 'Simulation of CO_2 hydrate formation in porous medium and comparison with laboratory trial data'. In: *Energy* 304 (2024), p. 133224. DOI: 10.1016/j.energy.2024.133224.

[248] M. B. Kowalsky and G. J. Moridis. 'Comparison of kinetic and equilibrium reaction models in simulating gas hydrate behavior in porous media'. In: *Energy conversion and management* 48.6 (2007), pp. 1850–1863. DOI: 10.1016/j.enconman.2007.01.017.

[249] B. Bouillot and J.-M. Herri. 'Framework for clathrate hydrate flash calculations and implications on the crystal structure and final equilibrium of mixed hydrates'. In: *Fluid Phase Equilibria* 413 (2016), pp. 184–195. DOI: 10.1016/j.fluid.2015.10.023.

[250] Z. Yin, G. J. Moridis, Z. R. Chong, H. Kiang Tan and P. Linga. 'Numerical analysis of experimental studies of methane hydrate dissociation induced by depressurization in a sandy porous medium'. In: *Applied Energy* 230 (2018), pp. 444–459. DOI: 10.1016/j.apenergy.2018.08.115.

[251] B. Li, X. S. Li and G. Li. 'Kinetic studies of methane hydrate formation in porous media based on experiments in a pilot-scale hydrate simulator and a new model'. In: *Chemical Engineering Science* 105 (Feb. 2014), pp. 220–230. DOI: 10.1016/J.CES.2013.11.016.

[252] G. Moridis and T. Collett. 'Strategies for gas production from hydrate accumulations under various geological and reservoir conditions'. In: *TOUGH Symposium*. 2003.

[253] L. A. García-Navarrete, F. J. Guerrero and E. Santotyo. 'Scope of TOUGH2 and open-DARTS for the simulation of transport in porous-fractured media: an application to enhanced geothermal systems'. In: *Geoenergy Science and Engineering* 258 (2026). DOI: 10.1016/j.geoen.2025.214343.

A

DARTS-flash library structure

A.1. C++

The `cpp` folder in DARTS-flash is divided into subfolders:

- `eos`: EoS implementations
  - `aq`: Fugacity-activity models for aqueous phase
  - `helmholtz`: Helmholtz-form EoS
  - `iapws`: IAPWS-95 and IAPWS-Ice EoS
  - `solid`: PureSolid EoS for Ice, NaCl, CaCl2
  - `vdwp`: VdWP hydrate EoS
- `flash`: Flash implementations and related data structures
- `global`: Global functions and data structures
- `maths`: Math tools
- `phase-split`: Phase split implementations
- `pybind`: Binding code for Python exposure
- `rr`: Rachford-Rice implementations
- `stability`: Stability test

A.1.1. EoS

EoS base class

The `eos` folder contains the EoS definition in the root. The EoS base class defines virtual (abstract) methods:

- `init_PT(P,T)`: initialize EoS computations at given P, T

- `solve_PT(n)`: solve EoS at given P, T, n. Switch for second-order derivatives calculation
- `lnphii(i)`, `dlnphii_d*(i)`, `d2lnphii_d*(i)`: fugacity coefficient of component i, first- and second-order partial derivatives
- `G(P,T,n)`, `H(P,T,n)`, `S(P,T,n)`: total Gibbs energy, enthalpy and entropy. Partial derivatives with respect to P, T, n are evaluated from `dY_dX(P,T,n)`

Implementations of the EoS class are provided for Helmholtz-form models, fugacity-activity models for aqueous phase (Section 3.2), pure solid EoS and VdWP hydrate EoS (Section 3.3). All implementations of EoS child classes have analytical partial derivatives. Note that some thermodynamic models are explicit in mole fractions and compositional derivatives must consequently be converted to partial derivatives with respect to mole numbers.

HelmholtzEoS base class

In addition to the PT-based computations from the EoS, HelmholtzEoS implementations contain additional logic for volume-based EoS:

- `init_VT(V,T)`: initialize EoS computations at given V, T
- `solve_VT(n)`: solve EoS at given V, T, n. Switch for second-order derivatives calculation
- `F()`, `dF_d*()`, `d2F_d*()`: residual Helmholtz free energy, first- and second-order partial derivatives
- `P()`, `dP_d*()`: pressure function and partial derivatives, required in VTn-based computations
- `V()`, `dV_d*()`: volume solver and partial derivatives, required in PT-based computations
- `zeroth_order()`, `first_order()`, `second_order()`: wrappers for solving volume-dependent terms as called in `solve_PT()` and `solve_VT()`, option to skip second-order
- `G(X,T,n)`, `H(X,T,n)`, `S(X,T,n)`, `A(X,T,n)`, `U(X,T,n)`: total Gibbs energy, enthalpy, entropy, Helmholtz energy, internal energy at either PT- or VTn-based specification

Implementations of the HelmholtzEoS are provided for `CubicEoS` in `eos/helmholtz/cubic.*pp` (see Section 3.1) and `IAPWS95` in `eos/iapws/iapws95.*pp`.

A.1.2. Flash

The `Flash` base class contains generic methods for stability and phase split computations:

- `evaluate(p,T,z)`: Main function to evaluate flash at state specification
- `run_stability()`, `run_split()`, `run_loop()`: Flash subroutines
- `get_flash_results()`: Function to wrap flash results into FlashResults object

The base implementation is a sequential stability and phase split algorithm for multiphase *PT*-flashes. Figure A.1 shows a flow chart describing the logic behind the sequential flash loops. The `NegativeFlash` class uses only `run_split()` and checks for negative flashes. The `PXFlash` class uses an inner loop of *PT*-flashes using base `Flash` functionality with an outer loop to solve specified enthalpy or entropy.

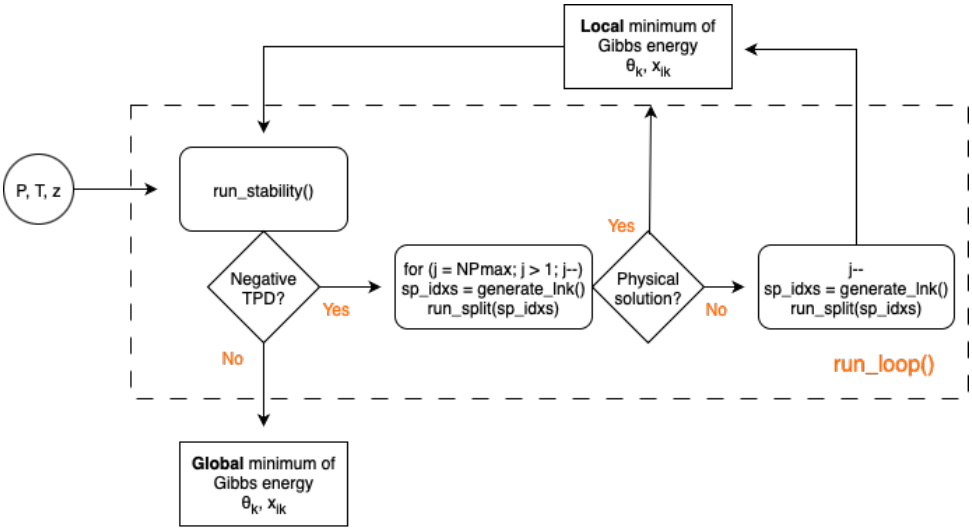

Figure A.1.: Structure of flash loop.

FlashResults

The `FlashResults` struct collects the flash results from a `Flash` call, including partial derivatives of the flash with respect to all primary variables if required (Section 4.2.3). In case of a *PH*- or *PS*-flash, the `FlashResults` of two flashes on both sides of the bracketing strategy are stored, such that the flash results can be combined in case the state is at a transition temperature. Partial derivatives of the *PH*- and *PS*-flashes are calculated using chain rules or by the dedicated logic at transition temperatures, as described in Section 4.4.2.

A.1.3. Stability, PhaseSplit and RR

The stability, phase split and Rachford-Rice procedures are organized in similar structures. `Stability` and `BaseSplit` have a similar solution procedure (Section 4.2):

- `run()`: Main function to run stability test or phase split
- `perform_*()`: Perform SSI/Newton steps with specified variables
- `construct_*()`: Construct matrices and inverse

Phase split has a `TwoPhaseSplit` and a `MultiPhaseSplit` implementation.

The `rr` folder contains solvers for two-phase and multiphase Rachford-Rice equations (Section 4.2). For two phases, the `RR_EqConvex2` equation solving algorithm using convex transformations is the preferred choice, while the multiphase Rachford-Rice is best solved using the minimization approach of `RR_Min`.

A.1.4. Data structures: CompData, FlashParams and EoSParams

The user can set component data, parameters and tolerances for flash and EoS-specific input through `CompData`, `FlashParams` and `EoSParams`.

CompData

The `CompData` struct is located in `global/components.hpp`. It contains component-specific data, such as properties T_c, P_c, M_w and ideal heat capacity coefficients, `CubicEoS`-specific parameters ac (acentric factor) and binary interaction coefficients k_{ij}. For ions, charges are stored.

FlashParams and EoSParams

The `FlashParams` and `EoSParams` structs are defined in `flash/flash_params.`
Flash-specific parameters are stored in `FlashParams`:

- `EoSParams` object for each EoS
- Tolerances and number of iterations for phase split and RR solvers
- Choice of variables for stability test and phase split
- Parameters for `PXFlash`
- Methods to perform property calculations over all phases

EoS-specific parameters for each employed `EoS` object are defined in `EoSParams`:

- Pointer to `EoS` object

- `root_order` and `rich_phase_order` define order of phase types in `FlashResults`
- Tolerances and number of iterations for stability test
- Initial guesses for stability test

A.2. Python

The Python interface of the DARTS-flash package provides an efficient way to perform flash computations over a user-specified parameter space. The `DARTSFlash` base class is a wrapper for C++-based functions, some typical fluid mixtures are predefined in `mixtures.py` and some common phase diagram plotting functionality is included in `plot.py`.

A.2.1. DARTSFlash

The `DARTSFlash` class is a Python wrapper for C++-based functionality of DARTS-flash. To properly define and initialize a `Flash` object, the user should make the following function calls:

- `DARTSFlash()` constructor
- `DARTSFlash.add_eos()` adds EoS object and EoS-specific parameters to `EoSParams` object
- `DARTSFlash.init_flash()` passes the flash-specific parameters. It wraps the defined EoS, EoSParams and FlashParams objects to create an instance of the specified Flash type

After initialization of the `DARTSFlash` object, it can perform single- and multicomponent flashes, hypothetical single-phase properties (thermodynamic potential and PVT-properties) as well as equilibrium properties based on the flash results.

A.2.2. Mixtures

The `mixtures.py` file contains predefined `DARTSFlash` classes for a number of typical mixtures:

- `IAPWS`: pure H_2O at V-L and V-L-Ice conditions
- `VL`: single EoS V-L mixtures
- `VLAq`: (hybrid-EoS) implementation of mixtures involving Aq and V-L phases
- `VLAqH`: extension of `VLAq` class to include hydrate phase(s)

A.2.3. Diagram and Plot

The `Diagram` base class contains methods for drawing line, surface and contour plots. `TernaryDiagram` generates a ternary diagram with scatter, line or contour plots. Predefined plotting functionality for common phase diagram types include:

- `PlotEoS` and `PlotProps`: EoS and phase property plotting
- `PlotFlash`: *PT*-, *PH*-, *PS*-, compositional and ternary phase diagrams and solubility curves

A.3. Tests

The test suite in the `tests` folder is designed to run consistency tests and test partial derivatives for EoS, unit tests of math tools, and integration tests of stability/phase split/RR subroutines and full flash algorithms. There is a set of C++-side tests in `tests/cpp` using `ctest` and Python-side tests in `tests/python` using `pytest`.

C++

The `cpp/unit` folder contains the following test files:

- `test_eos.cpp`: EoS consistency and partial derivatives tests
- `test_flash.cpp`: Tests of Flash and NegativeFlash (PT) including partial derivatives of the flash for different mixtures and conditions
- `test_maths.cpp`: Unit tests for math tools
- `test_phflash.cpp`: Tests of PXFlash implementation (PH) including partial derivatives of the flash for different mixtures and conditions
- `test_rr.cpp`: Tests of RR implementations
- `test_split.cpp`: Tests of standalone PhaseSplit (Two-/Multi-) routines
- `test_stability.cpp`: Tests of standalone Stability routines

Python

The Python tests in the `python` folder make use of `xarray` testing functionality. The results of EoS and Flash computations are compared with reference data in the `ref` folder. The `python` folder contains the following test files:

- `test_api.py`: Test of `DARTSFlash` API consistency
- `test_eos_properties.py`: Tests of EoS properties at PT and VTn
- `test_flash_*.py`: Tests of V-Aq NegativeFlash, pure H_2O, V-L, V-L-Aq and V-L-Aq-sI flashes

Acknowledgements

I would not have been able to complete this work with the same delight if it was not for the many people I have spent this journey with.

Dear **Denis**, I have enjoyed collaborating with you ever since my master project. Your style of leadership, leaving the autonomy for the most part and steering in the right direction when it matters, has given the perfect platform for me to lay out my project and gain expertise in my own branch. I enjoyed our trips to conferences, to Pau and to companies, the bbqs at your place. I am grateful for this time. Dear **Dan**, thank you for having me build on your pioneering work. For letting me bother you with brine and hydrates, and exchange ideas that enhanced my understanding of my own topic. Thank you for hosting me and Denis in Pau with many coffee breaks and good dinners on many occasions, these have been some of the most rewarding trips I have made during my PhD. Dear **Juan**, I appreciate your company during our joint PhD project. You joined one year later than me, but right away we were able to exchange ideas on the project as well as many other things. I am thankful for having you as a friend and colleague and hope we can continue our collaboration.

To the people at TotalEnergies, I appreciate the opportunity to involve in discussions about thermodynamics and simulation. Even though the end product is not yet there, who knows how we can one day contribute. Herve, I appreciate giving the platform and autonomy to follow our research path. Dickson, Martin and Francois were involved at different moments, I am thankful for having met them.

I also express my gratitude to the members of the doctoral committee, thank you for your valuable suggestions for my dissertation. Herve, Tina, Thijs, for your involvement in our workshops and discussions. Wei, the summer school at DTU were two of the most interesting weeks during my PhD and I enjoyed discussing with you on the numerous occasions we met. Rouhi, an important driver behind many projects around me. I admire your honest and humble nature, your sharp vision and engineering approach. Hadi, I admire your ambition and enthusiasm. You bring a fresh sense of curiosity to any discussion that I genuinely enjoy (we only don't run into the same meetings very often). I appreciate all of you for being part of the committee. I also cannot go without acknowledging the late Pacelli, one of the kindest people around at TUD, who was involved during my first year.

It has been great to meet so many people along the way. **George**, thank you for being my paranymph. Early memories of your membership of the DARTS group go back to Texas. You fit right in with a good American accent, podcast voice and a love for cars and Trump jokes, but I have most of all valued your empathy and observations in the right moments. **Sadegh**, I am thankful for having you as a friend and colleague. Great cook, great style, great coffee break and travel companion

that was only served awful food in France (what about London man?). I never met him but your friend Chat also seems cool. **Sajjad**, it was a pleasure to see your curiosity and ambition. To exchange beautiful long rallies at the table tennis table and witness the sheer talent going down the slopes, to share good food, listen to your fast-improving Dutch and talk about important things. To **Aleks**, one of the most versatile guys around. You have been driving many important developments in our team and your critical look always challenge my own views, most often for the better. Now head of the family and the agent as well, all the best. **Ilshat**, what a kind spirit you are. Knows how to fix problems better than what would be good for you. Yet always available for help and never in a rush. It has been a pleasure to have you as a colleague and in Rotterdam, hope you will be available for the team for a lot longer. **Gabriel**, you are on another level in many ways. An eye for niche applications and opportunities (all unknown to me), maintaining incredible fitness. Still, always a good chat and ready to help. Happy for you that you will be back in Brazil all year long now! All the best. **Yuan**, you may have lived the most parallel DARTS-life to me. Always a kind and helpful colleague, adapted to sandwich lunches. I don't know if you and your family will move back to China at some point, but this proves you would fit seamlessly in both worlds. **Jianxin**, another nice guy from the infamous third floor office. I know where to find you at 16.30h, I will be equipped with my new racket. Good luck with the PhD journey, you are onto good things. **Xiaoming**, you are an amazing friend and colleague. It was a pleasure to finish off the never-ending FluidFlower with a few beautiful trips to Norway, be honoured to be your paranymph, share good tea, food and snacks and learn about many languages from a Spanish- and German-speaking Chinese guy. I appreciate you taking the effort to be here again. **Xiaocong**, my friend who was already there to supervise my master project. I discussed new things through teams long after you were finished in Delft, even though you're the only one in the world still using that DARTS version. It was great seeing you in Texas, hope to see you and your family in China one day. **Luisa** and **Artur**, it was great to have you around for the professional software side of things. Above all, you were such nice people to work with, I wouldn't mind if our paths were to cross again.

Agha, thank you for being my paranymph, I feel like I was put high on the loyalty list. I enjoy our frequent discussions about food, honey and football and about topics that come very close to DARTS but just far enough to remain a CMG guy. I think I need a vacation to Baku soon. **Milad**, I wish you moved to our office earlier into my PhD. What a charismatic and sociable guy you are. We enjoyed memorable trips to France and Ilha Grande (feijoada) and spent many lunch and coffee breaks agreeing to disagree that the left is not so bad. On my side in these discussions were **Carolin** and **Patricia**, my wonderful office neighbours. I am sorry for somehow encouraging people to come by my desk to discuss and I hope your (1000 year) forecasts are proving accurate. It was a pleasure to have the company of the two greatest visiting Brazilians, **Gabriel** and **Berilo**, to share a love for music, football and Brazil with. To **Lingfei**, whom I owe thanks to for working on some important matters before I could use it, and for being great company in Pau, Delft and a bunch of conferences. To **Yasmine**, what can we say about hydrates? I did

my best to be on the right side of history. To **Tommy**, it was great having you as a visitor to our team, good luck on your treasure hunt with the 1934 maps. Thank you to my wonderful colleagues, **Entela**, **Willemijn**, the **David**s, **Amin** (sacrificed his sambas to hike on Ilha Grande), **Mahsa**, **Hester** (studied thermodynamics just for the occasion), **Ali Reza**, **Zahra**, **Guofeng** (great to see you back from China), **Lifei**, **Mahnaz**, **Michiel**, countless old and new colleagues to spend lunch (Greek?), coffee and sun breaks with. To the master students that we battled on the pitch but achieved great work with off the pitch. I enjoyed very much being in such international company.

To my friends, many of whom took the time to attend my defense and support throughout the process. My housemates who have become good friends and great people to hang out with. The teammates I spent many hitting and practice sessions with on the tennis court and football pitch to clear my mind. The friends I could travel with, go to concerts and movies, hang out. I appreciate you all and I am thankful for the support and new perspectives on things.

To my family. I am grateful for the unconditional support, even though you may have stopped trying to understand what I am doing a long time ago. I am blessed with a caring family that shows genuine interest in anyone. Grandma, Marjan, Johan and Dyane, Raph and Michelle. Thank you for attending and expressing so much interest, it makes me enjoy this moment even more. Eric, Sterre and my parents, let me kick off our year of milestones. Thank you for the ever warm welcome and for being the foundation of where I am today. I am quitting school.

Curriculum Vitæ

Michiel Wapperom

15-08-1994 Born in Zeist, Netherlands

Education

2006–2012 Gymnasium
KSG De Breul, Zeist

2013-2017 Bachelor of Science in Applied Earth Sciences
Delft University of Technology, Delft

2017-2019 Master of Science in Petroleum Engineering
Delft University of Technology, Delft

2021-2025 PhD. Engineering
Delft University of Technology, Delft
Thesis: A Thermodynamics-Based Simulation Framework for Modelling of Geological CO_2 Sequestration
Promotors: Dr. D.V. Voskov and Dr. D.V. Nichita

List of Publications

Journal publications:

5. **M. Wapperom**, S. M. Taghinejad, X. Lyu, R. Farajzadeh and D. Voskov. 'A thermodynamically consistent simulation of gas hydrates in porous media using Operator-Based Linearization'. In: *Energy Conversion and Management: X* 30 (2026), p. 101616. DOI: 10.1016/j.ecmx.2026.101616

4. J. Heringer, **M. Wapperom**, C. Secuianu, D. Voskov and D. V. Nichita. 'New initialization procedures from phase stability testing in three-phase flash calculations for CO_2-hydrocarbon mixtures'. In: *Fluid Phase Equilibria* 604 (2026), p. 114653. DOI: 10.1016/j.fluid.2025.114653

3. J. Heringer, **M. Wapperom**, C. Secuianu, D. Voskov and D. V. Nichita. 'A robust and efficient augmented free-water flash method for CO_2-water-hydrocarbon mixtures'. In: *Fluid Phase Equilibria* 594 (2025), p. 114378. DOI: 10.1016/j.fluid.2025.114378

2. D. Voskov, I. Saifullin, A. Novikov, **M. Wapperom**, L. Orozco, G. S. Seabra, Y. Chen, M. Khait, X. Lyu, X. Tian, S. de Hoop and A. Palha. 'open Delft Advanced Research Terra Simulator (open-DARTS)'. In: *Journal of Open Source Software* 9.99 (2024), p. 6737. DOI: 10.21105/joss.06737

1. **M. Wapperom**, X. Tian, A. Novikov and D. Voskov. 'FluidFlower Benchmark: Lessons Learned from the Perspective of Subsurface Simulation'. In: *Transport in Porous Media* 151 (2024), pp. 1033–1052. DOI: 10.1007/s11242-023-01984-8

Conference publications:

3. **M. Wapperom**, J. D. dos Santos Heringer, D. Nichita and D. Voskov. 'Thermal-Compositional Simulation of CO_2 Sequestration in Depleted Hydrocarbon Reservoirs'. In: *SPE Reservoir Simulation Conference 2025, Galveston, Texas, USA*. 2025, SPE-223902–MS. DOI: 10.2118/223902-MS

2. **M. Wapperom**, X. Lyu, D. Nichita and D. Voskov. 'A Unified Thermal-Reactive Compositional Simulation Framework for Modeling CO_2 Sequestration at Various Scales'. In: *SPE Reservoir Simulation Conference 2023, Galveston, Texas, USA*. 2023, SPE-212182–MS. DOI: 10.2118/212182-MS

1. **M. Wapperom**, X. Lyu and D. Voskov. 'Accurate Modeling of Near-Wellbore Effects Induced by Supercritical CO_2 Injection'. In: *ECMOR 2022*. 2022. DOI: 10.3997/2214-4609.202244092

Als ik zou willen dat je het begreep,
had ik het wel beter uitgelegd.